Deformation Behaviour and Processing of a Powder Metallurgy Metastable Beta Titanium Alloy

A thesis submitted in fulfilment

of the requirements for the degree

of

Doctor of Philosophy in Materials and Processing Engineering

at

The University of Waikato

by

Qinyang Zhao

THE UNIVERSITY OF
WAIKATO
Te Whare Wānanga o Waikato

2020

Abstract

Metastable beta titanium alloys have drawn great attention and became important structural materials in the aeronautical industry thanks to their overall physical and mechanical performance including ultra-high specific strength, excellent strength-ductility balance, outstanding corrosion resistance, wide service temperature range and great hardenability. However, the lack of enough understanding of the nature of their hot workability and deformation behaviour and insufficient data for optimising the respective hot processing conditions makes it difficult for the titanium manufacturing industry to implement the precise processing of metastable beta titanium alloys with required quality control. Furthermore, the exorbitant manufacturing cost limits their further widespread applications.

Our research group has initiated to fabricate titanium alloys from blended elemental powder mixtures by using the thermomechanical powder consolidation (TPC) approach, and it is demonstrated that the TPC process is a feasible method to cost-effectively produce titanium alloys from powder. In this research, a commercial metastable β titanium alloy, Ti-5Al-5V-5Mo-3Cr (Ti-5553), was fabricated via the TPC process from a blended elemental powder mixture, and its microstructure variation, mechanical properties, deformation behaviours and mechanisms (at both room temperature and elevated temperatures), workability, and post-heat treatment effects were systematically investigated. For comparison, similar research was undertaken for the ingot metallurgy (IM) counterpart Ti-5553 alloy that was prepared by conventional vacuum-arc melting and casting.

The as-consolidated power metallurgy (PM) Ti-5553 alloy has much finer grain size, higher β phase transformation temperature and higher interstitial element (oxygen and nitrogen) content than those of the IM counterpart. The PM alloy exhibits lower load-bearing capacity and tensile ductility than those of the IM alloy during the in-situ tensile test, and the coalesced grain boundary α (GB-α) and widened α″/β microcracks contribute to early brittle failure. The IM alloy has better compatible-slip-deformation capability than the PM alloy, and the serious cracking at the V-shape notch and the microcracks near α/β interfaces together lead to the gradual fracture of the IM alloy specimen. The residual pores and microvoids

existed in the PM alloy have little effects on the alloy's slip deformation and fracture behaviour.

The PM Ti-5553 alloy's flow stress is increased with decreasing the deformation temperature and increasing the strain rate, and vice versa. The alloy's deformation activation energy is 371.65 kJ/mol in the (α+β) region and 226.94 kJ/mol in the β region, respectively. The optimal processing window for PM Ti-5553 alloy is determined as: processing temperature of 900 °C-1050 °C combined with deformation strain rates below 1 s^{-1} with a high deformation degree to at least 70% height reduction. Furthermore, the potential "best" processing condition is recommended as the medium deformation temperature (about 950 °C) and moderate-low strain rate (about 0.01 s^{-1}). Because of flow localization and external cracking, unstable deformation happens when the deformation temperature is lower than 1025 °C and the strain rate is higher than 1 s^{-1}, and this region should be avoided for processing the PM Ti-5553 alloy.

The PM Ti-5553 alloy exhibits lower flow stress, slighter discontinuous yielding phenomenon and less adiabatic temperature rising than its IM counterpart for the same processing condition. Comparing to the IM Ti-5553 alloy, the PM Ti-5553 alloy has lower average activation energy, larger optimal processing windows, smaller flow instability region and higher cracking resistance. Dynamic α globularization and coarsening are the dominated mechanisms for the PM Ti-5553 alloy deformed at low temperature (700 °C to 800 °C) and low strain rate (less than 0.1 s^{-1}), while the IM Ti-5553 alloy is governed by dynamic α precipitation at these conditions. The complete dynamic recrystallization temperature for the PM alloy is about 100 °C lower than that of the IM counterpart, and dynamic recrystallization (DRX) mechanism is controlled by discontinuous dynamic recrystallization (DDRX) for the PM alloy but continuous dynamic recrystallization (CDRX) for the IM counterpart.

Based on the guidance of the hot processing map, the as-consolidated PM Ti-5553 alloy is safely thermomechanically-processed (single uniaxial open-die forging) at the temperatures of 950 °C and 1050 °C, strain rates about 0.5 s^{-1} and 0.01 s^{-1} to the deformation degree of 75%. The alloy forged at the condition of 950 °C/~0.01 s^{-1} (FR-1 alloy) shows the highest mechanical properties (UTS: 1450.9 MPa,

elongation: 3.23% and MH: 492.4 HV), comparing to those processed at either higher temperature or higher strain rate.

Various heat treatments were carried out for the forged PM Ti-5553 alloy to tailor the alloy's microstructure for achieving desired strength-ductility balance. Attributed to the harmonious concurrence of hierarchical α precipitation and heterogeneous grain structure, superior strength-ductility combinations are achieved for the FR-1 alloy after the heat treatment at 700 °C and 750 °C, with the UTS and elongation values of 1386.5 MPa/6.76% and 1252.3 MPa/8.64%, respectively. These strength-ductility combinations are comparable and/or even better than other IM metastable β titanium alloys.

Keywords: Powder metallurgy; Ti-5553 alloy; In-situ tensile observation; Fracture behaviour; Hot deformation behaviour; Microstructural evolution; Deformation mechanisms; Hot processing map; Thermomechanical processing; Heat treatment; Microstructure; Mechanical properties

List of publications

I: Publications in international journals

Publications related to this thesis:

[1] **Qinyang Zhao**, Fei Yang, Rob Torrens, Leandro Bolzoni, Comparison of hot deformation behaviour and microstructural evolution for Ti-5Al-5V-5Mo-3Cr alloys prepared by powder metallurgy and ingot metallurgy approaches, ***Materials & Design***, 169 (2019) 107682.

[2] **Qinyang Zhao**, Fei Yang, Rob Torrens, Leandro Bolzoni, In-situ observation of the tensile deformation and fracture behaviour of powder-consolidated and as-cast metastable beta titanium alloys, ***Materials Science and Engineering A***, 750 (2019) 45-59.

[3] **Qinyang Zhao**, Fei Yang, Rob Torrens, Leandro Bolzoni, Evaluation of the hot workability and deformation mechanisms for a metastable beta titanium alloy prepared from powder, ***Materials Characterization***, 149 (2019) 226-238.

[4] **Qinyang Zhao**, Fei Yang, Rob Torrens, Leandro Bolzoni, Comparison of the cracking behavior of powder metallurgy and ingot metallurgy Ti-5Al-5Mo-5V-3Cr alloys during hot deformation, ***Materials***, 12 (2019) 457.

[5] **Qinyang Zhao**, Fei Yang, Rob Torrens, Leandro Bolzoni, Effect of processing parameters on hot deformation behaviour and microstructural evolution of PM Ti-5553 alloy at a moderate-high strain rate, ***Materials Research***, 22 supl.2 (2019) e20180738.

[6] **Qinyang Zhao**, Fei Yang, Rob Torrens, Leandro Bolzoni, PM versus IM Ti-5Al-5V-5Mo-3Cr alloy in mechanical properties and fracture behaviour, ***Materials Research***, 22 supl.2 (2019) e20180739.

[7] **Qinyang Zhao**, Fei Yang, Rob Torrens, Leandro Bolzoni, Flow behavior and microstructure evolution of powder metallurgy Ti-5553 alloy during 0.1 s^{-1} hot deformation, ***International Journal of Modern Physics B***, 34 (2020) 2040026.

[8] **Qinyang Zhao**, Fei Yang, Rob Torrens, Leandro Bolzoni, Allotropic phase transformation, oxidation behaviour and high-temperature tensile behaviour of powder metallurgy Ti-5553 alloy, ***International Journal of Refractory Metals and Hard Materials***, 90 (2020) 105235.

Co-publications during the PhD research:

[9] **Qinyang Zhao**, Ziqiang Pi, Xin Lu, Yingdong Qu, Leandro Bolzoni, Fei Yang, Superior strength-ductility balance in hot pressed swarf Ti-6Al-4V alloy, ***Materials Science and Engineering A*** (Under review).

[10] Fei Yang, Ziqiang Pi, **Qinyang Zhao**, Stella Raynova, Qianchu Liu, Khan Sharp, Milan Brandt, Leandro Bolzoni, Ma Qian, Strong and ductile Ti-6Al-4V alloy produced by hot pressing of Ti-6Al-4V Swarf, ***JOM***, 71 (2019) 1056-1061.

[11] Fei Yang, Stella Raynova, Ajit Singh, **Qinyang Zhao**, Carlos Romero, Leandro Bolzoni, Producing high-quality titanium alloy by a cost-effective route combining fast heating and hot processing, ***JOM***, 70 (2018) 632-637.

[12] Shuzhi Zhang, J.W. Liu, **Qinyang Zhao**, Changjiang Zhang, Leandro Bolzoni, Fei Yang, Microstructure characterization of a high strength Ti-6Al-4V alloy prepared from a powder mixture of TiH_2 and 60Al40V masteralloy powders, ***Journal of Alloys and Compounds***, 818 (2020) 152815.

[13] Fei Yang, Yu Su, Shanquan Jia, **Qinyang Zhao**, Leandro Bolzoni, Tong Li, Ma Qian, Titanium-doped copper-diamond composites fabricated by hot-forging of powder mixtures or cold-pressed powder preforms, ***JOM*** 71 (2019) 4867-4871.

II: Contributions to international conferences

[1] **Qinyang Zhao**, Fei Yang, Rob Torrens, Leandro Bolzoni, Hot deformation behaviour and mechanisms for PM and IM Ti-5Al-5V-5Mo-3Cr alloys. *9th International Conference on Advanced Materials Processing*, Sep. 2018, Shenyang, China, **Invited lecture**.

[2] **Qinyang Zhao**, Fei Yang, Rob Torrens, Leandro Bolzoni, Effect of processing parameters on hot deformation behaviour and microstructural evolution of PM Ti-5553 alloy. *2nd International Symposium on Materials Manufacturing Processes and Devices*, Feb. 2019, Auckland, New Zealand, **Poster**.

Acknowledgements

First and foremost, I would like to express my heartfelt and immense gratitude to my chief supervisor Dr. Fei Yang for his incredible patience, continuous support and comprehensive guidance in the completion of this research work. He not only provided endless encouragement and tremendous help for my work but opened a window for me to benefit tremendously from his knowledge, experiences, persistence and striving for excellence during the whole PhD study. His rigorous research attitude, exquisite logical thinking and research enthusiasm have become the model for my academic career.

I would like to extend my sincere gratitude to my co-supervisor Dr. Leandro Bolzoni for offering substantial guidance and assistance during this study. His scientific advice and practical instruction played a vital role during my PhD research period. I would also like to give special thanks to my co-supervisor Dr. Rob Torrens for the careful review of the thesis and providing detailed and constructive comments on my English writing. Also, thanks for the opportunity to work as a tutorial assistant for the School of Engineering.

I am grateful to the financial support from the Ministry of Business, Innovation and Employment (MBIE) of New Zealand throughout this project. I appreciate the assistance and help of the research officers Dr. Stella Raynova and Dr. Mingtu Jia in our titanium research group. I am obliged to Helen Turner, Pete Higgins, Jonathan Van Harselaar, Duncan Barnard, Chris Wang, Yuanji Zhang and David Nicholls for their technical assistance. Special thanks to Mary Dalbeth and the people from the School of Graduate Research for their administrative support and kind assistance.

Big thanks to my colleagues in the titanium research group: Carlos Romero Villarreal, Yousef Alshammari, Shanquan Jia, Mohammad Al-Qattan, Abdullah Hussein, Ashok Kumar, Yutao Zhai and Jingnan Ma. My sincere appreciations also go to my mates and friends in China who helped a lot during my research: Dr. Shuzhi Zhang, Wei Sun, Dr. Xuan Wang, Dr. Ziqiang Pi, Yu Su, Lei Lei and Yingchao Guo.

Finally, I am truly thankful to my parents and family members for their endless understanding and support, without which the accomplishment of this work would be impossible.

Table of contents

List of abbreviations

In alphabetical order

AC: air cooling

AFM: atomic force microscopy

AM: additive manufacturing

AOI: areas of interest

ASB: adiabatic shear banding

ATR: adiabatic temperature rising

BCC: body-centred cubic

BE: blended elemental

CDRX: continuous dynamic recrystallization

CG: coarse grains

CHM: cold hearth melting

CIP: cold isostatic pressing

CRSS: critical resolved shear stress

DB: deformation bands

DDRX: discontinuous dynamic recrystallization

DMC: dynamic morphology changing

DMM: dynamic materials model

DRV: dynamic recovery

DRX: dynamic recrystallization

DYP: discontinuous yielding phenomenon

DαG: dynamic α globularization

EBM: electron beam melting

EBSD: electron backscatter diffraction

EDM: electric discharge machining

OM: optical microscopy

EL: elongation

FE-SEM: field emission scanning electron microscope

FL: flow localization

FR-1: alloy processed by route No.1

FR-2: alloy processed by route No.2

FR-3: alloy processed by route No.3

FR-4: alloy processed by route No.4

GA: gas atomization

GB: grain boundary

GB-α: grain boundary α

GDRX: geometric dynamic recrystallization

GOS: grain orientation spread

HAGB: high-angle grain boundary

HCP: hexagonal close-packed

HDH: hydride-dehydride

HIM: increase of misorientation

HIP: hot isostatic pressing

HT: heat treatment

IM: ingot metallurgy

IPF: inverse pole figure

IPS: induction plasma spheroidization

KAM: kernel average misorientation

LAGB: low-angle grain boundary

MIM: metal injection moulding

PA: pre-alloyed

PCHM: plasma cold hearth melting

PM: powder metallurgy

PREP: plasma rotating electrode process

RD: relative density

SAED: selected area electron diffraction

SEM: scanning electron microscopy

SFE: stacking fault energy

SIM: stress-induced martensite

SLM: selective laser melting

SPD: severe plastic deformation

STA: solution treatment and aging

TC: thermal conductivity

TD: theoretical density

TEC: thermal expansion coefficient

TEM: transmission electron microscopy

TMP: thermomechanical processing

TPC: thermomechanical powder consolidation

UFG: ultrafine grains

UTS: ultimate tensile stress

VAR: vacuum arc re-melting

WQ: water quenching

XRD: X-ray diffraction

YS: yield strength

α_p: primary α phase

α_s: secondary α phase

α_t: tertiary α phase

β_{TF}: transformed β structure

List of figures

List of tables

1 Introduction and literature review

1.1 Introduction

Titanium and its alloys have drawn great attention and become the research hotspot in high-performance engineering and biomedical fields, thanks to their excellent balanced properties, such as very high strength-density ratio, outstanding corrosion resistance, wide service temperature range and excellent biocompatibility. Particularly, the branch of metastable beta titanium alloys has been newly developed for commercial aerospace and marine applications, because of their extra merits of ultra-high-strength with reasonable toughness and good hardenability. This makes metastable beta titanium alloys to have the potential to replace those heavier high-strength and stainless steels to be used in the related areas.

However, the high cost for manufacturing titanium alloys and parts limits their wide applications. Great efforts have been made to reduce the cost of titanium products through varied manufacturing approaches. Powder metallurgy (PM) method is regarded as the most effective and reliable way to cost-effectively produce high-quality titanium alloy products. Thus, it becomes quite motivated to produce metastable beta titanium alloy with acceptable performance using PM approaches.

Furthermore, the performances of titanium alloys are highly depended on the thermomechanical processing (TMP) and post-heat treatment (HT) that eliminate the residual pores and adjust the microstructures of the produced titanium alloys. However, metastable beta titanium alloys are extremely sensitive to the thermomechanical processing variables and have a narrow processing window. It becomes crucial to understand the PM metastable beta alloy's deformation behaviour and evaluate its workability, for tailoring the microstructure and optimizing the mechanical properties to meet practical application's requirements.

Besides, PM titanium alloys will inevitably exhibit unique processing characteristics comparing to the conventional ingot metallurgy (IM) counterparts as the different raw feedstock and the manufacturing history. Therefore, the comparison research on the deformation behaviour and microstructure variation mechanisms between PM and IM titanium alloys are supposed to be well addressed.

In this research, a commercial metastable β titanium alloy, Ti-5Al-5V-5Mo-3Cr (Ti-5553), was fabricated via a low-cost approach, thermomechanical powder consolidation (TPC) process, from blended elemental powder mixture. Its microstructure variation, mechanical properties, deformation behaviours and mechanisms (at both room temperature and elevated temperatures), workability, and post-heat treatment effects were systematically investigated. For comparison, similar research has been undertaken for the IM counterpart Ti-5553 alloy that was prepared by conventional vacuum-arc melting and casting.

In this chapter, a comprehensive literature review has been carried out to provide basic knowledge that is related to the current research and identify the primary scientific gaps that need to be addressed. Six parts are included in this chapter: (1) Basic of titanium alloys; (2) Powder metallurgy titanium alloys; (3) Deformation behaviour of metastable beta titanium alloys; (4) Phase transformation of metastable beta titanium alloys; (5) Strengthening and toughening mechanisms of metastable beta titanium alloys; (6) Research motivation and thesis structure.

1.2 Basic of titanium alloys

1.2.1 Fundamental and application

The element of titanium (Ti) lies at the No. 22 place in the periodic table of the elements, belongs to the group of transition metal, and has an atomic mass of 47.87 and electronic configuration of $1s^2 2s^2 2p^2 3s^2 3p^2 3d^2 4s^2$ [1]. Titanium is present in the earth's lithosphere at the level about 0.6%, mainly in the forms of ilmenite ($FeTiO_3$) and rutile (TiO_2), and it is the fourth most abundant metal element (after aluminium, iron and magnesium) [2]. Before 1940s, titanium is hard to be smelted out efficiently for industrial application, and it becomes available until the development of Mg reduction (with $TiCl_4$) approach by Kroll [3].

Generally, pure titanium is light, strong, corrosion-resistant and lustrous with metallic colour. As a kind of structural metallic material, the comparison of basic physical properties between titanium and other common metallic materials is listed in Table 1.1.

Table 1.1 Comparison of the basic physical properties between titanium and other common metals [2].

Physical property	Ti	Fe	Al	Mg	Ni	Cu
Density (g/cm^3)	4.51	7.87	2.70	1.74	8.91	8.96
Melting point (°C)	1668	1538	660	650	1455	1085
Boiling point (°C)	3287	2862	1221	1091	2730	2562
TC (W/m·k)	14.03	83.74	217.71	146.54	59.45	385.18
TEC ($\alpha\times10^{-5}$/°C)	8.5	11.7	23.9	26	13.3	16.5
Young's modulus (GPa)	112.5	200	72.4	43.6	210	130

* The suggestted density is measured at room temperature; TC: thermal conductivity; TEC: thermal expansion coefficient.

It shows that titanium has relatively low density, thermal conductivity (TC) and thermal expansion coefficient (TEC), but higher melting point and boiling point accompanied by moderate Young's modulus, comparing to other metals. Pure titanium undergoes a stable allotropic transformation at the temperature about 882 °C (known as α/β phase transformation temperature). Beta (β) phase exists at high temperature (higher than 882 °C) with a body-centred cubic (BCC) crystal structure, while the low-temperature alpha (α) phase possesses a hexagonal close-packed (HCP) crystal structure. The unit cells showing the crystalline structure of BCC β phase and HCP α phase are shown in Figure 1.1.

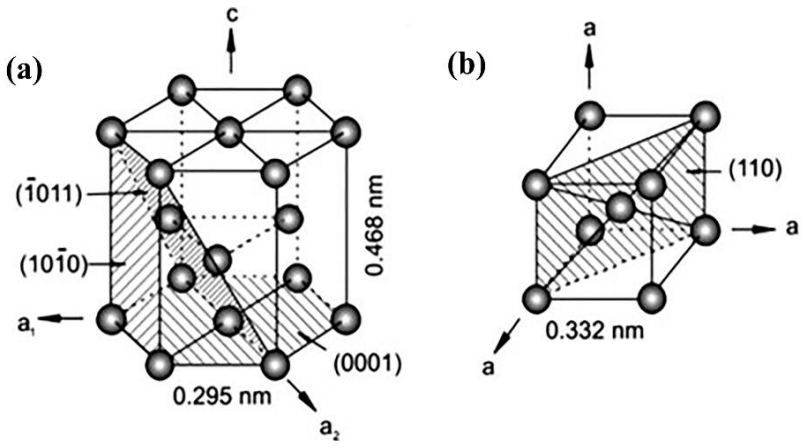

Figure 1.1 The crystalline structures of: (a) hexagonal closed packed unit of alpha-Ti; (b) body-centred cubic unit of beta-Ti [4].

Various elements are always added into titanium matrix to form titanium alloys with desired properties for practical applications. The amount of titanium alloys for engineering applications has increased significantly from 1980s, particularly in the aerospace industry, where the demand for high structural performance and light weight is becoming more and more imperative. Thus, titanium alloy has become

one of the most important materials used for structural and jet engine components on aircrafts. Furthermore, the application level of titanium alloys in the aerospace industry become an index for evaluating the advanced level of specific aircraft. Table 1.2 shows the weight percentage of titanium alloys used in primary USA military aircrafts which have been developed from 1970s to 2000s. It is obvious that the titanium alloy usage in those military aircrafts is continually increased, comparing to that of steel and aluminium.

Table 1.2 The utilization of various structural materials for the famous military aircrafts in recent decades [5].

Aircraft model	F-16	F-18 A/B	F-18 C/D	B1	B2	F-22
First servicing year	1978	1980	1986	1986	1991	2005
Titanium	2%	12%	13%	21%	26%	41%
Composites	3%	9.5%	10%	29%	38%	24%
Steel	5%	15%	16%	9%	6%	5%
Aluminium	83%	50%	50%	41%	19%	15%

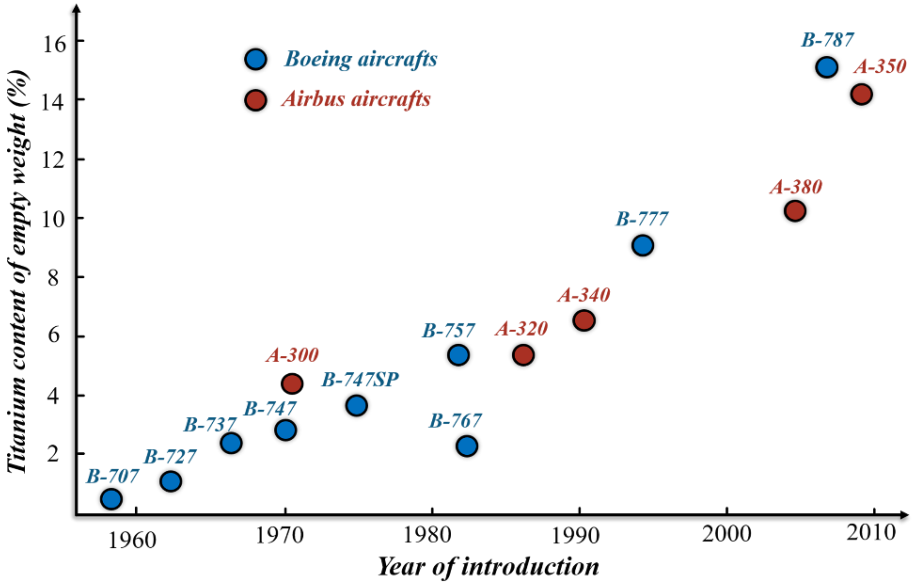

Figure 1.2 The application situation of titanium alloys in Boeing and Airbus civil aircrafts developed in recent decades.

Meanwhile, titanium alloys have also been used more and more in civil aircrafts. Figure 1.2 shows the application situation of titanium alloys in Boeing and Airbus aircrafts from 1960s (summarized from Refs. [2, 6-9]). It is clear that the usage of titanium alloy in civil aircrafts also become larger and larger, especially when it comes to the 21st century. The primary motivations for using titanium alloys to

replace steel and aluminium alloys in the aerospace industry are [10, 11]: (1) titanium alloys have the highest specific strength (strength to density ratio) among common metallic materials, it will help to reduce aircraft's weight with no sacrifice in structural dependability; (2) titanium alloys have a wide service temperature range, so it can keep their high-performance at different environments; (3) titanium alloys show excellent electrochemical compatibility when they are compositing with other materials to form various composite materials which also become important structure materials used in aerospace industry (see Table 1.2).

Titanium alloys also show the highest corrosion resistance among common structural metals, and this leads to their wide applications in chemical transportation [2] and utilization potentiality for marine industry [12]. Besides, titanium alloys are also regarded as the candidate materials in the automotive industry, to help reduce the weight of the heavy parts to improve fuel/electricity efficiency and reduce carbon emissions. The highest biocompatibility of titanium alloys among common metals also makes them very desirable for biomedical applications like body implants and dental replacements [13, 14].

In summary, titanium alloys have already played an important role in aerospace, chemical, biomedical, and marine industries and show a favourable development foreground.

1.2.2 Classification of titanium alloys

As mentioned above, various elements are always added into pure titanium matrix to form varied alloys with improved properties. The alloying elements added in titanium alloys are generally classified into three categories [2]: α stabilizers, β stabilizers and neutral elements. α stabilizers are composed of substitutional element Al and the interstitial elements (O, N, C), and they can increase the β phase transformation temperature and enlarge the α phase region with increasing the solute content. β stabilizers include isomorphous (V, Mo, Nb, Ta) and eutectoid elements (Fe, Mn, Cr, Ni, Cu, Si, H), which can reduce the β phase transformation temperature and enlarge the β phase region with increasing the solute content. There are also some other alloying elements like Zr and Sn that have little effect on the titanium phase transformation and are therefore called neutral elements. The

diagrams, showing the classification of alloying elements and their effects on the phase diagram of titanium alloys, is exhibited in Figure 1.3.

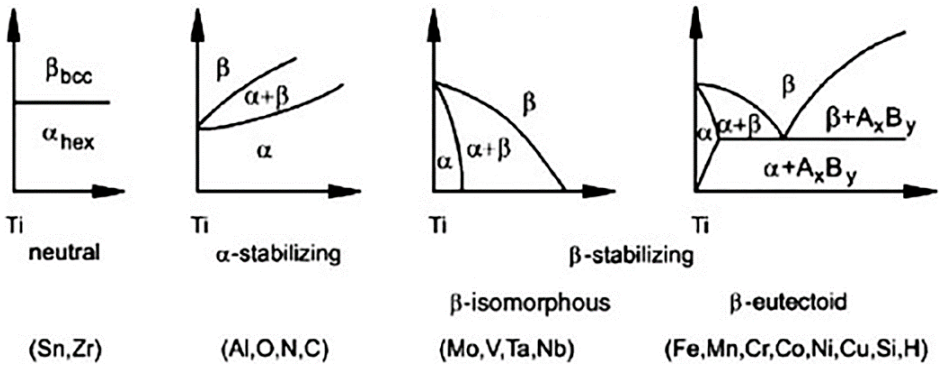

Figure 1.3 The schematic diagrams showing the classification of alloying elements and their effect on the phase diagram of titanium alloys [4].

Considered the content of β phase stabilizers and the stable phase constitutions at room temperature, titanium alloys are primarily classified into three groups [15], i.e. α titanium alloys, α+β titanium alloys and β titanium alloys. The content of β stabilizers in β titanium alloys is more than that in α and α+β titanium alloys, leading to the existence-possibility of extensive β phase at room temperature. β titanium alloys can be further divided into metastable β titanium alloys and stable β titanium alloys, depending on the stability of the β phase at room temperature [16].

The classification of titanium alloys as a function of β stabilizer content is also shown in Figure 1.4, in the form of the pseudo-binary phase diagram. In the diagram, β_c and β_s are the lowest/highest critical contents of β stabilizers for forming metastable β titanium alloys, respectively. The content of β stabilizers in titanium alloys can also be represented by the molybdenum equivalence ($[Mo]_{eq}$) [2], and the molybdenum equivalent equation is as follow:

$$[Mo]_{eq}=[Mo]+0.67[V]+2.9[Fe]+1.6[Cr]+0.28[Nb]+0.44[W]+1.25[Ni]+1.54[Mn]+ .... + (\text{other elements}) \quad (1.1)$$

Metastable β titanium alloys usually have the $[Mo]_{eq}$ value roughly between 10 (β_c) and 25 (β_s). When the $[Mo]_{eq}$ of a titanium alloy is lower than 10, then it can be classified into α+β alloy, while the stable β alloys always have the $[Mo]_{eq}$ of > 25.

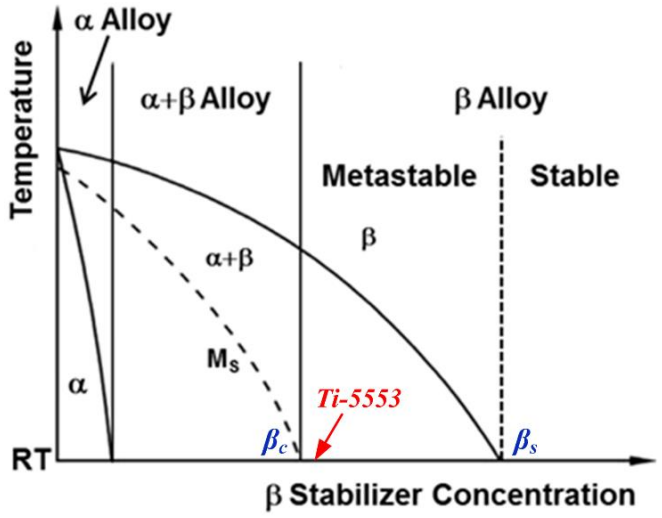

Figure 1.4 Schematic pseudo-binary phase diagram of titanium alloys showing the classification the titanium alloys, where the location of Ti-5553 alloy is also indicated [17].

Different type of titanium alloys are used for varied engineering applications as their different mechanical and/or physical performances. α alloys have a large amount of stable α phase in their microstructure and always exhibit good weldability and creep resistance, so they are mainly employed in piping and high-temperature applications [18]. α+β alloys can display a good combination of mechanical properties including strength, ductility and fatigue resistance, and Ti-6Al-4V alloy is well-known α+β alloy that has been widely used (about 60% of the titanium products) in titanium industry for decades as its great balance of the overall properties [10, 19]. There is only β phase in the stable β alloys, and it is difficult to tailor their microstructures and mechanical properties, leading to their industrial applications are limited.

Comparing to the well-developed α+β alloys, the phase transformation and microstructure variation are more complicated in the metastable β titanium alloys. These features provide the potential to tailor the metastable β alloy's microstructure and optimize its mechanical properties through thermomechanical processing (TMP) and heat treatment, achieving superior combination of balanced mechanical properties, especially for the ideal matching between ultra-high strength and moderate ductility. Therefore, the metastable β alloys have become very promising light structural materials in aerospace industries to replace high-strength/corrosion-resistance steels for its outstanding mechanical performance [20]. Actually, the significant increase of the titanium usage in civil aircrafts in 21st centenary (Figure

1.2) is mainly attributed to the application of metastable β alloys as large and thick structural components.

1.2.3 Ti-5553 metastable β titanium alloy

Ti-1023 (Ti-10V-2Fe-3Al) alloy is the first commercial metastable β titanium alloy developed collectively by Timet, Boeing and Wyman Gordon companies (USA) in 1971 [21]. It shows a very high strength with good ductility and fracture toughness [22], and the alloy has been utilized as the large-scale landing gears of Boeing-777 and Airbus-A380 [23]. However, because of the 2% Fe, segregation (β fleck) is easy to be generated in the microstructure during casting and processing of Ti-1023 alloy, leading to its significant reduction of ductility and fatigue resistance [24, 25]. Russian VT-22 (Ti-5Al-5Mo-5V-1Fe-1Cr) metastable β titanium alloy is also developed in 1970s with steadily ultra-high strength and considerable ductility of up to 1475 MPa and 8% [11, 26]. VT-22 alloy has been widely used in the Russian aircrafts and rockets.

Table 1.3 Typical room temperature mechanical properties (tensile and fracture toughness) of Ti-1023 and Ti-5553 metastable β titanium alloys [26, 27].

Alloy	Solution treatment and aging conditions:		Section size, mm	Typical mechanical properties				
				Ultimate strength, MPa	Yield strength, MPa	Elongation, %	Reduction of area,%	K_{1C}, MPa√m
Ti-1023	STA	Age 482-524°C, 8h, AC	32-140	1287	1202	7.7	26.7	56.5
	STA	752-774°C,2h,WQ+482-538°C,8h,AC	≥254	1256	1182	5.7	13.1	/
	STA	Age 510-566°C, 8h,AC	≤76	1141	1078	13.3	33.4	73-92
	STOA	Overage 566-621°C,8h,AC	≤76	1024	937	18.8	50.5	97-119
Ti-5553	STA	804°C,1h,AC+610°C,8h,AC	178	1294	1218	7	21	48.8
	STA	804°C,1h,AC+660°C,8h,AC	178	1163	1100	13	32	58.4
	STA	832°C,1h,AC+610°C,8h,AC	178	1332	1218	5	9	52.1
	STA	804°C,1h,AC+660°C,8h,AC	178	1189	1104	9	21	65.1

In order to develop a safe aircraft with high performance and reliability, Ti-5553 (Ti-5Al-5Mo-5V-3Cr-0.5Fe) alloy was designed by Boeing (USA) and VSMPO (Russia) in 1996, based on the previous VT-22 alloy by replacing element Fe with more Cr [28, 29]. This alloy has a superior combination of overall engineering performances including excellent mechanical properties (ultra-high-strength, considerable ductility, good fatigue resistance), good workability, excellent

weldability and high hardenability [30-36]. Tables 1.3 and 1.4 show the typical mechanical properties of Ti-1023 and Ti-5553 alloys at room temperature. It is clear that Ti-5553 alloy has a better combination of balanced mechanical properties, such as higher tensile strength-ductility matching, compressive strength and bearing strength, than the Ti-1023 alloy.

Table 1.4 Typical room temperature mechanical properties (compressive, shearing and bearing) of Ti-1023 and Ti-5553 metastable β titanium alloys [26, 27].

Alloy	Heat treatment condition	Product form	Compressive yield strength, MPa	Shear ultimate strength, MPa	Bearing, e/D=1.5		Bearing, e/D=2	
					Ultimate strength, MPa	Yield strength, MPa	Ultimate strength, MPa	Yield strength, MPa
Ti-1023	STA 730°C,1h,AC+580°C,8h,AC	Bar	963	670	1650	1310	2002	1560
Ti-5553	STA[a] 804°C,3h,AC+610°C,8h,AC	Billet	1276	731	/	/	/	/
	STA[b]	Casting	1138	670	/	/	2248	1931

[a] Properties of 178 mm Ti-5553 billet. Corresponding tensile properties: 1294MPa ultimate strength, 1218MPa yield strength, 7% elongation, 21% reduction of area; fracture toughness 49 MPa√m; [b] Properties of cast bulkhead component heat treated to 1158MPa ultimate tensile strength, 1055MPa yield strength, 9% elongation, and 93.9 and 106.4 MPa√m fracture toughness.

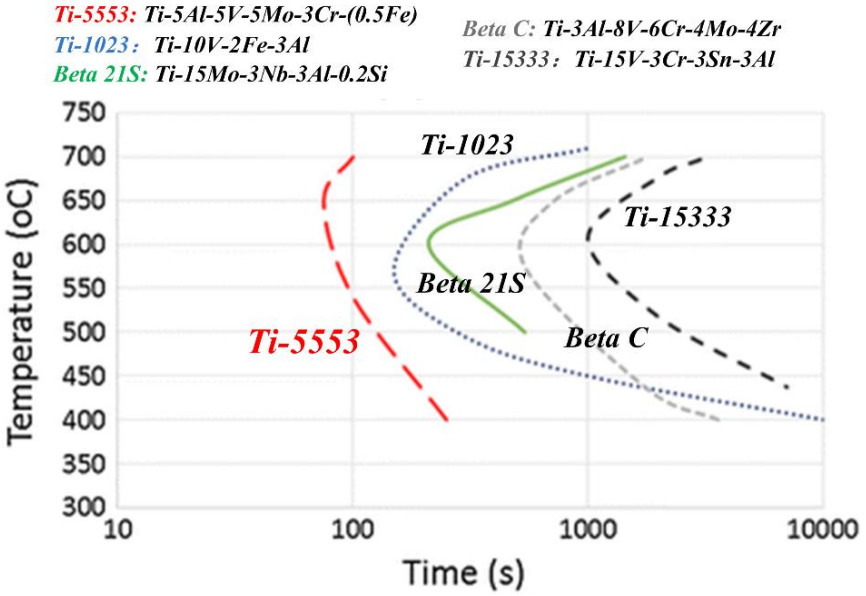

Figure 1.5 TTT C-curves for initial α phase precipitation (lower-temperature metastable phase reactions are omitted for clarity) in some typical metastable β titanium alloys following quenching from respective solution treatment temperatures [20].

Meanwhile, the reduction of Fe element also makes it easier to obtain a uniform and stable microstructure without serious segregation after casting and processing. Moreover, it is more favourable to use Ti-5553 alloy to manufacture large aircraft

components than using Ti-1023 alloy, because of its better hardenability (see the TTT curves in Figure 1.5). The large cross-section Ti-1023 alloy components are usually required well water-quenching to achieve the desired mechanical properties combining post-heat treatment, while the large and thick structural Ti-5553 alloy components are able to be air-cooled for achieving the same result of water-quenching with other metastable β titanium alloys. Additionally, the mechanical performance of Ti-5553 alloy is not as sensitive as that of Ti-1023 alloy to the component's thickness. Ti-1023 alloy components show an obvious reduction of mechanical properties when the component thickness is beyond 76 mm, while the mechanical properties of Ti-5553 components still have very good stability up to the thickness of 150 mm (see the section size of the alloys in Table 1.3) [30, 35, 37]. The excellent hardenability and segregation insensitivity enable it easier to manufacture qualified Ti-5553 alloy structural components by relatively simple/easy procedures, comparing to the former Ti-1023 alloy.

Ti-5553 alloy is even more superior than the widely-used Ti-6Al-4V alloy. Figure 1.6 shows the comparisons of representative tensile properties and fatigue resistance of those two industrial-focused titanium alloys. It is obvious that Ti-5553 has much higher strength and better high-cycle fatigue resistance than those of Ti-6Al-4V alloy.

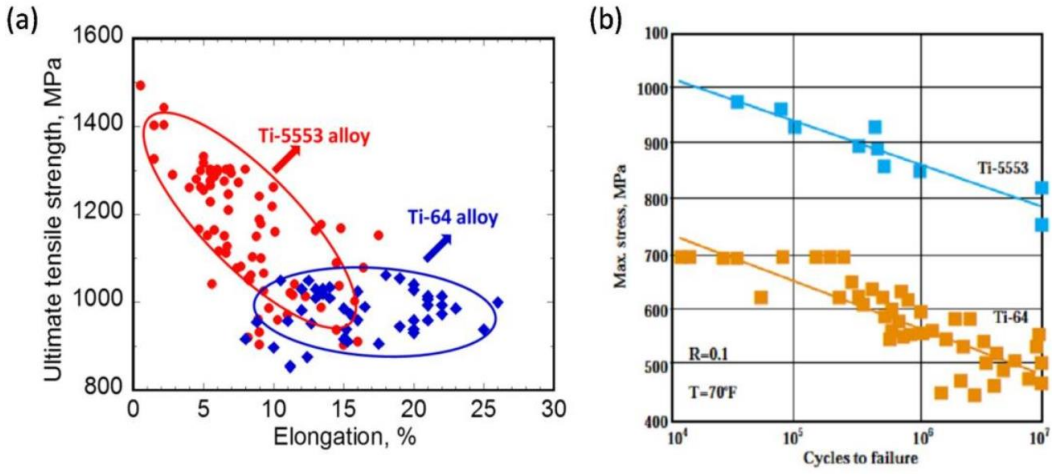

Figure 1.6 The comparisons of mechanical properties between Ti-5553 and Ti-6Al-4V alloys: (a) tensile properties [17, 27]; (b) high-cycle fatigue properties [27, 38].

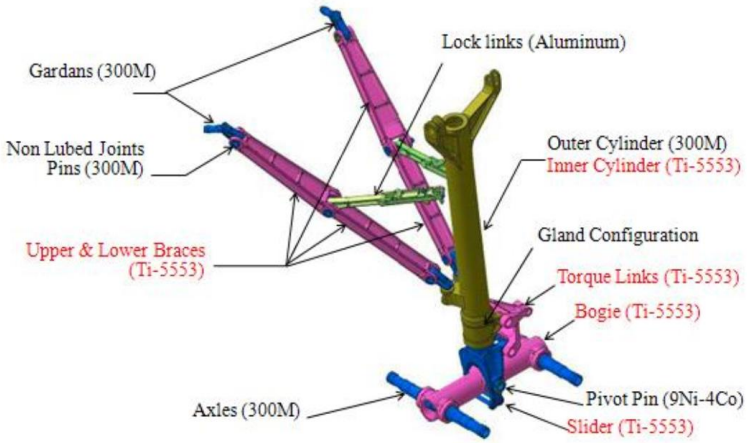

Figure 1.7 The application situation of Ti-5553 alloy in the main landing gear of Boeing 787 aircarft [39].

Nowadays, to meet the requirement of high engineering-structural performance and manufacturing stability, Ti-5553 alloy has been replacing the former Ti-1023 alloy to become critical materials for making large structural components used in aircrafts such as landing gears and frameworks [11]. Figure 1.7 shows the extensive utilization of Ti-5553 alloy in the landing gear system of the Boeing 787 aircraft.

1.3 Powder metallurgy titanium alloys

1.3.1 The high-cost problem of titanium alloy products

Although titanium alloys exhibit outstanding mechanical properties and favourable physical features, the cost for manufacturing titanium alloy products is much higher than that of aluminium alloys, magnesium alloys and steels. Table 1.5 and Figure 1.8 show the comparison of manufacturing cost between titanium, aluminium, magnesium alloys and steel. It is clear that titanium products have much higher production cost at each processing stage, and its finished product cost is about 20-30 times of steel, 10-20 times of aluminium, and 3-5 times of magnesium [40, 41].

Table 1.5 Cost of titanium alloy products compared to other competing metallic materials in US dollar [40, 42].

Material stages	Titanium	Aluminium	Magnesium	Steel
Ore	0.30	0.10	0.01	0.02
Metal	2.00	0.68	0.54	0.10
Ingot	4.50	0.70	0.60	0.15
Sheet	8.00-50.00	1.00-5.00	4.00-9.00	0.30-0.60

Furthermore, the buy-to-fly ratio of titanium alloy components is very low, and it is usually lower than 12:1 for the aerospace industry, which means almost 82% of the titanium become scrap material during the manufacturing [43]. The high cost and low buy-to-fly ratio for manufacturing titanium products have become obstacles to their widespread application, particularly in the civil industries, and about 80% of titanium products are used in aerospace industries (where the high-cost is not an important factor) [44]. Therefore, it is necessary to develop cost-effective manufacturing techniques to produce titanium alloys, and great efforts have been made by both researchers from academia and industry [42, 45-51].

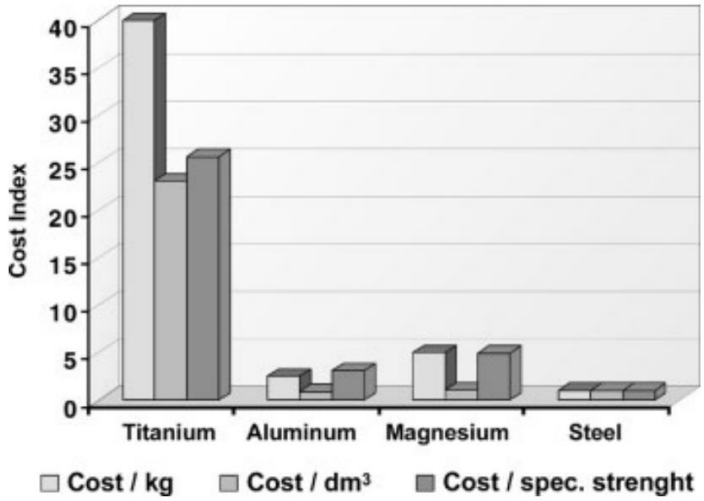

Figure 1.8 Cost comparison for manufacturing variety metal components [52].

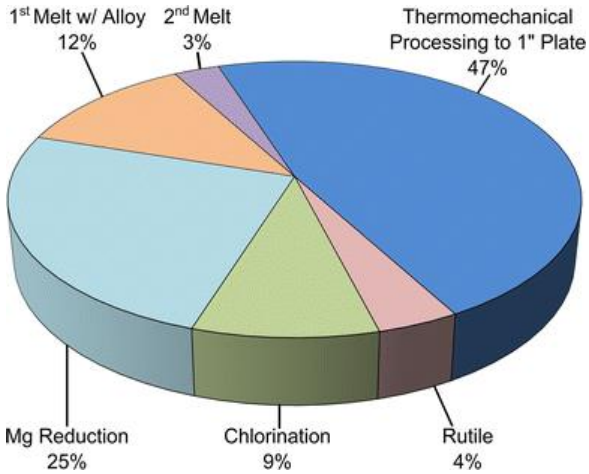

Figure 1.9 Cost breakdown for manufacturing a 25 mm thick Ti-6Al-4V alloy plate [53, 54].

The pie chart (Figure 1.9) demonstrates cost breakdown for manufacturing a 25 mm-thick Ti-6Al-4V alloy plate by conventional ingot metallurgy approach. The high overall cost of titanium products mainly includes metallurgical smelting (38%),

material melting/casting (15%) and material processing (47%). For metallurgical smelting, the well-developed Kroll's process needs Mg agent to produce titanium sponge from titanium tetrachloride [55, 56]. In the case of melting, the high melting point and low thermal conductivity of titanium (see table 1.1) lead to the consumption of high energy to melt sponge titanium and obtain homogeneous melt liquid. Meanwhile, titanium is very susceptible to the impurities, and the melting process needs to be conducted in the protective atmosphere or vacuum to avoid impurity pick-up. Titanium alloys are also hard to be processed and machined due to their narrow processing window and poor thermal conductivity (causing tool wear).

Therefore, great efforts have been made to reduce the cost of titanium parts through a variety of approaches [44]: (1) alternative processes are used to instead of Kroll's process to produce cheaper titanium sponge, like the later-developed FFC-Cambridge [57, 58] and Hunt [59, 60] techniques; (2) near-net-shape forming techniques are used to simplify processing and avoid melting, such as PM approaches; [61-63]; (3) simplifying and adjusting the titanium alloy compositions [64-67], i.e. "alloy plainification", but this is less focused in the titanium scientific community and industry due to the difficulty in achieving equivalent properties compared to those having relatively complicated compositions.

1.3.2 Powder metallurgy of titanium alloys in general

Generally, PM techniques primarily involve the utilization of metallic powders to produce solid and dense alloy products, which avoid the melting and simplify the processing. Besides the significant cost reduction offered by the near-net-shape forming features, PM approaches also make it possible to fabricate complicated-shaped parts with significantly refined grain structure, and PM approaches have been researched and applied for titanium production for decades. A comparison of typical PM titanium manufacturing approaches to the conventional IM processes is given in Figure 1.10.

The initial idea for manufacturing titanium alloy products from powder is using the pre-alloyed (PA) powders to produce near-net-shape and high-performance parts, avoiding expensive processing and massive machining procedures (see the PA

route in Figure 1.10). The feedstock powders utilized in the PA approach are produced from the cast alloy parts through the techniques of gas atomization (GA), plasma rotating electrode process (PREP) or induction plasma spheroidization (IPS) [43]. Subsequently, the spherical PA powder is consolidated and processed at the temperature lower than β phase transformation temperature into near fully-dense bulk materials (usually having a relative density of > 99%) via various approaches, such as hot isostatic pressing (HIP) [63], metal injection moulding (MIM) [68] and additive manufacturing (AM) [69, 70].

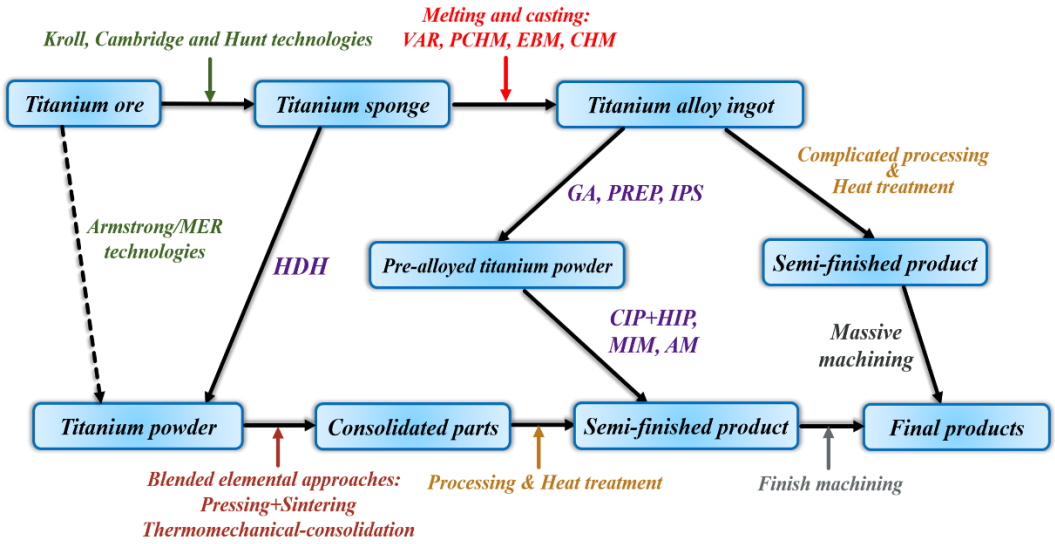

Figure 1.10 Flow chart of conventional IM and common PM approaches for manufacturing titanium alloy products.

The most obvious advantage of PA approach is that the chemical composition of the target titanium alloy has been already achieved, and the consolidation process just helps produce the shaped parts with high density, without considering the homogeneity of the composition. However, PA titanium alloy powders are usually expensive (range from 90$ to 450$ per Kg, depending on the composition and particle size [71]) as they are produced from well-made alloy ingot and atomised by various energy-intensive and time-consuming techniques. Additionally, the subsequent densification processes need expensive facilities and long-processing time. These make the PA-PM titanium alloy products become even more expensive than the IM counterpart products. Therefore, PA approaches are usually used for making near-net and complex-shaped components, which are required to have even better mechanical/physical performance than the IM counterparts and no consideration of the cost.

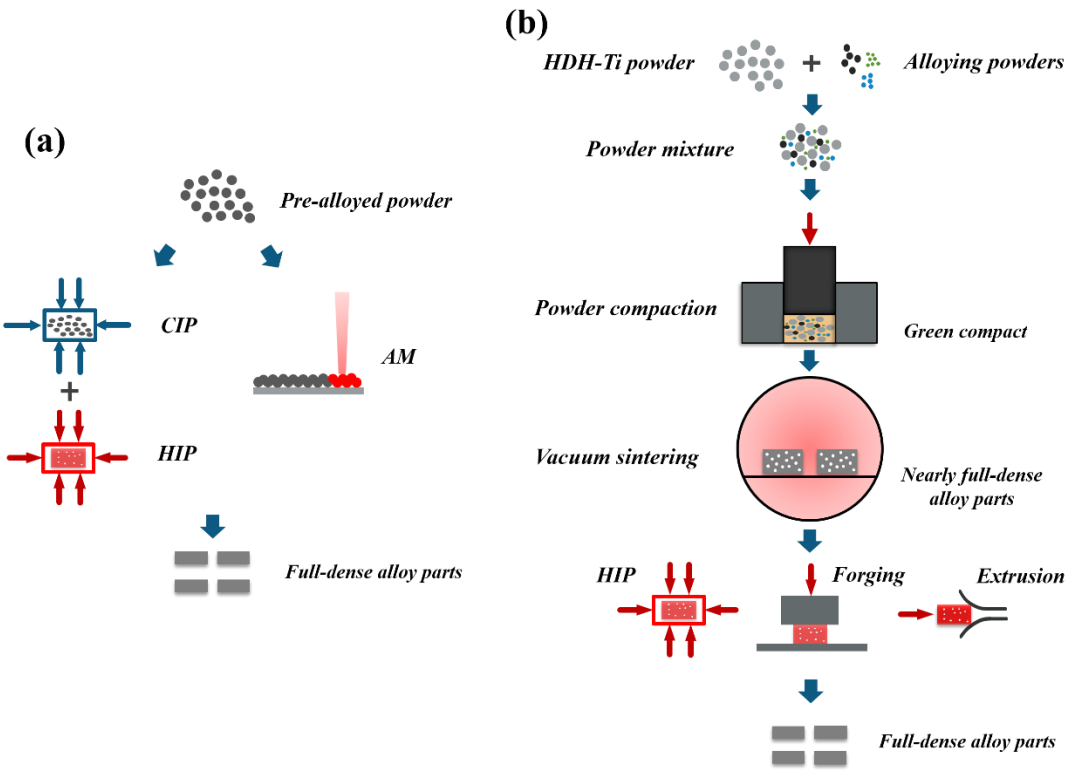

Figure 1.11 Schematic diagrams showing the typical procedures of two main PM titanium approaches: (a) pre-alloyed approach; (b) blended elemental approach.

Different from PA approach, blended elemental (BE) approach is developed to make titanium alloy parts from powder mixture that is consisted of pure titanium powder and other elemental/master-alloy powders. The schematic diagrams showing the typical procedures of PM approach are shown in Figure 1.11. The pure titanium powder is commonly obtained directly from titanium sponge by hydrogenation/dehydrogenation (HDH) reactions and mechanical crushing [72]. As the process of melting/casting and atomization is avoided (see the BE routes in Figure 1.10), the HDH titanium powder is much cheaper than PA powder, and its price is only from 15$ to 40$ per Kg [73]. Together with the near-net-shape forming feature, the significant cost reduction of the titanium products can be achieved with PM-BE approach. In addition, the recently developed Armstrong [74] and MER [44] processes are able to produce even cheaper titanium powders directly from titanium ores, and this enables to further reduce the cost of BE titanium parts. Apart from these aspects, BE approach also has freedom in selecting alloy's composition, which is superior to PA approach.

The BE powder mixture is always pressed (to green compact) and then sintered in vacuum above β phase transformation temperature to homogenize composition and

consolidate the material to near-full dense (usually about 95% relative density). However, the as-sintered BE-PM titanium alloy parts usually have poor mechanical performance caused by high residual porosity, relatively high oxygen level (mainly from HDH powder) and coarse microstructure [75]. Many researches have been conducted to eliminate the residual pores, adjust the microstructure and improve the mechanical properties of by using HIP and TMP methods [43, 76]. Because HIP process is long and needs expensive equipment, while the TMP process together with post-heat treatment are developed to produce BE-PM titanium alloy parts with wrought-like mechanical performance in a cost-effective way.

1.3.3 Thermomechanical powder consolidation approach

Vacuum sintering is usually utilized to consolidate the BE-PM titanium powder compact to produce nearly full-dense titanium parts. Metastable β titanium alloys have been reported to be prepared successfully following this approach. Savvakin et al. [77] investigated the effect of iron contents on the microstructure and mechanical properties of the vacuum-sintered Ti-10V-xFe-3Al metastable β alloy. Similarly, the role of alloying element in the microstructural evolution during multiple-step vacuum-sintering of Ti-5Al-5Mo-5V-2Cr-1Fe (Ti-55521) metastable β alloy has been studied by Carman et al. [78]. Yang et al. [79] and Luo et al. [80] sintered Ti-1023 metastable β alloy and evaluated the mechanical performance of the consolidated alloy. Also, a series of quite comprehensive work was presented by Ahmed et al. [81-87] to establish the processing-microstructure-property relationships for Ti-55521, Ti-5Al-5Mo-5V-1Cr-1Fe (Ti-55511) and Ti-10V-3Fe-3Al (Ti-1033) metastable β alloys and study their deformation behaviour.

However, it can take up to 10 hours to sinter a batch of titanium compacts at the desired temperature from the start of heating to the finish of sintering and cooling the billet down to room temperature. It is really time and energy consuming. These long-time processes lead to high energy consumption and low production efficiency during the manufacturing, which reduces the competitiveness of the BE-PM titanium products in term of their desired cost-effective nature. In order to further reduce the cost of BE-PM titanium products and improve processing efficiency, it is necessary to employ a short and fast approach to consolidate titanium powder compact.

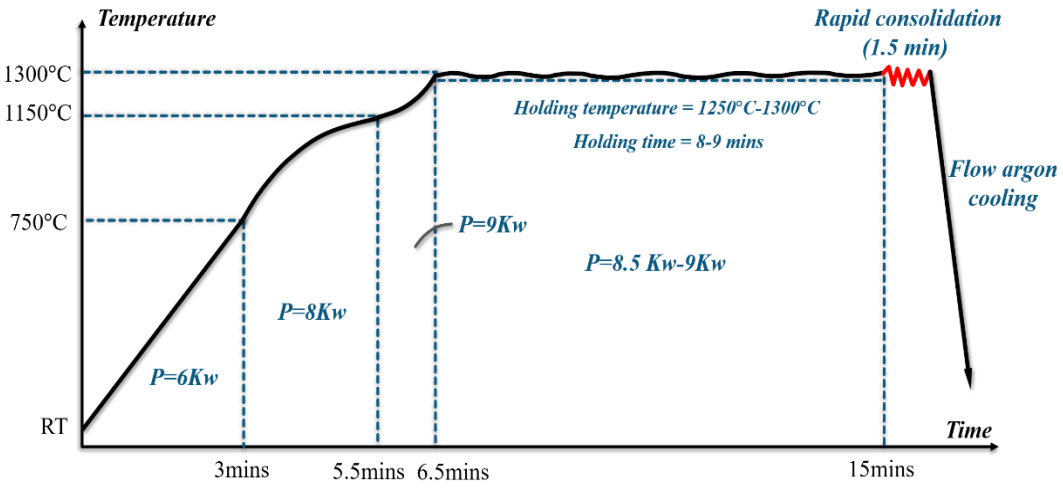

Figure 1.12 Schematic curve illustrating the temperature-time relationship and the detailed parameters during rapid thermomechanical consolidation approach for titanium alloy compact.

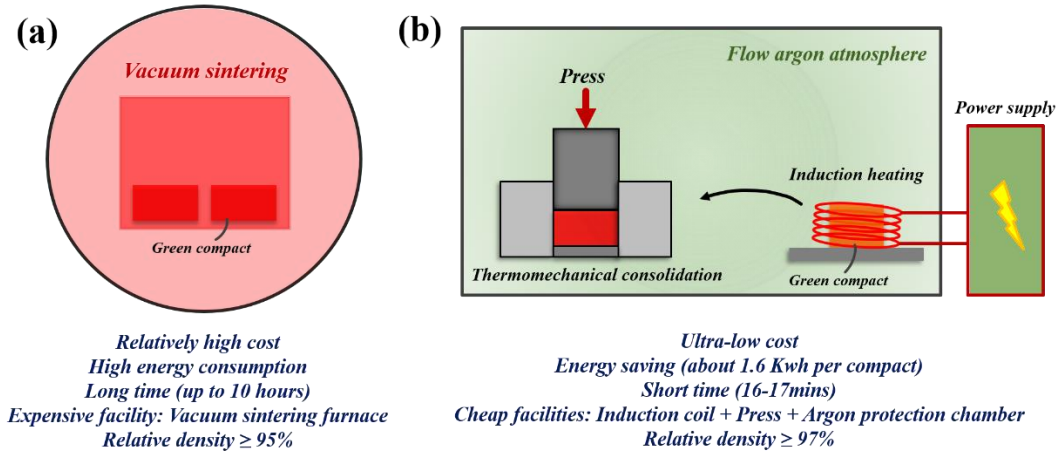

Figure 1.13 Schematic diagrams comparing the features of conventional vacuum sintering and rapid thermomechanical powder consolidation approaches.

Recently, our research group at the University of Waikato (Waikato Centre for Advanced Materials Manufacturing) has initiated a fast approach, thermomechanical powder consolidation (TPC), to fabricate titanium alloys, with a fine and homogeneous microstructure, from blended elemental powder mixtures in a short period [88-93]. In the developed TPC process, the green powder compact is firstly heated up to the desired temperature at a heating rate of about 180-200 °C/min, and kept at the temperature for 7-10 mins. Then a high pressure (about 400MPa) is applied to the hot compact for about 1.5 mins to fully consolidate the material. Furthermore, to limit impurity pick-up, especially for oxygen, the entire process is carried out under argon atmosphere protection. Figure 1.12 shows the

heating curve for consolidating Ti-5553 compact by the TPC approach. It is presented that the overall processing time is only about 16-17 mins with very low electricity consumption of about 1.6 Kwh per compact. Therefore, the cost for TPC approach is much lower than that of the conventional vacuum sintering, and the sketch diagram in Figure 1.13 shows the comparison results. Furthermore, it is also estimated that utilizing the developed TPC route to produce titanium alloy components from BE powder mixture can lead to 30%-40% and 40%-50% cost reduction than conventional IM and PA-PM routes, respectively.

Considering the alloy's microstructure and chemical composition homogeneity, Ti-5553 alloy fabricated by TPC approach shows very fine and homogeneous microstructure (Figure 1.14) and uniform elemental distribution across the observed microstructure without obvious segregation (Figure 1.15).

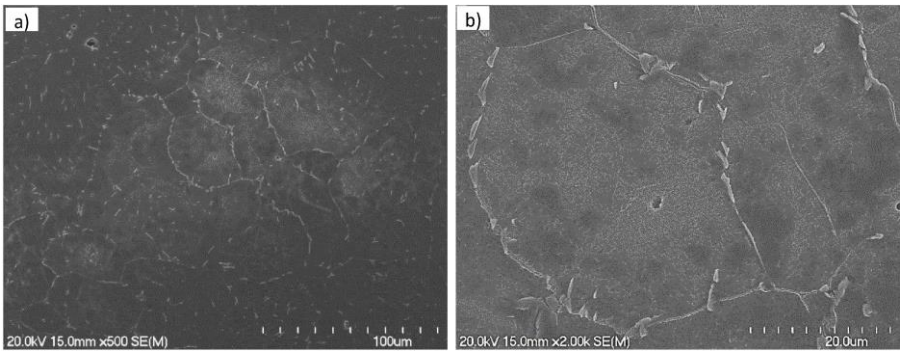

Figure 1.14 SEM microstructures of the Ti-5553 alloy billet after thermomechanical powder consolidation by modified hot processing [88].

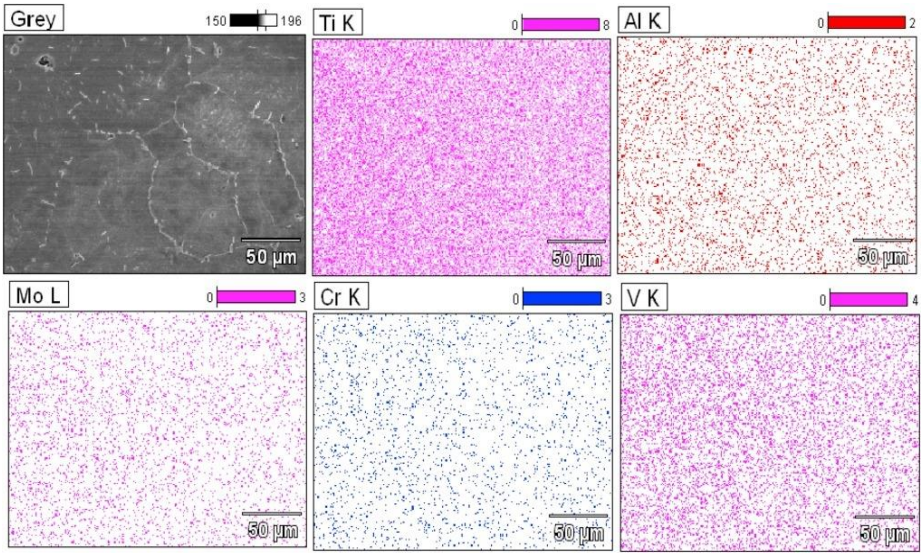

Figure 1.15 EDS mapping analysis of the Ti-5553 alloy billet after thermomechanical powder consolidation by modified hot processing [88].

Meanwhile, it is obvious that there are no undissolved master-alloy powder particles and large-sized pores in the microstructure. It is reported that the relative density of TPC-consolidated titanium alloy billets (Ti-6Al-4V and Ti-5553) can reach 97%-98% [89, 90, 94], which is higher than that of the vacuum-sintered titanium alloys (usually having a value of 92%-96%). All these reported results demonstrate that the TPC approach is feasible to cost-effectively produce titanium alloy products from powder in a short period [90].

The reason why the TPC approach can well consolidate titanium alloy compacts in a short time is mainly attributed to the concurrent effect of external deformation and high-temperature diffusion. This effect makes it possible for elemental powder particles to completely dissolve in the matrix rapidly due to the increase of diffusion rate and particle's movability. On the contrary, a longer time is required for particle dissolving and densifying in the pressure-less vacuum sintering approach.

1.4 Thermomechanical processing (TMP) of metastable β titanium alloys

TMP is a crucial step to shape the metallic materials with desired microstructure and properties for practical applications, and it is also a necessary process for PM titanium alloy to eliminate the residual porosity, modify microstructure, and improve mechanical performance. The practical TMP relies on selecting optimised processing parameters, based on understanding microstructural evolution during processing. Therefore, it is important to understand the deformation behaviour of metastable β titanium alloys to shape the material for practical application.

1.4.1 Titanium alloy processing

TMP is essential for producing qualified titanium alloy products, however, it is difficult to process titanium alloys as their intrinsic crystalline structure and high sensitivity to deformation variables. The specific reason for titanium alloys as hard-to-deformation metallic materials include:

(1) Titanium alloys show a high deformation resistance. This means titanium alloys need to be processed by more powerful facilities than other common materials at identical processing conditions.

(2) The flow stress and deformation behaviour of titanium alloys during TMP are sensitive to processing temperature and strain rate. The small fluctuation of deformation variables can lead to a large flow stress variation. For example, The processing temperature drops 50 °C for Ti-5553 alloy would cause an increase of 100 MPa of the flow stress [31]. Meanwhile, titanium alloys have a very narrow optimal processing window. If the processing temperature is too low and/or the strain rate is too high, the flow stress is dramatically increased and cracking happens during TMP. On the contrary, the high processing temperature and/or low strain rate would lead to the grain seriously grow and the produced products have poor mechanical performance.

(3) Titanium alloys have a very low thermal conductivity (see table 1.1), which would be highly possible to cause serious adiabatic temperature rising during TMP, and this is not safe/desired for hot processing.

(4) Titanium alloys have high viscosity but low flowability during TMP. These features cause a significant increase of friction force between the working piece and the facilities' die, and the alloy's deformation resistance as well.

Metastable β titanium alloys are even more difficult to be processed than other types of titanium alloys due to their complicated/active phase transformation and strong microstructure heredity. Therefore, it is essential to employ effective techniques to identify optimised hot processing windows for metastable β titanium alloys, achieving microstructure and property control.

1.4.2 Development and application of processing map

The processing map technique is a strong and effective tool to evaluate the hot (thermomechanical) workability of a specific metallic material at various processing conditions. It has become a powerful tool to identify the optimal

processing windows and achieve microstructure control for hot processing of titanium alloys.

The concept of processing map was firstly introduced by Ashby and Frost [95, 96] in 1970s, which emphasised on the creep mechanism of metals and ceramics at low-strain-rate deformation. Raj [97] extended the content using the atomic model in 1981, and described the damaged and un-damaged processing region of aluminium alloy with consideration of following mechanisms: cavity formation, wedge cracking, adiabatic shear banding and dynamic recrystallization. However, this kind of processing map failed to be widely applied because of its drawbacks and limitations: (1) the model is only applicable for pure metal or simple alloy at the stable conditions; (2) a large amount of basic parameters (diffusion coefficient, activation energy, grain size distribution, etc.) need to be ensured in advance; (3) the model is only constructed for the abovementioned deformation mechanisms, not applicable to practical TMP that is more complicated.

Prasad et al. introduced the dynamic materials model (DMM) to investigate the hot processing of titanium alloy (Ti-6Al-2Sn-4Zr-2Mo) in 1984 [98], and established the complete processing map that has been widely applied to various metallic materials until now. The DMM-based processing map consists of a flow instability map and a power dissipation map, which bridges the structural change in inside of the material and its exterior plastic deformation. It can be used to predict varying deformation mechanisms and determine optimal/unsafe processing windows [99, 100]. The data required for establishing the processing map is usually obtained via thermal physical simulation that is conducted at contrivable processing conditions. The detailed theoretical basis and procedures for constructing the processing map will be introduced in Chapter 4. As its wide applicability and high reliability, DMM-based processing map has been widely used to investigate the hot deformation behaviour of metallic material including titanium alloys [101-104], steels [105-107], aluminium alloys [108-110], nickel-based superalloys [111-113], magnesium alloys [114-116], copper alloys [117-119], high entropy alloys [120, 121], intermetallic compounds [122-124], metal-based composite materials [125-127] and even functional materials [128].

The processing map technique has been also used for research on metastable β titanium alloys prepared by IM method. Matsumoto et al. [129] constructed the processing maps for single-β phase Ti-5553 alloy to predict its deformation mechanisms. Zhang et al. [130] used the processing maps to identify the safe and unsafe processing regions of Ti-15V-3Cr-3Sn-3Al (Ti-15333) alloy. Wang et al. [131] established the processing map of Ti-4.5Al-6.5Mo-2Cr-2.6Nb-2Zr-1Sn (TB17) alloy and confirmed the alloy's narrow processing window. Zhao et al. [132] utilized the processing maps to identify a feasible hot working region for their newly-developed Ti-5Al-3Zr-4Cr-4Mo-4V (Ti-1300) alloy. Balasubrahmanyam et al. [133] evaluated the hot workability of Ti-10V-4.5Fe-1.5Al alloy at various processing regions using the established processing map. Dikovits et al. [134] revealed the various deformation mechanisms of Ti-5Al-5Mo-5V-3Cr-1Zr (Ti-55531) alloy in a wide range of processing parameters with the assistance of processing maps. Fan et al. [135] correlated the deformation mechanisms with respective processing regions in the established hot processing map and determine optimal processing conditions for the newly-designed Ti-7Mo-3Nb-3Cr-3Al (Ti-7333) alloy. Bai et al. [136] identified safe processing windows for the biomedical Ti-3Zr-2Sn-3Mo-25Nb (TLM) alloy and determined the detailed deformation mechanisms under those safe processing regions.

However, it is seldom reported to apply the processing map technique to research PM titanium alloys, especially for PM metastable β titanium alloy. Attributed to the differences in starting microstructure, chemical composition and physical characteristics between the IM and PM metastable β titanium alloys, it would cause discrepancies in deformation behaviour and hot workability between those two kinds of alloys with identical nominal composition. Furthermore, the knowledge and understanding of hot processing of IM alloys are not likely to be directly applied to the PM counterparts. Thus, it is necessary to investigate the deformation behaviour and hot workability of PM metastable β titanium alloys, and compare to the IM counterparts to determine respective dominated deformation mechanisms during hot processing and identify the differences and possible reasons form fundamental perspective.

1.4.3 Deformation mechanisms of metastable β titanium alloys

With reshaping the workpiece during the TMP process, its interior microstructures experience significant change, which affects the work piece's safe processing and finished mechanical properties. Thus, it needs to understand the deformation mechanisms of metastable β titanium alloys for achieving safe processing and microstructure and property control. Generally, work hardening and flow softening compete against each other and play important roles concurrently during hot processing of metallic materials [137, 138]. As increasing the deformation degree, the dislocations inside the materials interact between to promote the formation of assembled dislocations, leading to the increase of materials' flow strength [139-141]. There are several typical mechanisms for flow softening during hot processing of metallic materials, including grain coarsening, dynamic recovery (DRV), dynamic recrystallization (DRX), dynamic α phase morphology changing and instability flow (localized deformation band, external cracking and etc.) [93, 135, 142]. In this section, the mechanisms of grain coarsening, DRV, DRX and dynamic α phase morphology changing will be discussed as they are dominated mechanisms for hot processing of metastable β titanium alloys.

1.4.3.1 Grain coarsening

Grain coarsening is a spontaneous process during heating and processing of metallic materials, driven by reducing Gibbs energy (total interfacial energy) and proceeded in the form of grain boundary migration and/or grain merging [143-146]. The grain size has a significant effect on the mechanical properties of metastable β titanium alloys (will be discussed in Section 1.6.2). When the alloy is heated or processed in single β region, the grains are easy to grow coarse as the atomic's high self-diffusion coefficient. Moreover, the high processing temperature and long soaking time will accelerate the diffusion processes and grain coarsening effect [147-149]. On the contrary, while the metastable β titanium alloy is processed in α+β region, the grain coarsening process will be impeded remarkably due to the existence of α phase that causes the boundary migration resistance and relatively slow diffusion at a lower temperature [150].

1.4.3.2 Dynamic recovery (DRV) and dynamic recrystallization (DRX)

DRV and DRX are important softening mechanisms for metallic material, and can cause prominent microstructural variation to restructure the processed materials [92, 93, 151-154]. DRV helps to release the strain energy of the processed materials through dislocation sliding and climbing [155], and the dislocations are prone to be rearranged and polygonised to form low angle grain boundary (LAGB) and sub-grain boundary [156, 157]. Depending on the nucleation location and growth mode, DRX is primarily divided into two subcategories, i.e. discontinuous dynamic recrystallization (DDRX) and continuous dynamic recrystallization (CDRX) [158-161]. The nucleation of new DDRX grain is initiated at the prior grain boundary and then the nuclei grow coarse due to the existence of dislocation density gradient [162-164]. For CDRX, the grain nucleation and growth are achieved by the transformation of LAGB into high angle grain boundary (HAGB) in inside of the prior grain [165-167].

DRV is regarded as the mechanism that offers the necessary pre-conditions for the occurrence of DRX. Moreover, DRV is prone to happen in the metallic materials with high stacking fault energy (SFE) such as titanium alloy, aluminium alloy and ferrite steel, where the dislocation movement is much easier than those with low SFE during thermomechanical processing [135]. The deformation distortion energy that is generated during the hot processing is the driving force for both DRV and DRX. Therefore, it is easy to consider that the abundant occurrence of DRV hinders the process of DRX in high-SFE materials such as titanium alloy. However, it is reported that both DDRX and CDRX have been observed in the hot-processed titanium alloys [92, 93, 157, 164, 168-171].

1.4.3.3 Dynamic morphology change of alpha phase

In metastable β titanium alloys, DRV and DRX mainly occur in the β phase matrix, while the microstructure of α phase is varied by different dynamic morphology changing (DMC) ways/approaches. The α DMC in TMP is a very important mechanism for metastable β titanium alloys as it can cause irreversible microstructure changes for α phase, which cannot be reformed through further heat treatment and finally influences the mechanical properties of metastable β alloys (will be discussed in Section 1.6.3). Therefore, DMC of α phase in titanium alloys

has been investigated extensively. The dynamic morphology change of α phase includes fragmentation, globularization, precipitation and coarsening. The fragmentation and globularization mechanisms of α phase have been reported in some metastable β titanium alloys [135, 172-177], while there is no report regarding the dynamic precipitation and coarsening mechanisms in metastable β titanium alloys.

During TMP of metastable β titanium alloys, the α phase with a large aspect ratio is fragmented and globularized due to shearing pressure caused by external force and thermal activation. There are two established modes for describing the dynamic fragmentation and globularization mechanisms: grain boundary separation model and lath shearing model [81, 178-180]. These two models will be further discussed in Chapter 4 and Chapter 5.

It is demonstrated that the deformation mechanisms for titanium alloys are still not clear and there is no united understanding, especially for DRX and DMC of α phase. Furthermore, most of research and finding of the mechanisms are primarily based on ingot metallurgy titanium alloys, and more research need to be conducted on PM titanium alloys and the difference in deformation mechanisms between the IM and PM titanium alloys needs to be investigated and identified as well.

1.5 Phase transformation of metastable β titanium alloys

As mentioned in Section 1.2.2, the mechanical properties of metastable β titanium alloys are highly affected by the complicated phase transformation that causes significant microstructure change during TMP and subsequent heat treatment. Therefore, it becomes necessary to understand the basic regulation and mechanisms for the phase transformation in metastable β titanium alloys. In this section, a brief commentary will be focused on various phase transformations in metastable β titanium alloys including α phase transformation, ω phase transformation and martensite phase transformation.

1.5.1 Alpha phase transformation

The α phases in metastable β titanium alloys can be classified into primary and secondary phases based on the α phase morphology and formation process. The

primary α phase in metastable β titanium alloy is formed by cooling from above β phase transformation temperature and usually has relatively large grain size with an equiaxed and/or lath shape. On the contrary, the fine secondary α phase (having an acicular and/or stripe shape) is usually formed during the annealing or aging processes. There is a strict Burgers orientation relationship between β and α phases [181-183]: $\{0001\}_\alpha // \{110\}_\beta$ and $\langle 11\bar{2}0\rangle_\alpha // \langle 111\rangle_\beta$, as shown in figure 1.16.

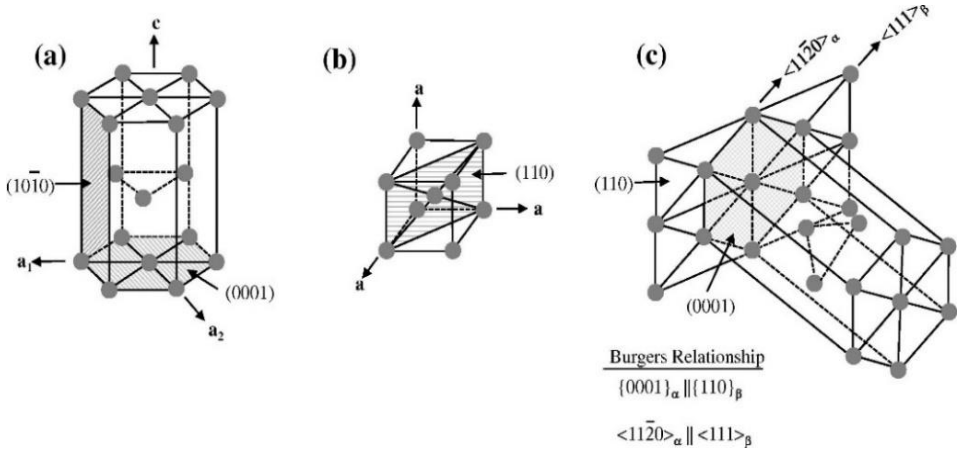

Figure 1.16 Schematic representation of (a) HCP α phase, (b) BCC β phase and (c) the Burgers orientation relationship between α and β phases during phase transformation [184].

When the aging/annealing temperature is high enough (usually higher than 500 °C), α phase can be directly precipitated from the prior β matrix. If the temperature is relatively low (usually less than 500 °C), α phase can be formed with the assistance of metastable phases ω phase and martensite phases [30]. Moreover, the crystalline defects induced by deformation provide a large number of nucleation sites for α phase, and then promoting the precipitation of α phase. For PM metastable β titanium alloy, due to the relatively higher content of the strong α stabilizer (O and N), the α phase transformation and variation mechanisms may be different from IM alloys during TMP and heat treatment, which worth a further investigation.

1.5.2 Omega phase transformation

Frost et al. [185] firstly identified ω phase in the low-temperature aged Ti-Cr and Ti-Mn alloys in 1954, and then the existence of ω phase was also proved in other alloys (Ti, Zr and Hf) [186]. ω phase has HCP crystalline structure but its lattice constants are different from HCP-α phase, as shown in Figure 1.17c. Table 1.6 shows the crystallographic information of common phases in metastable β titanium

alloy. It is widely accepted that ω phase is a transitional phase with a granular shape and nanoscale size in titanium alloys, which can promote the nucleation of dispersed fine α phases (ω-assisted nucleation) [30, 187-189] during heat treatment.

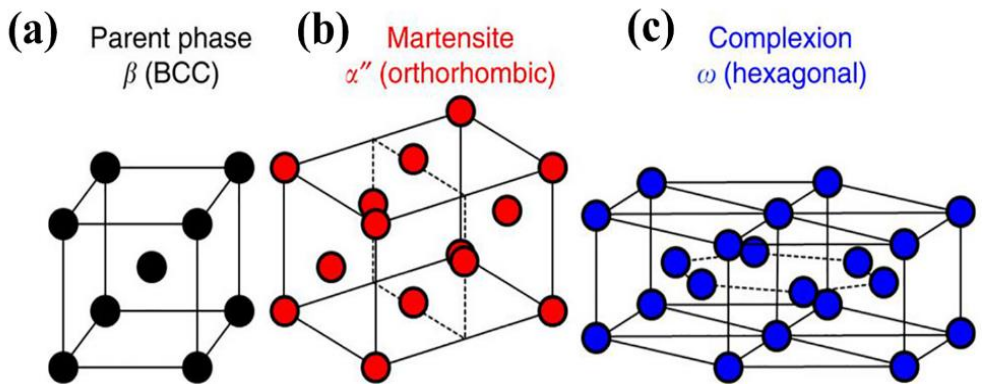

Figure 1.17 The crystalline structures of common metastable phases in metastable β titanium alloys: (a) HCP β phase; (b) Orthorhombic martensite phase; (c) HCP ω phase [190].

Table 1.6 The crystallographic information of common phases in metastable β titanium alloys.

Phases	Space group	Crystalline structure	Lattice constant	Atomic position
α	P63/mmc	HCP	a=2.95, c=4.68 c/a =1.587	(0,0,0); $(\frac{1}{3},\frac{2}{3},\frac{1}{2})$
β	Im3m	BCC	a=3.32	(0,0,0); $(\frac{1}{2},\frac{2}{2},\frac{1}{2})$
ω	P6/mmm	Orthorhombic	a=4.625, c=2.813 c/a =0.608	(0,y,$\frac{1}{4}$); (0,1-y,$\frac{1}{4}$); $(\frac{1}{2},\frac{1+2y}{2},\frac{1}{4})$; $(\frac{1}{2},\frac{1-2y}{2},\frac{3}{4})$
α″	Cmcm	HCP	a=3.01, c=2.813 c/a =1.587	(0,0,0); $(\frac{2}{3},\frac{1}{3},\frac{1+2z}{2})$; $(\frac{1}{3},\frac{2}{3},\frac{1-2z}{2})$

The ω phases in titanium alloys can be divided into two groups according to their formation mechanisms, i.e. athermal ω phase and isothermal ω phase [81, 191-193]. Athermal ω phase is formed during the process of rapid cooling titanium alloy from single β region, while the isothermal ω phase is usually formed during the low-temperature (usually lower than 550 °C) aging process. Athermal ω phase is initiated by the diffusionless shuffle mechanism, but the isothermal ω phase transformation is accomplished based on elemental diffusion processes. ω phase is unstable in the metastable β titanium alloys, and it starts to grow and become coarse

when the temperature is higher than 350 °C and is transformed to α phase gradually while the temperature is above 400 °C.

1.5.3 Martensite phase transformation

Martensite phase transformation is a kind of rapid diffusionless shearing process in metallic materials (such as steels, zirconium alloys and titanium alloys) formed during the rapid cooling from high temperatures, so that the martensite phase has the similar composition with the starting phase but different crystalline structure. For the metastable β titanium alloys, the martensite phase usually is existed as orthorhombic structure (α″) with fine-acicular shape. The crystalline structure and other information of α″ phase are exhibited in Figure 1.17b and Table 1.6, respectively. Furthermore, α″ phase also shows a strict orientation relationship with β phase matrix: $\{001\}_{\alpha''} // \{110\}_{\beta}$ and $\langle 110\rangle_{\alpha''} // \langle 111\rangle_{\beta}$ [194].

In addition, α″ phase can also be generated in the β matrix during low-temperature deformation for some metastable β titanium alloys, and this is so-called stress-induced martensite (SIM) transformation [85, 195]. The formation of quenching α″ phase is highly dependent on the stability of β phase and cooling rate. Besides the β phase stability, both of the deformation degree and deformation strain rate play important roles in the formation of SIM α″ as well. Similar to ω phase, α″ phase is also a kind of very unstable phase in the metastable β titanium alloys, and it is prone to be dissolved and transformed to the stable α phase and/or β phase at elevated temperatures.

1.6 Strengthening and toughening mechanisms of metastable β titanium alloys

There are four primary types of strengthening/toughening mechanisms for the metastable β titanium alloys, including solution strengthening, grain refinement strengthening/toughening, precipitation strengthening/toughening and stress-induced strengthening/toughening. Figure 1.18 schematically illustrates these primary strengthening/toughening mechanisms [196].

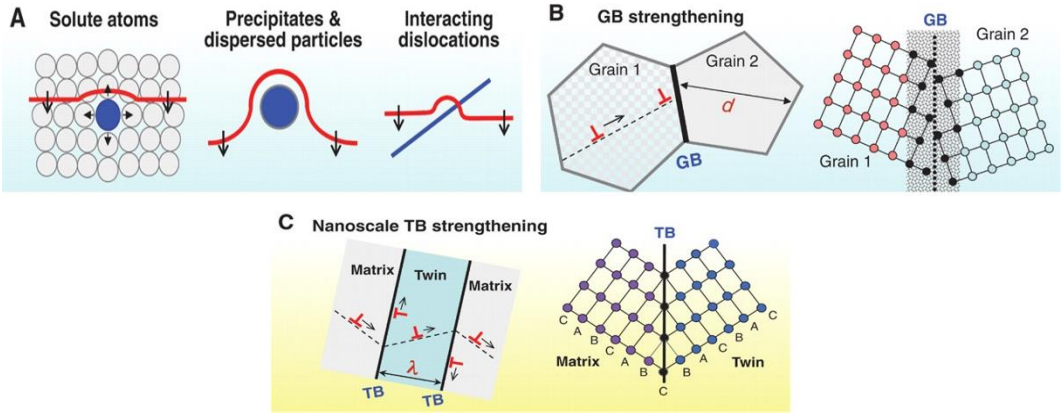

Figure 1.18 Schematic illustration of strengthening mechanisms for structural metals and alloys: (a) solution strengthening and precipitation strengthening; (b) grain refinement strengthening; (c) stress-induced strengthening (nano-twinning) [196].

1.6.1 Solution strengthening

The alloying elements dissolved in the metal matrix cause localized lattice distortion and strengthen the material through the interaction between solute atoms and dislocations movement (see Figure 1.18a) [197-200].

For the metastable β titanium alloys, there are both α stabilizers and β stabilizers in the alloy, so that the solution strengthening exists in both α and β phases. The alloying elements in titanium alloys can be classified into substitutional (Al, Mo, V, Cr, Fe, Nb and etc.) and interstitial (O, N) elements, depending on the atomic positions they occupied in Ti element. The interstitial elements usually show stronger strengthening effect comparing to the substitutional ones. Therefore, the element of O and N can be used to produce ultra-high-strength titanium alloys [45, 201-204] with appropriate content and proper processing routes. However, the high oxygen contents can lead to significant ductility reduction of titanium alloys as well [75, 205-207]. Thus, it is crucial to establish appropriate processing route that combines both TMP and heat treatment to adjust the microstructure of PM metastable β titanium alloys, retaining the strong O(N) strengthening effect and without scarifying the alloy's ductility. Furthermore, the strengthening effect of β stabilizers (Mo, V, Cr, Fe, Nb and etc.) in metastable β titanium alloys is dependent on their contents and interactions.

1.6.2 Grain refinement strengthening and toughening

Grain refinement strengthening/toughening is the most common and effective approach to increase the strength and ductility simultaneously for metallic alloys. This mechanism is used to produce advanced metallic materials with superior mechanical properties [208], such as titanium alloys [209, 210], steels [211], high entropy alloys [212], and copper alloys [213, 214]. Hall-Petch equation describes the relationship between the grain size and the strength for common metallic materials [215, 216]:

$$\sigma_s = \sigma_0 + K \cdot d^{-1/2} \qquad (1.2)$$

where σ_s is the yield stress, σ_0 is the dislocation movement resistance in a single crystal, K is the grain boundary resistance constant and d is the grain size. It is clear that the strength of the materials has a negative exponent relationship to the grain size. The finer the grain size is, the higher the grain boundary density would be, so that the material is strengthened and toughened by hindering the dislocation movement and its deformation compatibility is improved (see Figure 1.18b). Grain refinement of titanium alloys can be achieved by severe plastic deformation (SPD) [217, 218], grain refiner addition [219, 220] and surface treatments [221, 222], among which SPD is the most effective approach for refining the metastable β titanium alloys.

1.6.3 Precipitation strengthening and toughening

Precipitation strengthening mechanism is also known as secondary phase strength strengthening which refers to the strengthening effect caused by the dispersed precipitates in the material's matrix [223]. The dislocation movement of materials is pinned by the precipitations (see Figure 1.18a) during the deformation, and this pining effect is affected by the precipitates' size, amount and distribution. In the metastable β titanium alloys, the common secondary precipitations are ω, α and α″ phases. ω and α″ phases can increase the strength of the alloy remarkably but reduce the ductility seriously. Thus, the precipitation strengthening and toughening in the metastable β titanium alloys are highly relied on the stable α precipitates [224, 225]. By tailoring the morphology and distribution of α precipitation through TMP and

post-heat treatment, an optimized combination of strength and ductility is able to be achieved for the metastable β titanium alloys [226-228].

1.6.4 Stress-induced strengthening and toughening

For the metastable β titanium alloys with excessive β phases, the alloy's strengthening and toughening can also be achieved by applying external stress to cause stress-induced twinning and stress-induced phase transformation effects [229-231]. The stress-generated twinning (see Figure 1.18c) and α″ martensite phase can increase the strength and ductility of metastable β titanium alloys via hindering the dislocation movement and accommodating the plastic deformation. This kind of stress-induced strengthening and toughening approach has also been used for other metallic materials with metastable microstructure, such as steels [232] and high entropy alloys [233-235].

1.7 Motivation and thesis structure

From above review and analysis, we can conclude that extensive investigations have been conducted to optimize the thermomechanical processing, identify the deformation/phase transformation mechanism and improve the mechanical performance of IM-produced metastable β titanium alloys, however, there is only limited work carried out on the PM-manufactured titanium alloys, which make it difficult to well-process the PM metastable β titanium alloys in industrial production. Moreover, the processing-microstructure-properties relationship has not been established for PM titanium alloys, and their deformation/heat-treatment responses and underlying mechanisms are still not clear.

On the other hand, the previously reported PM metastable β titanium alloys were mainly synthesized by the time-consuming and energy-intensive pressing & sintering approach, seldom works refer the short-period and more cost-effective PM alloys. As a result, there is no guidance for the titanium industry to cost-effectively manufacture and process the PM metastable β alloys and produce qualified components for practical application.

Furthermore, the variations of starting microstructure, manufacturing history and physical characteristics shall undoubtedly have significant effects on the alloy's

flow behaviour and hot workability, however, there are almost no studies concerning the differences of hot deformation behaviour and dominated mechanisms between PM and IM titanium alloys with the same nominal composition.

Thus, this PhD research project will address and fill those gaps. We select a typical commercialized metastable β titanium alloy Ti-5553 (nominal composition: Ti-5Al-5Mo-5V-3Cr, in wt.%) to investigate, and the PM Ti-5553 alloy was fabricated by the cost-effective approach (thermomechanical powder consolidation, TPC) from blended-elemental powder mixture. Parallel to this, the IM alloy counterpart was obtained by the conventional arc-remelting and casting approach.

After the fundamental characterizations and investigations of the two alloys, an in-depth investigation on the hot deformation behaviour has been carried out to identify its deformation mechanisms and establish the hot processing map of PM Ti-5553 alloy. Then the constructed hot processing map was employed to provide guidance for optimizing TMP process of the low-cost PM Ti-5553 alloy. Also, the post-heat treatment effect was investigated to tailor the microstructures and achieve balanced mechanical properties for the PM Ti-5553 alloy to meet practical engineering application. In addition, the comparison research on deformation behaviour between the PM and IM Ti-5553 alloys was conducted to determine the underlying deformation mechanisms for IM and PM metastable β titanium alloys.

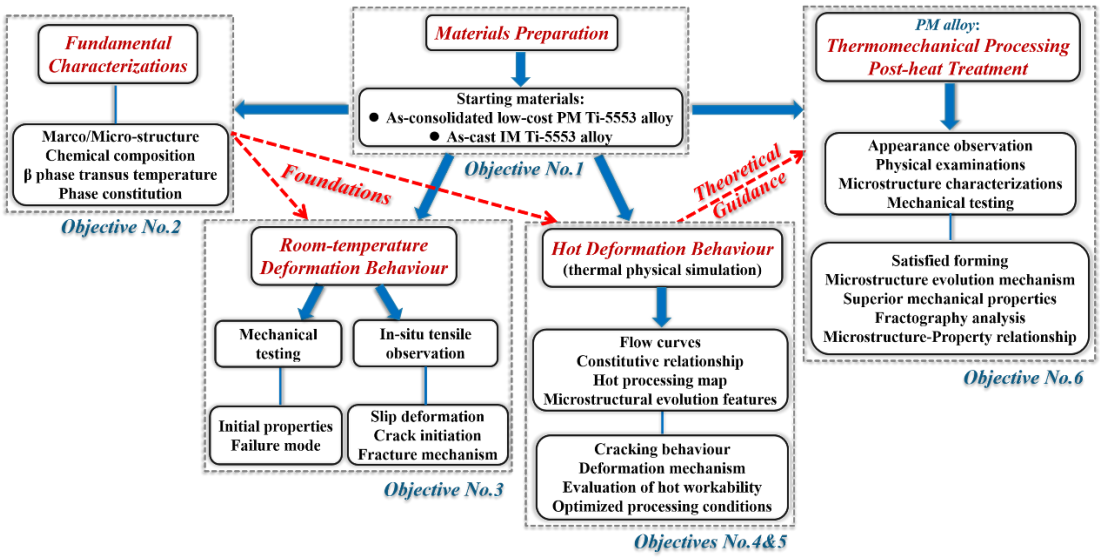

Figure 1.19 Schematic illustration showing the research organization and objectives of this thesis.

The primary contents and objectives of this thesis are shown in Figure 1.19 and briefly summarised below:

(1) Prepare PM Ti-5553 alloy by TPC process from the blended elemental powder mixtures and fabricate its IM counterpart following the conventional titanium ingot metallurgy route (vacuum arc-self-consumable electrode melting technique) (Chapter 2).
(2) Carry out fundamental characterizations (starting microstructure, initial phase constitution, chemical composition, and allotropic phase transformation temperature) on the powder-consolidated PM and as-cast IM Ti-5553 alloys to provide the basic information and understanding for further investigation (Chapter 3).
(3) Conduct room-temperature mechanical testing to obtain the initial mechanical properties and analysis failure mode of powder-consolidated PM and as-cast IM Ti-5553 alloys. Perform the advanced in-situ tensile observation on the two alloys to capture their detailed deformation responses and fracture mechanisms dynamically (Chapter 3).
(4) Investigate hot deformation behaviour, establish constitutive relationship and construct hot processing map for the as-consolidated PM alloy based on the results of thermal physical simulation (Chapter 4).
(5) Compare the hot deformation responses of PM and IM Ti-5553 alloys and contrast their softening mechanisms, then present the comparative evaluation of their hot workability (Chapter 5).
(6) Perform simple TMP on powder-consolidated PM Ti-5553 alloy at the optimized processing conditions obtained in Chapters 4 and 5, and then examine the resultant microstructure and mechanical properties. Apply short-time post-heat treatment on the processed PM alloys to tailor the microstructure and achieve superior strength-ductility balance, and eventually establishing the processing-microstructure-property relationship for the PM Ti-5553 alloy (Chapter 6).

Reference

[1] Titanium, Wikipedia, https://en.wikipedia.org/wiki/Titanium.

[2] G. Lütjering, J.C. Williams, Titanium, Springer, Berlin, 2007.

[3] A.F. Holleman, E. Wiberg, Inorganic Chemistry, Academic Press, San Diego, 2001.

[4] D. Banerjee, J.C. Williams, Perspectives on titanium science and technology, Acta Mater. 61 (2013) 844-879.

[5] C.X. Cao, General development situation of titanium alloys for aviation (In Chinese), Aerosp. Sci. Technol. (2005) 3-6.

[6] M. Peters, J. Kumpfert, C.H. Ward, C. Leyens, Titanium alloys for aerospace applications, Adv. Eng. Mater. 5 (2003) 419-427.

[7] C.X. Cao, Applications of titanium alloys on large transporter (In Chinese), Rare Metal Lett. 1 (2005) 17-21.

[8] V. Giurgiutiu, Chapter 1 - Introduction, in: V. Giurgiutiu (Ed.)Structural Health Monitoring of Aerospace Composites, Academic Press, Oxford, 2016, pp. 1-23.

[9] P. Lequeu, P. Lassince, T. Warner, Aluminum alloy development for the airbus A380-part 1, Adv. Mater. Process. 165 (2007) 3.

[10] R.R. Boyer, An overview on the use of titanium in the aerospace industry, Mater. Sci. Eng. A 213 (1996) 103-114.

[11] R.R. Boyer, R.D. Briggs, The use of β titanium alloys in the aerospace industry, J. Mater. Eng. Perform. 14 (2005) 681-685.

[12] I.V. Gorynin, Titanium alloys for marine application, Mater. Sci. Eng. A 263 (1999) 112-116.

[13] M. Niinomi, Mechanical properties of biomedical titanium alloys, Mater. Sci. Eng. A 243 (1998) 231-236.

[14] X.Y. Liu, P.K. Chu, C.X. Ding, Surface modification of titanium, titanium alloys, and related materials for biomedical applications, Mater. Sci. Eng. R 47 (2004) 49-121.

[15] C. Leyens, M. Peters, Titanium and Titanium Alloys, Fundamentals and Applications, Wiley Online Library, 2003.

[16] I. Weiss, S.L. Semiatin, Thermomechanical processing of beta titanium alloys-an overview, Mater. Sci. Eng. A 243 (1998) 46-65.

[17] B.Z. Jiang, Effect of severe plastic deformation on microstructure in metastable beta Ti alloys, University of Tsukuba, 2015.

[18] I. Weiss, S.L. Semiatin, Thermomechanical processing of alpha titanium

alloys-an overview, Mater. Sci. Eng. A 263 (1999) 243-256.
[19] W. Xu, E.W. Lui, A. Pateras, M. Qian, M. Brandt, In situ tailoring microstructure in additively manufactured Ti-6Al-4V for superior mechanical performance, Acta Mater. 125 (2017) 390-400.
[20] J.D. Cotton, R.D. Briggs, R.R. Boyer, S. Tamirisakandala, P. Russo, N. Shchetnikov, J.C. Fanning, State of the art in beta titanium alloys for airframe applications, JOM 67 (2015) 1281-1303.
[21] S.L. Raghunathan, A.M. Stapleton, R.J. Dashwood, M. Jackson, D. Dye, Micromechanics of Ti-10V-2Fe-3Al: In situ synchrotron characterisation and modelling, Acta Mater. 55 (2007) 6861-6872.
[22] M. Jackson, N.G. Jones, D. Dye, R.J. Dashwood, Effect of initial microstructure on plastic flow behaviour during isothermal forging of Ti-10V-2Fe-3Al, Mater. Sci. Eng. A 501 (2009) 248-254.
[23] W. Chen, Z. Song, L. Xiao, Q. Sun, J. Sun, P. Ge, Effect of prestrain on microstructure and mechanical behavior of aged Ti-10V-2Fe-3Al alloy, J. Mater. Res. 24 (2011) 2899-2908.
[24] H.B. Bomberger, F.H. Froes, The melting of titanium, JOM 36 (1984) 39-47.
[25] Z.B. Zhou, Y. Fei, M.J. Lai, H.C. Kou, H. Chang, G.Q. Shang, Z.S. Zhu, J.S. Li, L. Zhou, Microstructure and mechanical properties of new metastable β type titanium alloy, T. Nonferr. Metal. Soc. 20 (2010) 2253-2258.
[26] S.L. Nyakana, J.C. Fanning, R.R. Boyer, Quick reference guide for β titanium alloys in the 00s, J. Mater. Eng. Perform. 14 (2005) 799-811.
[27] J.K. Fan, Microstructural study of the β to α phase transformation induced by thermo-mechanical treatments in metastable β Ti-5553 alloy, Université de Lorraine, 2016.
[28] N.G. Jones, R.J. Dashwood, M. Jackson, D. Dye, β Phase decomposition in Ti-5Al-5Mo-5V-3Cr, Acta Mater. 57 (2009) 3830-3839.
[29] P. Barriobero-Vila, G. Requena, S. Schwarz, F. Warchomicka, T. Buslaps, Influence of phase transformation kinetics on the formation of α in a β-quenched Ti-5Al-5Mo-5V-3Cr-1Zr alloy, Acta Mater. 95 (2015) 90-101.
[30] S. Nag, R. Banerjee, R. Srinivasan, J.Y. Hwang, M. Harper, H.L. Fraser, ω-Assisted nucleation and growth of α precipitates in the Ti-5Al-5Mo-5V-3Cr-0.5Fe β titanium alloy, Acta Mater. 57 (2009) 2136-2147.
[31] N.G. Jones, R.J. Dashwood, D. Dye, M. Jackson, Thermomechanical processing of Ti-5Al-5Mo-5V-3Cr, Mater. Sci. Eng. A 490 (2008) 369-377.

[32] J.C. Fanning, Properties of TIMETAL 555 (Ti-5Al-5Mo-5V-3Cr-0.6Fe), J. Mater. Eng. Perform. 14 (2005) 788-791.
[33] N. Jones, R. Dashwood, M. Jackson, D. Dye, Development of chevron-shaped α precipitates in Ti-5Al-5Mo-5V-3Cr, Scripta Mater. 60 (2009) 571-573.
[34] S. Shekhar, R. Sarkar, S.K. Kar, A. Bhattacharjee, Effect of solution treatment and aging on microstructure and tensile properties of high strength β titanium alloy, Ti-5Al-5V-5Mo-3Cr, Mater. Des. 66 (2015) 596-610.
[35] H. Schwab, F. Palm, U. Kuhn, J. Eckert, Microstructure and mechanical properties of the near-beta titanium alloy Ti-5553 processed by selective laser melting, Mater. Des. 105 (2016) 75-80.
[36] K. Hua, X.Y. Xue, H.C. Kou, J.K. Fan, B. Tang, J.S. Li, Characterization of hot deformation microstructure of a near beta titanium alloy Ti-5553, J. Alloys Compd. 615 (2014) 531-537.
[37] V.C. Opini, K.N. Campo, M.G. Mello, E.S.N. Lopes, R. Caram, Effect of partial replacement of V with Nb on phase transformations and mechanical properties of Ti-5553 alloy, Mater. Lett. 220 (2018) 205-208.
[38] S. Veeck, D. Lee, R. Boyer, R. Briggs, The castability of Ti-5553 alloy: Its microstructure and properties, J. Adv. Mater. 37 (2005) 40-45.
[39] G. Tomchik, Overview of titanium applications on advanced commercial transports, AeroMat Conference, unpublished research, 2006.
[40] K. Faller, F.H. Froes, The use of titanium in family automobiles: Current trends, JOM 53 (2001) 27-28.
[41] F.H. Froes, M.N. Gungor, M.A. Imam, Cost-affordable titanium: The component fabrication perspective, JOM 59 (2007) 28-31.
[42] F.H. Froes, H. Friedrich, J. Kiese, D. Bergoint, Titanium in the family automobile: the cost challenge, JOM 56 (2004) 40-44.
[43] Z.Z. Fang, J.D. Paramore, P. Sun, K.S.R. Chandran, Y. Zhang, Y. Xia, F. Cao, M. Koopman, M. Free, Powder metallurgy of titanium-past, present, and future, Int. Mater. Rev. 63 (2017) 407-459.
[44] C.X. Cui, B.M. Hu, L.C. Zhao, S.J. Liu, Titanium alloy production technology, market prospects and industry development, Mater. Des. 32 (2011) 1684-1691.
[45] A. Devaraj, V.V. Joshi, A. Srivastava, S. Manandhar, V. Moxson, V.A. Duz, C. Lavender, A low-cost hierarchical nanostructured beta-titanium alloy with high strength, Nat. Commun. 7 (2016) 11176.
[46] A.D. Hartman, S.J. Gerdemann, J.S. Hansen, Producing lower-cost titanium

for automotive applications, JOM 50 (1998) 16-19.
[47] M. Ashraf Imam, F.H.S. Froes, Low cost titanium and developing applications, JOM 62 (2010) 17-20.
[48] Z. Liang, J.S. Miao, T. Brown, A.K. Sachdev, J.C. Williams, A.A. Luo, A low-cost and high-strength Ti-Al-Fe-based cast titanium alloy for structural applications, Scripta Mater. 157 (2018) 124-128.
[49] E. Calvert, B. Wynne, N. Weston, A. Tudball, M. Jackson, Thermomechanical processing of a high strength metastable beta titanium alloy powder, consolidated using the low-cost FAST-forge process, J. Mater. Process. Technol. 254 (2018) 158-170.
[50] S.H. Hong, Y.J. Hwang, S.W. Park, C.H. Park, J.T. Yeom, J.M. Park, K.B. Kim, Low-cost beta titanium cast alloys with good tensile properties developed with addition of commercial material, J. Alloys Compd. 793 (2019) 271-276.
[51] J. Wang, Z. Qin, F. Xiong, S. Wang, X. Lu, C. Li, Design and preparation of low-cost $\alpha+\beta$ titanium alloy based on assessment of Ti-Al-Fe-Cr system, Mater. Sci. Eng. A 732 (2018) 63-69.
[52] O. Schauerte, Titanium in automotive production, Adv. Eng. Mater. 5 (2003) 411-418.
[53] E.H. Kraft, Summary of emerging titanium cost reduction technologies, EHK technologies, Oak Ridge National Laboratory, 2003.
[54] N.S. Weston, F. Derguti, A. Tudball, M. Jackson, Spark plasma sintering of commercial and development titanium alloy powders, J. Mater. Sci. 50 (2015) 4860-4878.
[55] W. Kroll, The production of ductile titanium, J. Electrochem. Soc. 78 (1940) 35-47.
[56] S. Jiao, H. Zhu, Novel metallurgical process for titanium production, J. Mater. Res. 21 (2011) 2172-2175.
[57] G.Z. Chen, D.J. Fray, T.W. Farthing, Direct electrochemical reduction of titanium dioxide to titanium in molten calcium chloride, Nature 407 (2000) 361-364.
[58] M. Ma, D.H. Wang, W.G. Wang, X.H. Hu, X.B. Jin, G.Z. Chen, Extraction of titanium from different titania precursors by the FFC Cambridge process, J. Alloys Compd. 420 (2006) 37-45.
[59] D.J. Fray, Novel methods for the production of titanium, Int. Mater. Rev. 53 (2008) 317-325.

[60] W.S. Zhang, Z.W. Zhu, C.Y. Cheng, A literature review of titanium metallurgical processes, Hydrometallurgy 108 (2011) 177-188.
[61] Y. Liu, L.F. Chen, H.P. Tang, C.T. Liu, B. Liu, B.Y. Huang, Design of powder metallurgy titanium alloys and composites, Mater. Sci. Eng. A 418 (2006) 25-35.
[62] F.H. Froes, S.J. Mashl, V.S. Moxson, J.C. Hebeisen, V.A. Duz, The technologies of titanium powder metallurgy, JOM 56 (2004) 46-48.
[63] F.H. Froes, D. Eylon, Powder-metallurgy of titanium-alloys, Int. Mater. Rev. 35 (1990) 162-182.
[64] C. Romero, S. Raynova, F. Yang, L. Bolzoni, Ultrafine microstructures in eutectoid element bearing low-cost Ti-Fe alloys enabled by slow bainite formation, J. Alloys Compd. 769 (2018) 226-232.
[65] Y. Alshammari, F. Yang, L. Bolzoni, Low-cost powder metallurgy Ti-Cu alloys as a potential antibacterial material, J. Mech. Behav. Biomed. Mater. 95 (2019) 232-239.
[66] X. Li, K. Lu, Improving sustainability with simpler alloys, Science 364 (2019) 733-734.
[67] X. Li, K. Lu, Playing with defects in metals, Nat. Mater. 16 (2017) 700-701.
[68] G.A. Wen, P. Cao, B. Gabbitas, D. Zhang, N. Edmonds, Development and design of binder systems for titanium metal injection molding: an overview, Metall. Mater. Trans. A 44A (2013) 1530-1547.
[69] X. Zhao, S. Li, M. Zhang, Y. Liu, T.B. Sercombe, S. Wang, Y. Hao, R. Yang, L.E. Murr, Comparison of the microstructures and mechanical properties of Ti-6Al-4V fabricated by selective laser melting and electron beam melting, Mater. Des. 95 (2016) 21-31.
[70] D.D. Gu, W. Meiners, K. Wissenbach, R. Poprawe, Laser additive manufacturing of metallic components: materials, processes and mechanisms, Int. Mater. Rev. 57 (2012) 133-164.
[71] C.F. Yolton, F.H. Froes, 2-Conventional titanium powder production, in: M. Qian, F.H. Froes (Eds.)Titanium Powder Metallurgy, Butterworth-Heinemann, Boston, 2015, pp. 21-32.
[72] D.P. Barbis, R.M. Gasior, G.P. Walker, J.A. Capone, T.S. Schaeffer, 7-Titanium powders from the hydride-dehydride process, in: M. Qian, F.H. Froes (Eds.)Titanium Powder Metallurgy, Butterworth-Heinemann, Boston, 2015, pp. 101-116.
[73] M. Qian, Y.F. Yang, M. Yan, S.D. Luo, Design of low cost high performance

powder metallurgy titanium alloys: Some basic considerations, Key Eng. Mater. 520 (2012) 24-29.
[74] W. Chen, Y. Yamamoto, W.H. Peter, S.B. Gorti, A.S. Sabau, M.B. Clark, S.D. Nunn, J.O. Kiggans, C.A. Blue, J.C. Williams, B. Fuller, K. Akhtar, Cold compaction study of Armstrong Process® Ti-6Al-4V powders, Powder Technol. 214 (2011) 194-199.
[75] H.T. Wang, Z.Z. Fang, P. Sun, A critical review of mechanical properties of powder metallurgy titanium, Int. J. Powder Metall. 46 (2010) 45-57.
[76] P. Kumar, K. Chandran, Strength-ductility property maps of powder metallurgy (PM) Ti-6Al-4V alloy: A critical review of processing-structure-property relationships, Metall. Mater. Trans. A 48A (2017) 2301-2319.
[77] D.G. Savvakin, A. Carman, O.M. Ivasishin, M.V. Matviychuk, A.A. Gazder, E.V. Pereloma, Effect of iron content on sintering behavior of Ti-V-Fe-Al near-β titanium alloy, Metall. Mater. Trans. A 43 (2011) 716-723.
[78] A. Carman, L.C. Zhang, O.M. Ivasishin, D.G. Savvakin, M.V. Matviychuk, E.V. Pereloma, Role of alloying elements in microstructure evolution and alloying elements behaviour during sintering of a near-β titanium alloy, Mater. Sci. Eng. A 528 (2011) 1686-1693.
[79] Y.F. Yang, S.D. Luo, G.B. Schaffer, M. Qian, Sintering of Ti-10V-2Fe-3Al and mechanical properties, Mater. Sci. Eng. A 528 (2011) 6719-6726.
[80] S.D. Luo, Y.F. Yang, G.B. Schaffer, M. Qian, Warm die compaction and sintering of titanium and titanium alloy powders, J. Mater. Process. Technol. 214 (2014) 660-666.
[81] M. Ahmed, T. Li, G. Casillas, J.M. Cairney, D. Wexler, E.V. Pereloma, The evolution of microstructure and mechanical properties of Ti-5Al-5Mo-5V-2Cr-1Fe during ageing, J. Alloys Compd. 629 (2015) 260-273.
[82] M. Ahmed, D. Wexler, G. Casillas, O.M. Ivasishin, E.V. Pereloma, The influence of β phase stability on deformation mode and compressive mechanical properties of Ti-10V-3Fe-3Al alloy, Acta Mater. 84 (2015) 124-135.
[83] M. Ahmed, D.G. Savvakin, O.M. Ivasishin, E.V. Pereloma, The effect of cooling rates on the microstructure and mechanical properties of thermo-mechanically processed Ti-Al-Mo-V-Cr-Fe alloys, Mater. Sci. Eng. A 576 (2013) 167-177.
[84] M. Ahmed, D.G. Savvakin, O.M. Ivasishin, E.V. Pereloma, The effect of ageing on microstructure and mechanical properties of powder Ti-5Al-5Mo-5V-

1Cr-1Fe alloy, Mater. Sci. Eng. A 605 (2014) 89-97.
[85] M. Ahmed, D. Wexler, G. Casillas, D.G. Savvakin, E.V. Pereloma, Strain rate dependence of deformation-induced transformation and twinning in a metastable titanium alloy, Acta Mater. 104 (2016) 190-200.
[86] M. Ahmed, D.G. Savvakin, O.M. Ivasishin, E.V. Pereloma, The effect of thermo-mechanical processing and ageing time on microstructure and mechanical properties of powder metallurgy near β titanium alloys, J. Alloys Compd. 714 (2017) 610-618.
[87] M. Ahmed, A.A. Gazder, A.A. Saleh, D. Wexler, E.V. Pereloma, Stress-Induced Twinning and Phase Transformations during the Compression of a Ti-10V-3Fe-3Al Alloy, Metall. Mater. Trans. A 48A (2017) 2791-2800.
[88] F. Yang, B. Gabbitas, M. Dore, A. Ogereau, S. Raynova, L. Bolzoni, On microstructural evolution and mechanical properties of Ti-5Al-5V-5Mo-3Cr alloy synthesised from elemental powder mixtures, Mater. Chem. Phys. 211 (2018) 406-413.
[89] F. Yang, S. Raynova, A. Singh, Q.Y. Zhao, C. Romero, L. Bolzoni, Producing high-quality titanium alloy by a cost-effective route combining fast heating and hot processing, JOM 70 (2018) 632-637.
[90] F. Yang, B. Gabbitas, Feasibility of producing Ti-6Al-4V alloy for engineering application by powder compact extrusion of blended elemental powder mixtures, J. Alloys Compd. 695 (2017) 1455-1461.
[91] F. Yang, Z.Q. Pi, Q.Y. Zhao, S. Raynova, Q. Liu, K. Sharp, M. Brandt, L. Bolzoni, M. Qian, Strong and ductile Ti-6Al-4V alloy produced by hot pressing of Ti-6Al-4V swarf, JOM 71 (2019) 1056-1061.
[92] Q.Y. Zhao, F. Yang, R. Torrens, L. Bolzoni, Comparison of hot deformation behaviour and microstructural evolution for Ti-5Al-5V-5Mo-3Cr alloys prepared by powder metallurgy and ingot metallurgy approaches, Mater. Des. 169 (2019) 107682.
[93] Q.Y. Zhao, F. Yang, R. Torrens, L. Bolzoni, Evaluation of the hot workability and deformation mechanisms for a metastable beta titanium alloy prepared from powder, Mater. Charact. 149 (2019) 226-238.
[94] Q.Y. Zhao, F. Yang, R. Torrens, L. Bolzoni, In-situ observation of the tensile deformation and fracture behaviour of powder-consolidated and as-cast metastable beta titanium alloys, Mater. Sci. Eng. A 750 (2019) 45-59.
[95] M.F. Ashby, A first report on deformation-mechanism maps, Acta Metall. 20

(1972) 887-897.
[96] H.J. Frost, M.F. Ashby, Deformation mechanism maps: the plasticity and creep of metals and ceramics, Pergamon press, 1982.
[97] R. Raj, Development of a processing map for use in warm-forming and hot-forming processes, Metall. Mater. Trans. A 12 (1981) 1089-1097.
[98] Y.V.R.K. Prasad, H.L. Gegel, S.M. Doraivelu, J.C. Malas, J.T. Morgan, K.A. Lark, D.R. Barker, Modeling of dynamic material behavior in hot deformation-forging of Ti-6242, Metall. Mater. Trans. A 15 (1984) 1883-1892.
[99] Y.V.R.K. Prasad, T. Seshacharyulu, Processing maps for hot working of titanium alloys, Mater. Sci. Eng. A 243 (1998) 82-88.
[100] Y.V.R.K. Prasad, Processing maps: a status report, J. Mater. Eng. Perform. 12 (2003) 638-645.
[101] Q. Liu, S.X. Hui, K. Tong, Y. Yu, W.J. Ye, S.Y. Song, Investigation of high temperature behavior and processing map of Ti-6Al-4V-0.11Ru titanium alloy, J. Alloys Compd. 787 (2019) 527-536.
[102] D. Zhou, W. Zeng, J. Xu, W. Chen, S. Wang, Characterization of hot workability for a near alpha titanium alloy by integrating processing maps and constitutive relationship, Adv. Eng. Mater. 21 (2019) 1801232.
[103] C.L. Li, P.L. Narayana, N.S. Reddy, S.W. Choi, J.T. Yeom, J.K. Hong, C.H. Park, Modeling hot deformation behavior of low-cost Ti-2Al-9.2Mo-2Fe beta titanium alloy using a deep neural network, J. Mater. Sci. Technol. 35 (2019) 907-916.
[104] J.Z. Sun, M.Q. Li, H. Li, Deformation behavior of TC17 titanium alloy with basketweave microstructure during isothermal compression, J. Alloys Compd. 730 (2018) 533-543.
[105] K.A. Babu, S. Mandal, C.N. Athreya, B. Shakthipriya, V.S. Sarma, Hot deformation characteristics and processing map of a phosphorous modified super austenitic stainless steel, Mater. Des. 115 (2017) 262-275.
[106] A. Mohamadizadeh, A.Z. Hanzaki, H.R. Abedi, S. Mehtonen, D. Porter, Hot deformation characterization of duplex low-density steel through 3D processing map development, Mater. Charact. 107 (2015) 293-301.
[107] T. Xi, C.G. Yang, M.B. Shahzad, K. Yang, Study of the processing map and hot deformation behavior of a Cu-bearing 317LN austenitic stainless steel, Mater. Des. 87 (2015) 303-312.
[108] Y. Liu, C. Geng, Q.Q. Lin, Y.F. Xiao, J.R. Xu, W. Kang, Study on hot

deformation behavior and intrinsic workability of 6063 aluminum alloys using 3D processing map, J. Alloys Compd. 713 (2017) 212-221.
[109] Y. Sun, Z.H. Cao, Z.P. Wan, L.X. Hu, W.H. Ye, N.K. Li, C.L. Fan, 3D processing map and hot deformation behavior of 6A02 aluminum alloy, J. Alloys Compd. 742 (2018) 356-368.
[110] K.T. Son, M.H. Kim, S.W. Kim, J.W. Lee, S.K. Hyun, Evaluation of hot deformation characteristics in modified AA5052 using processing map and activation energy map under deformation heating, J. Alloys Compd. 740 (2018) 96-108.
[111] E.X. Pu, W.J. Zheng, Z.G. Song, H. Feng, H. Dong, Hot deformation characterization of nickel-based superalloy UNS10276 through processing map and microstructural studies, J. Alloys Compd. 694 (2017) 617-631.
[112] H. Jiang, J.X. Dong, M.C. Zhang, L. Zheng, Z.H. Yao, Hot deformation characteristics of Alloy 617B nickel-based superalloy: a study using processing map, J. Alloys Compd. 647 (2015) 338-350.
[113] D.G. He, Y.C. Lin, M.S. Chen, J. Chen, D.X. Wen, X.M. Chen, Effect of pre-treatment on hot deformation behavior and processing map of an aged nickel-based superalloy, J. Alloys Compd. 649 (2015) 1075-1084.
[114] W. Cheng, Y. Bai, S. Ma, L. Wang, H. Wang, H. Yu, Hot deformation behavior and workability characteristic of a fine-grained Mg-8Sn-2Zn-2Al alloy with processing map, J. Mater. Sci. Technol. 35 (2019) 1198-1209.
[115] X. Shang, J. Zhou, X. Wang, Y. Luo, Optimizing and identifying the process parameters of AZ31 magnesium alloy in hot compression on the base of processing maps, J. Alloys Compd. 629 (2015) 155-161.
[116] Z.W. Cai, F.X. Chen, F.J. Ma, J.Q. Guo, Dynamic recrystallization behavior and hot workability of AZ41M magnesium alloy during hot deformation, J. Alloys Compd. 670 (2016) 55-63.
[117] L. Zhang, Z. Li, Q. Lei, W.T. Qiu, H.T. Luo, Hot deformation behavior of Cu-8.0Ni-1.8Si-0.15Mg alloy, Mater. Sci. Eng. A 528 (2011) 1641-1647.
[118] Z. Ding, S. Jia, P. Zhao, M. Deng, K. Song, Hot deformation behavior of Cu-0.6Cr-0.03Zr alloy during compression at elevated temperatures, Mater. Sci. Eng. A 570 (2013) 87-91.
[119] Y.V.R.K. Prasad, K.P. Rao, Processing maps and rate controlling mechanisms of hot deformation of electrolytic tough pitch copper in the temperature range 300-950°C, Mater. Sci. Eng. A 391 (2005) 141-150.

[120] S. Samal, M.R. Rahul, R.S. Kottada, G. Phanikumar, Hot deformation behaviour and processing map of Co-Cu-Fe-Ni-Ti eutectic high entropy alloy, Mater. Sci. Eng. A 664 (2016) 227-235.
[121] H.T. Jeong, H.K. Park, K. Park, T.W. Na, W.J. Kim, High-temperature deformation mechanisms and processing maps of equiatomic CoCrFeMnNi high-entropy alloy, Mater. Sci. Eng. A 756 (2019) 528-537.
[122] Z. Du, S. Jiang, K. Zhang, The hot deformation behavior and processing map of Ti-47.5Al-Cr-V alloy, Mater. Des. 86 (2015) 464-473.
[123] J. Jia, K. Zhang, L. Liu, F. Wu, Hot deformation behavior and processing map of a powder metallurgy Ti-22Al-25Nb alloy, J. Alloys Compd. 600 (2014) 215-221.
[124] F.T. Kong, N. Cui, Y.Y. Chen, X.P. Wang, N.N. Xiong, Characterization of hot deformation behavior of as-forged TiAl alloy, Intermetallics 55 (2014) 66-72.
[125] S. Gangolu, A.G. Rao, I. Sabirov, B.P. Kashyap, N. Prabhu, V.P. Deshmukh, Development of constitutive relationship and processing map for Al-6.65Si-0.44Mg alloy and its composite with B_4C particulates, Mater. Sci. Eng. A 655 (2016) 256-264.
[126] K.K. Deng, J.C. Li, F.J. Xu, K.B. Nie, W. Liang, Hot deformation behavior and processing maps of fine-grained SiC_p/AZ91 composite, Mater. Des. 67 (2015) 72-81.
[127] B.N. Sahoo, S.K. Panigrahi, Deformation behavior and processing map development of AZ91 Mg alloy with and without addition of hybrid in-situ TiC+TiB_2 reinforcement, J. Alloys Compd. 776 (2019) 865-882.
[128] H.D. Zhang, Y. Liu, F. Zhang, D. Zhang, H.X. Zhu, T.X. Fan, Hot deformation behavior and processing maps of Diamond/Cu composites, Metall. Mater. Trans. A 49A (2018) 2202-2212.
[129] H. Matsumoto, M. Kitamura, Y. Li, Y. Koizumi, A. Chiba, Hot forging characteristic of Ti-5Al-5V-5Mo-3Cr alloy with single metastable β microstructure, Mater. Sci. Eng. A 611 (2014) 337-344.
[130] J.Q. Zhang, H.S. Di, H.T. Wang, K. Mao, T.J. Ma, Y. Cao, Hot deformation behavior of Ti-15-3 titanium alloy: a study using processing maps, activation energy map, and Zener-Hollomon parameter map, J. Mater. Sci. 47 (2012) 4000-4011.
[131] Z. Wang, X.N. Wang, Z.S. Zhu, Characterization of high-temperature deformation behavior and processing map of TB17 titanium alloy, J. Alloys Compd. 692 (2017) 149-154.

[132] H.Z. Zhao, L. Xiao, P. Ge, J. Sun, Z.P. Xi, Hot deformation behavior and processing maps of Ti-1300 alloy, Mater. Sci. Eng. A 604 (2014) 111-116.
[133] V.V. Balasubrahmanyam, Y.V.R.K. Prasad, Deformation behaviour of beta titanium alloy Ti-10V-4.5Fe-1.5Al in hot upset forging, Mater. Sci. Eng. A 336 (2002) 150-158.
[134] M. Dikovits, C. Poletti, F. Warchomicka, Deformation mechanisms in the near-β titanium alloy Ti-55531, Metall. Mater. Trans. A 45 (2013) 1586-1596.
[135] J.K. Fan, H.C. Kou, M.J. Lai, B. Tang, H. Chang, J.S. Li, Characterization of hot deformation behavior of a new near beta titanium alloy: Ti-7333, Mater. Des. 49 (2013) 945-952.
[136] X.F. Bai, Y.Q. Zhao, W.D. Zeng, Z.Q. Jia, Y.S. Zhang, Characterization of hot deformation behavior of a biomedical titanium alloy TLM, Mater. Sci. Eng. A 598 (2014) 236-243.
[137] E. Ghasemi, A. Zarei-Hanzaki, E. Farabi, K. Tesar, A. Jager, M. Rezaee, Flow softening and dynamic recrystallization behavior of BT9 titanium alloy: a study using process map development, J. Alloys Compd. 695 (2017) 1706-1718.
[138] J. Guo, M. Zhan, Y.Y. Wang, P.F. Gao, Unified modeling of work hardening and flow softening in two-phase titanium alloys considering microstructure evolution in thermomechanical processes, J. Alloys Compd. 767 (2018) 34-45.
[139] J. Guo, M. Zhan, M.W. Fu, P.F. Gao, F. Ma, Extrapolation based constitutive modeling of flow stress of titanium alloy sheet under hot-working condition, Mater. Des. 154 (2018) 96-107.
[140] T. Hama, H. Nagao, A. Kobuki, H. Fujimoto, H. Takuda, Work-hardening and twinning behaviors in a commercially pure titanium sheet under various loading paths, Mater. Sci. Eng. A 620 (2015) 390-398.
[141] R.K. Gupta, V.A. Kumar, C. Mathew, G.S. Rao, Strain hardening of titanium alloy Ti-6Al-4V sheets with prior heat treatment and cold working, Mater. Sci. Eng. A 662 (2016) 537-550.
[142] A.M. Zhao, H. Yang, X.G. Fan, P.F. Gao, R. Zuo, M. Meng, The flow behavior and microstructure evolution during (α+β) deformation of β wrought TA15 titanium alloy, Mater. Des. 109 (2016) 112-122.
[143] N.H. Heo, K.H. Chai, J.G. Na, Correlation between interfacial segregation and surface-energy-induced selective grain growth in 3% silicon-iron alloy, Acta Mater. 48 (2000) 2901-2910.
[144] F.J. Gil, J.A. Planell, Behaviour of normal grain growth kinetics in single

phase titanium and titanium alloys, Mater. Sci. Eng. A 283 (2000) 17-24.
[145] M. Maalekian, R. Radis, M. Militzer, A. Moreau, W.J. Poole, In situ measurement and modelling of austenite grain growth in a Ti/Nb microalloyed steel, Acta Mater. 60 (2012) 1015-1026.
[146] R. Darvishi Kamachali, I. Steinbach, 3-D phase-field simulation of grain growth: Topological analysis versus mean-field approximations, Acta Mater. 60 (2012) 2719-2728.
[147] R. Alizadeh, R. Mahmudi, A.H.W. Ngan, T.G. Langdon, Microstructural stability and grain growth kinetics in an extruded fine-grained Mg-Gd-Y-Zr alloy, J. Mater. Sci. 50 (2015) 4940-4951.
[148] S. Praveen, J. Basu, S. Kashyap, R.S. Kottada, Exceptional resistance to grain growth in nanocrystalline CoCrFeNi high entropy alloy at high homologous temperatures, J. Alloys Compd. 662 (2016) 361-367.
[149] S.X. Liang, L.X. Yin, L.Y. Zheng, M.Z. Ma, R.P. Liu, The microstructural evolution and grain growth kinetics of TZ20 alloy during isothermal annealing, Mater. Des. 99 (2016) 396-402.
[150] S.L. Semiatin, B.C. Kirby, G.A. Salishchev, Coarsening behavior of an alpha-beta titanium alloy, Metall. Mater. Trans. A 35A (2004) 2809-2819.
[151] Y.Q. Ning, X. Luo, H.Q. Liang, H.Z. Guo, J.L. Zhang, K. Tan, Competition between dynamic recovery and recrystallization during hot deformation for TC18 titanium alloy, Mater. Sci. Eng. A 635 (2015) 77-85.
[152] H.W. Li, X.X. Sun, H. Yang, A three-dimensional cellular automata-crystal plasticity finite element model for predicting the multiscale interaction among heterogeneous deformation, DRX microstructural evolution and mechanical responses in titanium alloys, Int. J, Plasticity 87 (2016) 154-180.
[153] B.C. Xie, B.Y. Zhang, Y.Q. Ning, M.W. Fu, Mechanisms of DRX nucleation with grain boundary bulging and subgrain rotation during the hot working of nickel-based superalloys with columnar grains, J. Alloys Compd. 786 (2019) 636-647.
[154] T. Sakai, A. Belyakov, R. Kaibyshev, H. Miura, J.J. Jonas, Dynamic and post-dynamic recrystallization under hot, cold and severe plastic deformation conditions, Prog. Mater. Sci. 60 (2014) 130-207.
[155] C.Q. Huang, J. Deng, S.X. Wang, L.L. Liu, A physical-based constitutive model to describe the strain-hardening and dynamic recovery behaviors of 5754 aluminum alloy, Mater. Sci. Eng. A 699 (2017) 106-113.
[156] K. Wang, M. Li, Q. Liu, Evolution mechanisms of the primary α and β phases

during α/β deformation of an α/β titanium alloy TC8, Mater. Charact. 120 (2016) 115-123.
[157] X.G. Fan, Y. Zhang, P.F. Gao, Z.N. Lei, M. Zhan, Deformation behavior and microstructure evolution during hot working of a coarse-grained Ti-5Al-5Mo-5V-3Cr-1Zr titanium alloy in beta phase field, Mater. Sci. Eng. A 694 (2017) 24-32.
[158] Y.X. Tian, G. Wang, S. Yu, Z.T. Yu, Microstructure characteristics and strain rate sensitivity of a biomedical Ti-25Nb-3Zr-3Mo-2Sn titanium alloy during thermomechanical processing, J. Mater. Sci. 50 (2015) 5165-5173.
[159] K. Huang, R.E. Loge, A review of dynamic recrystallization phenomena in metallic materials, Mater. Des. 111 (2016) 548-574.
[160] Y.C. Lin, J. Huang, D.G. He, X.Y. Zhang, Q. Wu, L.H. Wang, C. Chen, K.C. Zhou, Phase transformation and dynamic recrystallization behaviors in a Ti55511 titanium alloy during hot compression, J. Alloys Compd. 795 (2019) 471-482.
[161] Y.S. Wu, Z. Liu, X.Z. Qin, C.S. Wang, L.Z. Zhou, Effect of initial state on hot deformation and dynamic recrystallization of Ni-Fe based alloy GH984G for steam boiler applications, J. Alloys Compd. 795 (2019) 370-384.
[162] K.H. Wang, G. Liu, K. Huang, D.J. Politis, L.L. Wang, Effect of recrystallization on hot deformation mechanism of TA15 titanium alloy under uniaxial tension and biaxial gas bulging conditions, Mater. Sci. Eng. A 708 (2017) 149-158.
[163] C.K. Yan, A.H. Feng, S.J. Qu, G.J. Cao, J.L. Sun, J. Shen, D.L. Chen, Dynamic recrystallization of titanium: Effect of pre-activated twinning at cryogenic temperature, Acta Mater. 154 (2018) 311-324.
[164] X. Wang, L. Wang, L.S. Luo, H. Yan, X.Z. Li, R.R. Chen, Y.Q. Su, J.J. Guo, H.Z. Fu, High temperature deformation behavior of melt hydrogenated (TiB+TiC)/Ti-6Al-4V composites, Mater. Des. 121 (2017) 335-344.
[165] S.M. Abbasi, A. Momeni, Y.C. Lin, H.R. Jafarian, Dynamic softening mechanism in Ti-13V-11Cr-3Al beta Ti alloy during hot compressive deformation, Mater. Sci. Eng. A 665 (2016) 154-160.
[166] X. Wang, L. Wang, L.S. Luo, X.D. Liu, Y.C. Tang, X.Z. Li, R.R. Chen, Y.Q. Su, J.J. Guo, H.Z. Fu, Hot deformation behavior and dynamic recrystallization of melt hydrogenated Ti-6Al-4V alloy, J. Alloys Compd. 728 (2017) 709-718.
[167] Y. Wu, H.C. Kou, Z.H. Wu, B. Tang, J.S. Li, Dynamic recrystallization and texture evolution of Ti-22Al-25Nb alloy during plane-strain compression, J. Alloys Compd. 749 (2018) 844-852.

[168] Z.X. Zhang, S.J. Qu, A.H. Feng, X. Hu, J. Shen, Microstructural mechanisms during multidirectional isothermal forging of as-cast Ti-6Al-4V alloy with an initial lamellar microstructure, J. Alloys Compd. 773 (2019) 277-287.
[169] J.Y. Shen, Y. Sun, Y.Q. Ning, H. Yu, Z.K. Yao, L.X. Hu, Superplasticity induced by the competitive DRX between BCC beta and HCP alpha in Ti-4Al-3V-2Mo-2Fe alloy, Mater. Charact. 153 (2019) 304-317.
[170] D. Zhou, W. Zeng, J. Xu, S. Wang, W. Chen, Evolution of equiaxed and lamellar α during hot compression in a near alpha titanium alloy with bimodal microstructure, Mater. Charact. 151 (2019) 103-111.
[171] J. Zhao, K.H. Wang, K. Huang, G. Liu, Recrystallization behavior during hot tensile deformation of TA15 titanium alloy sheet with substantial prior deformed substructures, Mater. Charact. 151 (2019) 429-435.
[172] S. Long, Y.F. Xia, P. Wang, Y.T. Zhou, F.J. Gong, J. Zhou, J.S. Zhang, M.L. Cui, Constitutive modelling, dynamic globularization behavior and processing map for Ti-6Cr-5Mo-5V-4Al alloy during hot deformation, J. Alloys Compd. 796 (2019) 65-76.
[173] J. Fan, J. Li, Y. Zhang, H. Kou, L. Germain, C. Esling, Formation and crystallography of nano/ultrafine-trimorphic structure in metastable β titanium alloy Ti-5Al-5Mo-5V-3Cr-0.5Fe processed by dynamic deformation at low temperature, Mater. Charact. 130 (2017) 149-155.
[174] K. Hua, Y. Zhang, W. Gan, H. Kou, J. Li, C. Esling, Correlation between imposed deformation and transformation lattice strain on α variant selection in a metastable β-Ti alloy under isothermal compression, Acta Mater. 161 (2018) 150-160.
[175] S. Long, Y.F. Xia, J.C. Hu, J.S. Zhang, J. Zhou, P. Zhang, M.L. Cui, Hot deformation behavior and microstructure evolution of Ti-6Cr-5Mo-5V-4Al alloy during hot compression, Vacuum 160 (2019) 171-180.
[176] K. Hua, J. Li, H. Kou, J. Fan, M. Sun, B. Tang, Phase precipitation behavior during isothermal deformation in β-quenched near beta titanium alloy Ti-7333, J. Alloys Compd. 671 (2016) 381-388.
[177] W. Chen, Y. Lv, X. Zhang, C. Chen, Y.C. Lin, K. Zhou, Comparing the evolution and deformation mechanisms of lamellar and equiaxed microstructures in near β-Ti alloys during hot deformation, Mater. Sci. Eng. A 758 (2019) 71-78.
[178] N. Stefansson, S.L. Semiatin, Mechanisms of globularization of Ti-6Al-4V during static heat treatment, Metall. Mater. Trans. A 34 (2003) 691-698.

[179] S. Zherebtsov, M. Murzinova, G. Salishchev, S.L. Semiatin, Spheroidization of the lamellar microstructure in Ti-6Al-4V alloy during warm deformation and annealing, Acta Mater. 59 (2011) 4138-4150.
[180] S. Roy, S. Suwas, The influence of temperature and strain rate on the deformation response and microstructural evolution during hot compression of a titanium alloy Ti-6Al-4V-0.1B, J. Alloys Compd. 548 (2013) 110-125.
[181] S. Balachandran, S. Kumar, D. Banerjee, On recrystallization of the α and β phases in titanium alloys, Acta Mater. 131 (2017) 423-434.
[182] S. Balachandran, A. Kashiwar, A. Choudhury, D. Banerjee, R. Shi, Y. Wang, On variant distribution and coarsening behavior of the α phase in a metastable β titanium alloy, Acta Mater. 106 (2016) 374-387.
[183] Z.B. Zhao, Q.J. Wang, Q.M. Hu, J.R. Liu, B.B. Yu, R. Yang, Effect of β (110) texture intensity on α-variant selection and microstructure morphology during β to α phase transformation in near α titanium alloy, Acta Mater. 126 (2017) 372-382.
[184] H. Beladi, Q. Chao, G.S. Rohrer, Variant selection and intervariant crystallographic planes distribution in martensite in a Ti-6Al-4V alloy, Acta Mater. 80 (2014) 478-489.
[185] P.D. Frost, W.M. Parris, L.L. Hirsch, J.R. Doig, C.M. Schwartz, Isothermal transformation of titanium-chromium alloys, Trans. Asm 46 (1954) 231-256.
[186] B.S. Hickman, The formation of omega phase in titanium and zirconium alloys: A review, J. Mater. Sci. 4 (1969) 554-563.
[187] R. Shi, Y. Zheng, R. Banerjee, H.L. Fraser, Y. Wang, ω-Assisted α nucleation in a metastable β titanium alloy, Scripta Mater. 171 (2019) 62-66.
[188] T. Li, D. Kent, G. Sha, H. Liu, S.G. Fries, A.V. Ceguerra, M.S. Dargusch, J.M. Cairney, Nucleation driving force for ω-assisted formation of α and associated ω morphology in β-Ti alloys, Scripta Mater. 155 (2018) 149-154.
[189] Y. Zheng, D. Choudhuri, T. Alam, R.E.A. Williams, R. Banerjee, H.L. Fraser, The role of cuboidal ω precipitates on α precipitation in a Ti-20V alloy, Scripta Mater. 123 (2016) 81-85.
[190] J. Zhang, C.C. Tasan, M.J. Lai, A.C. Dippel, D. Raabe, Complexion-mediated martensitic phase transformation in Titanium, Nat. Commun. 8 (2017) 14210.
[191] S.K. Sikka, Y.K. Vohra, R. Chidambaram, Omega-phase in materials, Prog. Mater. Sci. 27 (1982) 245-310.
[192] J. Chen, W. Xiao, M.S. Dargusch, C. Ma, The dependence of isothermal omega precipitation on the quenching rate in a metastable beta-Ti alloy, Sci. Rep. 5

(2015) 14632.
[193] A. Devaraj, S. Nag, R. Srinivasan, R.E.A. Williams, S. Banerjee, R. Banerjee, H.L. Fraser, Experimental evidence of concurrent compositional and structural instabilities leading to ω precipitation in titanium-molybdenum alloys, Acta Mater. 60 (2012) 596-609.
[194] R. Davis, H.M. Flower, D.R.F. West, Martensitic transformations in Ti-Mo alloys, J. Mater. Sci. 14 (1979) 712-722.
[195] S. Ehtemam-Haghighi, Y. Liu, G. Cao, L.C. Zhang, Influence of Nb on the beta→alpha" martensitic phase transformation and properties of the newly designed Ti-Fe-Nb alloys, Mater. Sci. Eng. C 60 (2016) 503-510.
[196] K. Lu, L. Lu, S. Suresh, Strengthening materials by engineering coherent internal boundaries at the nanoscale, Science 324 (2009) 349-352.
[197] L. Gao, R.S. Chen, E.H. Han, Effects of rare-earth elements Gd and Y on the solid solution strengthening of Mg alloys, J. Alloys Compd. 481 (2009) 379-384.
[198] P. Kwasniak, H. Garbacz, K.J. Kurzydlowski, Solid solution strengthening of hexagonal titanium alloys: Restoring forces and stacking faults calculated from first principles, Acta Mater. 102 (2016) 304-314.
[199] G.S. Dyakonov, S. Mironov, I.P. Semenova, R.Z. Valiev, S.L. Semiatin, Microstructure evolution and strengthening mechanisms in commercial-purity titanium subjected to equal-channel angular pressing, Mater. Sci. Eng. A 701 (2017) 289-301.
[200] H. Conrad, Effect of interstitial solutes on the strength and ductility of titanium, Prog. Mater. Sci. 26 (1981) 123-404.
[201] Q. Yu, L. Qi, T. Tsuru, R. Traylor, D. Rugg, J.W. Morris, Jr., M. Asta, D.C. Chrzan, A.M. Minor, Metallurgy. Origin of dramatic oxygen solute strengthening effect in titanium, Science 347 (2015) 635-639.
[202] S.J. Li, M.T. Jia, F. Prima, Y.L. Hao, R. Yang, Improvements in nonlinear elasticity and strength by grain refinement in a titanium alloy with high oxygen content, Scripta Mater. 64 (2011) 1015-1018.
[203] M.T. Jia, D.L. Zhang, B. Gabbitas, J.M. Liang, C. Kong, A novel Ti-6Al-4V alloy microstructure with very high strength and good ductility, Scripta Mater. 107 (2015) 10-13.
[204] H.Z. Niu, H.R. Zhang, Q.Q. Sun, D.L. Zhang, Breaking through the strength-ductility trade-off dilemma in powder metallurgy Ti-6Al-4V titanium alloy, Mater. Sci. Eng. A 754 (2019) 361-369.

[205] Z. Liu, G. Welsch, Effects of oxygen and heat-treatment on the mechanical-properties of alpha and beta titanium-alloys, Metall. Mater. Trans. A 19 (1988) 527-542.
[206] C. Veiga, J.P. Davim, A.J.R. Loureiro, Properties and applications of titanium alloys: a brief review, Rev. Adv. Mater. Sci 32 (2012) 133-148.
[207] Q.Q. Wei, L.Q. Wang, Y.F. Fu, J.N. Qin, W.J. Lu, D. Zhang, Influence of oxygen content on microstructure and mechanical properties of Ti-Nb-Ta-Zr alloy, Mater. Des. 32 (2011) 2934-2939.
[208] M.A. Meyers, A. Mishra, D.J. Benson, Mechanical properties of nanocrystalline materials, Prog. Mater. Sci. 51 (2006) 427-556.
[209] S. Zherebtsov, E. Kudryavtsev, S. Kostjuchenko, S. Malysheva, G. Salishchev, Strength and ductility-related properties of ultrafine grained two-phase titanium alloy produced by warm multiaxial forging, Mater. Sci. Eng. A 536 (2012) 190-196.
[210] J.Z. Lu, U. Wu, G.F. Sun, K.Y. Luo, Y.K. Zhang, J. Cai, C.Y. Cui, X.M. Luo, Microstructural response and grain refinement mechanism of commercially pure titanium subjected to multiple laser shock peening impacts, Acta Mater. 127 (2017) 252-266.
[211] A. Belyakov, K. Tsuzaki, H. Miura, T. Sakai, Effect of initial microstructures on grain refinement in a stainless steel by large strain deformation, Acta Mater. 51 (2003) 847-861.
[212] B. Schuh, F. Mendez-Martin, B. Volker, E.P. George, H. Clemens, R. Pippan, A. Hohenwarter, Mechanical properties, microstructure and thermal stability of a nanocrystalline CoCrFeMnNi high-entropy alloy after severe plastic deformation, Acta Mater. 96 (2015) 258-268.
[213] L. Lu, Y. Shen, X. Chen, L. Qian, K. Lu, Ultrahigh strength and high electrical conductivity in copper, Science 304 (2004) 422-426.
[214] Y. Wang, M. Chen, F. Zhou, E. Ma, High tensile ductility in a nanostructured metal, Nature 419 (2002) 912-915.
[215] E.O. Hall, The deformation and ageing of mild steel: III discussion of results, Proc. Phys. Soc. 64 (1951) 747-753.
[216] N.J. Petch, The cleavage strength of polycrystals, Tetsu To Hagane 174 (1953) 25-28.
[217] Y.J. Chen, Y.J. Li, J.C. Walmsley, S. Dumoulin, S.S. Gireesh, S. Armada, P.C. Skaret, H.J. Roven, Quantitative analysis of grain refinement in titanium during equal channel angular pressing, Scripta Mater. 64 (2011) 904-907.

[218] R. Valiev, Nanostructuring of metals by severe plastic deformation for advanced properties, Nat. Mater. 3 (2004) 511-516.
[219] S. Tamirisakandala, R.B. Bhat, J.S. Tiley, D.B. Miracle, Grain refinement of cast titanium alloys via trace boron addition, Scripta Mater. 53 (2005) 1421-1426.
[220] M.J. Bermingham, S.D. McDonald, M.S. Dargusch, D.H. StJohn, The mechanism of grain refinement of titanium by silicon, Scripta Mater. 58 (2008) 1050-1053.
[221] Y.D. Ye, S.Z. Kure-Chu, Z.Y. Sun, X.P. Li, H.B. Wang, G.Y. Tang, Nanocrystallization and enhanced surface mechanical properties of commercial pure titanium by electropulsing-assisted ultrasonic surface rolling, Mater. Des. 149 (2018) 214-227.
[222] Y.G. Liu, M.Q. Li, H.J. Liu, Surface nanocrystallization and gradient structure developed in the bulk TC4 alloy processed by shot peening, J. Alloys Compd. 685 (2016) 186-193.
[223] S. Jiang, H. Wang, Y. Wu, X. Liu, H. Chen, M. Yao, B. Gault, D. Ponge, D. Raabe, A. Hirata, M. Chen, Y. Wang, Z. Lu, Ultrastrong steel via minimal lattice misfit and high-density nanoprecipitation, Nature 544 (2017) 460-464.
[224] K. Hua, Y. Zhang, H. Kou, J. Li, W. Gan, J. Fundenberger, C. Esling, Composite structure of α phase in metastable β Ti alloys induced by lattice strain during β to α phase transformation, Acta Mater. 132 (2017) 307-326.
[225] Y. Zheng, R.E.A. Williams, D. Wang, R. Shi, S. Nag, P. Kami, J.M. Sosa, R. Banerjee, Y. Wang, H.L. Fraser, Role of ω phase in the formation of extremely refined intragranular α precipitates in metastable β-titanium alloys, Acta Mater. 103 (2016) 850-858.
[226] Z.X. Du, S.L. Xiao, Y.P. Shen, J.S. Liu, J. Liu, L.J. Xu, F.T. Kong, Y.Y. Chen, Effect of hot rolling and heat treatment on microstructure and tensile properties of high strength beta titanium alloy sheets, Mater. Sci. Eng. A 631 (2015) 67-74.
[227] W. Zhu, J. Lei, C. Tan, Q. Sun, W. Chen, L. Xiao, J. Sun, A novel high-strength β-Ti alloy with hierarchical distribution of α-phase: The superior combination of strength and ductility, Mater. Des. 168 (2019) 107640.
[228] L. Ren, W. Xiao, H. Chang, Y. Zhao, C. Ma, L. Zhou, Microstructural tailoring and mechanical properties of a multi-alloyed near β titanium alloy Ti-5321 with various heat treatment, Mater. Sci. Eng. A 711 (2018) 553-561.
[229] J.H. Gao, Y.H. Huang, D.K. Guan, A.J. Knowles, L. Ma, D. Dye, W.M. Rainforth, Deformation mechanisms in a metastable beta titanium twinning induced

plasticity alloy with high yield strength and high strain hardening rate, Acta Mater. 152 (2018) 301-314.
[230] J.Y. Zhang, J.S. Li, Z. Chen, Q.K. Meng, F. Sun, B.L. Shen, Microstructural evolution of a ductile metastable β titanium alloy with combined TRIP/TWIP effects, J. Alloys Compd. 699 (2017) 775-782.
[231] M. Marteleur, F. Sun, T. Gloriant, P. Vermaut, P.J. Jacques, F. Prima, On the design of new β-metastable titanium alloys with improved work hardening rate thanks to simultaneous TRIP and TWIP effects, Scripta Mater. 66 (2012) 749-752.
[232] M.I. Latypov, S. Shin, B.C. De Cooman, H.S. Kim, Micromechanical finite element analysis of strain partitioning in multiphase medium manganese TWIP plus TRIP steel, Acta Mater. 108 (2016) 219-228.
[233] Z. Li, K.G. Pradeep, Y. Deng, D. Raabe, C.C. Tasan, Metastable high-entropy dual-phase alloys overcome the strength-ductility trade-off, Nature 534 (2016) 227-230.
[234] E.P. George, D. Raabe, R.O. Ritchie, High-entropy alloys, Nat. Rev. Mater. (2019).
[235] J. Su, D. Raabe, Z.M. Li, Hierarchical microstructure design to tune the mechanical behavior of an interstitial TRIP-TWIP high-entropy alloy, Acta Mater. 163 (2019) 40-54.

2 Research methodology

2.1 Introduction

The research methods and approaches of this thesis can be primarily divided into six main domains: material preparation and processing, physical and chemical characterizations, thermal physical simulation, microstructure characterizations, mechanical property testing and in-situ tensile observation. The schematic diagram showing the whole research methodology design and the utilized research techniques is presented in Figure 2.1.

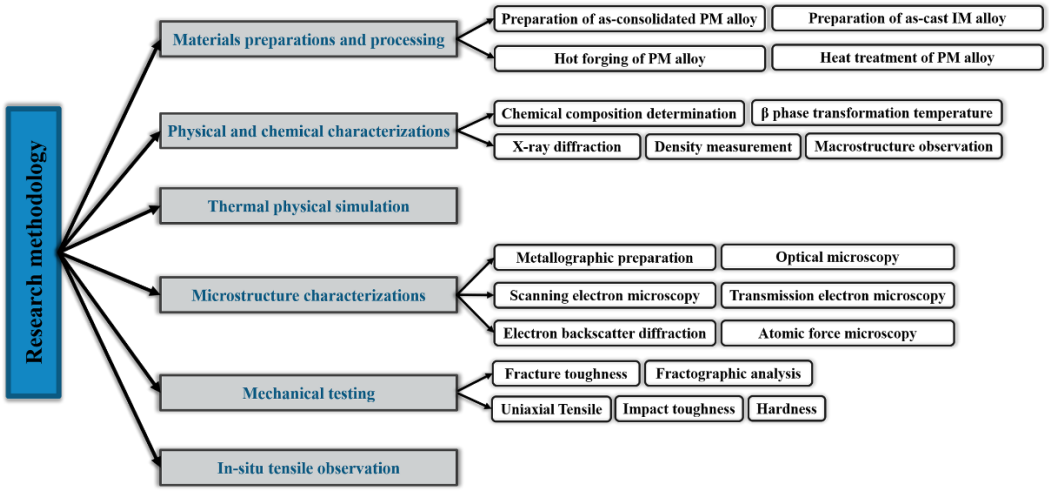

Figure 2.1 Schematic diagram of the whole research methodology design and the utilized research techniques.

2.2 Materials preparations and processing

2.2.1 Raw materials

The PM Ti-5553 alloy in this study was synthesized by TPC process from a powder mixture with the nominal composition of Ti-5Al-5Mo-5V-3Cr (wt.%) prepared from elemental powders of pure-Ti (hydride-dehydride, HDH), pure-Al and master alloy powders of V-Al (65%-35%, wt.%), Mo-Al (85%-15%, wt.%) and Cr-Al (70%-30%, wt.%). The HDH-Ti and Al powder were supplied from Goodfellow Ltd. (UK), and the master alloy powders were provided by Dalian Rongde Ltd. (China). The detailed information about the measured oxygen content, nominal purity, nominal particle size and measured particle size distribution of the raw powders and the obtained powder mixtures is shown in Table 2.1. The SEM images showing the morphology of the raw powders are shown in Figure 2.2. It can be

found that the particle size of all raw powders is close to their nominal size (< 75 μm) and the mixed powder also suggests a similar size and acceptable oxygen level (0.33 wt.%). It is further observed that HDH-Ti powder (Figure 2.2a) and all master alloy powders (Figure 2.2c-e) have an irregular shape, while the Al powder (Figure 2.2b) is in the spherical shape.

Table 2.1 Basic information and characters of the raw powders and powder mixture for synthesizing the PM Ti-5553 alloy.

Powders	Nominal purity	Measured oxygen content (wt.%)	Nominal particle size	Particle size distribution (μm)		
				d (10)	d (50)	d (90)
HDH-Ti	99.6%	0.23	＜75 μm	27.043	53.252	84.458
Al	99.9%	0.25	＜40 μm	20.578	38.678	63.559
V65-Al35	Commercial	0.35	＜63 μm	28.882	52.790	85.627
Mo85-Al15	Commercial	0.32	＜63 μm	22.689	34.587	75.547
Cr70-Al30	Commercial	0.25	＜63 μm	25.548	32.487	76.971
Powder mixture	/	0.33	/	32.654	44.987	83.547

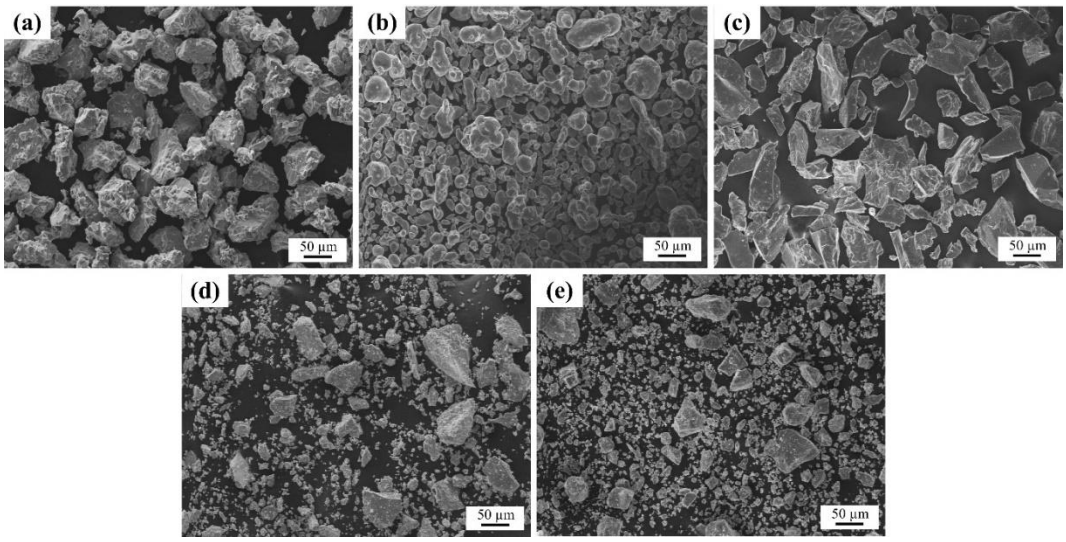

Figure 2.2 The morphology of raw powders for synthesizing PM Ti-5553 alloy: (a) HDH-Ti powder; (b) pure-Al powder; (c) V65-Al35 master alloy powder; (d) Mo85-Al15 master alloy powder; (e) Cr70-Al30 master alloy powder.

The choice of these raw powders is based on their cost-effective nature, small size and the irregular surface morphology (except Al powder) which makes them favourable to be compacted and consolidated during warm compaction and modified hot pressing.

For the IM alloy counterpart, raw materials employed were Ti sponge (magnesium metallothermic reduction), pure-Al pieces, pure-Cr pieces and master alloy pieces of Mo-Al (80%-20%, wt.%) and V-Al (70%-30%, wt.%). The Ti sponge was supplied by PanGang Titanium Ltd. (China), other metallic and alloy bulks were supplied by Western Metal Materials Ltd. (China).

2.2.2 Mixing, warm compaction and hot pressing of PM alloy

The PM alloy was consolidated from the raw powders through the processes of powder mixing, warm compaction and modified hot pressing (thermomechanical powder consolidation, TPC). The schematic diagram showing this preparation route is exhibited in Figure 2.3.

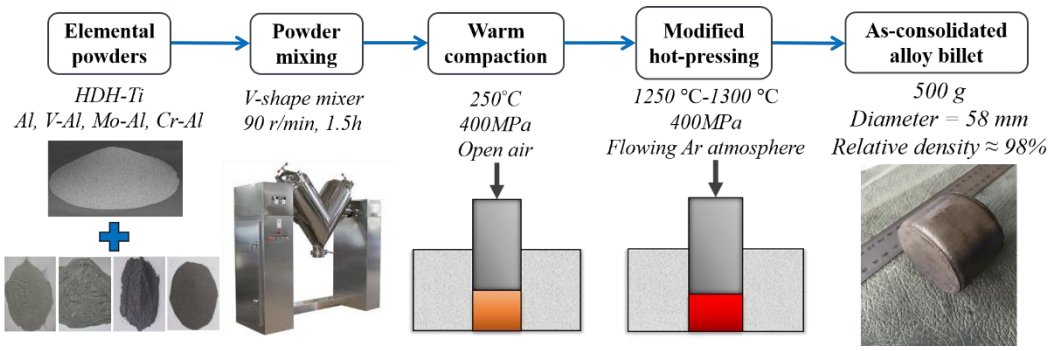

Figure 2.3 Schematic diagram of the preparation route for as-consolidated PM alloy.

The raw powders were first weighted (500 g) to make the nominal composition of Ti-5Al-5Mo-5V-3Cr (wt.%). Afterwards, a V-shaped blender was used to mix the powders into the homogeneous mixture at a rotation rate of 60 rpm for 90 min. The powder mixture was then warm-compacted into the green compact using a graphite lubricated die (cylinder shape, diameter = 56 mm) at the temperature about 250 °C and a uniaxial pressure about 400 MPa in the open air.

TPC of the green compact was achieved by modified hot pressing, performed using a 100-ton oil hydraulic press equipped with a glove chamber. Related facilities employed during the hot pressing are shown in Figure 2.4. The green compact was firstly inductive-heated to the target temperature of 1250 °C-1300 °C with a very high heating rate up to 200 °C/min. The rapid-inductive heating of the green powder compact is enabled by the copper induction coil (Figure 2.4d) and the external high-frequency power supply (Figure 2.4b, Inductotherm Ltd., Australia). The induction

coil carries an alternating current, which creates a magnetic field that induces an eddy current in the conductive metal powder compact to produce strong thermal effect. More detailed induction heating mechanism and the experimental set-up can be seen in the sketch exhibited in Figure 2.5 [1].

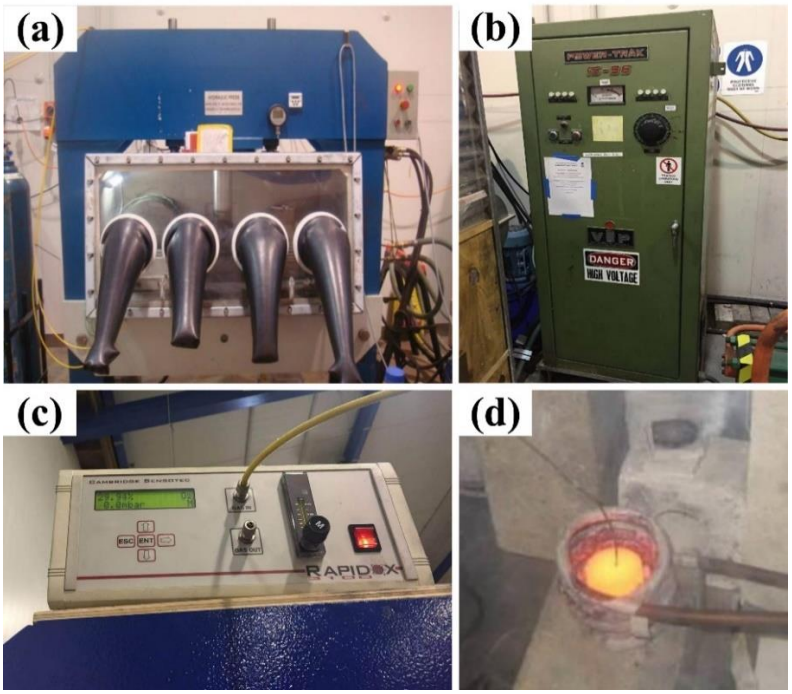

Figure 2.4 Related facilities employed during TPC: (a) 100-ton press with the glove chamber; (b) high-frequency power supply; (c) oxygen analyser; (d) copper induction coil around the green powder compact.

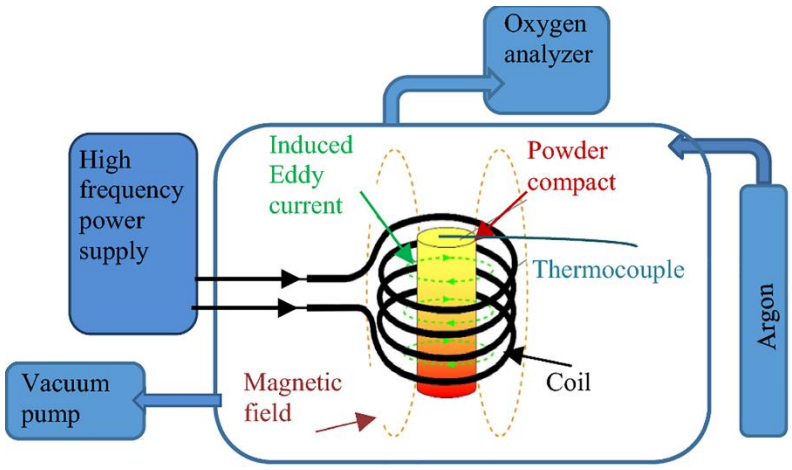

Figure 2.5 Schematic diagram showing the mechanism and the experimental set-up of induction heating [1].

After holding at the temperature for 7-10 minutes, the hot compact was transferred into a slightly larger graphite lubricated die (cylinder shape, the diameter is 58 mm), followed by uniaxial hot pressing to consolidate the alloy billet thermomechanically.

Flowing argon atmosphere was applied to the chamber during the heating, pressing and cooling processes to control the oxygen level below 200 ppm (measured by an oxygen content analyser, Figure 2.4c, Cambridge Sensotec Ltd., UK) for the elimination of serious oxidation.

2.2.3 Electrode pressing, arc-melting and casting of IM alloy

The IM alloy was produced from the raw materials through the processes of electrode pressing, arc-melting and ingot casting. The schematic diagram showing this preparation route is exhibited in Figure 2.6.

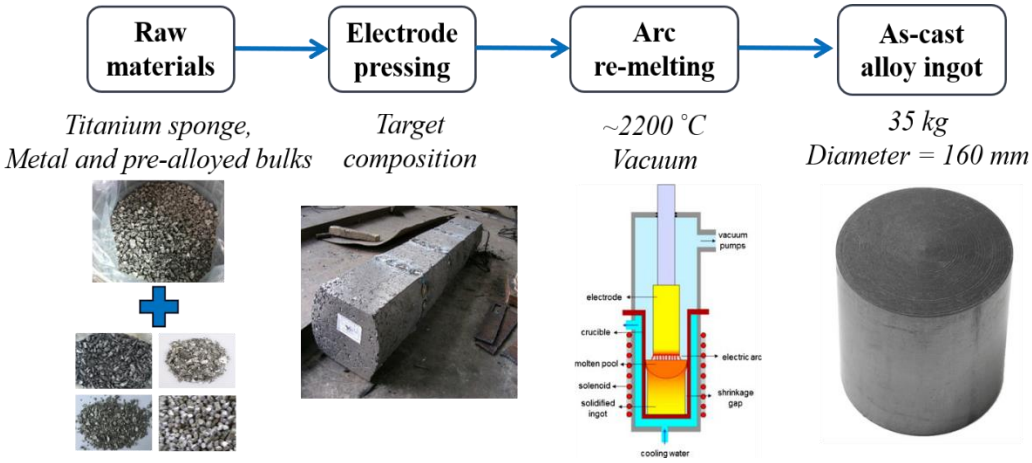

Figure 2.6 Schematic diagram of the production route for as-cast IM alloy.

Figure 2.7 50 kg vacuum consumable electrode melting furnace from BaoTi Ltd.

The raw materials were firstly weighted (40 kg) to make the nominal composition of Ti-5Al-5Mo-5V-3Cr. After that, the mixture was pressed and welded to make the electrode which will be melted in a vacuum consumable electrode melting furnace (shown in Figure 2.7, BaoTi Ltd., 50kg, China) for titanium alloys. The material was melted by high-voltage electric-arc twice to ensure the chemical homogeneity followed by vacuum casting to the alloy ingot with a weight of 35 kg and diameter of 160 mm.

2.2.4 Thermomechanical processing of PM alloy

The as-consolidated PM alloy billets (after TPC) were thermomechanical processed (single uniaxial open-die forging) at elevated temperatures using a 650-ton industrial-scale hydraulic quick-forging press (Northwest Institute of Nonferrous Metal Research, China), as shown in Figure 2.8. The alloy billet with pre-painted anti-oxidation coating was heated-up in a muffle furnace to the target temperature and held for 30 minutes to ensure the homogenous temperature distribution throughout the billet. Then the hot billet was transferred to the pre-heated (500 ℃) working platform of the 650-ton press for the uniaxial open-die hot forging. Upon the completion of the processing, the as-forged alloy pancakes are cooled to room temperature in air or quenched in water for further characterizations and heat treatment. The detailed procedures and parameters for the thermomechanical processing of PM alloy will be discussed in Chapter 6.

Figure 2.8 Industrial-scale 650-ton hydraulic forging press.

2.2.5 Heat treatment of PM alloy

Heat treatment of as-forged PM alloy pancakes was performed in a muffle furnace (Detlow, Melbourne). The samples were placed in the furnace once the target temperature was reached. Upon the completion of the heat treatment, the samples were cooled in open-air or quenched in water depending on the specific regime. The heat treatments applied in the study is mainly fast annealing. The detailed parameters used in the various heat treatments of as-forged PM alloy will be discussed in Chapter 6.

2.3 Physical and chemical characterizations

2.3.1 Chemical composition determination

Actual chemical composition determinations were performed on two alloys (as-consolidated PM and as-cast IM Ti-5553 alloys). The contents of metallic elements (Al, V, Mo and Cr) were measured by the method of inductively coupled plasma atomic emission spectrometry using the machined swarf of the bulk materials. Whereas, the levels of the interstitial elements (O and N) were determined by inert gas melting-infrared ray (for oxygen) and distillation separation-spectrophotometry (for nitrogen) methods. The composition measurements were performed three times, and the average value was finally employed in the study.

2.3.2 Density measurement

Relative density (RD) is an important factor for PM titanium alloys, which represents the consolidation degree and reflects the porosity of the PM components. The RD always has a significant effect on the mechanical properties and further processing of PM titanium alloys. A low RD can lead to poor performance and the unexpected failure of the materials. In this work, the density of the PM Ti-5553 alloy at different stages (green compact, as-consolidated and as-forged) were determined the Archimedes principle by weighing the samples in water and air according to the standard of ASTM B962 (ASTM B962, 2008) [2-5]. Figure 2.9 shows the photo and the schematic illustration of the experimental set-up for density measurement.

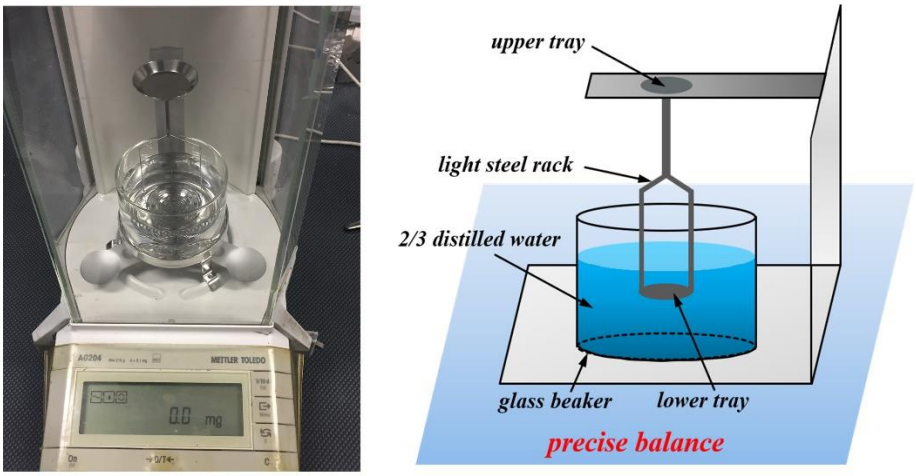

Figure 2.9 Experimental apparatus and schematic diagram demonstrating the density measurement method for PM Ti-5553 alloys at various stages.

The weights of a bulk sample were measured both in the air (upper tray in the figure) and in distilled water (lower tray in the figure). After that, the relative density of the bulk sample can be calculated by the following equations:

$$\rho_s = \frac{W_{\text{air}}}{W_{\text{air}} - W_{\text{water}}} \cdot \rho_{\text{water}} \qquad (2.1)$$

$$RD = \frac{\rho_s}{TD} \cdot 100\% \qquad (2.2)$$

where ρ_s is the sample density (g/cm^3), W_{air} is the weight of the sample in air (g), W_{water} is the weight of the sample in distilled water (g), and ρ_{water} is the density of pure water at room temperature (i.e. 0.977 g/cm^3 at room temperature). The density measurement of each sample was repeated for five times and their average value was considered as its density. The applied theoretical density (TD) of bulk Ti-5553 alloy is 4.65 g/cm^3 [6, 7]. After the calculation, the RD of the green alloy compact and as-consolidated alloy billet (using the samples from the centre areas) are determined as 84% and 98% of TD, respectively. Furthermore, the relative density (RD) of the powder mixture was about 31% theoretical density (TD) of Ti-5553, measured by its apparent mass and dimension. Additionally, after TMP, the RD of the alloy can reach full dense, which will be discussed later in Chapter 6. Based on these results, the RD variation of the PM Ti-5553 alloy at different stages is shown schematically in Figure 2.10, together with the related densification/consolidation mechanisms.

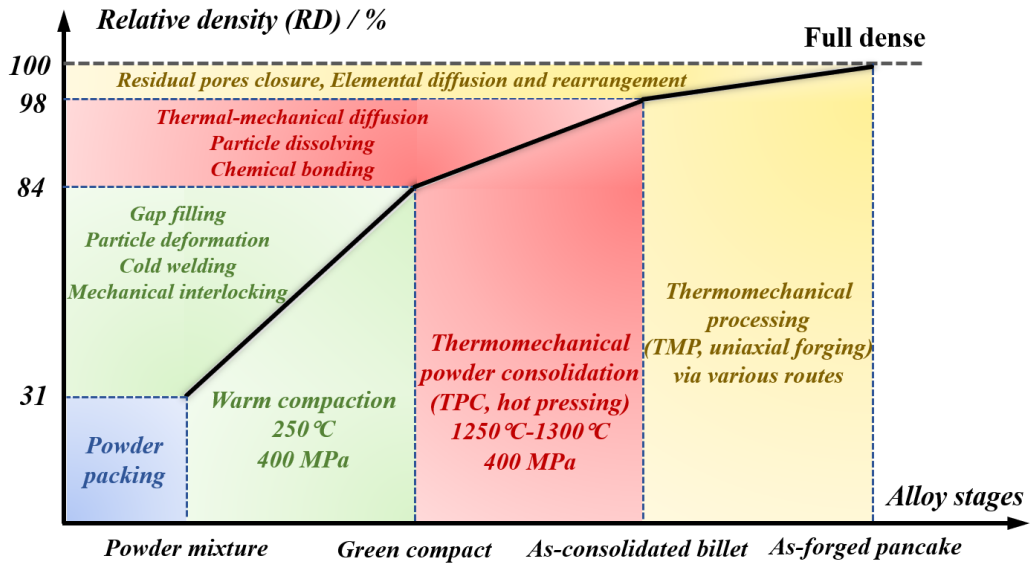

Figure 2.10 Relative density variation situation and relevant densification/consolidation mechanisms during the whole synthesis/processing procedures of PM Ti-5553 alloy.

During the warm compaction process of the raw powder mixture, the relevant densification mechanisms are mainly associated with the physical response of the powder particles including particle gap filling, particle deformation, cold welding among particles and their mechanical interlocking. These physical responses lead to a great RD increment (from 31% to 84%) during the compaction of powder feedstock and make it become bulk material for further consolidation. Subsequently, the novel modified hot pressing (TPC) plays the most important role for the densification of PM Ti-5553 alloy. During this process, the induction-generated high temperature (up to 1300 °C) and external load (400 MPa) work concurrently to procedure the strong thermomechanical effects on the green compact. During the high-temperature heating, chemical responses like elemental diffusion, particle dissolving and chemical bonding occur at the same time to consolidate the compact effectively. More critically, with the assistance of the thermomechanical effects, the elemental diffusion and particle dissolving are accelerated significantly comparing to the conventional pressure-less sintering. The novel modified hot pressing overcome the most difficult step to consolidate the material, with an obvious RD enhancement from 84% to a very high value of 98%, which is higher than the most of other PM titanium alloy components produced by conventional sintering [8-10] and even some additive-manufactured components [5, 11, 12] (selective laser melting and electron beam melting) At last, the residual 2% porosity in the as-consolidated alloy is finally eliminated during the applied uniaxial open-die hot

forging as the results of the residual pore closure effect and deformation-induced elemental rearrangement to achieve the full dense in as-forged alloy pancakes.

2.3.3 Macrostructure of PM alloy billet

The macrostructural observation was conducted on the as-consolidated PM alloy billet (after TPC). The billet was wire-cut along the cross-section direction and then the surface was precisely machined. The cross-section surface was etched directly and uniformly in a modified Kroll's reagent containing 10 vol.% HF, 20 vol.% HNO_3 and 70 vol.% H_2O to reveal the macrostructure of the billet.

2.3.4 Beta phase transformation temperature measurement

The beta phase transformation temperatures of the alloys studied in this work were measured by the heat treatment and metallographic method, which is a common and reliable method used when investigating titanium alloys [13-17]. The specimens were heat-treated for 40 mins in the furnace and then water-quenched at various temperatures close to the theoretical beta phase transformation temperatures (calculated by the chemical composition) of the alloys. Metallographic examinations were subsequently performed on these specimens, the lowest heat treatment temperature with only beta phase in the microstructure was determined as the beta phase transformation temperatures of the alloys.

2.3.5 X-ray diffraction

Figure 2.11 Bruker D8 Advanced X-ray diffractometer.

X-ray diffraction (XRD) analyses were performed on a D8 Advanced X-ray diffractometer (Bruker Ltd., USA, shown in Figure 2.11) equipped with a Cu Kα radiation source (λ = 0.154157 nm) to determine the phase constitutions of the samples. Bulk samples were cut from the initial, deformed and processed alloys with the surface finely-ground to 2000 grit.

2.4 Thermal physical simulation

Thermal physical simulation experiments were conducted on a Gleeble® 3800-GTC thermal physical simulator (Dynamic Systems Inc., USA), as shown in Figure 2.12. The Gleeble® thermal-mechanical physical testing platform has obtained a widespread application in the physical simulation field of metallic materials. As almost the latest model, Gleeble® 3800-GTC simulator has been developed as the highly integrated examination system with accurate digital control and reliable data acquisition [18]. During the testing, various kinds of data (like stress, temperature, displacement, testing time and loading mode) can be obtained through the thermomechanical process performed at different conditions for the simulation of the actual processing and deformation processes of the materials.

Figure 2.12 Gleeble® 3800-GTC thermal physical simulator.

Cylindrical testing specimens with a size of 10 mm in diameter and 15 mm in height were used in this testing. The specimens were firstly wire-cut from the centre areas near the half radius of as-consolidated PM alloy billets and as-cast IM alloy ingots, as shown in the sampling sketch in Figure 2.13. After that, the cylindrical testing specimens were machined precisely into the required size with good surface finishing and parallel surfaces (top and bottom).

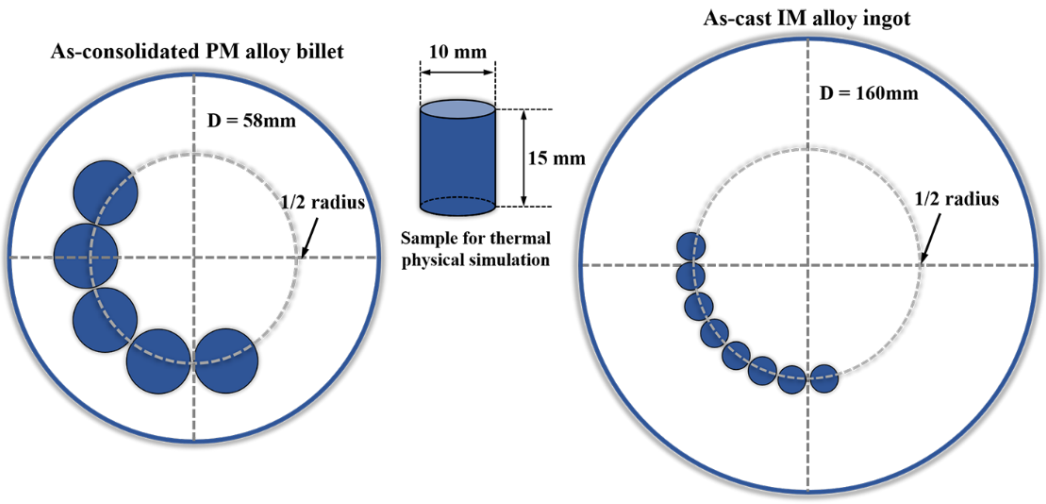

Figure 2.13 Schematic diagram demonstrating the sampling positions of as-consolidated PM and as-cast IM Ti-5553 alloys for thermal physical simulation.

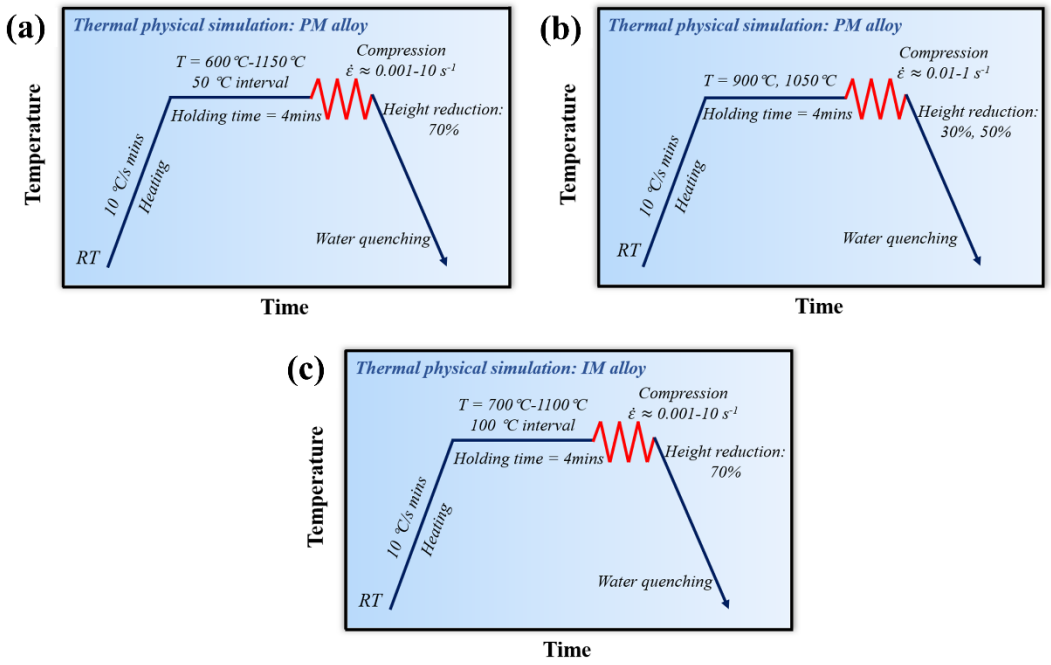

Figure 2.14 Schematic diagrams demonstrating the experimental details and parameters for thermal physical simulation: (a) 70% deformation tests for PM alloy; (b) 30% and 50% deformation tests for PM alloy; (c) 70% deformation tests for IM alloy.

The thermal physical simulation tests were performed in the form of isothermal hot compression in this study at various temperatures, strain rates and deformation degree in vacuum. The temperature range was set as 600 °C to 1150 °C (50 °C interval) of PM alloy and 700 °C to 1100 °C (100 °C interval) of IM alloy, and the strain rates used were 0.001 s^{-1}, 0.01 s^{-1}, 0.1 s^{-1}, 1 s^{-1} and 10 s^{-1} for both alloys. Most of the hot compression were processed to the total deformation degree of 70% sample height reduction (from 15 mm to 4.5 mm height), while 30% and 50%

deformations of the PM alloy were also performed at some temperatures and strain rates.

Table 2.2 Detailed variables during the thermal physical simulation of PM alloy with a height reduction of 70%.

Items	Detailed variables
Temperature (°C)	600, 700, 750, 800, 850, 900, 950, 975, 1000, 1050, 1100, 1150
Strain rate (s^{-1})	0.001, 0.01, 0.1, 1, 10
Height reduction (%)	70%
Pre-heating rate (°C/s)	10
Holding time (s)	240
Cooling mode	Water quenching

Table 2.3 Detailed variables during the thermal physical simulation of PM alloy with a height reduction of 30% and 50%.

Items	Detailed variables
Temperature (°C)	900, 1050
Strain rate (s^{-1})	0.01, 0.1, 1
Height reduction (%)	30%, 50%
Pre-heating rate (°C/s)	10
Holding time (s)	240
Cooling mode	Water quenching

Table 2.4 Detailed variables during the thermal physical simulation of IM counterpart with the height reduction of 70%.

Items	Detailed variables
Temperature (°C)	700, 800, 900, 1000, 1100
Strain rate (s^{-1})	0.001, 0.01, 0.1, 1, 10
Height reduction (%)	70%
Pre-heating rate (°C/s)	10
Holding time (s)	240
Cooling mode	Water quenching

Before the isothermal compressive testing, the specimens were firstly heated up to the set temperature at a heating rate of 10 °C/s, and then the temperature was held for 4 minutes to ensure that the temperature was homogeneous throughout the

whole specimen. After the compression test, the deformed specimens were immediately water quenched to freeze the deformed microstructure for further characterizations. The detailed variables and schematic illustrations of the testing process during the thermal physical simulation of PM and IM alloys are shown in Figure 2.14 and Tables 2.2-2.4.

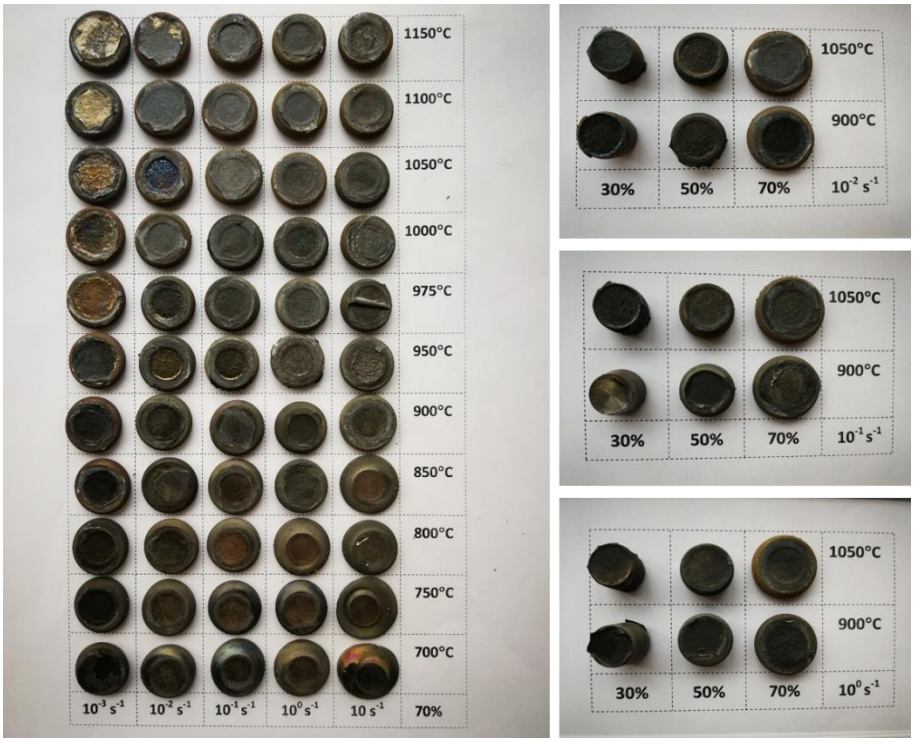

Figure 2.15 Deformed PM alloy samples after thermal physical simulation at various conditions.

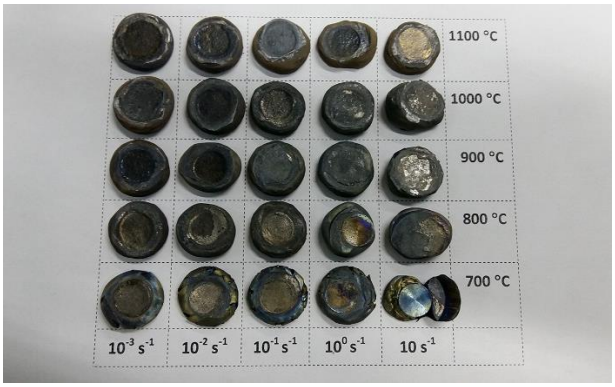

Figure 2.16 Deformed IM alloy samples after thermal physical simulation at various conditions.

Tantalum sheets and graphite foils were placed between the machine anvil and the specimen to reduce the friction and improve the electroconductivity of the testing system. The Pt-Rh thermocouple was welded to the centre surface of the specimen to measure the testing temperature during the heating and deformation processes.

The temperature during the simulation was controlled by the testing system automatically and all the data (stress, strain, temperature and time) of the simulation was recorded by the digital system. At least two specimens were applied for this simulation at each condition to ensure the accuracy and reliability of the testing. The deformed PM and IM alloy samples (partial) after thermal physical simulation are displayed in Figure 2.15 and 2.16, respectively. Afterwards, the deformed samples were sectioned by electric discharge machining (EDM) in the middle along the longitudinal direction, and the areas near the centre of the sample were chosen as the areas of interest (AOI) for further microstructure characterizations (see Figure 2.17).

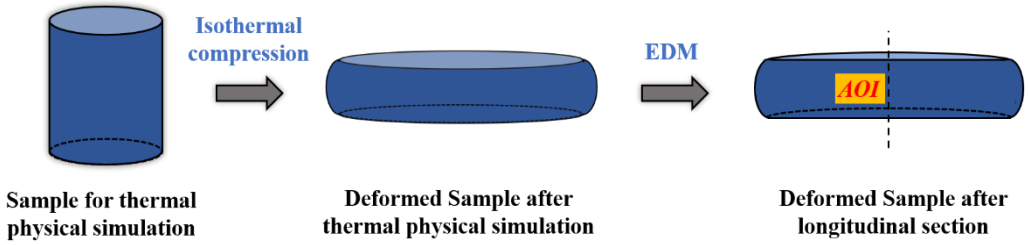

Figure 2.17 Schematic diagram demonstrating the cutting mode and the areas of interest (AOI) of the deformed samples after thermal physical simulation.

2.5 Microstructure characterizations

2.5.1 Metallographic preparation

Metallographic samples used for optical and scanning electron microscopy observations were prepared through the grinding, polishing and etching processes. The samples were firstly cold (room temperature) mounted in epoxy resins or warm (120 °C) mounted in phenol-formaldehyde resins and then ground by SiC papers with the grit size of 320, 600, 1000 and 2000 with water lubrication. Final polishing of the well-ground samples was conducted using an automatic polisher (Tegramin®, Struers Inc., Denmark), as shown in Figure 2.18. The samples were polished for 20 mins with a suspension of colloidal silica (OP-S) gel having a particle size of 0.04 μm. Subsequently, acid-etching was performed to reveal the microstructure of the samples with a modified Kroll's reagent containing 10 vol.% HF, 20 vol.% HNO_3 and 70 vol.% H_2O.

Figure 2.18 Struers Tegramin® automatic polisher.

2.5.2 Optical microscopy

Optical microscopy (OM) observations were performed on an Olympus PMG3 inverted light microscope (Figure 2.19) equipped with a Canon digital camera. The imaging magnifications were 50X, 100X, 200X and 500X.

Figure 2.19 Olympus PMG3 inverted light optical microscope.

2.5.3 Scanning electron microscopy

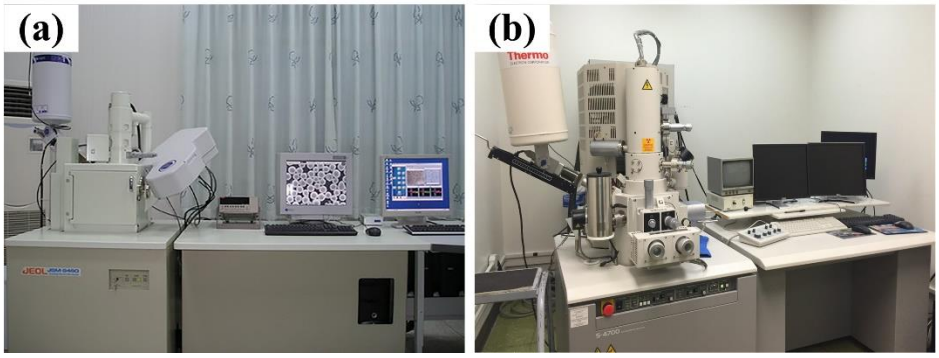

Figure 2.20 Scanning electron microscopes used in the studied: (a) JEOL JSM-6460; (b) Hitachi S-4700 FE.

Scanning electron microscopy (SEM) observations were performed on JEOL JSM-6460 (Figure 2.20a) and Hitachi S-4700 field emission (Figure 2.20b) electron microscopes in vacuum to obtain magnifications up to 50000X in the secondary electron (SE) imaging mode.

2.5.4 Transmission electron microscopy

Transmission electron microscopy (TEM) observations were performed on a JEOL JEM-2100 electron microscope (Figure 2.21) to reveal the detailed microstructure of the specimen in nanometre-scale. Specimens with a 3 mm diameter (punched from alloy samples) were ground to 60 μm in thickness. PM specimens were then ion-beam milled (PIPS-II, Gatan Inc., USA), while IM specimens were twin-jet polished (TenuPol-5, Struers Inc., Denmark), to enlarge the thin area (thickness = 50-100 nm) for TEM observations. Selected area electron diffraction (SAED) was also performed using the high-energy concentrated electron beam.

Figure 2.21 JEOL JEM-2100 transmission electron microscope.

2.5.5 Electron backscatter diffraction

Electron backscatter diffraction (EBSD) technique is an advanced approach to characterize microstructural-crystallographic features of the sample by statistically collecting the data of diffraction patterns. Various information can be obtained through this characterization including basic microstructure (grain type, morphology and distribution), crystal orientation distribution, misorientation analysis, micro-texture determination, grain boundary analysis and phase distribution.

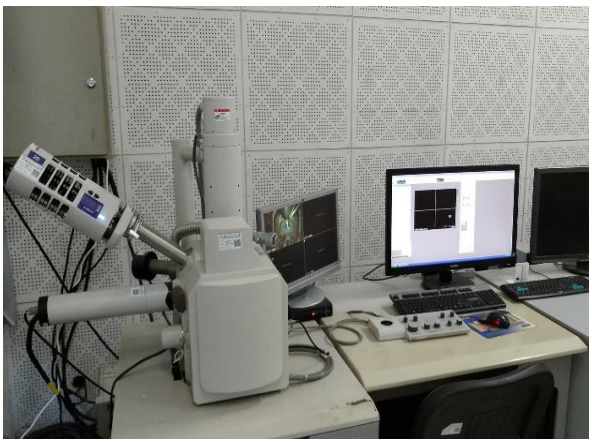

Figure 2.22 Hitachi S-3400N SEM equipped with an EBSD detector.

EBSD characterizations in this study were conducted on a Hitachi S-3400N SEM facility equipped with a Channel 5 data acquisition and analysis system (Figure 2.22, HKL Technology, Oxford Instruments). The specimens were ground (finished by 2000 grit) and electropolished at a voltage of 25 V at - 20 °C in a chemical solution containing 6 vol% perchloric acid, 34 vol% butanol and 60 vol% methanol.

2.5.6 Atomic force microscopy

Atomic force microscopy (AFM) observations were performed on a Dimension Icon microscope (Figure 2.23, Bruker Ltd., USA) with a RTESP-300 probe to characterize the surface topography and morphology of the samples in nanometer scale. The AFM imaging was achieved in the probe-tapping mode with a scanning frequency of 0.5 Hz.

Figure 2.23 Bruker Dimension Icon atomic force microscope.

2.6 Mechanical testing

2.6.1 Tensile testing

Three kinds of tensile specimen were utilized in this work due to different material size and the testing temperature. The schematic drawings of these tensile specimens are shown in Figure 2.24. The large-scale rectangular cross-section specimens (Figure 2.24a) with the cross-section size of 4 mm × 2.5 mm (total length is 51 mm) were prepared through EDM and precise machining for the comparison of room-temperature tensile properties of the two starting alloys. Round specimens (Figure 2.24b) with a gauge length of 20 mm and a diameter of 4 mm (external diameter is 6 mm, total length is 51 mm) were prepared through EDM and precise machining for the high-temperature tensile testing of PM alloy. The small-scale dog-bone-shaped specimens (Figure 2.24c) with the cross-section size of 2 mm × 2 mm (total length is 36.2 mm) were used to examine the room-temperature tensile properties of as-forged PM alloy pancakes before and after heat treatment. The accurate cross-section size of the specimen was measured by a calliper with 0.05 mm of precision before tensile testing.

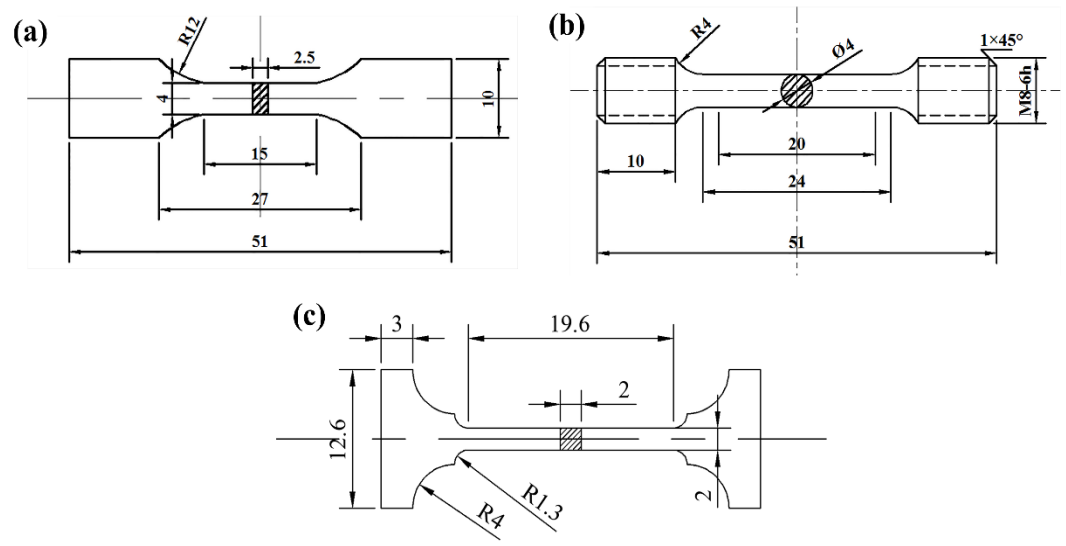

Figure 2.24 Dimensional drawing of the tensile testing specimens: (a) large-scale rectangular cross-section specimen; (b) round cross-section specimen; (c) small-scale dog-bone-shaped specimen.

Figure 2.25 Instron-5982 universal testing machine for tensile and fracture toughness tests.

The room-temperature and elevated-temperature tensile tests were conducted on Instron-5982 electronic universal test machine (Figure 2.25) at the rate of 10^{-3} s^{-1} with a load cell of 50 kN. The data for strain and displacement during the tests were recorded accurately using a static extensometer with a gauge length of 10 mm. For the high-temperature tensile tests, the protective-layer coated samples were heated in a furnace chamber to the target temperature at a heating rate of 20 °C/min and held for 20 mins to ensure the uniform temperature distribution and minimize oxidation during the testing. At least three specimens were tested during various tensile testing at each condition for accuracy and reliability. The tensile properties including yield strength (YS), ultimate tensile stress (UTS), strain at failure (ε_f) can be obtained from the tensile stress-strain curves and related calculations. In this study, the value of ε_f is considered as the total elongation of the specimen during tensile testing.

2.6.2 Fracture toughness testing

The single notched (V-shape) specimens were cut by EDM from the materials followed by precise machining and surface polishing to perform fracture toughness tests on the Instron-5982 electronic universal test machine (Figure 2.25) at room temperature. The employed specimen has a thickness (B) of 2.5 mm, a width (W) of 4.5 mm, a loading span (S) of 16 mm and a pre-made 45° V-shape notch with the depth (a) of 2.0 mm. The Dimensioned drawing of the fracture toughness testing specimen is shown in Figure 2.26.

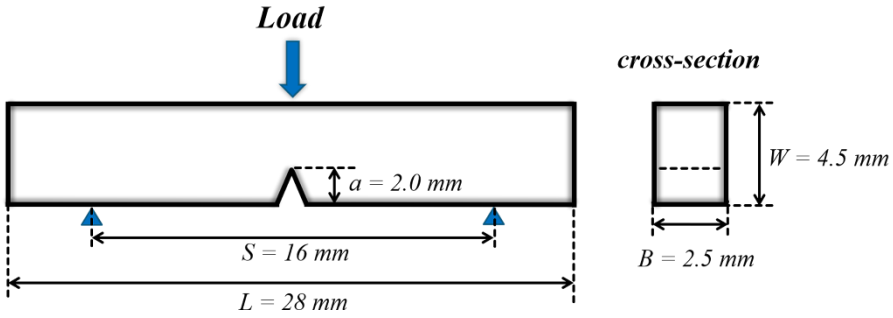

Figure 2.26 Dimensioned drawing of the fracture toughness testing specimen.

The testing specimen provides plane-strain conditions at the notch tip, and the tests were conducted with a loading rate of 0.5 mm/min. The load-displacement curves were recorded during the test, and the apparent fracture toughness K_Q (for small-scale specimen) can be calculated using Equation 2.3 and Equation 2.4. However, K_Q is not perfectly equal to the value of K_{IC} (for standard-scale specimen) due to the different specimen size. In this work, the values of K_Q were utilized to compare the fracture toughness of alloys at different conditions.

$$K_Q = (F_Q/BW^{1/2}) \times f\,(a/W) \tag{2.3}$$

$$f\,(a/W) = (2+a/W) \times \frac{0.866 + 4.64(a/W) - 13.32(a/W)^2 - 14.72(a/W)^3 - 5.6(a/W)^4}{(1-a/W)^{3/2}} \tag{2.4}$$

2.6.3 Impact toughness testing

Charpy V-notch specimens were obtained by EDM from the materials followed by machining and surface polishing to perform impact toughness tests on a NJ780C pendulum bob impact-testing machine at room temperature. The utilized specimen has a length of 50 mm, a square-shaped cross-section with 10 mm side length and a pre-made 45° V-shape notch of 2 mm in depth. The dimensioned drawing of the impact toughness testing specimen is shown in Figure 2.27. The testing was performed at room temperature using with a maximum energy rating of 400 J and impact velocity of 5.0 m/s.

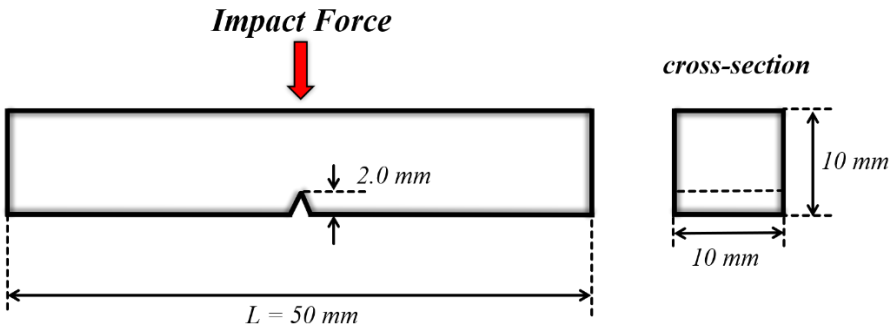

Figure 2.27 Dimensioned drawing of the impact toughness testing specimen.

2.6.4 Fractographic analysis

Fractographic analyses were conducted on the fractured surfaces of the specimens after tensile, fracture toughness, and impact toughness tests using SEM (JEOL JSM-6460, Figure 2.20a). The fracture mechanism and failure mode of the specimen can be revealed by the observations of the fractographic characteristics. A diagram showing the fractographic observation mode and direction of the fractured samples are exhibited in Figure 2.28.

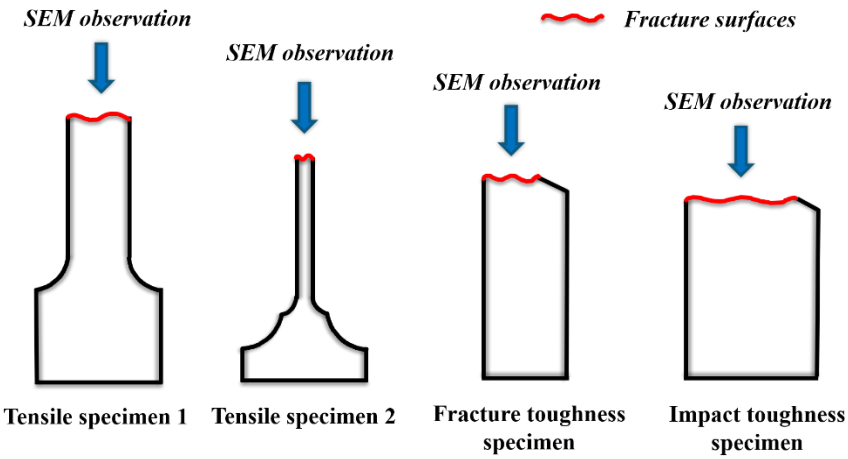

Figure 2.28 Diagrams showing the fractographic observation mode and direction of the fractured samples.

2.6.5 Hardness measurement

Vickers hardness measurement was employed as a supplementary method to evaluate the mechanical properties of the material. Hardness measurements were conducted using a microhardness tester (Figure 2.29, FM-700, Leco Ltd.) with a diamond right-square-pyramid indenter having the taper angle of 136°. Then, the

Vickers hardness value can be calculated by measuring the diagonal length of the indentation with the following equation:

$$HV = \frac{2F\sin\frac{\alpha}{2}}{d^2} = 1.8544\frac{F}{d^2}\ (\mathrm{Kgf \cdot mm^{-1}}) \qquad (2.5)$$

Figure 2.29 FM-700 microhardness tester for Vickers hardness measurement.

where F is the external load applied (300 gf) for the measurement, α is the taper angle, d is the average of indentation diagonal length. The load was pressurized for 10 seconds for the test, and the measurements were repeated 10 times to obtain the averaged behaviour of the sample. Prior to testing, the target surfaces were fine-ground (finished by 4000 grit) and polished with OP-S gel to remove the residual stress of the sample.

2.7 In-situ tensile observation

In-situ tensile scanning electron microscopy (SEM) observation has recently become a powerful and effective tool to study the deformation behaviour from the perspective of the microstructure aspect by capturing the microstructural variations dynamically. Through this technique, the microscopic processes of plastic deformation and the underlying fracture mechanisms can be studied profoundly and comprehensively.

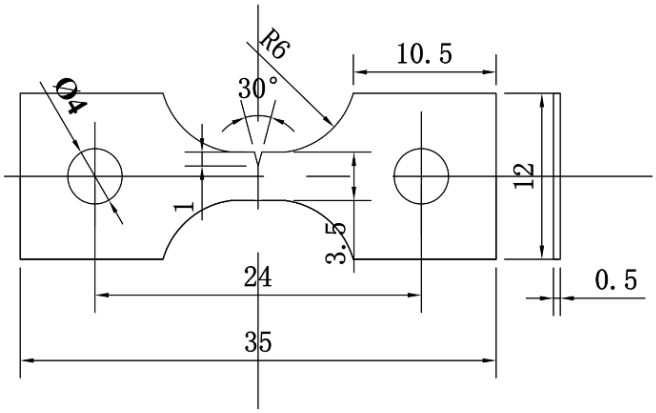

Figure 2.30 Dimensioned drawing of the in-situ tensile observation specimen.

The specimens for the in-situ tensile tests were obtained from as-consolidated PM alloy billet and as-cast IM alloy ingot by EDM and subsequent fine grinding (finished by 4000 grit) to the required dimension with a single-side pre-made V-shape notch. The dimensioned drawing of the in-situ tensile specimen is shown in Figure 2.30. Afterwards, the specimens were electropolished in a solution containing 6 vol% perchloric acid and 94 vol% acetic acid to remove the residual stress and reach the mirror-surface finish followed by etching with modified Kroll's reagent (10 vol% HF, 20 vol% HNO_3 and 70 vol% H_2O) to uncover the microstructure.

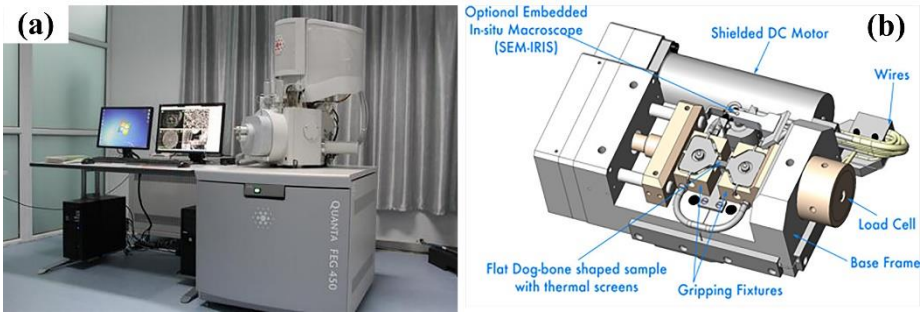

Figure 2.31 Facilities for in-situ tensile observation: (a) Quanta FEG-450 field emission; (b) schematic picture showing the in-situ loading system accessory in SEM [19].

Uniaxial in-situ tensile observations were performed on a Quanta FEG-450 field emission scanning electron microscope (FE-SEM) fitted with a Gatan servo-hydraulic loading system accessory (see Figure 2.31) with a maximum load capacity of 2000 N, using an accelerating voltage of 15 kV. The area near the V-shape notch was locked as the area of interest for the convenience in capturing plastic deformation processes and crack propagation features. The tensile tests were

conducted at a stretching speed of 0.05 mm/min at room temperature in vacuum, and the data was recorded every 500 ms. Several interruption stops were allowed by the loading system during the tensile testing, holding the load, to allow SEM imaging, after which the tensile test was resumed at the same applied load and displacement level.

After the in-situ tensile tests, the fracture surfaces of the specimens were examined using SEM (JEOL JSM-6460, Figure 2.20a). The detailed microstructure characteristics of the alloys before and after the in-situ tensile tests were characterized by TEM (JEOL JEM-2100, Figure 2.21). The specimen surface topography and morphology after the in-situ tensile tests were also detected by AFM (Bruker Dimension Icon, Figure 2.23).

Reference

[1] S. Raynova, Y. Collas, F. Yang, L. Bolzoni, Advancement in the pressureless sintering of CP titanium using high-frequency induction heating, Metall. Mater. Trans. A 50A (2019) 4732-4742.

[2] Y. Alshammari, F. Yang, L. Bolzoni, Mechanical properties and microstructure of Ti-Mn alloys produced via powder metallurgy for biomedical applications, J. Mech. Behav. Biomed. Mater. 91 (2019) 391-397.

[3] M. Ahmadipour, M. Arjmand, M.F. Ain, Z.A. Ahmad, S.Y. Pung, Effect of WO_3 loading on structural, electrical and dielectric properties of $CaCu_3Ti_4O_{12}$ ceramic composites, J. Mater. Sci. 30 (2019) 6806-6810.

[4] J. Suryawanshi, K.G. Prashanth, U. Ramamurty, Mechanical behavior of selective laser melted 316L stainless steel, Mater. Sci. Eng. A 696 (2017) 113-121.

[5] H. Gong, K. Rafi, H. Gu, G.D. Janaki Ram, T. Starr, B. Stucker, Influence of defects on mechanical properties of Ti-6Al-4V components produced by selective laser melting and electron beam melting, Mater. Des. 86 (2015) 545-554.

[6] C. Zopp, S. Blumer, F. Schubert, L. Kroll, Processing of a metastable titanium alloy (Ti-5553) by selective laser melting, Ain Shams Eng. J. 8 (2017) 475-479.

[7] C. Leyens, M. Peters, VCH, Weinheim, 2003.

[8] I.M. Robertson, G.B. Schaffer, Review of densification of titanium based powder systems in press and sinter processing, Powder Metall. 53 (2010) 146-162.

[9] Y. Liu, L.F. Chen, H.P. Tang, C.T. Liu, B. Liu, B.Y. Huang, Design of powder metallurgy titanium alloys and composites, Mater. Sci. Eng. A 418 (2006) 25-35.

[10] L. Bolzoni, E.M. Ruiz-Navas, E. Gordo, Quantifying the properties of low-cost powder metallurgy titanium alloys, Mater. Sci. Eng. A 687 (2017) 47-53.

[11] S.Y. Liu, Y.C. Shin, Additive manufacturing of Ti6Al4V alloy: a review, Mater. Des. 164 (2019) 107552.

[12] X. Zhao, S. Li, M. Zhang, Y. Liu, T.B. Sercombe, S. Wang, Y. Hao, R. Yang, L.E. Murr, Comparison of the microstructures and mechanical properties of Ti-6Al-4V fabricated by selective laser melting and electron beam melting, Mater. Des. 95 (2016) 21-31.

[13] Z. Li, J. Li, Y. Zhu, X. Tian, H. Wang, Variant selection in laser melting deposited α + β titanium alloy, J. Alloys Compd. 661 (2016) 126-135.

[14] L. Zhuo, L. Changmeng, L. Dong, W. Huaming, Effect of heat treatment on microstructure and tensile properties of laser deposited titanium alloy TC21, Mater. Res. Innovations 18 (2014) S4-929-932.

[15] J.L. Li, B.Y. Wang, H. Huang, S. Fang, P. Chen, J.X. Shen, Unified modelling of the flow behaviour and softening mechanism of a TC6 titanium alloy during hot deformation, J. Alloys Compd. 748 (2018) 1031-1043.
[16] J.Z. Sun, M.Q. Li, H. Li, Deformation behavior of TC17 titanium alloy with basketweave microstructure during isothermal compression, J. Alloys Compd. 730 (2018) 533-543.
[17] Y.Q. Ning, B.C. Xie, H.Q. Liang, H. Li, X.M. Yang, H.Z. Guo, Dynamic softening behavior of TC18 titanium alloy during hot deformation, Mater. Des. 71 (2015) 68-77.
[18] Gleeble 3800®-GTC, Thermal-mechanical physical simulation system. http://www.gleeble.com/products/gleeble-systems/gleeble-3800
[19] Newtec, Tensile stage for automated in-situ SEM/OM mechanical & thermal testing. http://www.newtec.fr/en/mt1000/

3 Characterization and room temperature deformation behaviour of PM Ti-5553 alloy and the comparison to IM Ti-5553 alloy

3.1 Introduction

*Partial contents (text and figures) in this chapter have been published in refereed journals:

1. **Qinyang Zhao**, Fei Yang, Rob Torrens, Leandro Bolzoni, Comparison of hot deformation behaviour and microstructural evolution for Ti-5Al-5V-5Mo-3Cr alloys prepared by powder metallurgy and ingot metallurgy approaches, ***Materials & Design***, 169 (2019) 107682.
2. **Qinyang Zhao**, Fei Yang, Rob Torrens, Leandro Bolzoni, PM versus IM Ti-5Al-5V-5Mo-3Cr alloy in mechanical properties and fracture behaviour, ***Materials Research***, 22 supl.2 (2019) e20180739.
3. **Qinyang Zhao**, Fei Yang, Rob Torrens, Leandro Bolzoni, In-situ observation of the tensile deformation and fracture behaviour of powder-consolidated and as-cast metastable beta titanium alloys, ***Materials Science and Engineering A***, 750 (2019) 45-59.

This chapter documents the characterization of as-consolidated PM and as-cast IM Ti-5553 alloys, including chemical composition, initial microstructure, phase constitution and beta phase transformation temperature. Also covered are the room temperature mechanical testing including tensile, fracture toughness and impact toughness test conducted on PM and IM alloys to examine and compare their mechanical properties. Fractographic observations, to reveal the fracture mode of the materials during the tests, are presented and discussed. Room temperature in-situ tensile observations were performed on these two alloys to capture their plastic deformation processes and reveal their cracking mechanisms dynamically and comprehensively inside the scanning electron microscope. Particularly, the effects of common defects in PM (residual pores and microvoids) and IM (casting cavity) alloys on the tensile deformation behaviour and fracture mechanism were caught

and investigated. Lastly, the different slip deformation behaviour and fracture modes between PM and IM counterparts were explained and discussed thoroughly.

The work in this chapter is intended to provide the theoretical support of the direct application and further processing of metastable beta titanium alloys at powder-consolidated and as-cast stages by revealing the tensile strain responses at the microstructural level and uncovering the fracture mode. Meanwhile, the comparative investigations between PM and IM alloys also provide an opportunity for the industry to understand the differences between powder-based and conventional ingot-produced metallic materials in the aspects of room-temperature deformation behaviour and mechanisms.

3.2 Characterization of PM and IM Ti-5553 alloys

3.2.1 Chemical composition

The actual chemical compositions of PM (as-consolidated) and IM alloys (as-cast) are listed in Table 3.1. It is obvious that the chemical composition of both PM and IM alloy are close to the nominal composition of Ti-5Al-5V-5Mo-3Cr.

Table 3.1 Chemical compositions of the studied PM and IM Ti-5553 alloys (wt.%).

	Ti	Al	V	Mo	Cr	O	N
PM alloy	Bal.	4.99	4.93	4.94	2.90	0.36	0.021
IM alloy	Bal.	5.14	5.03	5.02	3.10	0.08	0.008

PM alloy has an obvious higher oxygen (0.36 wt.%) and nitrogen content (0.021 wt.%) than those of IM alloy (0.08 wt.% and 0.008 wt.%). Comparing to the oxygen level of the powder mixture of PM alloy (see Table 2.1 in Chapter 2), it can be deduced that most of the oxygen is brought by the raw powders. In another word, the oxidation has been well controlled during warm compaction and rapid consolidation, and the oxygen absorption during these processes is very limited. The relatively high oxygen (and nitrogen) nature of PM alloy compared to its IM counterpart can lead to different deformation behaviour and mechanisms, which will be discussed in this chapter and the later chapters.

3.2.2 Initial macrostructure and microstructure

The macrostructure images of the PM alloy billet are shown in Figure 3.1. As shown in the images, the macrostructure of the PM alloy billet is homogeneous and there are no undissolved master-alloy powder particles. Particle dissolution is promoted by both the high-temperature heating and hot pressing processes [1, 2]. This macrostructure observation indicated that homogeneous PM Ti-5553 alloy was synthesized successfully following the developed fast-consolidation (TPC) approach for further investigation and characterization.

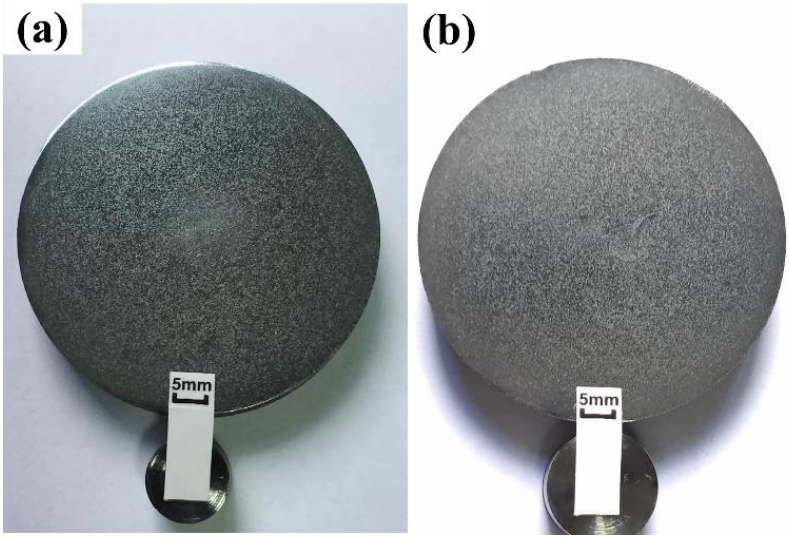

Figure 3.1 Macrostructure images of PM alloy billet: (a) upper cross-section; (b) lower cross-section.

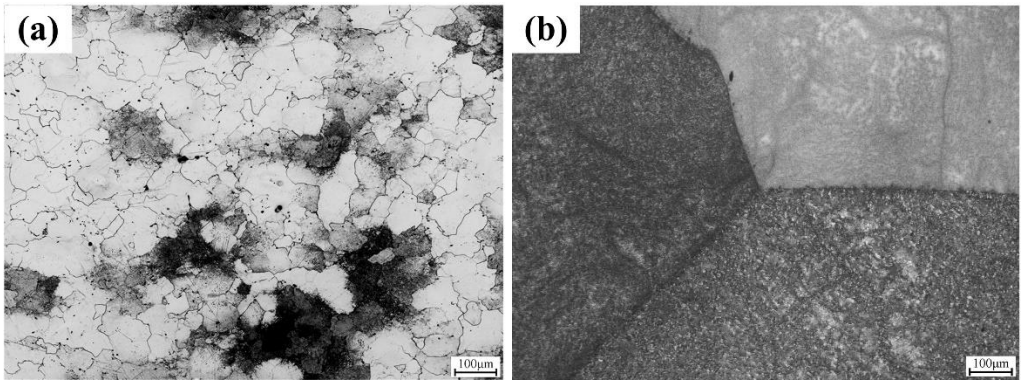

Figure 3.2 Initial microstructures of Ti-5553 alloys: (a) PM alloy; (b) IM alloy.

Figure 3.2 shows the initial microstructures of the as-consolidated PM and as-cast Ti-5553 alloys, it can be seen that the PM Ti-5553 alloy consists of primary equiaxed β phase, with an average grain size of about 100 μm, and a small amount of precipitation phases from the β matrix near the primary β grain boundaries (Figure 3.2a). A similar microstructure for the IM Ti-5553 alloy can be observed in

Figure 3.2b, with the primary differences of a larger amount of precipitates inside β grains and coarser equiaxed β phase (about 1000 μm) than those of the PM Ti-5553 alloy.

3.2.3 Phase constitution

Figure 3.3 shows XRD patterns of the PM and IM Ti-5553 alloys. It is clear, for PM alloy, that there are β peaks, α peaks and α″ peaks in the XRD pattern. Combining the observation from Figure 3.2a, the precipitation phases in PM alloy can be determined as α and α″ phases. As for IM alloy, both α and β peaks can be clearly identified, and the intensity of β peaks is obviously weaker and the intensity of α peaks is stronger than PM alloy, this indicates a larger amount of α phase but less β phase formed in IM alloy than PM alloy. Meanwhile, no α″ phase appears on the XRD results of IM alloy.

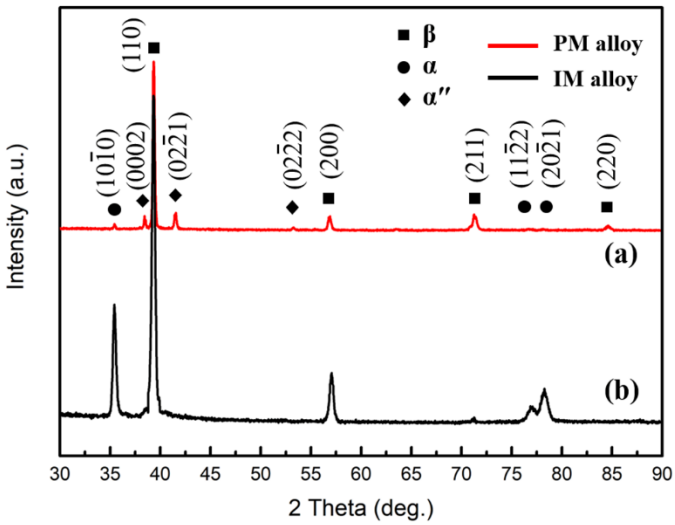

Figure 3.3 XRD patterns of Ti-5553 alloys: (a) PM alloy; (b) IM alloy.

It is obvious that, the phase constitutions of the two alloys are different. The main reason is attributed to the difference in the cooling rates after powder consolidation and ingot casting processes. For PM Ti-5553 alloy, the powder compact is about 500 g and the hot-pressing temperature of 1250 °C-1300 °C is higher than the alloy's β transus temperature of 975 °C. The flowing-argon used during processing can rapidly cool the hot-pressed billet to room temperature after consolidation. The fast cooling rate leads to the generation of α″ martensite in the microstructure of PM Ti-5553 alloy. Meanwhile, the α phase precipitation from β phase is suppressed in the cooling process, leading to only a small amount of α phase found in the PM

alloy. However, the Ti-5553 ingot is about 20 kg and the ingot is furnace cooled to room temperature after casting, the cooling rate is very slow and close to an equilibrium state. Therefore, the α phase has enough time to precipitate from β phase during the cooling process, resulting in a large amount of α phase formed in IM alloy.

3.2.4 The beta phase transformation temperature

The determination of the (α+β)→β phase transformation temperature (beta transus) of titanium alloys is essential as it is a vital property and has huge significance on the hot deformation and heat treatment processes of the alloys. The beta transus temperature of titanium alloys is depends mainly on their chemical compositions. Table 3.2 shows the effect of the alloying element content (in Ti-5553 alloy) on the β transus temperature of titanium alloys (the composition shown in Table 3.1).

Table 3.2 The effect of element content on the β transus temperature of titanium alloys (empirical) [3].

Type of alloying elements	Alloying elements	Element content (wt.%)	The effect on the β transus temperature		
			The effect of each element	PM alloy	IM alloy
α stabilizers	Al	0 ~ 2.0	+14.5 °C/1.0%	29 °C	29 °C
		2.0 ~7.0	+23 °C/1.0%	68.8 °C	72.2 °C
	O	0 ~ 1.0	+2 °C/0.01%	72 °C	16 °C
	N	0 ~ 0.5	+5.5 °C/0.01%	11.6 °C	4.4 °C
β stabilizers	Mo	0 ~ 5.0	-5.5 °C/1.0%	-27.2 °C	-27.5 °C
		5 ~ 30.0	-10 °C/1.0%	/	-0.2 °C
	V	0 ~ 10.0	-14 °C/1.0%	-69.0 °C	-70.4 °C
	Cr	0 ~ 7.0	-15.5 °C/1.0%	-44.9 °C	-48.1 °C
Total				+40.3 °C	-25.15 °C

A rough calculation based on the chemical composition (Table 3.1) was performed to determine the temperature range of further heat treatments. The original β transus temperature of pure titanium is 885 °C, so the equation to calculate the β transus temperature (roughly) of the titanium alloys is:

$$T_{(\alpha+\beta)/\beta} = 885\ °C + \text{Content of alloying element} \times \text{The effect of each element} \quad (3.1)$$

According to Equation 3.1, the β transus temperatures of IM and PM alloy are calculated as 860.4 °C and 925.3 °C, respectively. Based on these values, the heat treatments of PM alloy were conducted at the temperatures range of 870 °C-990 °C, the optical images of some samples treated at typical temperatures of 870 °C, 880 °C , 900 °C, 950 °C, 960 °C, 970 °C, 975 °C, 980 °C and 990 °C are shown in Figure 3.4.

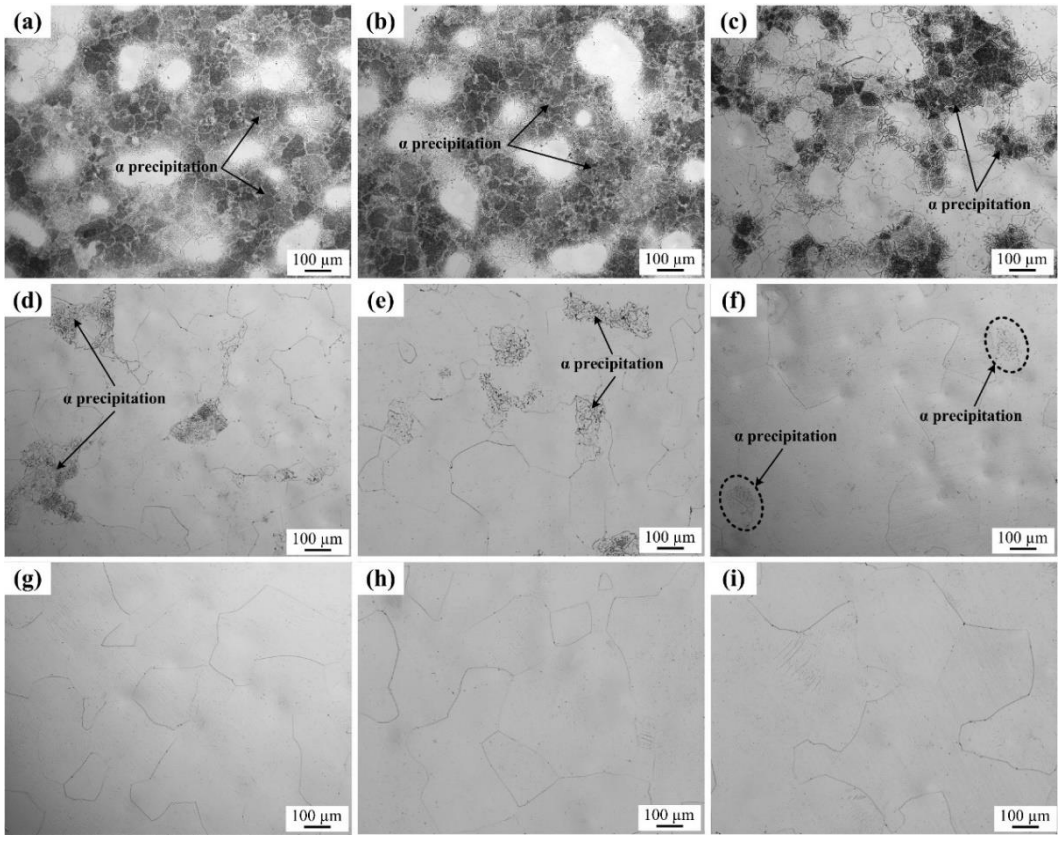

Figure 3.4 Optical images showing the β transus temperature measurement results of PM Ti-5553 alloy: (a) 870 °C; (b) 880 °C; (c) 900 °C; (d) 950 °C; (e) 960 °C; (f) 970 °C; (g) 975 °C; (h) 980 °C; (i) 990 °C.

It can be clearly observed in Figure 3.4a-c that, a large number of α precipitations can be observed in the microstructures of the specimens heat-treated in the temperature range of 870 °C-900 °C. These results indicate the β-transus of PM Ti-5553 alloy can be much higher than the conventional IM Ti-5553 alloys. In the temperature range of 950 °C-970 °C (Figure 3.4d-f) the proportion of α precipitates reduces significantly with increasing heat treatment temperature. The α precipitates disappear from the samples at temperatures of 975 °C, and there is only β phase in the microstructure (Figure 3.4g-i). These results reveal that the β-transus of PM Ti-5553 alloy is 975 °C±5 °C.

In the same way, heat treatments of IM alloy were conducted in the temperature range of 840 °C-890 °C. Optical images of some typical samples treated at 850 °C, 860 °C, 870 °C, 875 °C, 880 °C and 890 °C are shown in the Figure 3.5. It is obvious that, at temperatures below 875 °C (Figure 3.5a-c), there are some α precipitates in the microstructure. When the heat treatment temperature is higher than 875 °C (Figure 3.5d-f), there is only β phase in the microstructure. Therefore, the β-transus temperature of IM alloy is determined as 875 °C±5 °C.

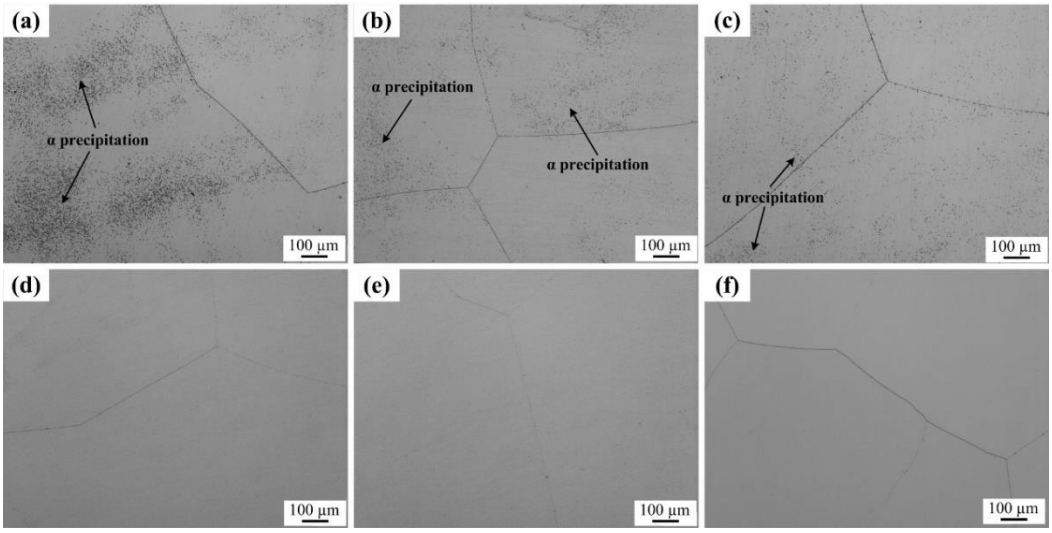

Figure 3.5 Optical images showing the results of β transus temperature measurement of IM Ti-5553 alloy: (a) 850 °C; (b) 860 °C; (c) 870 °C; (d) 875 °C; (e) 880 °C; (f) 890 °C.

The large gap between the two studied alloys is attributed to the high oxygen level (as well as nitrogen level) of the PM alloy. It is widely believed and verified that the element of oxygen (and nitrogen) can acts as a strong α stabilizer in titanium alloys, which promote the transformation of $\beta \rightarrow \alpha$ and increase the β transus temperature significantly [4, 5]. The much higher β phase transformation temperature of PM alloy compared to its IM counterpart can lead to different hot deformation behaviour and mechanisms, which will be discussed in later chapters.

3.3 Regular tensile, fracture toughness and impact toughness testing of PM and IM Ti-5553 alloys

3.3.1 Mechanical properties

The test results of tensile, fracture toughness and impact toughness tests for the as-consolidated PM and as-cast IM Ti-5553 alloys are listed in Table 3.3. It is clear

that IM alloy has overall better mechanical properties than PM alloy, in particular, the ductility and toughness, with a value of 3.8% for the ductility, and 64 MPa·√m and 19 J/cm^3 for the fracture and impact toughness, respectively. However, the PM counterpart has a ductility of 2.1%, and fracture and impact toughness of 28 MPa·√m and 4 J/cm^3, respectively.

Table 3.3 Mechanical properties of PM and IM Ti-5553 alloy.

Alloy Conditions	Tensile properties*			K_Q (MPa·√m)	Impact toughness (J/cm^3)
	Yield stress (MPa)	Ultimate stress (MPa)	Elongation (%)		
PM alloy	935	1008	2.1	28	4
IM alloy	1126	1220	3.8	64	19

* Using the rectangular-shaped cross-section specimens for tensile tests.

3.3.2 Fracture behaviour

The fracture surfaces of tensile specimens of the IM and PM Ti-5553 alloys are exhibited in Figure 3.6. A relative flat fracture surface composed of continuous small fracture facets and tear ridges can be observed in the macroscopic images of PM alloy (Figure 3.6a), the detailed fracture surface morphologies are revealed in Figure 3.6b and Figure 3.6c, with typical cleavage fracture facets with river-like patterns divided by tear ridges, some non-uniformly distributed shallow and small dimples can be clearly identified. These fracture surface morphologies indicate that the fracture mechanism of PM alloy during the tensile tests is a quasi-cleavage mixed ductile-brittle fracture. However, IM alloy specimens display a significant tortuous fracture surface after tensile tests in macroscopic images shown in Figure 3.6d, and the homogenous deep dimples spread over fluctuant fracture surface can be observed in enlarged images in Figure 3.6e and Figure 3.6f. An entirely ductile fracture mechanism with a large amount of plastic deformation and energy absorption can be proposed based on the fracture surface features of IM alloy.

The macroscopic and microscopic fracture surface morphology and the dominant fracture mechanisms suggest higher tensile properties of IM Ti-5553 alloy than PM Ti-5553 alloy especially in ductility, which agrees with the obtained tensile properties Table 3.3.

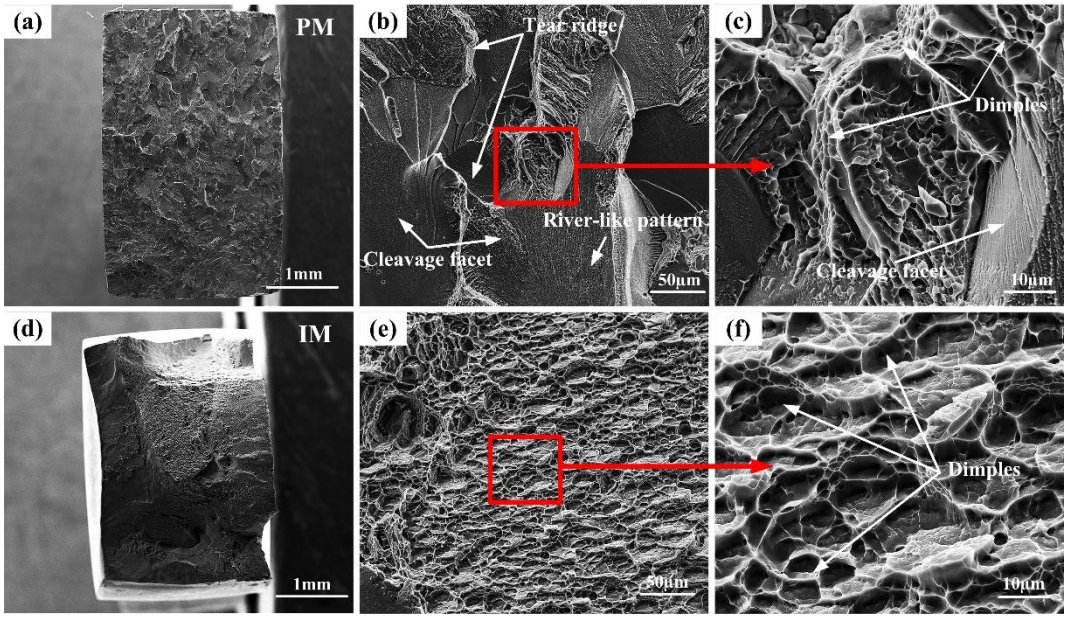

Figure 3.6 SEM images of macroscopic and microscopic fracture surface morphologies of the specimens after tensile tests of as-consolidated PM and as-cast IM Ti-5553 alloys: (a) PM macroscopic scale; (b) and (c) PM microscopic scale; (d) IM macroscopic scale; (e) and (f) IM microscopic scale.

Figure 3.7 presents the fracture surfaces of the specimens of the PM and IM Ti-5553 alloys from fracture toughness tests at room temperature. First of all, similar to the macroscopic tensile fracture surfaces, flat and even crack surfaces can be seen in PM alloy fracture toughness specimen in Figure 3.7a. Large cleavage facets in conjunction with tear ridges and secondary cracks can be found in Figure 3.7b and Figure 3.7c, while Figure 3.7c also presents a number of small and irregular dimples arranged between flat cleavage facets. A lower energy consumption of PM alloy during the crack propagation and the cleavage dominated crack mechanism can be inferred and identified during the fracture toughness test of PM alloy.

As for IM alloy, as shown in Figure 3.7d, topography morphology of the rough cracking propagation surface is clear in the macroscopic scale fracture surface images, suggesting a higher energy consumption during the crack propagation than PM alloy. Meanwhile, the regular and uniform distribution of dimples in the enlarged fracture surface in Figure 3.7e and Figure 3.7f demonstrate the distinct ductile crack mechanism of IM alloy.

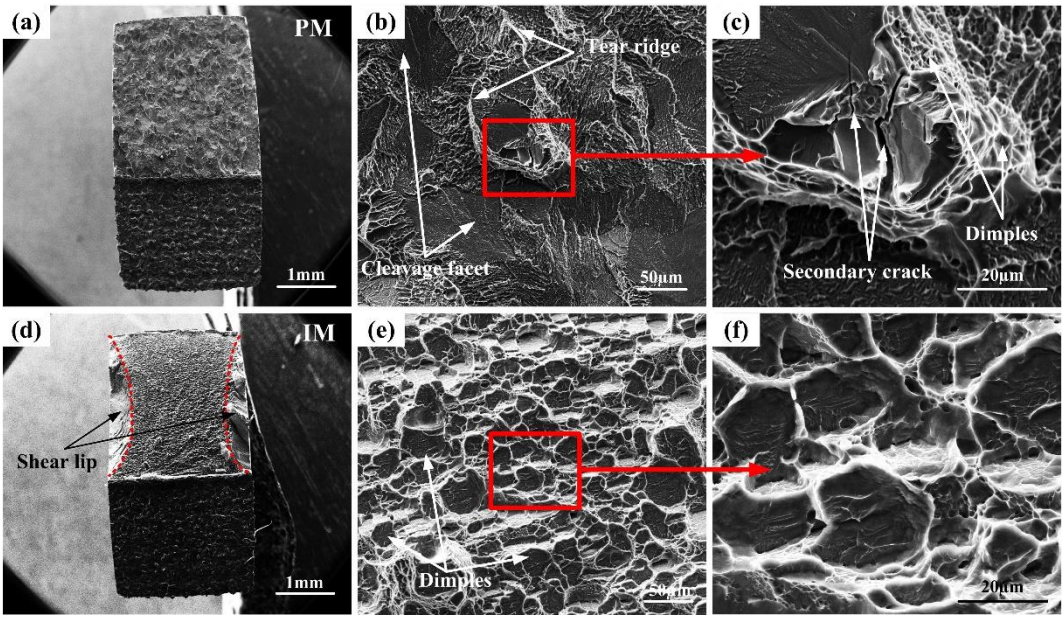

Figure 3.7 SEM images of macroscopic scale and microscopic scale fracture surface morphologies of the specimens after fracture toughness tests of as-consolidated PM and as-cast IM Ti-5553 alloys: (a) PM macroscopic scale; (b) and (c)PM microscopic scale; (d) IM macroscopic scale; (e) and (f) IM microscopic scale.

By analysing the crack surface morphology of the fracture toughness specimens, there is no doubt that PM alloy exhibits a much lower fracture toughness than IM alloy due to the ease of crack propagation and brittle fracture mechanism. However, the appearance of the small dimples in the PM specimen suggest the crack propagation is inhibited by these dimples and increases the fracture toughness value to some extent [6]. Moreover, it worth noticing that, after the fracture toughness test, obvious shear lips can be identified in the macroscopic fracture surface of IM alloy in Figure 3.3d, but they are not observed in PM specimen. It is well known that plane stress conditions can be realized at the notched side surface of fracture toughness specimen, and with the increasing distance from the surface, the stress triaxiality during the static loading in the fracture toughness tests goes up. The areas with low-stress triaxiality tended to suffer from shear cracking which involves a large amount of plastic deformation and provides sizable fracture resistance, the ‘shear lips’ are one of the features of the shear cracking in the macroscopic scale of the fracture toughness specimen fracture surface [7]. The appearance of the shear lips indicates higher plastic deformation during the test and higher fracture toughness of IM alloy than PM alloy.

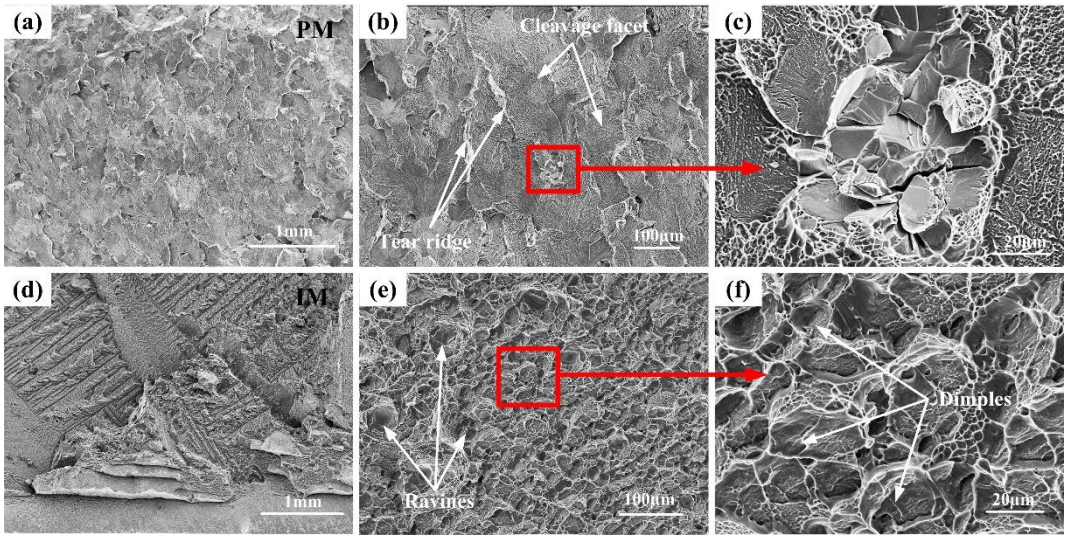

Figure 3.8 SEM images of macroscopic scale and microscopic scale fracture surface morphologies of the specimens after impact toughness tests of as-consolidated PM and as-cast IM Ti-5553 alloys: (a) PM macroscopic scale; (b) and (c)PM microscopic scale; (d) IM macroscopic scale; (e) and (f) IM microscopic scale.

The impact toughness specimens of IM and PM Ti-5553 alloy were examined macroscopically after testing to analyse the dynamic fracture behaviour of the alloys. From Figure 3.8a and Figure 3.8d, it is clear that dynamic fracture surfaces of these two alloys show entirely different features. The IM alloy impact toughness specimen has a tortuous surface (Figure 3.8b), demonstrating a longer crack path during the impact fracture process, with higher energy consumption and reflecting the change of the amplitude of the crack path during the impact test [8]. However, a relatively even and smooth impact fracture surface (Figure 3.8a) can be observed in the PM specimen which gave a lower impact fracture energy during the impact test.

More detailed impact toughness fracture surface morphologies of PM and IM Ti-5553 alloys are shown in the enlarged surface image segments. As shown in Figure 3.8b, large and uninterrupted cleavage facets accompanied by tear ridges tightly distributed in the impact fracture surface of PM alloy specimen. Meanwhile, it is worth noticing that some areas are sticking out from the flat fracture surface accompanied by the secondary cracks surrounded by some tiny and shallow dimples in PM alloy impact fracture surface (Figure 3.8c). These features suggest that brittle intergranular fracture is the dominant mechanism in PM alloy during the impact toughness test. Conversely, as shown in Figure 3.8e and Figure 3.8f, large and deep dimples accompanied by several ravines spread uniformly over the impact fracture

surface characterizes a ductile fracture mechanism and signifies a considerable improvement of the IM impact toughness specimen.

Corresponding to the mechanical properties in Table 3.3, the much higher impact toughness of IM alloy than PM alloy is verified by the fracture behaviour and mechanisms in this section.

By analysing and comparing the room temperature mechanical properties of as-cast IM and as-consolidated PM Ti-5553 alloys, the remarkable gaps between tensile ductility, fracture toughness and impact toughness can be clearly viewed. These results may be attributed to the residual pores and phase distribution in PM alloy, which reduce its mechanical properties at the as-consolidation stage. However, all of these speculations are based on the current regular room temperature mechanical testing and the final fracture surface morphology. The detailed comparative investigation of the room-temperature deformation behaviour and the effect of the defects will be presented in the following section with in-situ tensile observation.

3.4 In-situ observation of the tensile deformation and fracture behaviour of the alloys

3.4.1 In-situ tensile curves

The applied load versus displacement curves of the PM and IM alloys obtained from the in-situ tensile tests are displayed in Figure 3.9. The intermediate interruptions at varying displacements for SEM imaging are marked on the curves as Arabic numbers (1-4) of PM alloy and Roman numbers (I-V) of IM alloy, respectively. It can be clearly seen that the curves suggest a consecutive increase in the load and then fracture instantly after the peak applied load points. IM alloy displays a maximum load of 1343 N, which is 179 N higher that of PM alloy (1164 N). Meanwhile, an obvious higher elongation can also be identified in IM alloy which fractured at the displacement of 0.728 mm, while the fracture displacement of PM alloy is only 0.312 mm. These results indicate that IM alloy has slightly higher strength and considerably higher ductility than PM alloy.

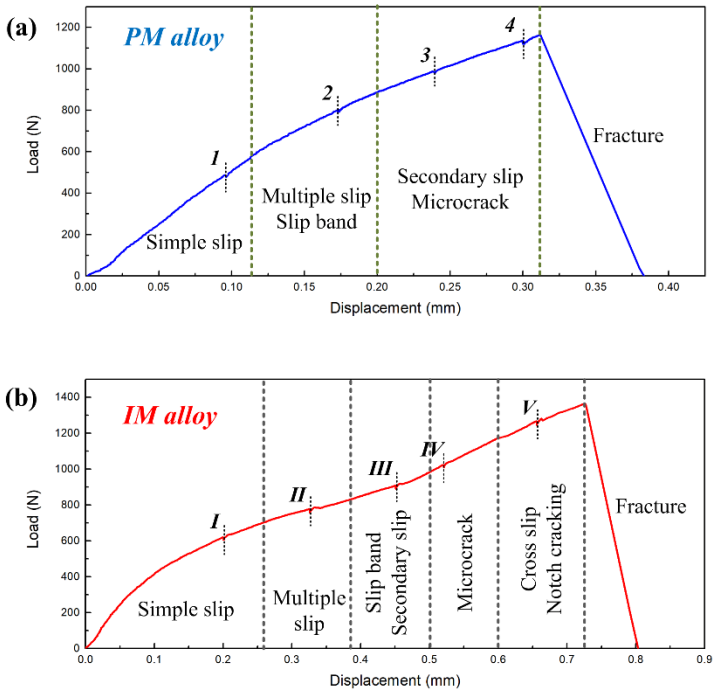

Figure 3.9 In-situ tensile load-displacement curves of the Ti-5553 alloys: (a) PM alloy; (b) IM alloy. The stops are marked by the Arabic and Roman numbers, respectively.

The relatively low ductility of the alloys at as-cast and as-consolidation states together with the pre-made V-shape notches lead to the absence of the work-softening stages in their in-situ tensile curves.

3.4.2 Plastic deformation behaviour

3.4.2.1 PM alloy

The in-situ SEM images obtained at different pauses during the tensile testing of PM alloy are displayed in Figure 3.10. The images are labelled with the numbers corresponding to those stops on the in-situ tensile curve (Figure 3.9a) and the tensile loading axis is along the horizontal direction.

The initial microstructure of the PM specimen is exhibited in Figure 3.10a, the alloy is clearly composed of β matrix and isolated precipitation areas. As is shown in Figure 3.10b, at the deformation of Stage 1 (S-1), a small number of slip lines distribute primarily along two directions can be identified in the microstructure, suggesting the features of simple slip. When the tensile deformation comes to S-2, the number of the slip lines is obviously increased to form slip bands and they are

distributed along three different directions, indicating the occurrence of multiple slip (Figure 3.10c). Furthermore, the detailed slip deformation characteristics at S-2 can be observed in the locally amplified image of Figure 3. 10d: (1) the length of the developed slip lines is about 50-100 μm; (2) the slip lines can be arranged across each other; (3) the slip line can propagate to cross the whole grain (marked by A) and experience bending during its spread (marked by B); (4) when the slip lines encounter the grain boundaries (indicated as yellow dashed lines), they can overcome the obstacle by deflection (marked by C) or directly pass (marked by D); (5) the slip lines can go through the micro-voids without stopping or direction-change (marked by E).

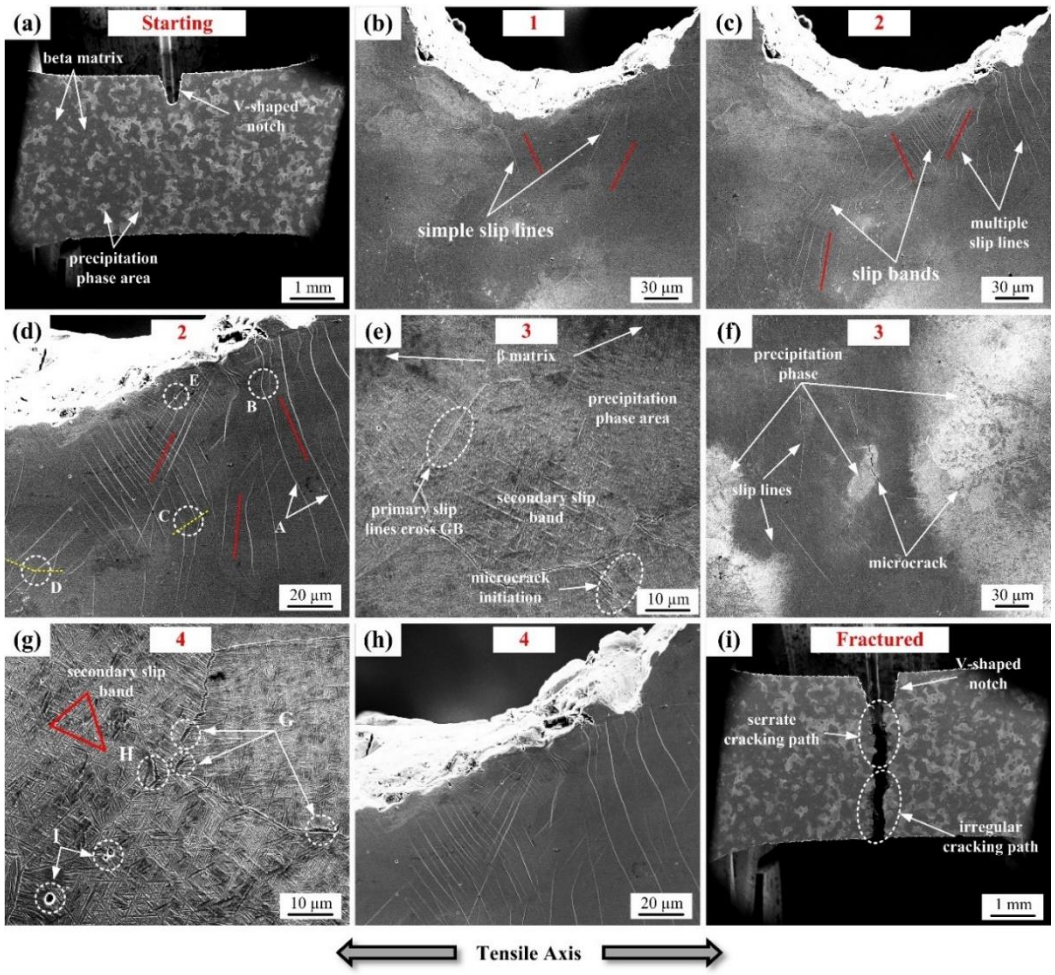

Figure 3.10 In-situ SEM images obtained at varying pauses during the tensile process of PM alloy, corresponding to the different stages marked in Figure 3.9a.

As the displacement value increases to S-3 (Figure 3.10e-f), massive secondary slip bands are visible at the precipitation phase areas, and the primary slip lines can pass through the β grain boundary. Moreover, microcracks with a length of about 40 μm can be clearly witnessed to be formed at the precipitation phase areas at this stage

(Figure 3.10f). Only multiple slip lines are observed in β matrix, which reveals that the slip deformation situation of the β matrix still remains at the multiple slip stage. When it comes to S-4, a large amount of primary and secondary slip bands (mainly allocated along three directions) at the precipitation phase area and several microcracks at the grain boundary α (GB-α) phase (marked by G) are significantly illustrated in Figure 3.10g. The plastic slip deformation and dislocation movement can be strongly impeded and blocked by the precipitation phase during the tensile test, so the secondary slip is activated nearby to release the extra stress concentration effect at the corresponding interfaces. Meanwhile, the extension of the slip lines is notably prevented by the GB-α and the generated microcracks can propagate along the boundary or toward the inside of the grain (marked by H). There is no obvious evolution of the slip deformation features in the matrix of S-4 (Figure 3.10h) comparing to S-2, indicating the slip deformation process is difficult to continue at S-3 and S-4. This means the specimen is elongated mainly by microcrack initiation and further propagation at the latter stages. Additionally, there are no microcracks formed near the micro-voids (marked by I in Figure 3.10g) and the specimen fractured at the peak applied load point immediately after S-4. The cracking path morphology of the specimen after its failure is illustrated in Figure 3.10i. The crack path can be divided into serrated and irregular parts. The serrated part is probably formed by microcrack coalescence and interconnection, and the irregularly crooked part is caused by subsequent fast brittle fracture attributed to the enhanced stress concentration effect after the coalescence of the microcracks.

3.4.2.2 IM alloy

Figure 3.11 exhibits the in-situ SEM images of IM alloy during the deformation process with the same labelling methods to match the various stops in Figure 3.9b. As is shown in Figure 3.11a, abundant and short simple slip lines with a length about 5-10 μm mainly distributed along a preferred direction can be clearly found in the microstructure near the V-shape notch at Stage I (S-I). For S-II, a large amount of the multiple short slip lines can be observed and they are distributed along two directions (Figure 3.11b). For S-III (Figure 3.11c and Figure 3.11d), well-developed slip band system containing primary and secondary slip bands can be clearly identified in the microstructure and they are arranged along three directions which are nearly 60° deviated from each other. Additionally, microcracks start to

nucleate at the grain boundary at S-III, and the primary and secondary slip lines are not able to cross the grain boundary of IM alloy, which makes the direction arrangement of slip lines become distinct between two adjacent coarse grains.

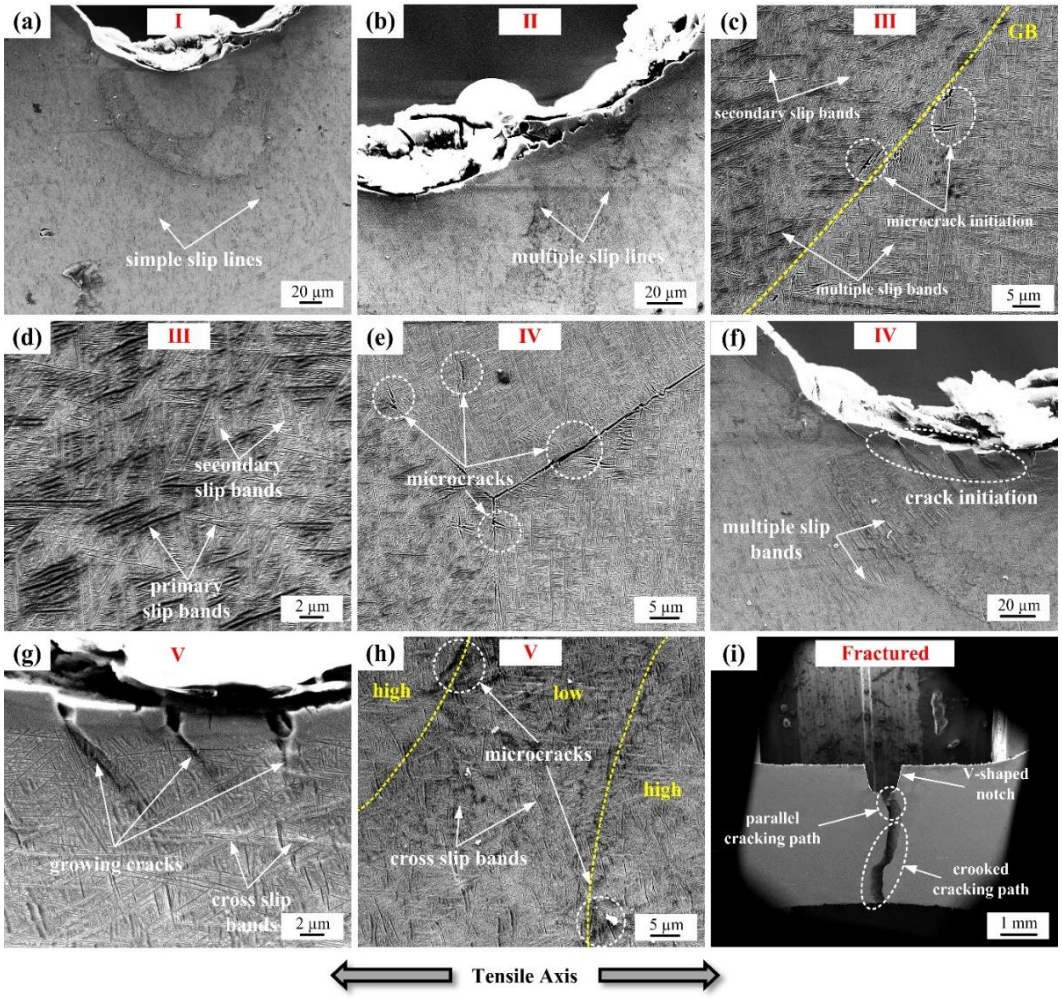

Figure 3.11 In-situ SEM images obtained at varying pauses during the tensile process of IM alloy, corresponding to the different stages marked in Figure 3.9b.

Hereinafter, At S-IV (Figure 3.11e and Figure 3.11f), obvious microcracks having the length about 5 μm can be identified on the grain boundary near the triple-junction. At the same time, the nucleation of the cracks at the V-shape notch area is visible. The density of the primary and secondary slip bands in the microstructure maintains the increasing tendency from S-III to S-IV. However, the propagation of the V-shape notch cracks become significant when the displacement increases to S-V (Figure 3.11g), accompanied by a considerable increase of multiple slip band density and the occurrence of cross slip (zigzag and tortuous slip lines) in the microstructure. What is more, there are some deep microcracks generated inside the grain at the areas where there are obvious height differences (see the different areas

divided by the yellow dash lines in Figure 3.11h). This phenomenon discloses the presence of slip steps during the deformation of IM alloy, and they can promote the initiation of microcracks nearby. Finally, the failure of the specimen occurs at a displacement of 0.14 mm straight after S-V. The crack path morphology of the IM specimen after the fracture is shown in Figure 3.11i. A small proportion of straight path and the rest of the crooked path can be clearly distinguished. The straight path next to the V-shape notch is formed by the crack expansion at the notch-edge while the crooked part is probably formed by the gradually ductile crack propagation.

Based on the claimed slip deformation processes of the two alloys at various interruptions during the in-situ tensile observation, the load-displacement curves can be divided into different sections according to the varying deformation mechanisms, which are also signified in Figure 3.9a and Figure 3.9b, respectively.

3.4.3 Fractographic morphology

Figure 3.12 shows the fractography images of the PM and IM alloys after in-situ tensile testing. The whole fracture surfaces of the two alloys can be classified into V-shape notch region, crack propagation region and fast fracture region depending on the specific surface morphology characteristics.

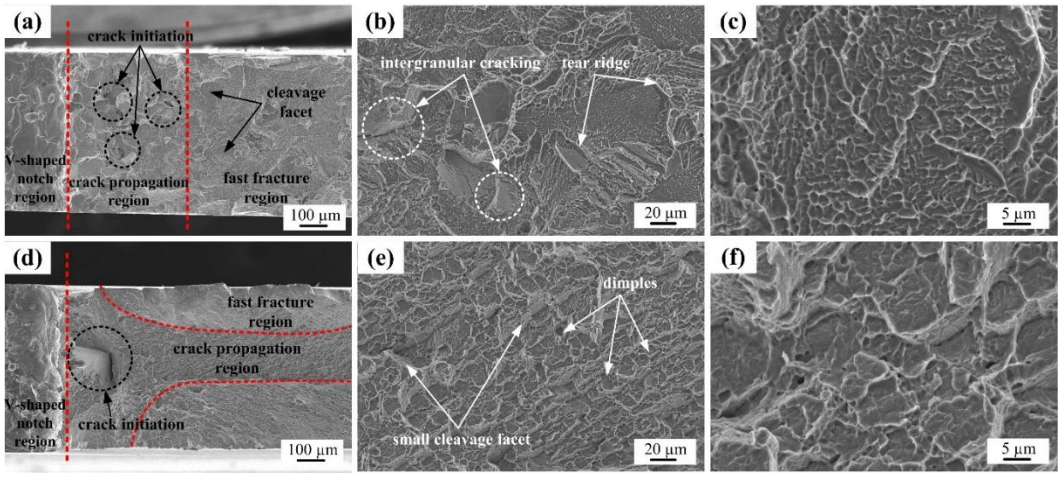

Figure 3.12 Fracture surface morphologies of Ti-5553 alloys after in-situ tensile tests: (a)-(c) PM alloy; (d)-(f) IM alloy.

As shown in Figure 3.12a, several crack initiation sites distributed randomly and the cleavage facets with a dimension about 40 μm can be recognized in the crack propagation region of PM alloy, while the relatively flat surface composed by

continuous cleavage facets can be distinctly observed in the fast fracture region. Meanwhile, the tearing ridges, intergranular fracture features (i.e. bulge of the grain and appearance of the grain boundary) and swallow dimples are noticeable in the locally amplified images (Figure 3.12b and Figure 3.12c) of the fast fracture region, revealing that the fracture of PM alloy is the brittle cleavage type with intergranular fracture accompanied by slight plastic deformation.

With respect to the fractography features of IM alloy, as seen in Figure 3.12d, the separation of the regions is different from PM alloy. The fluctuating crack propagation region penetrates across the whole fracture surface in the middle of the specimen, while the fast fracture region locates at the two side areas. Particularly, a singular extensive crack nucleation area lies adjacent to the V-shape notch of the crack propagation region. The rest of this region is covered by uniform dimples and undersized cleavage facets (having a size less than 10 μm), which are revealed by the partial high magnification images of Figure 3.12e and Figure 3.12f. Moreover, the fast fracture region is primarily featured by the quasi-cleavage facets and the diminished dimples, implying a smaller plastic deformation and less energy absorption at this area compared to the crack propagation region. These fractographic characteristics indicate that the fracture of IM alloy is dominated by the dimple cleavage-ductile mixed mechanism with better plastic deformation ability than PM alloy.

The better ductility and larger plastic deformation of IM alloy revealed by the fractography characteristics correspond well to its higher displacement value at the fracture point of the tensile test than PM alloy. Meanwhile, the fast fracture regions are consistent with the sudden fractures at the peak load points of both the two alloys. The detailed analysis of the microcrack initiation and the fracture mechanism will be discussed essentially in the following sections.

3.5 Discussion

3.5.1 Microcrack initiation and propagation mechanism

3.5.1.1 PM alloy

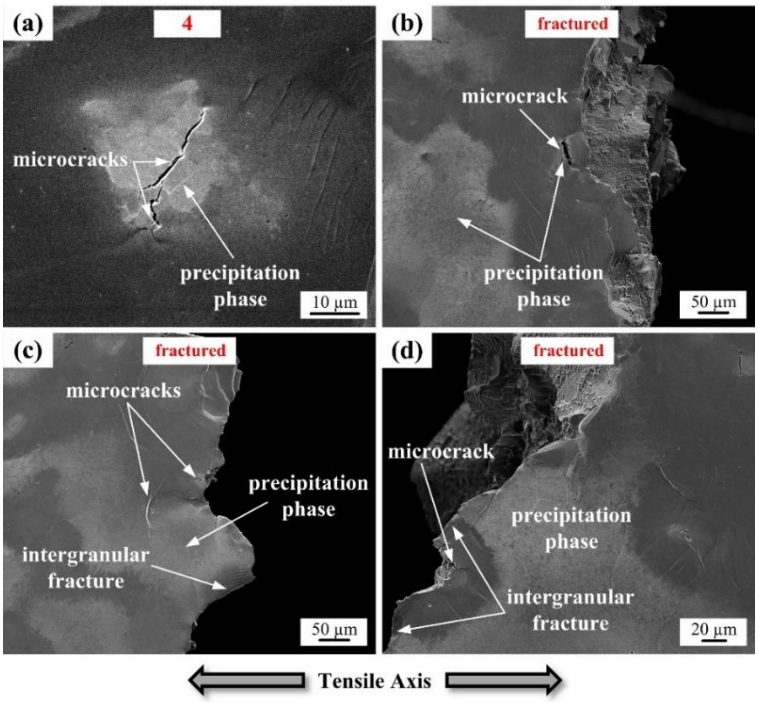

Figure 3.13 In-situ SEM images showing the microcrack initiation and propagation mechanisms of PM Ti-5553 alloys obtained at various interrupted stages with the corresponding marks: (a) S-4; (b)-(d) fractured.

The in-situ observation images illustrating the microcrack initiation and the propagation modes of PM alloy are presented in Figures 3.13a-c utilizing the same labelling method with the previous sections. Both Figure 3.13a and Figure 3.10f suggest that microcracks with a length of about 35-40 μm originated at the precipitation phase area and they further extend to the β matrix at S-4. Furthermore, after the fracture of the specimen (Figure 3.13b and Figure 3.13c), the precipitation phase microcrack suggests an obvious broadening process rather than propagation as it has a similar length but much wider gap comparing to the microcracks at S-4 in Figure 3.10f and Figure 3.13a. At the same time, it worth noticing that, the scales of the precipitation phase microcracks during and after the stretching are sharing the similar value to the dimension of the cleavage facet in Figure 3.12a and Figure 3.12b. That means this kind of microcrack has a poor ability to extend and propagate, which may lead to the cleavage brittle fracture of the PM alloy. Additionally, Figure 3.13c and Figure 3.13d also reveal that the cracking path is formed along the precipitation area and the grain boundary, which confirms that the final failure of

the specimen is caused by the combination of grain boundary microcracks and precipitation microcracks in the form of mixed transgranular-intergranular fracture.

In order to comprehend the detailed constitution of the precipitation phase and its effect on the fracture behaviour of PM alloy, TEM examinations were further performed on the alloys before and after the in-situ tensile test and the results are shown in Figure 3.14. As is shown in Figure 3.14a, the phase constitution of the PM alloy can be proposed as β matrix, α (bulk and acicular) and orthorhombic α″. Particularly, the existence of substantial lath α″ precipitation containing abundant micro-twinning structures in the matrix is verified by the magnified images and the selected area electron diffraction (SAED) pattern shown in Figure 3.14b and Figure 3.14c, with the ensured orientation relationship of: $\{001\}_{\alpha''} // \{110\}_{\beta}$ (also mentioned in Section 1.5.3). The phase constitution of the initial PM alloy is also verified by the XRD pattern, as shown in Figure 3.3a, with the appearance of β, α″ and α peaks. The dislocation accumulation and pile-up are clearly captured by the side of hard α″ precipitation after the tensile (Figure 3.14d and Figure 3.14e), indicating that dislocation slip is strongly hindered by the α″ precipitates.

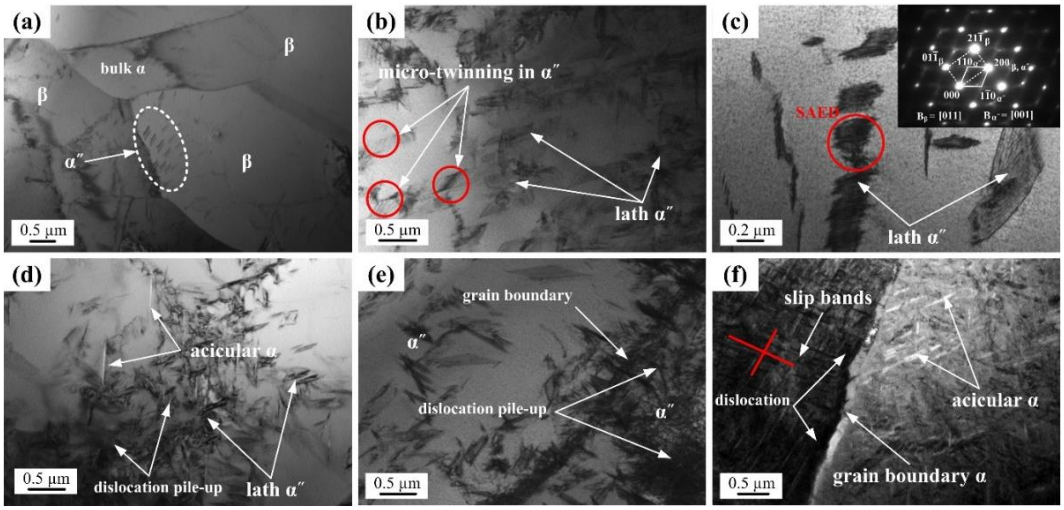

Figure 3.14 TEM images of the PM Ti-5553 alloy specimens obtained from: (a)-(c) Initial alloy; (d)-(f) the area near the fracture surface after the in-situ tensile test.

The internally twinned orthorhombic α″ martensite in PM alloy is formed by the rapid diffusionless shear transformation, as a result of the high β-stabilizer content of Ti-5553 alloy and the high undercooling of the fast-cooling process after consolidation [9, 10] (the concurrence of considerable α-stabilizer content introduced by Al, O and N alloy also contributes to the formation of α″ in PM alloy). This non-equilibrium supersaturated phase contains considerable internal stress and

lattice distortion due to the quick rearrangement of the atoms, which can concentrate the deformation strain significantly and lead to microcrack nucleation [11, 12]. Besides, the intensive impediment of dislocation movement is also realized by the GB-α phase, as shown in Figure 3.14f. The slip bands distributed along two directions are not able to cross the GB-α stripe and the formation of dislocation tangles against the GB-α is prominent. Whereas, the acicular α phase shows a weak inhibition of the slip deformation with slight dislocation pile-up (Figure 3.14d).

Based on the presented results, it can be concluded that dislocation glide is primarily arrested by the α″ precipitations and the GB-α phase during the tensile process of PM alloy. The deformation is concentrated at these areas, leading to the subsequent generation of the microcracks, among which the α″ precipitation (α″/β interface) microcracks are more detrimental due to their facile-nucleation and fast-widening features. Afterwards, the final rupture of the material is induced by the nucleation of α″/β microcracks near the V-shape notch and they then propagate along the GB-α microcracks which produce the intergranular fracture path, as clearly characterised in Figure 3.13c and Figure 3.13d. Shortly thereafter, the fast cleavage fracture happens at the area away from the notch when the crack's density reaches the critical limit, corresponding to the fractography morphology and surface partition situation in Figure 3.12a.

3.5.1.2 IM alloy

The microcrack initiation and propagation mechanism of IM alloy were also studied during in-situ tensile observation and are displayed in Figure 3.15. As is shown in Figure 3.11e and Figure 3.15a, microcracks can be observed on the grain boundary and inside the coarse grains near the boundary at S-IV and S-V. By comparing the microcrack characteristics in the same area, there is no doubt that the applied strain does not show the obvious effect on the growth and aggravation of grain boundary microcracks from S-IV to S-V. Apart from the strain-insensitive grain boundary microcracks in IM specimen, microcracks can also be found inside the grains in the vicinity of the slip steps (Figure 3.15b-d, the areas with obvious altitude differential). In Figure 3.15c, this kind of microcrack is mainly formed at the edge of the slip steps, where the level of stress concentration is high. More specifically,

the slip step microcracks are highly likely to expand and propagate with increasing degree of deformation, based on comparing the morphology variation of the microcracks at S-IV (Figure 3.15b) and S-V (Figure 3.15d). Similarly, the cracks initiated from the V-shape notch of IM alloy also show a high strain sensitivity, as demonstrated in Figure 3.11f and Figure 3.11g.

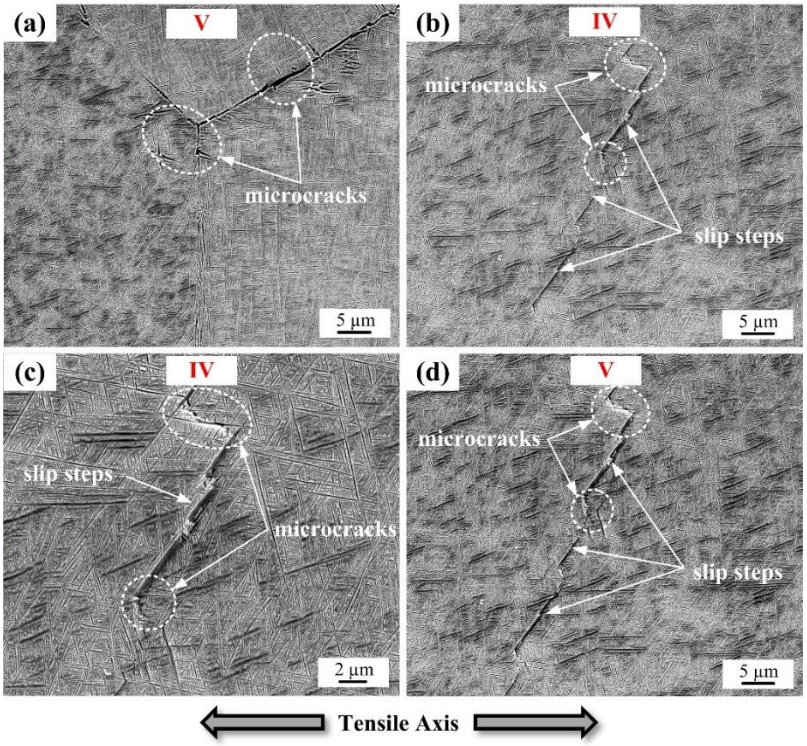

Figure 3.15 In-situ SEM images showing the microcrack initiation and propagation mechanisms of IM Ti-5553 alloys obtained at various interrupted stages with the corresponding marks: (a) S-V of the grain boundary area; (b) and (c) S-IV of the slip step area; (d) S-V of the slip step area.

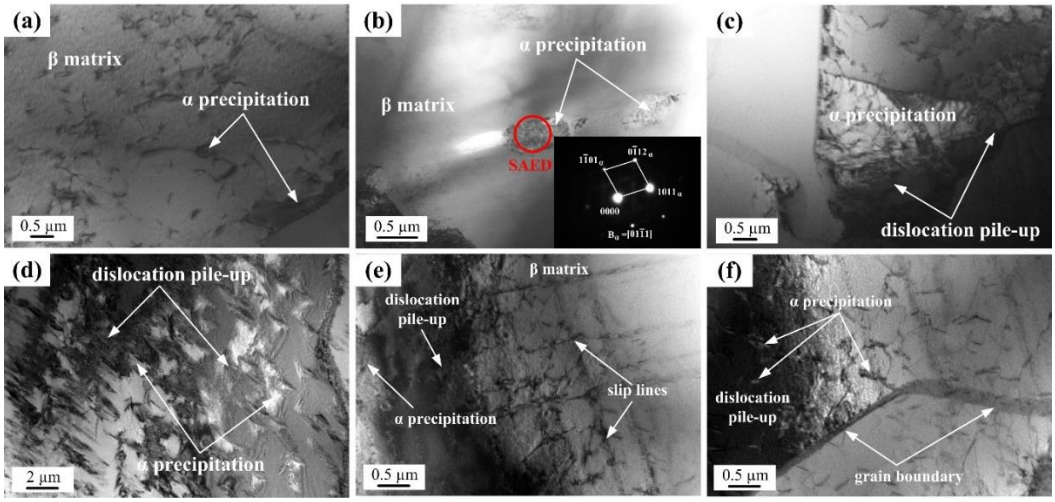

Figure 3.16 TEM images of the IM Ti-5553 alloy specimens obtained from: (a)-(b) Initial alloy; (c)-(f) the area near the fracture surface after the in-situ tensile test.

From the TEM images of IM alloy before the tensile test in Figure 3.16a and Figure 3.16b, there are abundant α precipitates (confirmed by the SAED results in Figure 3.16b) with various shapes and sizes in the β matrix of IM alloy. Meanwhile, the XRD pattern of IM alloy (Figure 3.3b) reveals the presence of copious α phase in the initial microstructure of IM alloy as well. During the tensile test, these hard α precipitates will act as obstacles for slip deformation and produce dislocation pile-up nearby, which are undoubtedly illustrated in the fractured specimen in Figure 3.16c and Figure 3.16d. Also, as is shown in Figure 3.16e and Figure 3.16f, the progress of the slip lines is blocked by α precipitates, leading to the formation of tangled dislocation at the front. Additionally, in Figure 3.16f, the grain boundaries in IM alloy are strong enough to prevent the spreading of slip line and dislocation movement.

It can be affirmed based on the obtained results, the failure of IM specimen is mainly induced by the severe and fast-developing crack nucleated at the V-shape notch. Hereinafter, the propagation of the crack is generally accelerated by the internal slip step microcracks generated by the hard α precipitates rather than the grain boundary microcracks. The crack path passes through the whole specimen, while the fast fracture occurs at the edge of the specimen as the critical limit is reached (Figure 3.12d).

3.5.2 Slip morphology analysis

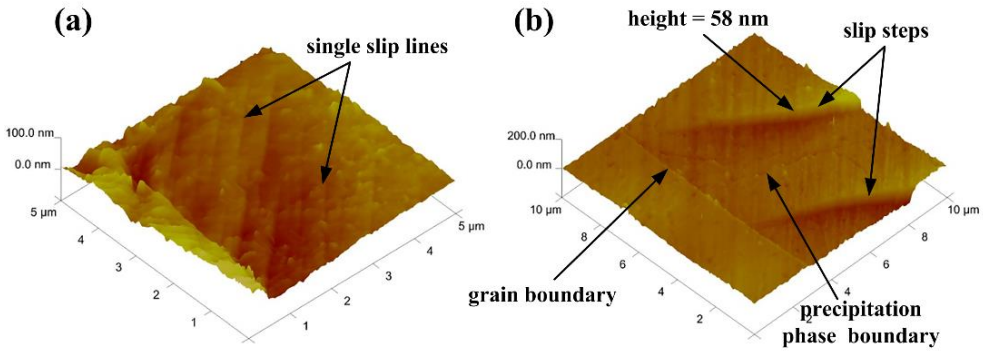

Figure 3.17 High magnification 3D AFM scanning images of the fractured specimen surfaces of PM Ti-5553 alloy.

More detailed slip deformation characteristics and the slip step features of PM and IM alloys can be unveiled by AFM scanning of the fractured specimen surfaces. As demonstrated in Figure 3.17 and Figure 3.18, it is obvious that there are extensive

variances of the configuration of the slip lines and slip steps between PM and IM alloys. A series of primary single slip lines distributed through the whole scanning surface (with the same direction) can be found in Figure 3.17a. Also, it is observed that the extension of the long primary slip lines is not stopped by the grain boundary and slip steps, as shown in Figure 3.17b. The slip steps in PM specimen are mainly formed near the α″/β interphase with the height about 58 nm.

Furthermore, as shown in Figure 3.18, the slip steps in IM specimen with an altitude of about 100 nm are obviously higher than those in PM specimen, and they are generated near the α precipitate phase (see the sunk areas).

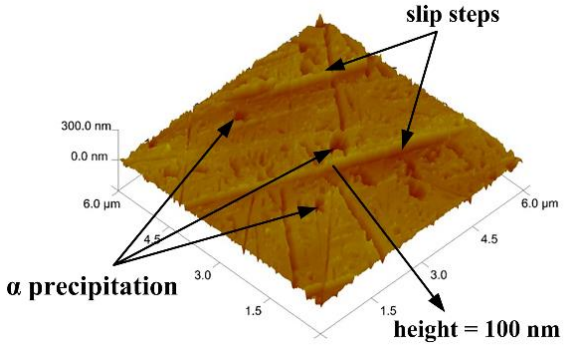

Figure 3.18 High magnification 3D AFM scanning images of the fractured specimen surfaces of IM Ti-5553 alloy.

The slip steps are formed by the dissection effect of the slip lines on the microstructure near the phase interface during plastic deformation [13]. The higher altitude the slip step has, the more dislocations have glided through the corresponding phase interface [14]. According to the work reported by Lewis et al. [15] and Gey et al. [16], the first-order preferred slip plane and slip direction in the body-centred cubic β phase of titanium alloy is {110}<111>, so the Burgers vector length (*b*) of this slip mode can be calculated as 0.283 nm. In other words, a tiny slip step with a height of 0.283 nm will remain at the precipitation/matrix interface after a single dislocation glides through. Based on this, it can be derived that about 205 dislocations have glided through the α″/β interface when the fracture occurs in PM specimen, while the dislocation amount in IM specimen through the α/β boundary is 353. These results reveal that the α″ phase in PM alloy performed a stronger inhibiting effect on the dislocation movement, while more dislocations can glide across the α phase in IM alloy to form the slip steps with higher altitudes nearby. The continuously developing slip steps in IM alloy can accelerate the

concentration of the stress and then lead to the gradual propagation of the produced microcracks. Whereas, the intensive dislocation accumulation at α″/β interface leads to the quick formation and subsequent broadening of the microcracks of PM alloy.

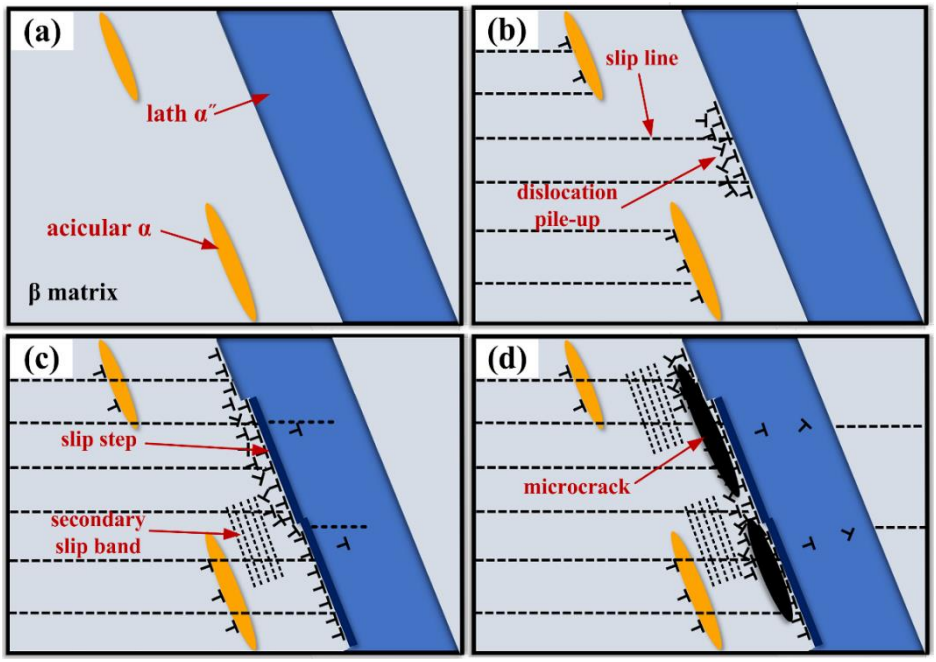

Figure 3.19 Schematic illustration of the formation processes of slip steps and precipitation microcracks of PM alloy: (a) before deformation; (b) dislocation pile-up at α/β (slightly) and α″/β (significantly) interfaces; (c) formation of slip steps (low altitude) at α″/β interface; (d) microcracks at α″/β interface.

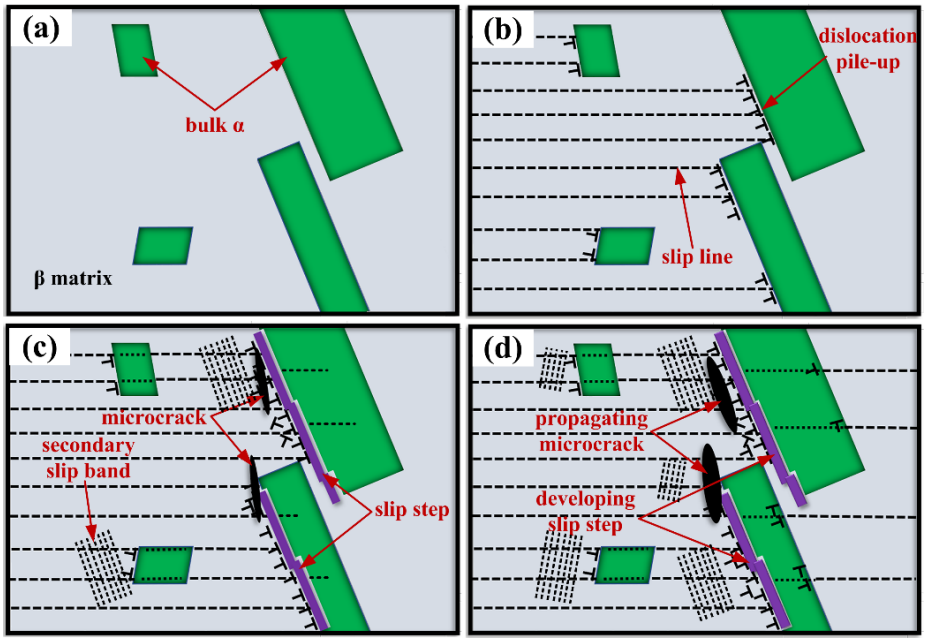

Figure 3.20 Schematic illustration of the formation processes of slip steps and microcracks of IM alloy: (a) before deformation; (b) dislocation pile-up at α/β interfaces; (c) formations of the slip steps and microcracks at α/β interface; (d) developing (dislocation slip across the α/β interface) slip steps (high altitude) and microcracks.

According to the TEM and AFM results, the detailed slip step formation and microcrack generation processes at the precipitate phases of PM and IM alloys are exhibited schematically in Figure 3.19 and Figure 3.20, respectively.

3.5.3 The effect of residual porosity and casting cavity

As is mentioned in Section 3.4.2.1, the residual micro-voids in PM alloy do not suggest obvious effects on the movement of dislocation and the progress of slip lines. Figure 3.21a-c further illustrates the presence of residual defects and their effects on tensile behaviour during the test of PM alloy at S-3 and S-4. Similar to the results observed in Figure 3.10d and Figure 3.10g, the primary slip bands can spread and the secondary slip lines are formed in the microstructure with minimal effect from the micro-voids (randomly distributed along the grain boundary and inside the grain). Although the dislocation slip is hindered by the residual pore (Figure 3.21a), there is no microcrack generated around the pores in PM alloy at S-3, at which stage the microcracks are already generated at the orthorhombic α″ phase precipitates. That is to say, the residual pores have a lower priority than α″ phase precipitates for the initiation of the microcracks, and the micro-voids are not the preferred site for the microcrack nucleation in PM alloy.

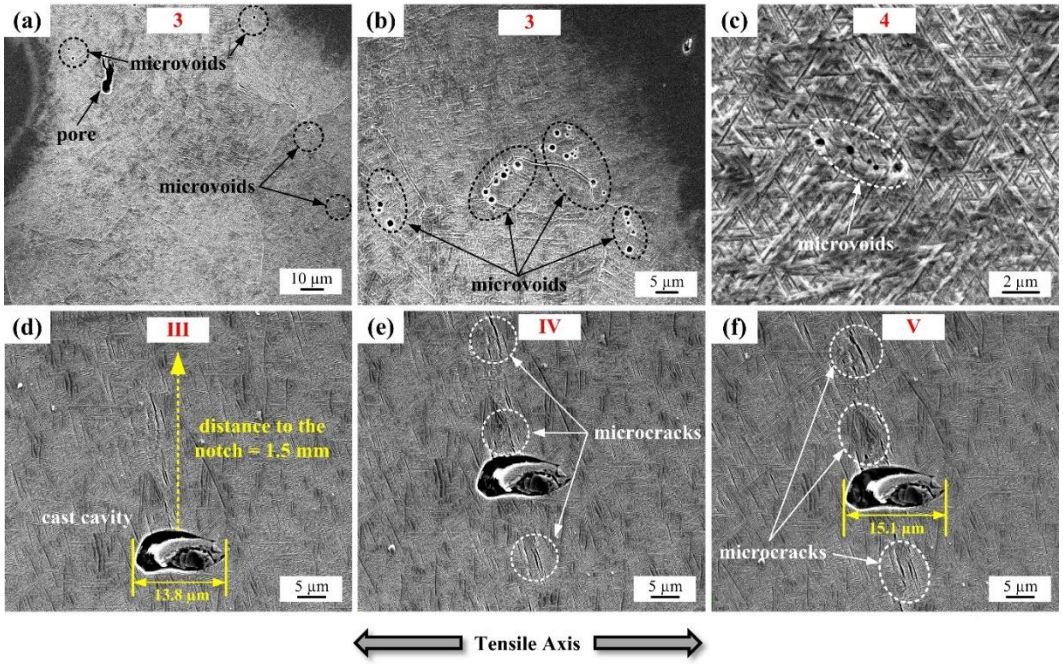

Figure 3.21 In-situ SEM images showing the effect of the residual defects of Ti-5553 alloys obtained at various interrupted stages with the corresponding marks: (a)-(c) microvoids and residual pores in PM alloy; (d)-(f) casting cavity (1.5 mm to the V-shape notch) in IM alloy.

The occurrence of residual pores and micro-voids are common phenomena in PM metallic materials especially components fabricated from blended elemental powder mixtures. Upon most of the occasions, they have always been ascribed an important reason for some insufficient mechanical properties like tensile property, fracture toughness and fatigue resistance of the products [17-20]. However, the in-situ tensile test in this work reveals that the previous evaluations of the negative effects of the pores and micro-voids in PM metallic materials may be excessively exaggerated.

Still not only such, Figures 3.21d-f exhibit the variation of the casting cavity (the distance to the V-shape notch is about 1.5 mm) morphology and the surrounding plastic deformation characteristics in IM alloy from S-III to S-V. An obvious casting cavity (vacuous area) with a dimension of 13.8 μm along the loading direction surrounded by plentiful primary and secondary slip bands can be observed in Figure 3.21d at S-III. Meanwhile, the initiation of the microcrack can be seen at the area along the transversal direction next to the cavity. Hereinafter, increasing the deformation degree to S-IV (Figure 3.21e) and S-V (Figure 3.21f), the cavity is elongated to a dimension of 15.1 μm (the deformation degree of the cavity is calculated as 7.9%) and the near-by microcrack only suggests a gently enhanced tendency without the formation of severe microcrack coalescence and further propagation. However, the IM specimen fractured at a strain of 3.4%, and microcracks are obviously deeper and more serious in other areas at S-V, i.e. V-shape notch and slip step areas. As a result, it can be revealed that the casting cavity in IM alloy has better plastic deformation ability than the matrix and it is not the prior site for the cracking initiation. Moreover, the fracture surface of the IM specimen (Figure 3.12d and Figure 3.12f) also suggests that the final cracking of IM alloy has not propagated through the casting cavity.

Similar to the residual micro-voids and pores in PM alloy, the casting cavity in as-cast metallic materials is also often regarded as one of the factors which lead to the poor mechanical performance and the unexpected failure of the working components [21-25]. Whereas, the results obtained in this chapter uncover that the casting cavity can be considerably deformed and its fracture-acceleration effect is highly dependent on the microstructure of the specific material, which updates the awareness of the influences the cavity in casting pieces has during deformation.

3.5.4 The comparison between the tensile deformation behaviour of PM and IM alloy

From the in-situ tensile observation and further characterization results in the previous section, it is clear that IM and PM alloys perform distinct different mechanisms in their in-situ deformation behaviour including slip deformation, microcrack initiation and final fracture. In order to deliver a comprehensive and meticulous comparison of the deformation behaviour and fracture mechanism of PM and IM alloy, the schematic diagrams demonstrating their tensile deformation processes are shown in Figure 3.22 and Figure 3.23, respectively.

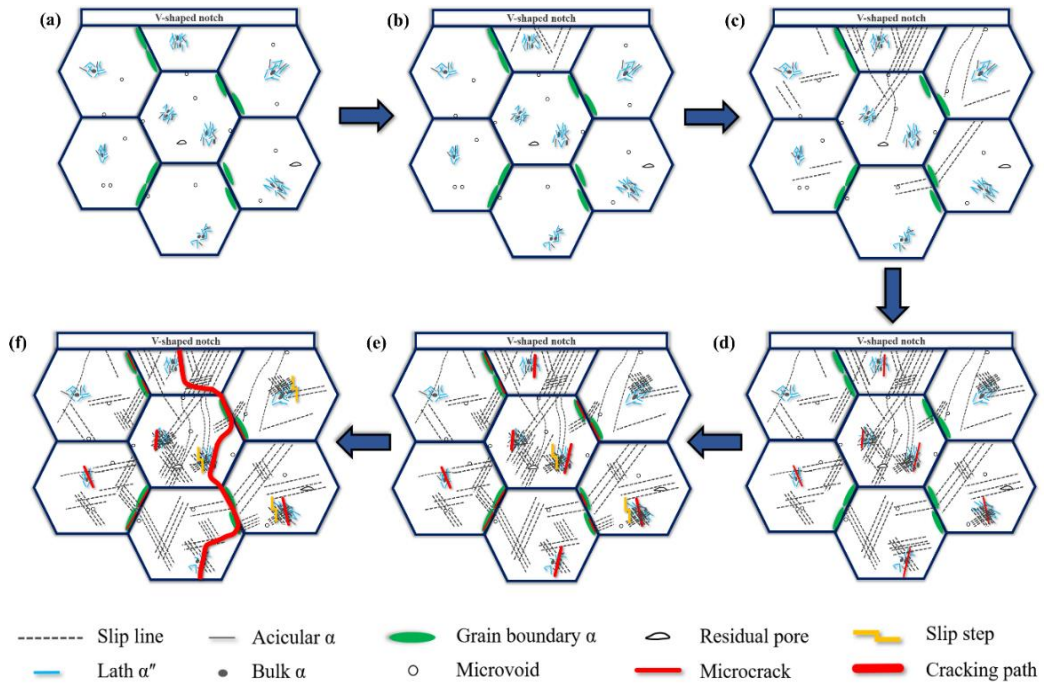

Figure 3.22 Schematic illustration of the tensile deformation behaviour and fracture mechanisms of PM Ti-5553 alloy: (a) initial microstructure; (b) slip line initiation; (c) slip line expansion; (d) slip band formation and microcrack at α″ and α precipitations; (e) α″/β microcrack broadening, GB-α microcrack initiation and slip step formation; (f) cracking propagation and final fracture.

Firstly, at the early stages of the tensile deformation (Figures 3.22a-c and Figure 3.23a-c), slip lines and slip bands are more liable to be generated and formed earlier in IM alloy, while the slip lines in PM alloy are obviously longer than those in IM alloy. As for the intermediate sections (Figures 3.22d-e and Figure 3.23d-e), a larger amount of multiple slip bands (secondary and tertiary bands) and more obvious cross slip features can be observed in IM alloy, while PM alloy shows a poor slip deformation ability due to the difficulty in continuing the slip band densification. In addition, a larger amount of slip steps with higher altitude intercept are exhibited

in IM alloy at the α/β interface areas (Figure 3.23e), contrasting to the smaller amount and vague slip steps at α″/β interface areas in PM alloy (Figure 3.22e). In terms of the final sections, the microcracks are likely to nucleate at the α″/β interface and then at the GB-α areas in PM alloy (Figure 3.22d and Figure 3.22e), after which the α″/β microcracks become wider without obvious propagation (Figure 3.22e). Afterwards, the GB-α microcracks can propagate along the boundaries and connect the widened α″/β microcracks, leading to the fast brittle transgranular-intergranular mixed fracture of the specimen (Figure 3.22f). Things can be more complicated in IM alloy, the microcracks are firstly initiated at the grain boundary (Figure 3.23d), then various microcracks can be observed at the V-shape notch, around casting cavity and slip step (α/β interface) areas (Figure 3.23e and Figure 3.23f). At last, the mixed ductile-brittle transgranular fracture is caused by the fatal crack developed at the V-shape notch and its gradual coalescence with slip step microcracks (Figure 3.23g).

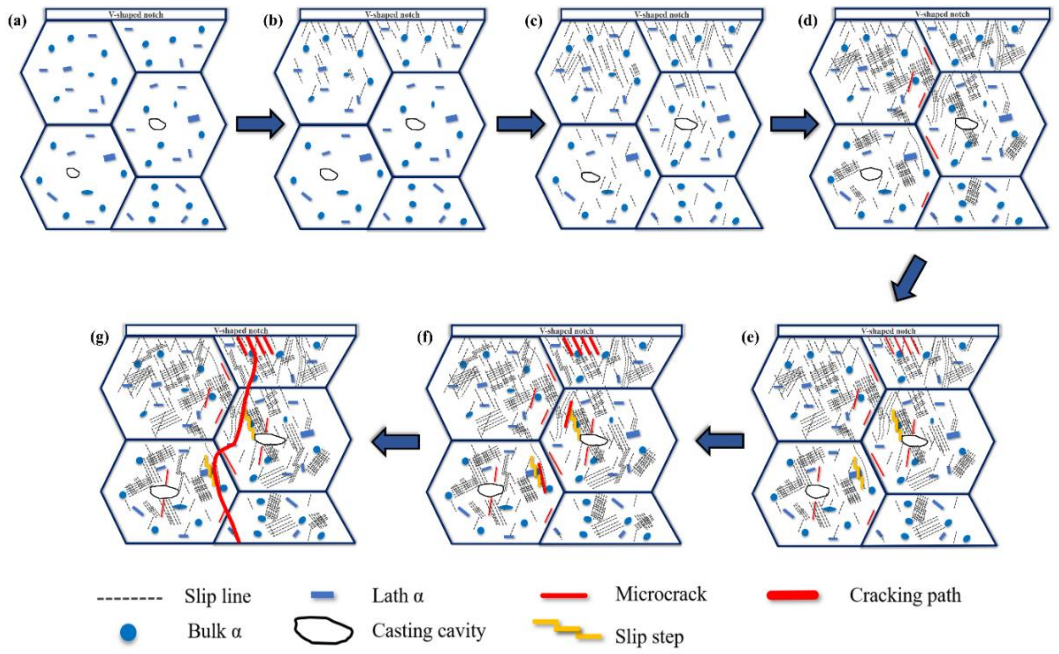

Figure 3.23 Schematic illustration of the tensile deformation behaviour and fracture mechanisms of IM Ti-5553 alloy: (a) initial microstructure; (b) slip line initiation; (c) slip line expansion; (d) slip band development and microcrack at grain boundary; (e) V-shape notch microcrack generation and slip step formation at α/β interface; (f) serious cracking at V-shape notch and slip steps; (g) cracking propagation and final fracture.

Based on these results, it is shown that IM alloy has better plastic deformation ability than PM alloy with a good compatible deformation capability and dislocation glide mode diversification at the slip deformation stages, which are

mainly ascribed to the differences in the oxygen content of the alloys. The high oxygen level of PM alloy (i.e. 0.36% in PM alloy and 0.08% in IM alloy) plays a significant role in its slip deformation mechanism. It is well accepted that oxygen exists as a solid solution element in titanium alloys in the form of interstitial atoms which can provide a large lattice distortion. Then, the increased distortion energy will hinder the generation of slip lines/bands by increasing the critical resolved shear stress (CRSS) [26-28]. Furthermore, it is reported that the increase of oxygen in titanium alloys can lead to the reduction of their stacking fault energy (SFE) [29, 30]. The lower SFE the metallic material has, the more difficulty in slip deformation it will suffer [31, 32]. In addition, the slip lines are stopped by the grain boundaries in IM alloy, while the grain boundaries in PM alloy are not able to arrest the slip lines, only changing the direction of some slip lines. This means that the grain boundaries of IM alloy are much stronger than that in PM alloy. With the respect to the longer slip lines in PM alloy, uniformly distributed α precipitates and the strong grain boundary in IM alloy prevent the long-distance spread of the slip lines instead of the isolated α″/α precipitation and weak grain boundary in PM alloy which allows the dislocations to glide for a longer distance.

In the case of microcrack initiation and fracture mechanisms, the differences between PM and IM alloys primarily come from the precipitate phase constitution and the grain boundary strength. The microcracks in PM alloy are found in α″/β precipitate interface and GB-α areas due to their strong pinning effect of dislocation movement, and the weak boundary makes it easy for the crack to propagate along the grain boundary. Although grain boundary microcracks are also found in IM alloy, the relatively strong boundaries hinder further propagation. As a result, the crack from the V-shape notch makes its way through the intercrystalline microcracks produced by the slip steps and leads to the gradual fracture of the specimen. The better deformation ability and transgranular fracture mechanism of IM alloy correspond well to its higher finial tensile displacement and better ductility than PM alloy in the in-situ tensile test. On the contrary, the difficulties in compatible deformation and the inferior crack propagation resistance of PM alloy results in its relatively low fracture ductility and brittle type fracture of the specimen.

3.6 Summary

The research work presented in this chapter is mainly focused on the initial microstructures, mechanical properties, fracture mode, and the dynamic tensile deformation responses/mechanisms of the as-consolidated PM and as-cast IM alloy evaluated by regular mechanical testing and advanced in-situ SEM observation. The substantial results and intensive discussion is summarized in the bullet points below:

(1) IM alloy has a slightly higher tensile strength including yield stress and ultimate stress than PM alloy in the regular tensile test. However, much higher ductility during the quasi-static tensile and fracture toughness tests can be measured in IM alloy. The ductility gap between IM and PM alloy becomes more significant in the dynamic loading of the impact toughness test.

(2) All the PM alloy specimens after the mechanical tests suggest flatter and more even fracture surfaces than IM alloy specimens in macroscopic views, indicating the relatively low ductility and toughness of PM alloy. The fracture mechanism of PM alloy during the regular mechanical tests is a brittle cleavage dominated mechanism, while ductile dimple fracture characteristics can be observed in IM alloy specimens.

(3) Unlike the consistent ductile dimple fracture mechanism of IM alloy at different loading rates, the fracture behaviour and mechanisms of PM alloy are sensitive to the loading rate. Mixed ductile-brittle and quasi-cleavage transgranular fracture mechanism change into complete brittle cleavage fracture mechanism with the appearance of intergranular features as the loading rate of PM alloy increases.

(4) PM alloy exhibits an ultimate tensile load of 1164 N and a fracture displacement of 0.312 mm during the in-situ tensile test. Nevertheless, IM alloy shows a better load-bearing capacity and ductility, fracturing at a load of 1343 N and the displacement of 0.728 mm.

(5) Simple and then the multiple slip lines are generated in PM alloy at the early stage deformation. Later, the movement of dislocation and the spread of slip lines are hindered by the α″ precipitation and GB-α phase, leading to the initiation of microcracks at these areas.

(6) IM alloy exhibits a better compatible deformation capability characterized by a larger amount of slip bands, secondary slip bands and cross-slip features. The grain boundaries and the intercrystalline α precipitation in IM specimen can

impede the slip lines and dislocation movement, where the microcracks are generated.

(7) The slip steps with higher altitude are formed by the dissection effect of the slip line on the α precipitation in IM alloy, while the harder α″ precipitation in PM alloy produces the low-altitude slip steps nearby due to its stronger inhibition of the dislocation movement.

(8) The residual pores and microvoids do not have a significant effect on the slip deformation and fracture behaviour in PM alloy. The casting cavity in IM specimen shows a reasonable deformation ability, and it is not the first-order generation site of cracking despite the adjacent microcracks.

(9) The final failure of PM alloy is caused by the coalescence of the GB-α and the widened α″/β microcracks, resulting in the sudden brittle transgranular-intergranular mixed fracture. For IM alloy, the serious cracking at the V-shape notch finds its way through the microcracks nucleated at the slip steps near α/β interface, leading to the gradual transgranular fracture with better ductility.

As is presented in this section, the studied PM alloy shows a relatively low ductility and unique phase constitution at the as-consolidated stage, which leads to its early fracture during room temperature deformation. Therefore, hot processing and subsequent heat treatment are required to be performed on the PM alloy for the adjustment of microstructure and improvement of mechanical properties.

Reference

[1] F. Yang, B. Gabbitas, M. Dore, A. Ogereau, S. Raynova, L. Bolzoni, On microstructural evolution and mechanical properties of Ti-5Al-5V-5Mo-3Cr alloy synthesised from elemental powder mixtures, Mater. Chem. Phys. 211 (2018) 406-413.

[2] F. Yang, B. Gabbitas, Feasibility of producing Ti-6Al-4V alloy for engineering application by powder compact extrusion of blended elemental powder mixtures, J. Alloys Compd. 695 (2017) 1455-1461.

[3] L. Geng, B. Xu, Y.T. Li, A.B. Li, G.S. Wang, Characterization of (α+β)/β Transformation in a TC11 Titanium Alloy, Solid State Phenom. 127 (2007) 91-96.

[4] D. Banerjee, J.C. Williams, Perspectives on titanium science and technology, Acta Mater. 61 (2013) 844-879.

[5] G. Lütjering, J.C. Williams, Titanium, Springer, Berlin, 2007.

[6] G. Srinivasu, Y. Natraj, A. Bhattacharjee, T.K. Nandy, G.V.S. Nageswara Rao, Tensile and fracture toughness of high strength β Titanium alloy, Ti-10V-2Fe-3Al, as a function of rolling and solution treatment temperatures, Mater. Des. 47 (2013) 323-330.

[7] X. Shi, W. Zeng, Q. Zhao, The effect of surface oxidation behavior on the fracture toughness of Ti-5Al-5Mo-5V-1Cr-1Fe titanium alloy, J. Alloys Compd. 647 (2015) 740-749.

[8] J. Xu, W. Zeng, Y. Zhao, Z. Jia, Effect of microstructure evolution of the lamellar alpha on impact toughness in a two-phase titanium alloy, Mater. Sci. Eng. A 676 (2016) 434-440.

[9] J. Zhang, C.C. Tasan, M.J. Lai, A.C. Dippel, D. Raabe, Complexion-mediated martensitic phase transformation in Titanium, Nat. Commun. 8 (2017) 14210.

[10] P. Barriobero, V. Biancardi Oliveira, S. Schwarz, T. Buslaps, G. Requena, Tracking the α″ martensite decomposition during continuous heating of a Ti-6Al-6V-2Sn alloy, Acta Mater. 135 (2017) 132-143.

[11] S.G. Lee, S.S. Sohn, B. Kim, W.G. Kim, K.K. Um, S. Lee, Effects of martensite-austenite constituent on crack initiation and propagation in inter-critical heat-affected zone of high-strength low-alloy (HSLA) steel, Mater. Sci. Eng. A 715 (2018) 332-339.

[12] F. Archie, S. Zaefferer, On variant selection at the prior austenite grain boundaries in lath martensite and relevant micro-mechanical implications, Mater. Sci. Eng. A 731 (2018) 539-550.

[13] K.Y. Xie, Z. Alam, A. Caffee, K.J. Hemker, Pyramidal I slip in c-axis compressed Mg single crystals, Scripta Mater. 112 (2016) 75-78.
[14] C. Tan, Q. Sun, L. Xiao, Y. Zhao, J. Sun, Slip transmission behavior across α/β interface and strength prediction with a modified rule of mixtures in TC21 titanium alloy, J. Alloys Compd. 724 (2017) 112-120.
[15] A.C. Lewis, S.M. Qidwai, A.B. Geltmacher, Slip Systems and Initiation of Plasticity in a Body-Centered-Cubic Titanium Alloy, Metall. Mater. Trans. A 41A (2010) 2522-2531.
[16] N. Gey, M. Humbert, M.J. Philippe, Y. Combres, Modeling the transformation texture of Ti-64 sheets after rolling in the β-field, Mater. Sci. Eng. A 230 (1997) 68-74.
[17] H.T. Wang, Z.Z. Fang, P. Sun, A Critical Review of Mechanical Properties of Powder Metallurgy Titanium, Int. J. Powder Metall. 46 (2010) 45-57.
[18] T. Fujita, A. Ogawa, C. Ouchi, H. Tajima, Microstructure and properties of titanium alloy produced in the newly developed blended elemental powder metallurgy process, Mater. Sci. Eng. A 213 (1996) 148-153.
[19] S. Leuders, M. Thöne, A. Riemer, T. Niendorf, T. Tröster, H.A. Richard, H.J. Maier, On the mechanical behaviour of titanium alloy Ti-6Al-4V manufactured by selective laser melting: Fatigue resistance and crack growth performance, Int. J. Fatigue 48 (2013) 300-307.
[20] Y.J. Liu, S.J. Li, H.L. Wang, W.T. Hou, Y.L. Hao, R. Yang, T.B. Sercombe, L.C. Zhang, Microstructure, defects and mechanical behavior of beta-type titanium porous structures manufactured by electron beam melting and selective laser melting, Acta Mater. 113 (2016) 56-67.
[21] B. Li, Y. Shen, W. Hu, Casting defects induced fatigue damage in aircraft frames of ZL205A aluminum alloy-a failure analysis, Mater. Des. 32 (2011) 2570-2582.
[22] M. Niinomi, T. Akahori, T. Takeuchi, S. Katsura, H. Fukui, H. Toda, Mechanical properties and cyto-toxicity of new beta type titanium alloy with low melting points for dental applications, Mater. Sci. Eng. C 25 (2005) 417-425.
[23] J.Y. Hwang, H.W. Doty, M.J. Kaufman, The effects of Mn additions on the microstructure and mechanical properties of Al-Si-Cu casting alloys, Mater. Sci. Eng. A 488 (2008) 496-504.
[24] K. Nakata, Y.G. Kim, H. Fujii, T. Tsumura, T. Komazaki, Improvement of mechanical properties of aluminum die casting alloy by multi-pass friction stir

processing, Mater. Sci. Eng. A 437 (2006) 274-280.
[25] C.H. Cáceres, B.I. Selling, Casting defects and the tensile properties of an AlSiMg alloy, Mater. Sci. Eng. A 220 (1996) 109-116.
[26] Q. Yu, L. Qi, T. Tsuru, R. Traylor, D. Rugg, J.W. Morris, Jr., M. Asta, D.C. Chrzan, A.M. Minor, Metallurgy. Origin of dramatic oxygen solute strengthening effect in titanium, Science 347 (2015) 635-639.
[27] H. Conrad, Effect of interstitial solutes on the strength and ductility of titanium, Prog. Mater. Sci. 26 (1981) 123-404.
[28] M.L. Wasz, F.R. Brotzen, R.B. McLellan, A.J. Griffin, Effect of oxygen and hydrogen on mechanical properties of commercial purity titanium, Int. Mater. Rev. 41 (1996) 1-12.
[29] R. Salloom, R. Banerjee, S.G. Srinivasan, Effect of β-stabilizer elements on stacking faults energies and ductility of α-titanium using first-principles calculations, J. Appl. Phys. 120 (2016) 175105.
[30] P. Kwasniak, M. Muzyk, H. Garbacz, K.J. Kurzydlowski, Influence of C, H, N, and O interstitial atoms on deformation mechanism in titanium-first principles calculations of generalized stacking fault energy, Mater. Lett. 94 (2013) 92-94.
[31] Y.H. Zhao, Y.T. Zhu, X.Z. Liao, Z. Horita, T.G. Langdon, Tailoring stacking fault energy for high ductility and high strength in ultrafine grained Cu and its alloy, Appl. Phys. Lett. 89 (2006) 121906.
[32] Y.H. Zhao, Z. Horita, T.G. Langdon, Y.T. Zhu, Evolution of defect structures during cold rolling of ultrafine-grained Cu and Cu-Zn alloys: Influence of stacking fault energy, Mater. Sci. Eng. A 474 (2008) 342-347.

4 Hot deformation behaviour and microstructural evolution of PM Ti-5553 alloy

4.1 Introduction

*Partial contents (text and figures) in this chapter have been published in refereed journals:

1. **Qinyang Zhao**, Fei Yang, Rob Torrens, Leandro Bolzoni, Evaluation of the hot workability and deformation mechanisms for a metastable beta titanium alloy prepared from powder, ***Materials Characterization***, 149 (2019) 226-238.
2. **Qinyang Zhao**, Fei Yang, Rob Torrens, Leandro Bolzoni, Flow behaviour and microstructure evolution of powder metallurgy Ti-5553 alloy during 0.1 s^{-1} hot deformation, ***International Journal of Modern Physics B*** (In press).
3. **Qinyang Zhao**, Fei Yang, Rob Torrens, Leandro Bolzoni, Effect of processing parameters on hot deformation behaviour and microstructural evolution of PM Ti-5553 alloy at a moderate-high strain rate, ***Materials Research***, 22 supl.2 (2019) e20180738.

In Chapter 3, the starting microstructure, mechanical properties and room-temperature deformation mechanisms of as-consolidated PM Ti-5553 alloy have been studied. The results suggest that as-consolidated PM Ti-5553 alloy has uneven-distributed α and α″ precipitates and residual pores in the microstructure, which leads to relatively low resultant mechanical properties. Thermomechanical processing is ideal for further optimizing the alloy's microstructure and improving its mechanical properties.

To carry out practical thermomechanical processing of the as-consolidated PM Ti-5553 alloy and achieve processing and quality control, the alloy's hot deformation behaviour will be investigated systematically in this chapter, via isothermal compressing test at the wide ranges of temperature, strain rate and deformation degree. The constitution relationships of as-consolidated PM Ti-5553 alloy are constructed in α and α+β regions, respectively. The hot processing maps are

established for PM Ti-5553 alloy based on the understanding and calculation of PM alloy's power dissipation efficiency and instability criterion during hot processing. With the utilization of TEM and EBSD techniques, the detailed microstructural characteristics of the specimens deformed in various processing regions are characterized to identify the respective active deformation mechanisms. The effects of deformation variables, including deformation temperature, strain rate and deformation degree, on the deformation behaviour have also been discussed in detail. Together with the investigation of the softening mechanism variation such as dynamic recovery and dynamic recrystallization mechanisms at different processing conditions, the microstructural evolution during hot deformation is unveiled profoundly for PM Ti-5553 alloy.

The research work in this chapter is intended to provide theoretical support and direct guidance for titanium industry to select optimal processing windows and facilities to hot process PM Ti-5553 alloy and achieve the precise control of microstructure, properties and quality.

4.2 Flow behaviour of the PM Ti-5553 alloy

4.2.1 True stress-true strain curves

During the hot deformation of metallic materials, the interrelationship between the flow stress and deformation parameters (temperature, strain rate and deformation degree) can be reflected in the true stress-true strain curves. Meanwhile, true stress-true strain curves are the macro-behaviour of the internal microstructure changing and property variation of the deforming materials [1-4]. Therefore, it becomes quite necessary to uncover the features of flow curves firstly to understand the flow softening mode and underlying deformation mechanism [5, 6]. The true stress-true strain curves can be directly obtained from the thermal physical simulation at varying conditions.

The typical true stress-strain curves of the PM Ti-5553 alloy deformed at 950 °C and 1050 °C and various strain rates are showed in Figure 4.1. It can be clearly seen that (1) the flow stress is first rapidly increased to the peak stress and then gradually decreased, for the samples deformed at 950 °C and strain rate of higher than 1 s^{-1} (Figure 4.1a), and (2) the flow stress is kept steady with increasing the deformation

strain, when the samples deformed at 950 °C and strain rate of lower than 0.1 s^{-1} (Figure 4.1a) or 1050 °C (Figure 4.1b). These phenomena indicate that obvious flow softening behaviour occurs during the hot deformation, and the softening mechanisms are varied at the different hot deformation conditions.

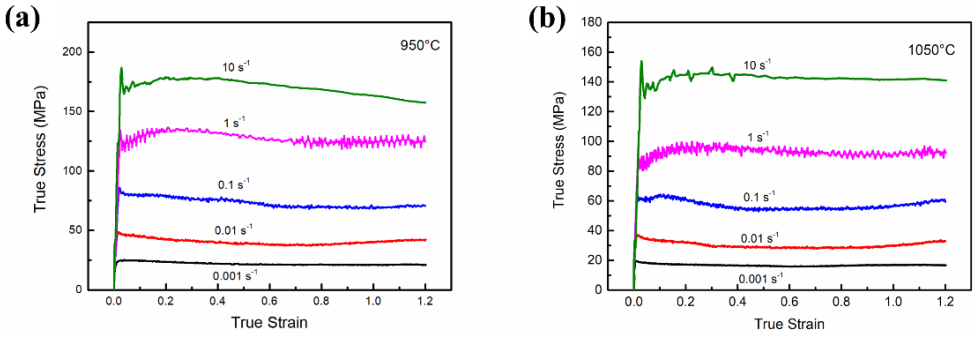

Figure 4.1 Typical true stress-strain curves of the PM Ti-5553 alloy at: (a) 950 °C; (b) 1050 °C.

The steep increase for the flow stress curves before reaching the peak stress is attributed to working hardening effect, and the curves become steady after reaching the peak stress indicate that dynamic recovery (DRV) and/or dynamic recrystallization (DRX) occur at the corresponding deformation conditions. When the flow stress is continuously decreasing, it suggests that the dominated softening mechanism could be either adiabatic temperature rising or flow localization. It is difficult to determine the hot deformation mechanisms for the PM Ti-5553 alloy at different deformation conditions only through interpreting the obtained flow stress curves, since the different microstructural variations for the deformed alloy may give similar stress-strain curves [5, 7]. Therefore, the establishment of processing map and the microstructure observation for the PM Ti-5553 alloy deformed at different processing conditions needs to be undertaken to understand the related deformation mechanisms, which will be exhibited in the later sections of this chapter.

In addition, as suggested in Figure 4.1, considerable yield drop after the peak stress can be found for the curves of specimens deformed at high strain rate (1 s^{-1} and 10 s^{-1}). Such discontinuous yielding phenomena have also been found for IM metastable β titanium alloys including Ti-5553 [8], Ti-1023 [9] and Ti-7333 [5]. The discontinuous yielding behaviour of PM Ti-5553 alloy can be explained using the dynamic theory that ascribes it to the generation of newly movable dislocations at grain boundaries. Meanwhile, it is worth noticing that the flow curves for the PM

Ti-5553 alloy deformed at 1 s^{-1} and 10 s^{-1} show obvious serrated oscillation, and this is attributed to flow localization.

4.2.2 Effect of deformation strain rate on the flow stress

It can be observed from the true stress-strain curves of PM Ti-5553 alloy in Figure 4.1 at the temperatures of 950 °C and 1050 °C, the flow stress is very sensitive to the strain rate. For a more straightforward observation, the effect of deformation strain rate on the peak flow stress and steady-state stress of the curves in Figure 4.1 (at 950 °C and 1050 °C) are plotted in Figure 4.2.

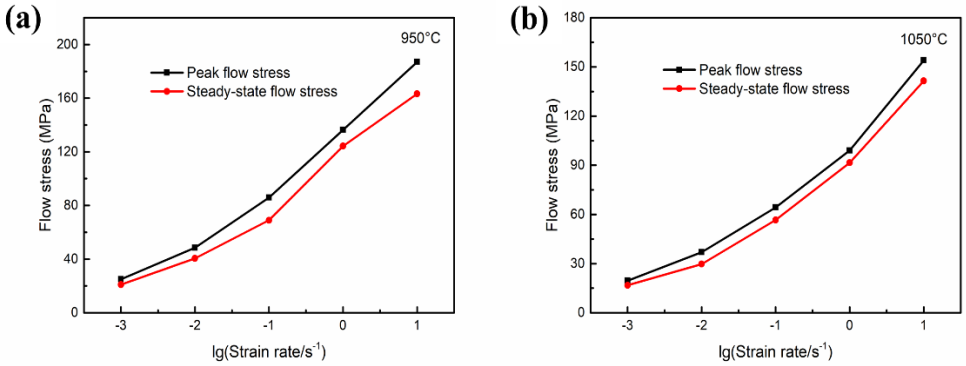

Figure 4.2 The change of peak flow stress(σ_p) and steady-state flow stress ($\sigma_{1.0}$) of as-consolidated PM Ti-5553 alloy deformed at: (a) 950 °C and (b) 1050 °C with varying strain rates.

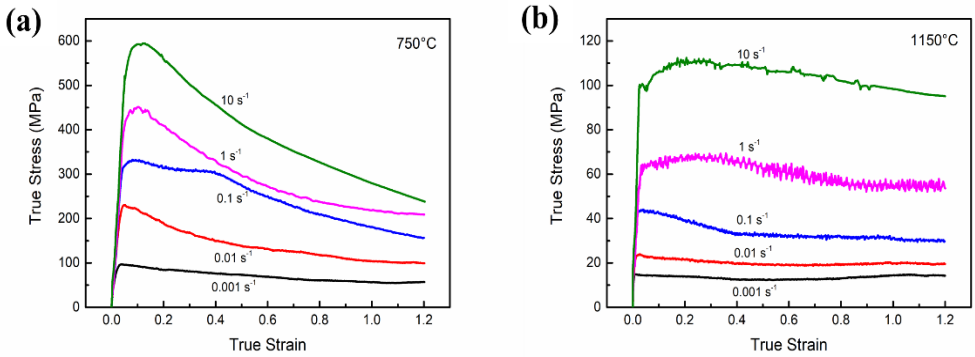

Figure 4.3 True stress-strain curves of the PM Ti-5553 alloy deformed at: (a) 750 °C; (b) 1150 °C.

As can be clearly found in Figure 4.2, both of the peak and steady-state flow stress decreases significantly with reducing the strain rate at 950 °C and 1050 °C. This tendency can also be witnessed in the hot deformation of the alloy at all other temperatures like 750 °C (low temperature) and 1150 °C (high temperature), as

shown in Figure 4.3. These results can be primarily attributed to the applied stress σ increasing as the strain rate $\dot{\varepsilon}$ increases, with respect to the dislocation density, according to the equations following [5, 10, 11]:

$$\dot{\varepsilon} = \rho b v \text{ and } v = A\sigma^m \qquad (4.1)$$

where $\dot{\varepsilon}$ is strain rate, ρ is mobile dislocation density, b is Burgers vector of a perfect dislocation, v is average dislocation velocity, while A and m are material's constants. That means the higher deformation strain rate can accelerate the dislocation multiplication and stimulate work-hardening effects at the beginning of deformation. Also, the high deformation strain rate in the testing can lead to the completion of the deformation in a relatively short time, which impedes the activation of the flow softening effect and thus increases the flow stress.

4.2.3 Effect of deformation temperature on the flow stress

Figure 4.4 displays the true stress-strain curves of the PM Ti-5553 alloy deformed at 0.1 s^{-1} in the temperature range of 700 °C to 1150 °C. Obviously, both the peak flow stress and steady-state stress shows a high sensitivity to the deformation temperature, as shown in Figure 4.5a and b. On the whole, the flow stress is obviously reducing with increasing the temperature.

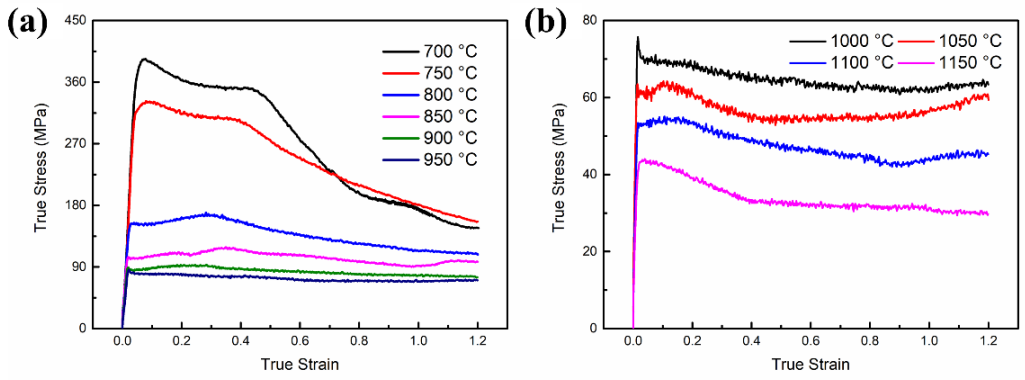

Figure 4.4 True stress-strain curves of as-consolidated PM Ti-5553 alloy deformed at 0.1 s^{-1} and various temperatures: (a) (α+β) region and (b) single βregion.

This is because: (1) thermal activation and diffusion process are more prominent at high temperature and thus reduce the barrier of the hot deformation with lower peak flow stress [12]; (2) the critical resolved shear stress (CRSS) is reduced and then more slip systems are active when the deformation is processed at high temperature; (3) the higher deformation temperature can promote the phase transformation of α

phase (HCP) into β phase (BCC), and the β phase with BCC crystal structure is easier to be deformed than α phase as there are more slip systems [13, 14].

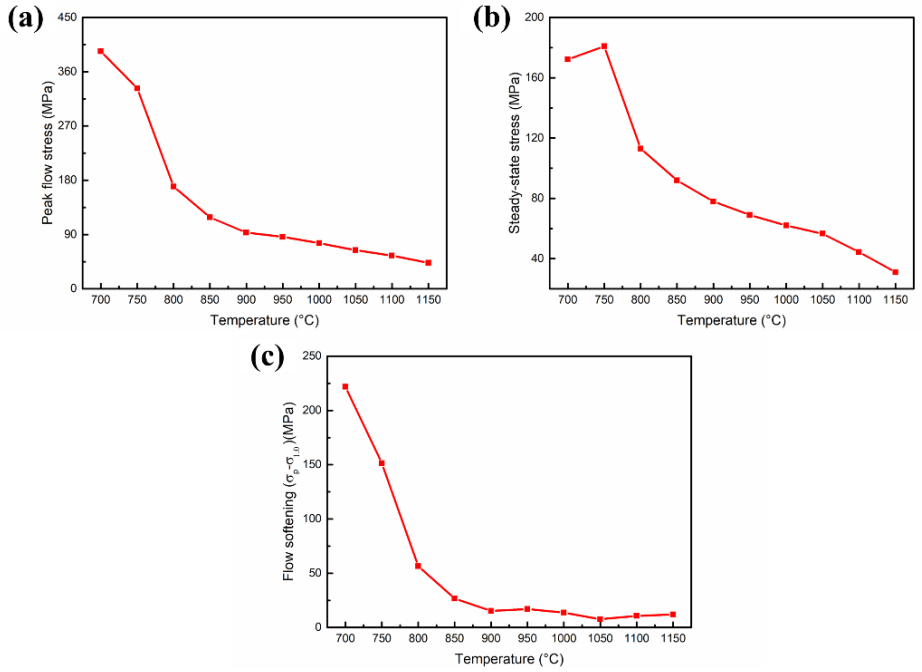

Figure 4.5 The change of peak flow stress(σ_p), steady-state flow stress ($\sigma_{1.0}$) and flow softening values of as-consolidated PM Ti-5553 alloy deformed at 0.1 s^{-1} and various temperatures: (a) peak flow stress; (b) steady-state flow stress and (c) flow softening (σ_p-$\sigma_{1.0}$) value.

In addition, the flow softening values (using the deviation of peak stress and the steady-state stress at the strain of 1.0) also illustrate a constant-reduction trend at the temperature range lower than beta transformation temperature (975 °C), while the flow softening stays at a low and stable stage above the beta transformation temperature (Figure 4.5c). These means the softening mechanism can be strongly influenced by the deformation temperature.

4.2.4 Flow stress comparison

Flow stress reflects the materials deformation resistance during thermomechanical processing, the lower flow stress the material has, the easier the material will be deformed. Figure 4.6 shows the peak flow stress comparison between the PM Ti-5553 alloy and counterparts produced by ingot metallurgy approaches, having a single β phase and dual-phase, respectively. It is clear that the PM Ti-5553 alloy has a lower peak flow stress at moderate and low strain rate (0.001 s^{-1}~ 0.1 s^{-1}) when the deformation is at 900 °C [15, 16]. This means that the PM Ti-5553 alloy has

lower deformation resistance and better hot workability comparing to the other two IM Ti-5553 alloys. The relatively lower flow stress of the PM Ti-5553 is mainly attributed to its initial microstructure, because (1) the absence of the dispersed precipitation phase in the β matrix causes fewer obstacles for dislocation movement compared to that of the dual-phase alloys [17]; (2) much finer grains leads to a higher grain boundary density in the PM Ti-5553 alloy than in the single β phase alloy, and this will intensify the viscous flow of grain boundaries and make it easier for dislocation glide and climb during hot deformation [18, 19].

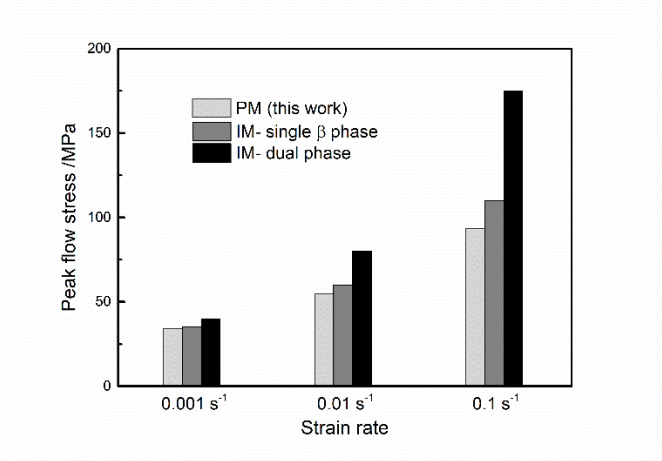

Figure 4.6 Peak flow stress for the PM Ti-5553 alloy in this study and IM Ti-5553 alloy with single β phase [15] and dual-phase [16] at 900 °C and different strain rates.

4.3 Constitutive relationship and deformation activation energy

It is well believed and verified that the essence of the hot processing of metallic materials is controlled by thermal activation processes. The form of the constitutive equations can express the relationships between the flow stress and the deformation variables during hot deformation of metallic materials. The flow stress can be directly calculated by the constitutive relationship with the given deformation variables. Thus, it becomes an important physical-mathematical mode to characterize the hot deformation behaviour and indispensable information for the finite element modelling of the material. The determination of the constitutive relationship has great significance in describing the microstructural variations and choosing suitable tonnage of processing equipment.

In addition, the deformation activation energy (Q, which is the most important parameter in the constitutive relationship) of metallic materials is related to thermal-activated mechanisms at the atomic scale [20]. It is an indicator of how easy the

materials would be hot processed and helps in determining the dominant softening mechanisms at different conditions and the optimal processing windows [21].

According to the Arrhenius-type constitutive equation, the inter-relationships between flow stress (σ), strain rate ($\dot{\varepsilon}$) and temperature (T) can be expressed as the following equation [22]:

$$\dot{\varepsilon} = A f(\sigma) \exp\left(\frac{-Q}{RT}\right) \quad (4.2)$$

where $f(\sigma)$ is the function of stress (σ), this formula is a general constitutive equation for hot deforming of metallic materials. As a result of the different dynamic response of various materials to the changing processing variables, there are three types of mathematical expressions of this function ($f(\sigma)$) depending on the range of stress [23, 24]:

At low-stress region:

$$f(\sigma) = A_1 \sigma^{n_1} \quad (4.3)$$

At high-stress region:

$$f(\sigma) = A_2 [\exp(\beta\sigma)] \quad (4.4)$$

At all stress region:

$$f(\sigma) = A [\sinh(\alpha\sigma)]^n \quad (4.5)$$

Then the Arrhenius-type constitutive equation (4.2) can be expressed as follows:

At low-stress region:

$$\dot{\varepsilon} = A_1 \sigma^{n_1} \exp\left(\frac{-Q}{RT}\right) \quad (4.6)$$

At high-stress region:

$$\dot{\varepsilon} = A_2 [\exp(\beta\sigma)] \exp\left(\frac{-Q}{RT}\right) \quad (4.7)$$

At all stress region:

$$\dot{\varepsilon} = A [\sinh(\alpha\sigma)]^n \exp\left(\frac{-Q}{RT}\right) \quad (4.8)$$

where A_1, A_2, A, α and β are constants, n and n_1 are stress exponent, A is structure factor (s^{-1}), R is universal gas constant (8.314 $J \cdot mol^{-1} \cdot K^{-1}$), *T* is deformation temperature (K, Kelvin temperature), *Q* is deformation activation energy, and there is a relationship between α, β and n_1:

$$\alpha = \beta/n_1 \tag{4.9}$$

Afterwards, logarithm operations (with e) are performed on the Equations of 4.6-4.8 to obtain the following equations (supposing that *Q* is independent of *T*):

$$\ln\dot{\varepsilon} = \ln A_1 + n_1 \ln\sigma - \left(\frac{Q}{RT}\right) \tag{4.10}$$

$$\ln\dot{\varepsilon} = \ln A_2 + \beta\sigma \exp - \left(\frac{Q}{RT}\right) \tag{4.11}$$

$$\ln\dot{\varepsilon} = \ln A + n \ln[\sinh(\alpha\sigma)] - \left(\frac{Q}{RT}\right) \tag{4.12}$$

The unitary linear recursive analysis is then performed on Equations 4.10-4.12 to calculate the parameters of n_1, β and n:

$$n_1 = \left(\frac{\partial \ln\dot{\varepsilon}}{\partial \ln\sigma}\right)_T \tag{4.13}$$

$$\beta = \left(\frac{\partial \ln\dot{\varepsilon}}{\partial \sigma}\right)_T \tag{4.14}$$

$$n = \left(\frac{\partial \ln\dot{\varepsilon}}{\partial \ln[\sinh(\alpha\sigma)]}\right)_T \tag{4.15}$$

As the peak flow stress represents the maximum bearing capacity of the material, it is crucial to establish the constitutive relationships between the peak flow stress and the processing variables. Therefore, the peak flow stress is applied in the calculation and fitting for the constitutive relationships in this section. As it is obvious from Equations 4.13 and 4.14, the value of n_1 and β can be obtained from the reciprocal slope of ($\ln\dot{\varepsilon}$ - $\ln\sigma$) and ($\ln\dot{\varepsilon}$ - σ) fitting plot. Due to the large deformation temperature range during the thermal physical simulation of PM Ti-5553 alloy in this chapter, the constitutive relationships are constructed in α+β (700 °C, 750 °C, 800 °C, 850 °C, 900 °C and 950 °C) and single β (1000 °C, 1050 °C, 1100 °C and 1150 °C) regions separately using the data of four temperatures in each region for the elimination of unacceptable error. The unary linear regression plots of ($\ln\dot{\varepsilon}$ - ln

σ) and ($\ln \dot{\varepsilon}$ - $\ln \sigma$) are shown in Figure 4.7 and 4.8, respectively. Then, the value of α in the hyperbolic sine constitutive relationship at each temperature can be obtained by $\alpha = \beta / n_1$.

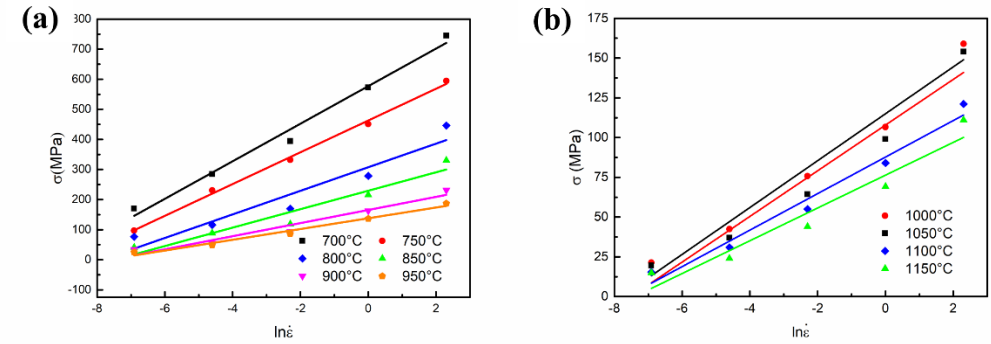

Figure 4.7 Relationship between σ and $\ln\dot{\varepsilon}$ for the PM Ti-5553 alloy deformed in: (a) (α+β) region; (b) β region.

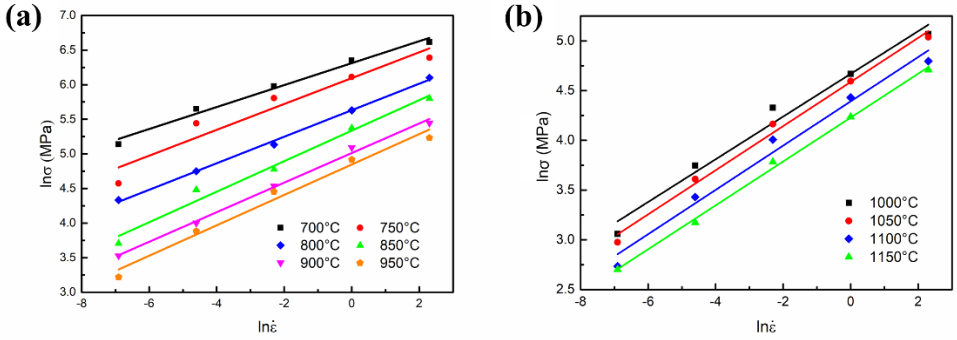

Figure 4.8 Relationship between $\ln\sigma$ and $\ln\dot{\varepsilon}$ for the PM Ti-5553 alloy deformed in: (a) (α+β) region; (b) β region.

Taking the differential calculation on Equation 4.12 and considering the strain rate as a certainty, the following equation can be obtained for the computation of deformation activation energy (Q):

$$Q = \mathrm{R} \cdot n \cdot \left\{\frac{\partial \ln[\sinh(\alpha\sigma)]}{\partial (1/T)}\right\}_{\dot{\varepsilon}} = \mathrm{R} \cdot \left\{\frac{\partial \ln \dot{\varepsilon}}{\partial \ln[\sinh(\alpha\sigma)]}\right\}_{T} \cdot \left\{\frac{\partial \ln[\sinh(\alpha\sigma)]}{\partial (1/T)}\right\}_{\dot{\varepsilon}} \qquad (4.16)$$

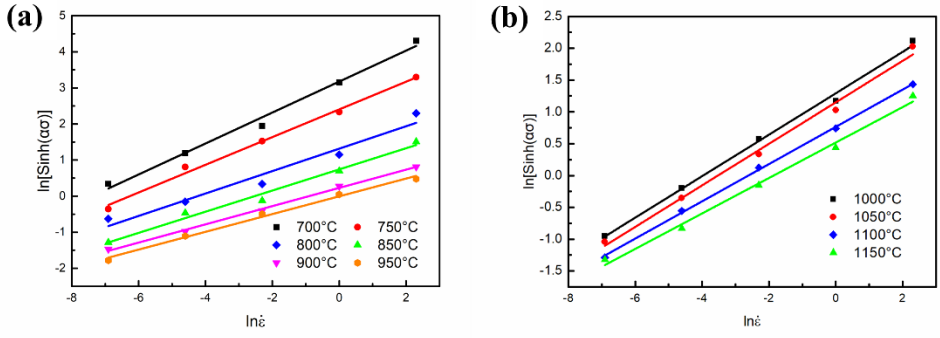

Figure 4.9 Relationship between $\ln[\sinh(\alpha\sigma)]$ and $\ln\dot{\varepsilon}$ for the PM Ti-5553 alloy deformed in: (a) (α+β) region; (b) β region.

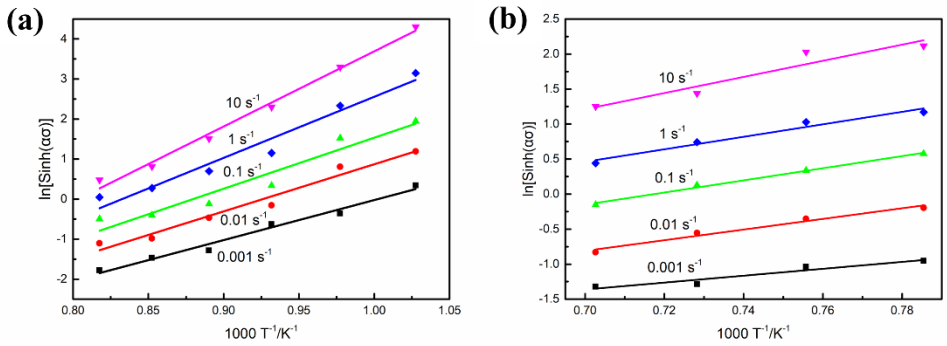

Figure 4.10 Relationship between ln[sinh (ασ)] and 1/*T* for the PM Ti-5553 alloy in: (a) (α+β) region; (b) β region.

Table 4.1 Parameters in hyperbolic sine constitutive equation for PM Ti-5553 alloy deformed in (α+β) region at different temperatures.

Temperature (°C)	n_1	β	α	Average α	n	Average n
700	6.30	0.0160	0.00254	0.00671	2.33	3.26
750	5.35	0.0189	0.00353		2.60	
800	5.22	0.0255	0.00489		3.22	
850	4.53	0.0326	0.00720		3.41	
900	4.68	0.0459	0.00981		3.96	
950	4.55	0.0559	0.01229		4.06	

Table 4.2 Parameters in hyperbolic sine constitutive equation for PM Ti-5553 alloy deformed in single β region at different temperatures.

Temperature (°C)	n_1	β	α	Average α	n	Average n
1000	4.66	0.0679	0.01455	0.01769	3.06	3.28
1050	4.51	0.0696	0.01544		3.06	
1100	4.49	0.0871	0.01937		3.42	
1150	4.53	0.0970	0.02139		3.59	

After that, the value of n at various temperatures can be calculated (using the average α value) by the reciprocal slope of ($\ln \dot{\varepsilon}$ – ln [sinh(ασ)]) fitting plot, as shown in Figure 4.9. Meanwhile, the value of the last item at various strain rates can be calculated (using the average α value) by the slope of (ln [sinh(ασ)] – 1/*T*) fitting plot, as shown in Figure 4.10. The parameters obtained from the fitting and calculations (Equation 4.13 to 4.15) of the different deformation temperatures in (α+β) and single β regions are listed in Table 4.1 and 4.2, respectively. Finally, the average deformation activation energy of the alloy deformed at (α+β) and single β

regions can be calculated with average n and average slope of (ln [sinh($\alpha\sigma$)] –1/T) fitting plot. The parameters for the calculation of Q and the final results are listed in Table 4.3 and 4.4.

Table 4.3 Parameters for the calculation of the deformation activation energy of PM Ti-5553 alloy deformed in (α+β) region.

Strain rate (s^{-1})	$\frac{\partial \ln [\sinh(\alpha\sigma)]}{\partial(1/T)}$	Mean $\frac{\partial \ln [\sinh(\alpha\sigma)]}{\partial(1/T)}$	Average n	R	Q (kJ/mol)
10	18.78				
1	15.26				
0.1	12.75	13.712	3.26	8.314	371.65
0.01	11.77				
0.001	10.00				

Table 4.4 Parameters for the calculation of the deformation activation energy of PM Ti-5553 alloy deformed in β region.

Strain rate (s^{-1})	$\frac{\partial \ln [\sinh(\alpha\sigma)]}{\partial(1/T)}$	Mean $\frac{\partial \ln [\sinh(\alpha\sigma)]}{\partial(1/T)}$	Average n	R	Q (kJ/mol)
10	11.51				
1	8.91				
0.1	8.66	8.322	3.28	8.314	226.94
0.01	7.60				
0.0001	4.93				

* The calculation of deformation activation energy can be slightly different at the different selected temperature range.

According to the results in Table 4.3 and 4.4, the calculated deformation activation energy for the PM Ti-5553 alloy is 371.65 kJ·mol^{-1} in (α+β) region and 226.94 kJ·mol^{-1} in β region. This suggests that the deformation activation energy is very sensitive to the deformation temperature and the dominant deformation mechanisms are different between (α+β) and β regions. The deformation activation energy of PM Ti-5553 alloy in (α+β) region is much higher than the Ti self-diffusion activation energy in titanium alloys (i.e. 135-161 kJ·mol^{-1}) [7, 25] and the diffusion activation energy of Al (92-107 kJ·mol^{-1}) and V (135 kJ·mol^{-1}) [5, 26], indicating that DRX and/or dynamic phase morphology-changing are the most possible dominant deformation mechanisms for the PM Ti-5553 alloy in the (α+β) region. The deformation activation energy in β region is close to the self-diffusion

energy of Ti in titanium alloys and this implies that the dominant deformation mechanism might be DRV.

In addition, the obtained activation energy of the studied PM alloy is comparable with other metastable beta titanium alloys fabricated by IM approaches. Matsumoto et al. [15] reported the deformation activation energy of a full-β-phase Ti-5553 alloy as 296 kJ·mol^{-1} for (α+β) region and 188 kJ·mol^{-1} for single β region. Fan et al. [5] reported the deformation activation energy of Ti-7333 alloy as 333.74 kJ·mol^{-1} for (α+β) region and 213.83 kJ·mol^{-1} for single β region. Hua et al. [16] found the deformation activation energy for a forged Ti-5553 alloy is 316.59 kJ·mol^{-1} for the deformation near and below its beta transformation temperature. Warchomicka et al. [27] illustrated the deformation activation energy of forged Ti-55531 alloy to be 275 kJ·mol^{-1} for (α+β) region and 148 kJ·mol^{-1} for single β region. Zhao et al. [28] reported the deformation activation energy of Ti-1300 alloy as 178 kJ·mol^{-1} for (α+β) region and 216 kJ·mol^{-1} for single β region. It is obvious that the obtained activation energy of the studied PM Ti-5553 alloy is closed to or slightly higher than that of other IM metastable beta titanium alloys. The discrepancy of activation energy can be attributed to the different testing parameter (temperature, strain rate, deformation degree), chemical composition and phase constitution in these researches.

As is well accepted that, the inter-relationships between flow stress, strain rate and temperature for the metallic materials can be described by the Zener-Hollomon parameter, Z :

$$Z = \dot{\varepsilon} \exp\left(\frac{Q}{RT}\right) \tag{4.17}$$

Then, as is demonstrated in equation 4.8 (the equation given by Sellars and McTegart [29] is the most applicable one in the wide range of deformation temperatures and strain rates), Equation 4.17 can be converted into:

$$Z = \dot{\varepsilon} \exp\left(\frac{Q}{RT}\right) = A\,[\sinh(\alpha\sigma)]^n \tag{4.18}$$

Taking natural logarithm for Equation 4.18, it can be further rearranged into:

$$\ln Z = \ln A + n \ln [\sinh(\alpha\sigma)] \quad (4.19)$$

After substituting the value of Q into Equation 4.19, the value of ln Z at varying deformation temperatures and strain rates can be determined. The linear correlations between ln Z and ln [sinh ($\alpha\sigma$)] are shown in Figure 4.11. The intercept of the fitted lines represents the value of ln A, and n (more accurate value) is the slope of the fitted lines. The detailed values of the parameters in ln Z-ln [sinh ($\alpha\sigma$)] fittings are shown in Table 4.5.

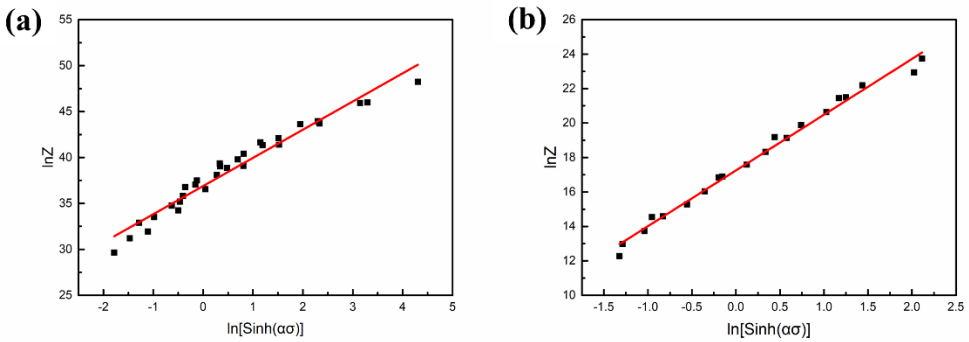

Figure 4.11 Relationship between peak flow stress and the Zener-Hollomon parameter for the PM Ti-5553 alloy in: (a) (α+β) region; (b) β region.

Table 4.5 Detailed values of the parameters in ln Z-ln [sinh (ασ)] fittings for PM Ti-5553 alloy.

Temperature region	n	ln A	A	Linearly dependent coefficient
α+β	3.07	36.89	1.05×10^{16}	95.9%
β	3.24	17.25	3.10×10^{7}	98.9%

It is worth mentioning that, in the drawings (Figure 4.11), the regions with lower Z represent the deformation with lower resistance (at relatively high T and low $\dot{\varepsilon}$), while the regions with higher Z represent the deformation with higher resistance (at relatively low T and high $\dot{\varepsilon}$). More importantly, as it can be found in the fittings, the regression coefficients of the two lines (α+β and β regions) are 95.9% and 98.9%, respectively. These high linearly dependent coefficients demonstrate the excellent linear correlation between Z and the flow stress. They also further confirm the validity of using the classical Arrhenius-type equation to describe the relationship between the variables (σ, T and $\dot{\varepsilon}$) during the hot deformation of the PM Ti-5553 alloy.

Substituting the deformation activation energy *Q*, stress exponent n, constant *A* and α into Equation 4.18, the constitution equations of the PM Ti-5553 alloy in (α+β) and β regions for the hot processing are:

$$\dot{\varepsilon} = e^{36.89} [\sinh (0.00671\sigma)]^{3.07} \exp [-371650/\mathrm{R}T]$$

and

$$\dot{\varepsilon} = e^{17.25} [\sinh (0.01769\sigma)]^{3.24} \exp [-226900/\mathrm{R}T],$$

respectively.

Meanwhile, based on the hyperbolic sine function, Equation 4.17 can be rearranged into another type of hot deformation constitution equation:

$$\sigma = \frac{1}{\alpha} \ln\{(\frac{Z}{\mathrm{A}})^{1/n} + [(\frac{Z}{\mathrm{A}})^{2/n} + 1]^{1/2}\} \qquad (4.20)$$

Then, after substituting the value of constants α and A into Equation 4.20, the hot deformation equations which illustrate the relationship between peak flow stress and Zener-Hollomon parameter (*Z*) can be finally obtained for the PM Ti-5553 alloy in (α+β) and β regions as:

$$\sigma = \frac{1}{0.00671} \ln\{(\frac{Z}{1.05\times10^{16}})^{1/3.07} + [(\frac{Z}{1.05\times10^{16}})^{2/3.07} + 1]^{1/2}\}$$

and

$$\sigma = \frac{1}{0.01769} \ln\{(\frac{Z}{3.10\times10^{7}})^{1/3.24} + [(\frac{Z}{3.10\times10^{7}})^{2/3.24} + 1]^{1/2}\}$$

The equations constructed in this section can be employed to evaluate the hot deformation resistance of alloy during the actual hot processing under different conditions and provided the theoretical basis for the choice of the industrial processing facilities with suitable tonnage and parameters. Furthermore, they also provide the opportunity for the titanium industry to handle the level of flow stress and control the flow behaviour of the alloy during the hot processing.

4.4 Hot processing map

Hot processing map technique is developed on the foundation of the dynamic materials model (DMM) and has become a powerful and effective approach to

design and optimize the hot processing of metallic materials [30-32]. The “safe” and “unsafe” processing regions are suggested on the processing map to guide the actual hot processing. Moreover, the detailed potential deformation mechanisms at different conditions are indicated on the processing map. The “safe” processing regions are always associated with deformation mechanisms of DRX, DRV, phase globularization and super-plasticity. On the contrary, adiabatic shear banding, cracking, localized deformation and internal damage are always found in the material processed in the “unsafe” region, which should be avoided during the hot processing of the alloy [33-35].

In addition, utilizing the hot processing map technique can drastically reduce the time and cost to study the hot processing of a newly designed alloy and hard-to-process alloys. Therefore, it has great significance to establish the hot processing map of the developed as-consolidated Ti-5553 alloy prepared with novel powder metallurgy approach in this research for the optimization of its hot processing parameters and better control of the microstructure after processing.

In this section, the hot processing maps of as-consolidated PM Ti-5553 alloy are established based on the data acquired from the thermal physical simulation at varying deformation temperatures and strain rates to characterize the hot deformation behaviour and evaluate the hot workability of the alloy. With the combination of the microstructure evolution characteristics at typical processing regions on the maps (Section 4.5), the determination of the “safe”/“unsafe” processing windows and the optimization processing parameters were finally obtained.

4.4.1 Dynamic materials model

Based on the continuum mechanics of large plastic deformation, physical systematic simulation and irreversible thermodynamic theory, Prasad et al. [36] developed the generalized Dynamic Materials Model (DMM) with Ti-6242 titanium alloy. This developed DMM can be regarded as a bridge that connects the large plastic deformation processes (forging, rolling, extrusion) and microstructure variation of the material, which demonstrates how the external input energy is consumed during plastic deformation. In this model, the hot processing system

(workpiece, mould and facility) is considered to be acted as a closed adiabatic system, and the workpiece in the hot processing can be treated as a non-linear power dissipater, which makes the power dissipation directly related to the hot processing processes [30].

According to the dissipative structure theory in this model [37], the total external power (P) input during the deformation of the materials is dissipated into two harmonizing parts (as shown in Figure 4.12a):

$$P = \sigma\dot{\varepsilon} = G + J = \int_0^{\dot{\varepsilon}} \sigma \mathrm{d}\dot{\varepsilon} + \int_0^{\sigma} \dot{\varepsilon} \mathrm{d}\sigma \tag{4.21}$$

Where G (content) represents the external power dissipated in the form of heat, and J (co-content) is related to the power dissipated by the microstructural changes. The ratio of these two kinds of energy is determined by the strain rate sensitivity coefficient (m), which can be defined as:

$$m = \frac{\partial J}{\partial G} = \left(\frac{\partial \ln \sigma}{\partial \ln \dot{\varepsilon}}\right)_{\varepsilon,T} \tag{4.22}$$

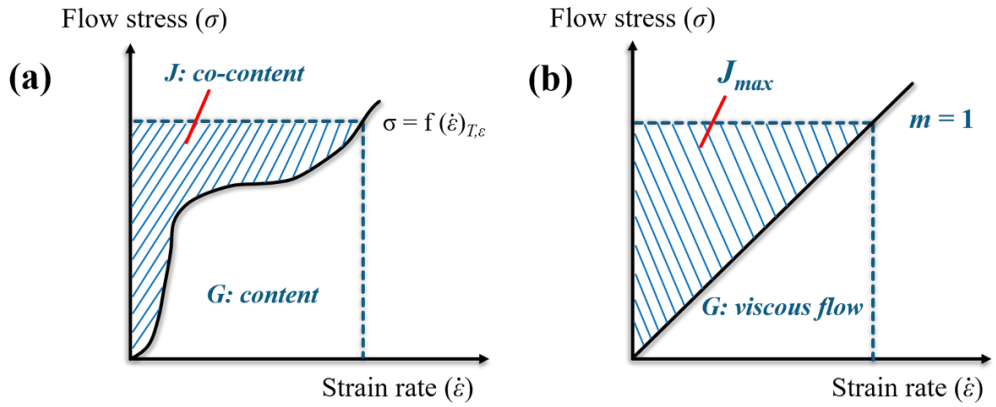

Figure 4.12 Schematic maps showing the power dissipation situation of the processing system in dynamic materials model: (a) non-linear power dissipation of the workpiece; (b) ideal linear power dissipation of the workpiece with J_{max}.

From the aspect of atomic arrangement and motion theory, the distribution of the power dissipation in the deforming system can be illustrated more clearly. As is well believed that, the power dissipation of the metallic materials can be divided into two parts: (1) atomic potential energy, which relates to the relative position of the atoms; (2) atomic kinetic energy, which relates to the thermal movement of

atoms (i.e. the movement of dislocations). The changing of the atomic potential energy is mainly caused by the variation of the microstructure, which corresponds to the co-content *J* in the DMM model. On the other hand, most of the kinetic energy is transferred into the form of thermal energy, which corresponds to the content *G* in the DMM model.

According to Equation 4.21, the integration of co-content *J* can be expressed as:

$$dJ = \dot{\varepsilon}\, d\sigma \tag{4.23}$$

and assuming the alloy is in accordance with the constitutive relationships:

$$\sigma = \mathrm{C}\, \dot{\varepsilon}^{m} \tag{4.24}$$

Then the co-content *J* can be given as follow:

$$J = \int_0^{\dot{\varepsilon}} \sigma \mathrm{d}\dot{\varepsilon} = \frac{m}{m+1}\, \dot{\varepsilon} \tag{4.25}$$

It is worth mentioning that Equation 4.25 will only become valid when the value of *m* is a constant at the specific condition. Generally speaking, the value of *m* varies with the deformation temperature and strain rate non-linearly. With respect to the stable-state flow situation, the value of *m* always varies from 0 to 1. When the value of m is 0, it means there is no power dissipation of the system. When the value of m is 1, it means the system is at the ideal linear dissipating condition, with the maximum value of co-content *J* (J_{max}, as shown in Figure 4.12b):

$$J_{max} = \frac{\sigma\, \dot{\varepsilon}}{2} \tag{4.26}$$

Based on Equations 4.25 and 4.26, a dimensionless parameters η was defined as power dissipation efficiency to describe the ratio of the co-content *J and* J_{max}, which represents the proportion of the total input energy used for the microstructural evolution during the plastic deformation:

$$\eta = \frac{J}{J_{max}} = \frac{2m}{m+1} \tag{4.27}$$

The variation of η with deformation temperature (T) and strain rate ($\dot{\varepsilon}$) constitutes a power dissipation map, which characterizes microstructural changes happening in the deformation. The power dissipation map show domains where the power efficiency has a local maximum value corresponding to the softening mechanisms with significant microstructural variation.

Not only the power dissipation efficiency map to characterizes microstructural changes happened in the hot deformation of metallic materials, Prasad et al. [36-38] also further presented a flow instability criterion based on the extremum principles of irreversible thermodynamics and the principle of the maximum rate of entropy production. Considering the deforming system will become unstable when the dissipation function D ($\dot{\varepsilon}$) and $\dot{\varepsilon}$ satisfy the following equation:

$$\frac{\mathrm{d}D}{d\dot{\varepsilon}} < \frac{\mathrm{D}}{\dot{\varepsilon}} \tag{4.28}$$

According to the presented DMM, the dissipation function $D(\dot{\varepsilon})$ at a specific temperature can be equal to the co-content J, therefore, the equation can be transferred into:

$$\frac{\mathrm{d}J}{d\dot{\varepsilon}} < \frac{J}{\dot{\varepsilon}} \tag{4.29}$$

Using the expression of J in Equation 4.25, and taking the natural logarithm, Equation 4.29 becomes:

$$\ln J = \ln \frac{m}{m+1} + \ln \sigma + \ln \dot{\varepsilon} \tag{4.30}$$

After the partial differential operation with $\ln \dot{\varepsilon}$ of the above equation:

$$\frac{\mathrm{d} \ln J}{\mathrm{d} \ln \dot{\varepsilon}} = \frac{\partial (\ln \frac{m}{m+1})}{\partial \ln \dot{\varepsilon}} + \frac{\partial \ln \sigma}{\partial \ln \dot{\varepsilon}} + 1 \tag{4.31}$$

Then Equation 4.29 can be rearranged into：

$$\frac{\mathrm{d} \ln J}{\mathrm{d} \ln \dot{\varepsilon}} < 1 \tag{4.32}$$

After substituting Equation 4.22 and 4.31 into Equation 4.32, the final continuum criterion of flow instability can be given as below:

$$\xi(\dot{\varepsilon}) = \frac{\partial \ln [\frac{m}{m+1}]}{\partial \ln \dot{\varepsilon}} + m < 0 \tag{4.33}$$

The physical significance of this criterion can be expressed as: during the hot deformation of materials, if the strain rate acting on the deforming system is larger than the generated entropy increment, localized flow and/or flow instability will occur. Flow instability occurs when this instability parameter $\xi(\dot{\varepsilon})$ become negative, and the variation of $\xi(\dot{\varepsilon})$ with the deformation temperature and strain rate constitutes the flow instability map.

The flow instability map is superimposed over the power dissipation map to obtain the final completed hot processing map, which exhibited the characteristics of various domains in terms of deformation microstructure evolution and flow instability.

4.4.2 Construction of hot processing map

There are mainly four procedures for the construction of processing maps using the data obtained from the thermal physical simulation: parameter calculation; construction of power dissipation map; construction of flow instability map and superposition of the two maps. The detailed processes are listed here:

(1) Collecting every single value of flow stress at various conditions (temperature, strain rate, deformation strain) from the true strain-true stress curves of the thermal physical simulation.
(2) Equal interval interpolation (using Matlab® software) is introduced for the finer data gap of deformation temperature and strain rate.
(3) Cubic spline function (using Matlab® software) is employed for the fitting of the data of ($\log \sigma - \log \dot{\varepsilon}$) at various temperatures, then $\log \sigma$ can be expressed by $\log \dot{\varepsilon}$ as:

$$\log \sigma = a + b \log \dot{\varepsilon} + c (\log \dot{\varepsilon})^2 + d (\log \dot{\varepsilon})^3 \qquad (4.34)$$

(4) Based on Equation 4.22 and 4.34, the corresponding m can be obtained by introducing $\log \dot{\varepsilon}$ at different strain rates:

$$\mathrm{m} = \frac{\mathrm{d}(\log \sigma)}{\mathrm{d}(\log \dot{\varepsilon})} = b + 2c \log \dot{\varepsilon} + 3d (\log \dot{\varepsilon})^2 \qquad (4.35)$$

(5) Duplicating the steps by selecting various temperatures and deformation strain, and calculating the value of power dissipation efficiency (η) according to Equation 4.27. Plotting the contour diagram (Origin® software) showing the variation of η with deformation temperature and strain rate to obtain the power dissipation map. Figure 4.13 shows the 3-Dimensional power dissipation maps (at temperature range of 800 °C-1150 °C and strain rate range of 0.001 s^{-1}-10 s^{-1}) of the PM Ti-5553 alloy as constructed at the true strain of 0.7 (30% height reduction), 1.0 (50% height reduction) and 1.2 (70% height reduction), respectively.

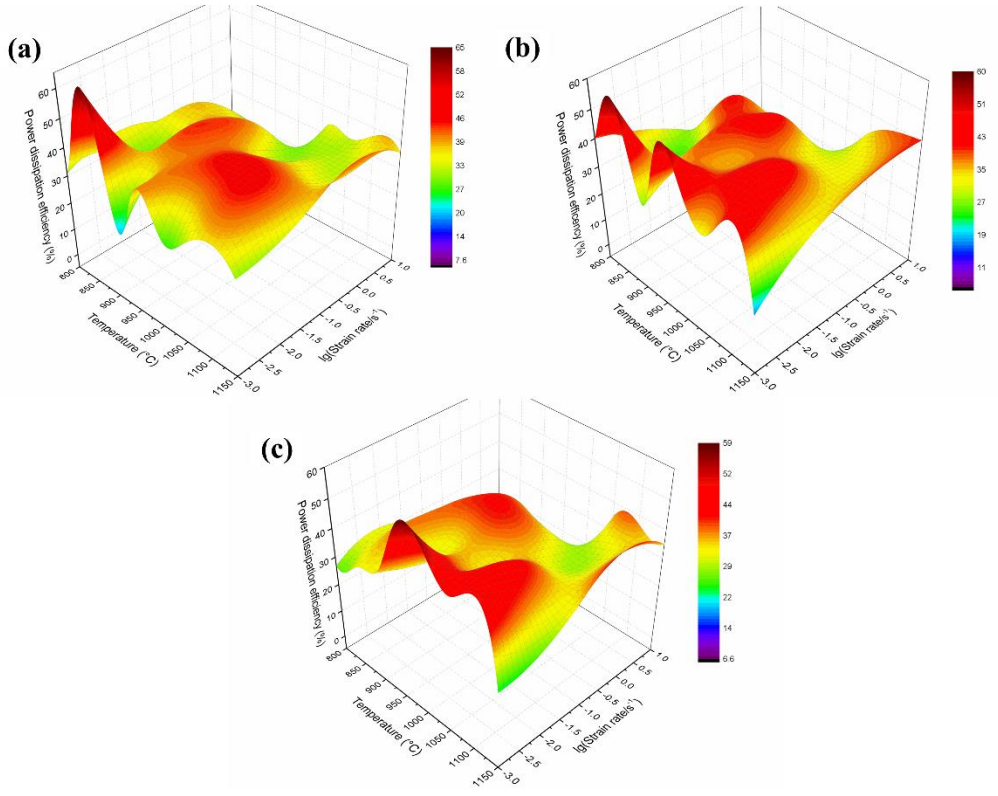

Figure 4.13 Three-dimensional power dissipation maps of PM Ti-5553 alloy constructed at the temperature range of 800 °C-1150 °C and strain rate range of 0.001 s^{-1}-10 s^{-1} for various true strain: (a) 0.7; (b) 1.0 and (c) 1.2. The contour numbers represent the power dissipation efficiency η.

(6) Based on Equation 4.33 and 4.35, the corresponding $\xi(\dot{\varepsilon})$ can also be obtained by introducing log $\dot{\varepsilon}$ at different strain rates:

$$\xi(\dot{\varepsilon}) = \frac{2c + 6d(\log \dot{\varepsilon})}{\mathrm{m(m+1)}} + m < 0 \qquad (4.36)$$

(7) Duplicating the steps by selecting various temperatures and deformation strain, and calculating the value of flow instability criterion (ξ). Plotting the contour diagram (Origin® software) showing the areas with negative ξ at varying temperatures and strain rates to obtain the flow instability map. Figure 4.14 shows the 2-Dimensional flow instability maps (at temperature range of 800 °C-1150 °C and strain rate range of 0.001 s^{-1}-10 s^{-1}) of the PM Ti-5553 alloy as constructed at the true strain of 0.7, 1.0 and 1.2, respectively.

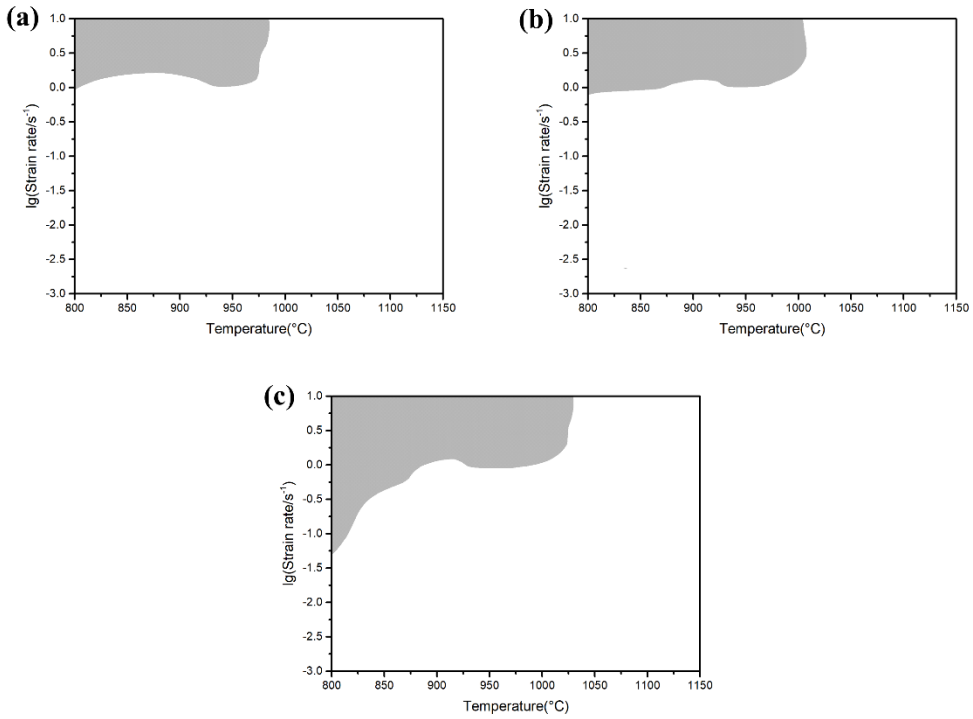

Figure 4.14 Two-dimensional flow instability maps of PM Ti-5553 alloy constructed at the temperature range of 800 °C-1150 °C and strain rate range of 0.001 s^{-1}-10 s^{-1} for various true strain: (a) 0.7; (b) 1.0 and (c) 1.2. The grey-shaded regions represent the instability domains.

(8) Superimposing the contour diagrams in Figure 4.13 and 4.14 at the same true strain, the establishment of integrated hot processing maps of PM Ti-5553 alloy is finally achieved. Figure 4.15 shows the whole hot processing maps (at temperature range of 800 °C-1150 °C and strain rate range of 0.001 s^{-1}-10 s^{-1}) of the PM Ti-5553 alloy as constructed at the true strain of 0.7, 1.0 and 1.2, respectively. The contour number represents the percentage of constant power dissipation efficiency, while the grey-shaded areas refer to the instability regions. The β phase transformation temperature is also indicated on the maps.

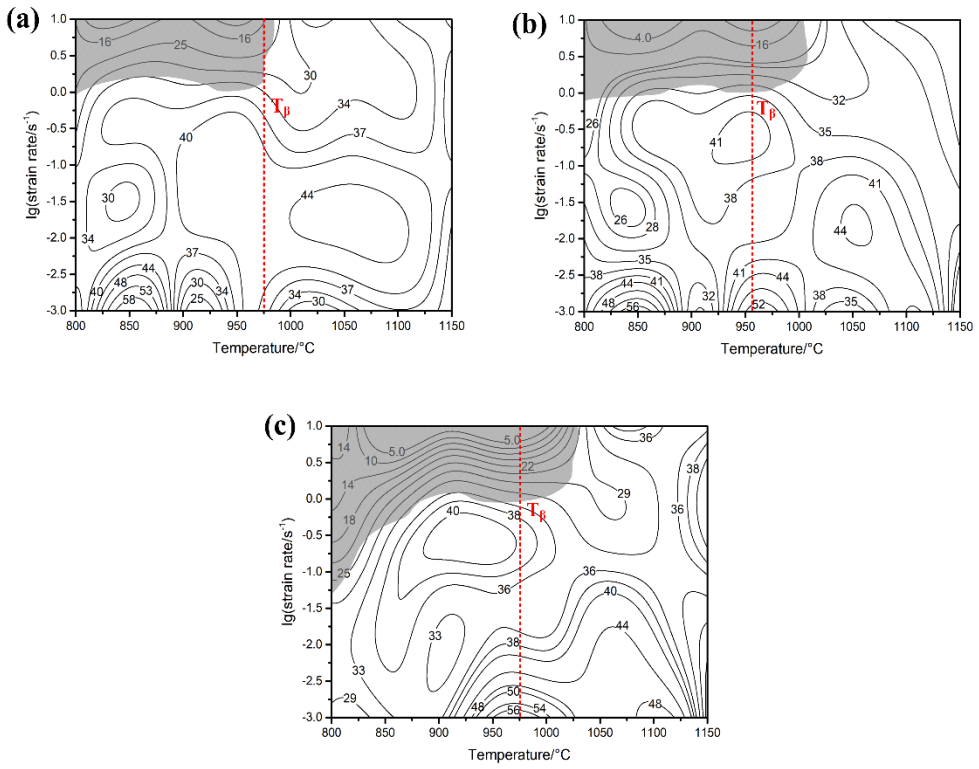

Figure 4.15 Typical hot processing maps of PM Ti-5553 alloy constructed at the temperature range of 800 °C-1150 °C and strain rate range of 0.001 s^{-1}-10 s^{-1} for various true strain: (a) 0.7; (b) 1.0 and (c) 1.2. The contour numbers represent the power dissipation efficiency η, and the grey-shaded regions represent the instability domains.

4.4.3 Power dissipation efficiency and instability criterion

First of all, in the processing maps at all deformation degree, it is obvious that the power dissipation efficiency increases with increasing the deformation temperature and decreasing the strain rate. There is always a relatively low-efficiency area located at the left top corner (low temperature and high strain rate) of the processing maps. That means the microstructure variation is promoted at high temperature and low strain rate conditions, but impeded at low temperature and high strain rate conditions.

The processing map at true strain of 1.0 (Figure 4.16) is chosen for further discussion and identification of the deformation mechanisms of the PM Ti-5553 alloy. According to Prasad and Seshacharyulu [30], the region with optimum power dissipation efficiency is always chosen as a processing window for metallic materials, and the value of power dissipation efficiency is highly dependent on the materials' stacking fault energy (SFE). For titanium alloys, the reported optimum

power dissipation efficiency is in the range of 35% ~ 50% because of its relatively high SFE. It can be seen, in Figure 4.16, that there are large areas with power dissipation efficiency higher than 35%, and this suggests that the potential hot processing windows for the PM Ti-5553 alloy are wide. These possible processing windows are wider than those of other similar IM metastable β titanium alloys, e.g. Ti-5553 [15], Ti-55511[39], Ti-55531 [40], and Ti-1023 alloys [9].

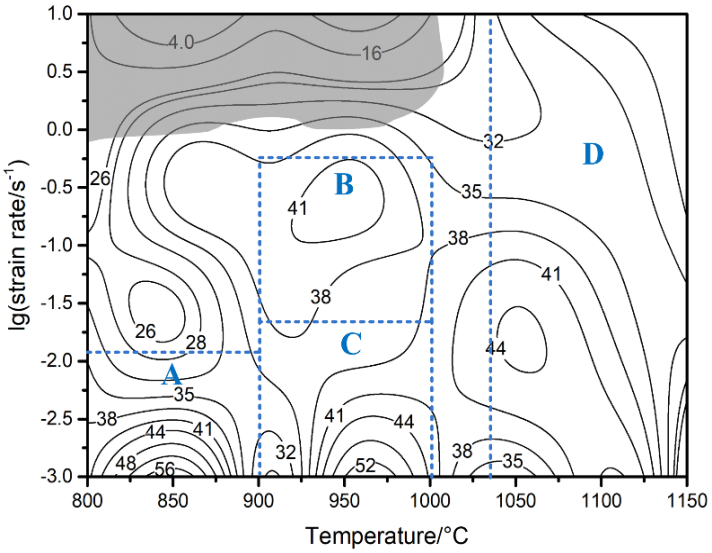

Figure 4.16 The hot processing maps of PM Ti-5553 alloy constructed at the temperature range of 800 °C-1150 °C and strain rate range of 0.001 s^{-1}-10 s^{-1} for the various true strain of 1.0. The contour numbers represent the power dissipation efficiency *η*, and the grey-shaded regions represent the instability domains. Four peak power dissipation efficiency domains (A, B, C and D) are suggested on the map.

Four peak power dissipation efficiency domains are exhibited in the hot processing map of PM Ti-5553 alloy at the true strain of 1.0 (Figure 4.16), and all the peak-domains mainly appear at the medium and low stain rate regions. The first domain is located at the temperature between 800 °C and 900 °C and strain rate of 0.001 s^{-1} (Domain A), with the peak power dissipation efficiency of 56%. The second and third domains can be found at the temperature of about 950 °C and the strain rate of 0.1 s^{-1} (Domain B) and 0.001 s^{-1} (Domain C), with a peak power dissipation efficiency of 41% and 52%, respectively. The fourth domain is at the temperature of around 1050 °C (above the β transformation temperature) and strain rate of 0.01 s^{-1} (Domain D), showing the peak power dissipation efficiency of 44%.

It can also be seen that there is a constant instability domain located at the region of the strain rate of higher than 1 $s^{-1}$and the temperatures lower than 975 °C in Figure 4.15a. The instability domain area expands to the higher temperature (1025 °C) region in Figure 4.15b and lower strain rate (0.1 s^{-1}) region in Figure 4.15c. This illustrates that the flow instability region, which is always related to the formation of adiabatic shear bands, cracking and/or flow localization [38], is expanded with increasing the deformation degree. Meanwhile, the deformation degree also affects the power dissipation efficiency of the PM Ti-5553 alloy, and this can be clearly seen in Figure 4.15. The value of η become larger and the optimal processing regions are getting wider with increasing the deformation degree. These results demonstrate that the microstructure of the alloy may be changed more when the alloy is deformed to a higher deformation degree than that to a lower deformation degree, and the higher deformation degree will be a benefit for the optimized hot processing of the alloy.

4.5 Microstructural evolution characteristics

In order to determine the deformation mechanisms and verify the reliability of the optimized processing parameters predicted by the hot processing map, the microstructure changes for the PM Ti-5553 alloy deformed at each domain in Figure 4.16 have to be characterized and discussed.

4.5.1 Domain A

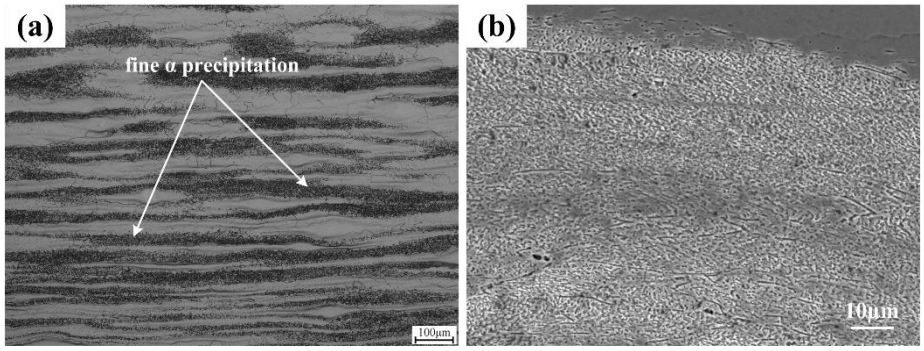

Figure 4.17 The deformation microstructures for the PM Ti-5553 alloy at 850 °C/0.001 s^{-1}: (a) OM and (b) locally amplified SEM.

Figure 4.17 shows the microstructure of the PM Ti-5553 deformed at 850 °C/0.001 s^{-1}, it is clear that the α precipitate bands appear in the β matrix, which is consisted of short rod-like and/or tiny-globular α particles (less than 2 μm), suggesting that

the α phase globularization occurs during the hot processing. This phenomenon mainly occurs for metastable β titanium alloys during the heat preservation process in the (α+β) region, and the α precipitates characteristics are significantly influenced by the hot deformation parameters [5].

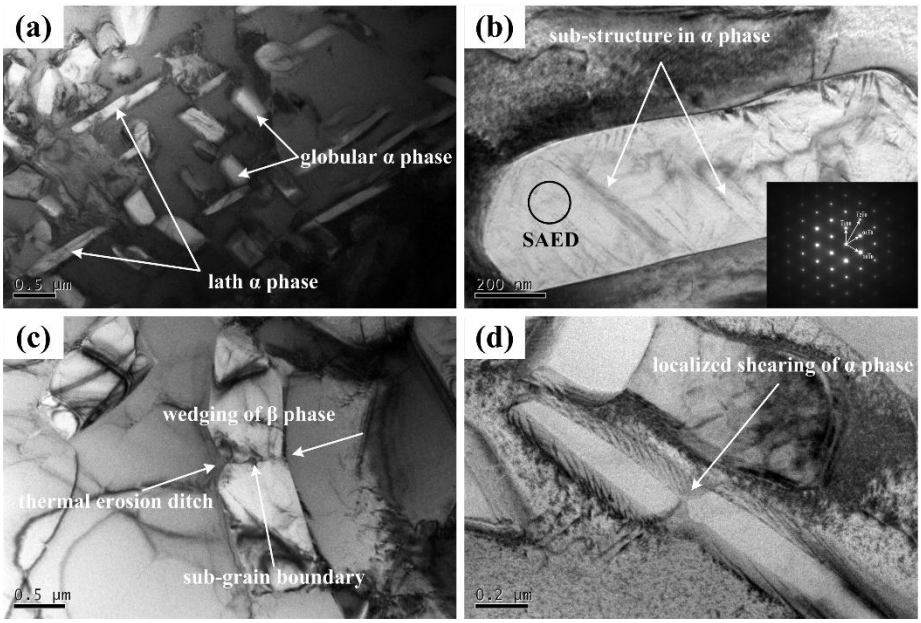

Figure 4.18 TEM microstructures of the PM Ti-5553 alloy deformed at 850 °C/0.001 s^{-1}: (a) α phase precipitates; (b) sub-structure and SAED pattern; (c) β phase wedging at the sub-grain boundary; (d) localized shearing of lath α phase.

The corresponding TEM microstructures for the PM Ti-5553 alloy deformed at 850 °C/0.001 s^{-1} are shown in Figure 4.18. It is obvious that a large amount of lath-shaped and globular α precipitates with different aspect ratios appear in Figure 4.18a, and this further confirms significant α phase globularization occurs. Obvious sub-grain boundaries (dark areas) are formed in the columnar α precipitate (verified by the SAED pattern), as shown in Figure 4.18b, which is related to the early stage of the globularization process. The β phase wedging at the sub-grain boundary in the original lath α phase and formation of thermal erosion ditch can be clearly seen in Figure 4.18c. Moreover, the localized shearing of α grains is visible in Figure 4.18d and the prior α lath is sheared and slipped into two parts. The formation of sub-grain boundaries and/or the localized shearing may become active in the original lath α precipitates with increasing the deformation to a certain degree, and this will lead to increasing the shear stress in the lath α precipitates and eventually cause the lath α phase is torn into two parts. Thus, two α phase globularization mechanisms can be summarised and sketched for the PM Ti-5553 alloy deformed in the Domain A, as shown in Figure 4.19. These two α phase globularization

mechanisms are also separately revealed and explained by Margolin et al [41] and Weiss et al. [42] using the grain boundary separation model. The detailed mechanism of the dynamic α morphology changing and its globularization will be further discussed in Chapter 5.

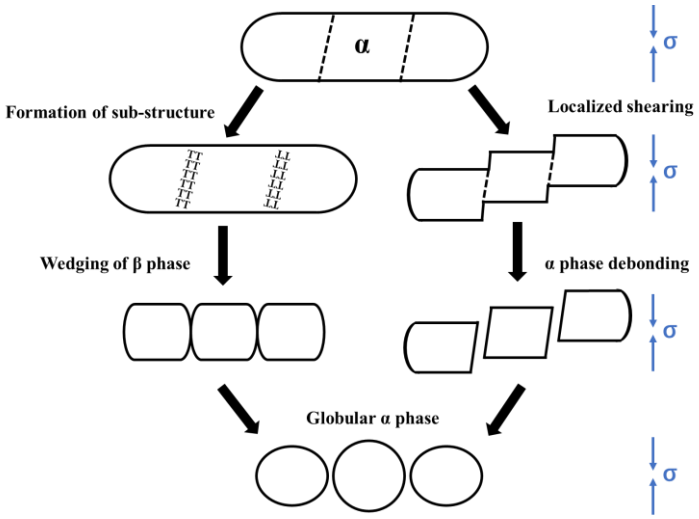

Figure 4.19 Schematic map illustrating the two possible α phase globularization processes for the PM Ti-5553 alloy hot processed in (α+β) region.

Additionally, as is shown in Figure 4.20, the tensile test of the alloy conducted at the condition of 850 °C/0.001 s^{-1} verifies the occurrence of superplastic deformation at the peak efficiency region (56% in Figure 4.16) of the low-temperature region. Thus, it can be claimed that dynamic α globularization and super-plasticity are the dominated deformation mechanisms in the Domain A. Furthermore, besides the α precipitate bands, some dim serrated grain boundaries of β matrix can also be found in the microstructure in Figure 4.17a, which means DRV also occurs at this condition.

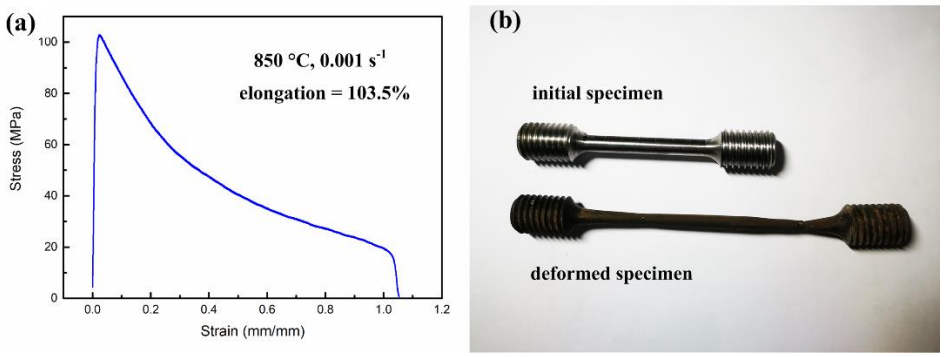

Figure 4.20 Superplastic deformation of the alloy at 850 °C/0.001 s^{-1}: (a) stress-strain curve; (b) samples (round-cross section, diameter = 4mm and gauge length = 20 mm) before and after the tensile test.

4.5.2 Domains B and C

Figure 4.21 shows the EBSD microstructure orientation maps of the PM Ti-5553 alloy deformed at 950 °C/1 s^{-1} and 950 °C/0.1 s^{-1} (Domain B) and at 950 °C/0.01 s^{-1} and 950 °C/0.001 s^{-1} (Domain C). It is clear that most of the β grains for the alloy deformed at 1 s^{-1} have serrated grain boundaries and are elongated along the perpendicular direction of compression axis (Figure 4.21a, compression axis is the vertical direction), and large amount of sub-structures (represent by different colour) are visible in the inside of the β grains besides small amounts of fine necklace-shaped equiaxed grains located along the grain boundaries. These microstructure characteristics are obvious evidence of DRV and the nucleation and formation of DRX grains. When the strain rate decreases to 0.1 s^{-1}, more and finer DRX grains are formed along the serrated β grain boundaries in the PM Ti-5553 alloy (Figure 4.21b). Grain orientation spread (GOS) distribution analysis can be used to identify the recrystallized grains in the microstructure [43, 44], and the recrystallized grains usually show low GOS value (usually less than 2°) comparing to those deformed and DRV grains that contain a large numbers of sub-structures and dislocation.

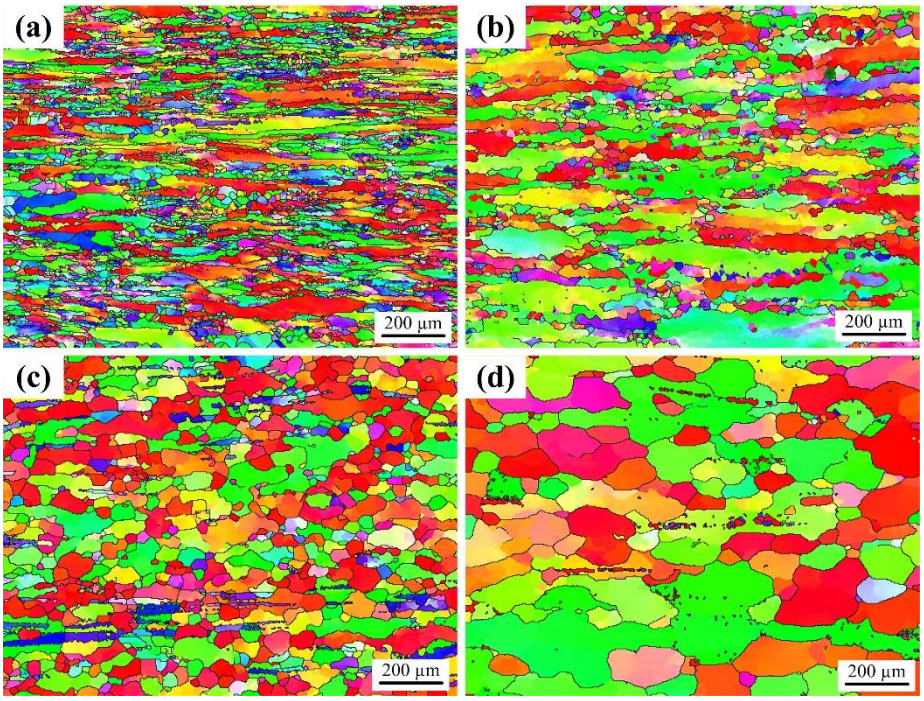

Figure 4.21 EBSD orientation maps of the PM Ti-5553 alloy deformed at 950 °C: (a) 1 s^{-1}; (b) 0.1 s^{-1}; (c) 0.01 s^{-1}; (d) 0.001 s^{-1}.

Figure 4.22 shows the β phase GOS maps for the PM Ti-5553 alloy deformed at 950 °C and different strain rates (either in Domains B or C). For the alloy deformed in Domain B, a larger amount of fine necklace DRX grains (blue grains) can be

identified in the microstructure of the alloy deformed at 0.1 s^{-1} (Figure 4.22b) than at 1 s^{-1} (Figure 4.22a). Furthermore, compared to the PM Ti-5553 alloy deformed in Domain A, DRX grains and DRV features begin to appear in the Domain B, because the recovery and recrystallization driving forces are larger and dislocation glide is easier at high deformation temperature than at low temperature [1]. It is speculated that the dominant deformation mechanisms in the Domain B are DRV and partially DRX.

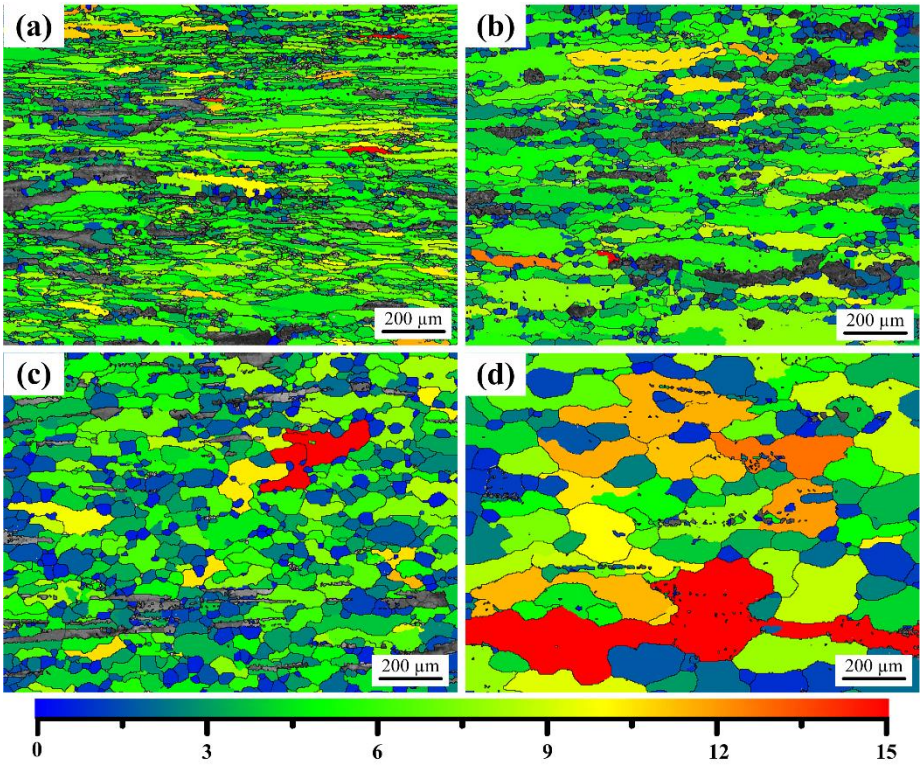

Figure 4.22 β phase GOS maps (α phase is indicated as grey areas) of the PM Ti-5553 alloy deformed at 950 °C: (a) 1 s^{-1}; (b) 0.1 s^{-1}; (c) 0.01 s^{-1}; (d) 0.001 s^{-1}.

When the deformation strain rate decreases to 0.01 s^{-1} at 950 °C, homogeneous equiaxed microstructure and widespread low-GOS-value grains are shown in Figure 4.21c and Figure 4.22c, respectively, suggesting that fully DRX happens. Thus, it is confirmed that DRX becomes the dominated deformation mechanism at 950 °C/0.01 s^{-1}. Further decreasing the deformation strain rate to 0.001 s^{-1} at 950 °C, the equiaxed grains grow coarser (Figure 4.21d) comparing to that in Figure 4.21c, and large elongated grains with serrated grain boundaries and substructures can also be identified in Figure 4.21d. The GOS values of the corresponding grains are relatively high (Figure 4.22d), and this indicates that the recrystallized grains undergone further growth, and some experience post-DRV. The main deformation mechanisms in Domain C are DRX growth and post-DRV.

4.5.3 Domain D

Figure 4.23 shows the optical and TEM microstructures of the PM Ti-5553 alloy deformed at 1150 °C and strain rate of 1 s^{-1} and 0.01 s^{-1}. A large amount of coarse β grains with obvious serrated boundaries and no obvious DRX grains are observed in Figure 4.23a and b, suggesting that the deformation mechanism for the PM Ti-5553 alloy deformed at temperatures higher than 1150 °C and strain rates lower than 1 s^{-1} (Domain D) is dominated by DRV. Corresponding high-magnification TEM images show that the sub-grains, which are with flat grain boundaries, have high dislocation density, and part of the dislocations have already been piled up (Figure 4.23c and d). This further confirms that DRV is the dominant deformation mechanism in Domain D. The reason why no DRX grains are observed in the microstructure is that the glide and climb of dislocations are more likely to occur in the metastable β titanium alloys when they are processed in the β region, due to the relatively high SFE of titanium alloys, so that the distortion energy is greatly consumed and the DRX is inhibited [40].

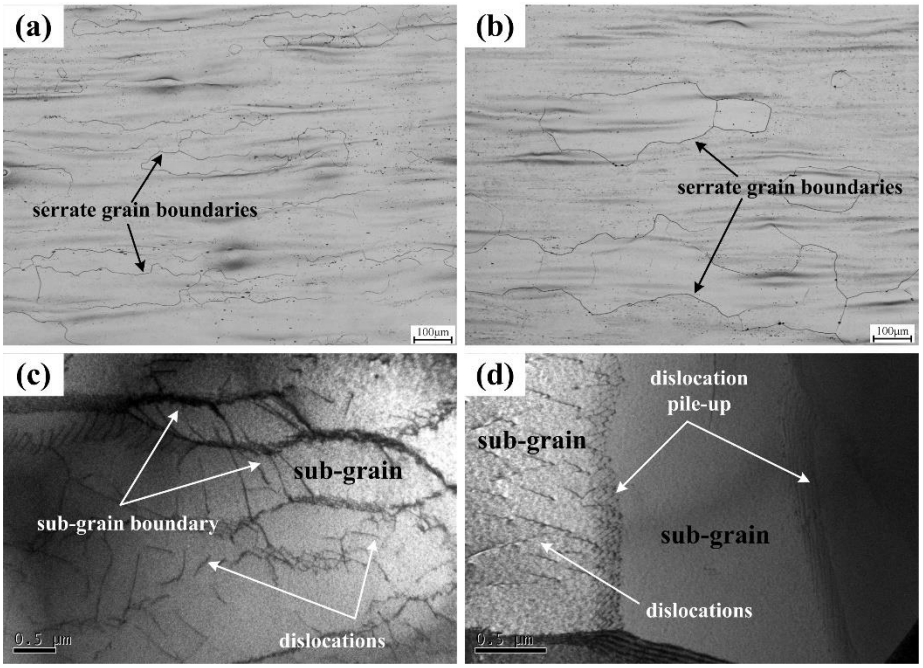

Figure 4.23 OM and TEM microstructures of the PM Ti-5553 alloy deformed at: (a) and (c) 1150 °C/1 s^{-1}; (b) and (d) 1150 °C/0.01 s^{-1}.

4.5.4 Instability domain

According to the hot processing map of PM Ti-5553 alloy (Figure 4.16), the instability occurs in the region consisting of the high strain rate ($\dot{\varepsilon} > 1\ s^{-1}$) and low deformation temperature (T < 1025 °C) region (as marked as grey-shaded area).

The metallic materials' flow instability during hot processing is related to the occurrence of adiabatic shear bands, cracking and localized plastic flow. As shown in Figure 4.24, the microstructure observation for the PM Ti-5553 alloy deformed at 800 °C/10 s^{-1} and 900 °C/10 s^{-1} clearly exhibit that flow localization bands and inhomogeneous deformation features (in macroscopic images). These features are associated with local temperature rise that is mainly caused by fast deformation and relatively low thermal conductivity of titanium alloys. Similar results can be found in other titanium alloys deformed at low temperature and high strain rate [5, 7, 39, 45]. Furthermore, the degree of flow localization is more serious for the PM Ti-5553 alloy deformed at low temperature (800 °C) than at relatively high temperature (900 °C). This is because the deformation inducing temperature rise will be higher in the alloy deformed at lower temperature than at higher temperature under the given strain rate and deformation degree. Therefore, it can be confirmed that the formation of flow localization bands is the primary cause of instability for the PM Ti-5553 alloy deformed in the instability domain.

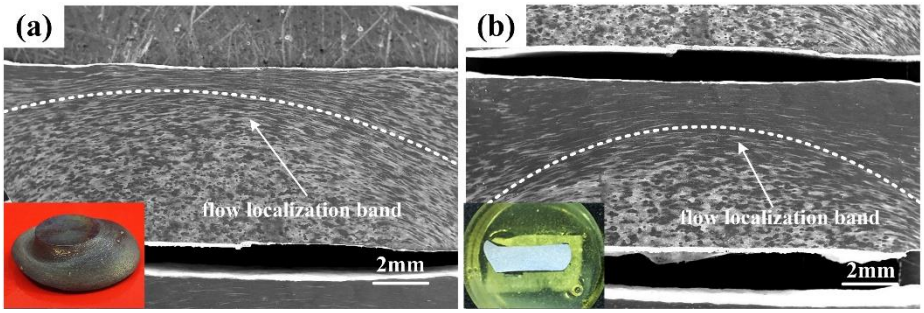

Figure 4.24 Microstructures of the PM Ti-5553 alloy deformed at: (a) 800 °C/10 s^{-1}; (b) 900 °C/10 s^{-1}.

4.5.5 The optimization of deformation degree

For investigating reasons that why the value of η becomes larger and the optimal processing regions are getting wider with increasing the deformation degree, EBSD analysis is conducted on the PM Ti-5553 alloy deformed at 950 °C/0.1 s^{-1} and with the deformation degree of 30% and 50%, respectively. The corresponding results are shown in Figure 4.25. It can see in Figure 4.25a that the grains almost kept the original equiaxed shape and no new grains formed when the deformation degree is 30%. With increasing the deformation degree to 50%, it is clear that the grains are obviously elongated, serrated grain boundaries are also visible, and some small necklace-shaped DRX grains are formed at the serrated grain boundaries (Figure

4.25c). The GOS maps (as shown in Figure 4.25b and d) confirm that the fraction of recrystallized grains is higher in the alloy with a deformation degree of 50% than with 30%. It has been shown that the PM Ti-5553 alloy deformed at 950 °C/0.1 s^{-1} and with deformation degree of 70% contains obvious DRX and DRV grains (as discussed in the Domains B and C), therefore, it is proposed that increasing deformation degree can promote the processes of DRX and DRV. This is because the dislocation movement and softening driving force are accelerated and enhanced by the large plastic deformation, and the DRX and DRV become correspondingly more activated [46, 47]. Hereinafter, the higher degree of DRX and DRV lead to the larger microstructural changes in the microstructure, which manifests as increased power dissipation efficiency in the processing map.

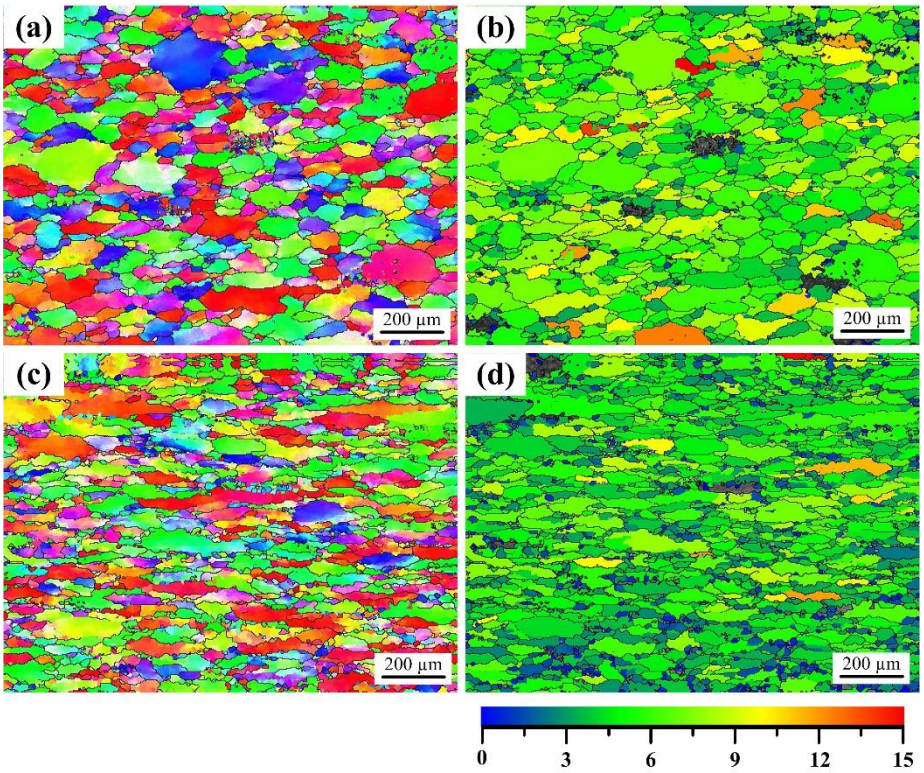

Figure 4.25 EBSD analysis results for PM Ti-5553 alloy deformed at 950 °C/0.1 s^{-1} with the deformation degree of 30%: (a) orientation map and (b) β phase GOS map, and 50%: (c) orientation map and (d) β phase GOS map.

From the analysis and discussion above, it is confirmed that the optimized hot processing window for the PM Ti-5553 alloy is at the medium deformation temperature (between 900 °C to 1050 °C) and moderate/moderate-low strain rates (less than 1 s^{-1}). At this processing window, PM alloy shows the resultant deformed microstructure with the dominant deformation mechanisms of DRV plus partial DRX and compete DRX with stable deformation and grain refinement. Meanwhile,

the power dissipation efficiency is relatively high within this window. In addition, the processing condition of 950 °C/0.01 s^{-1} could be the potential "best" one, as the occurrence of extensive DRX to produce fine and homogeneous DRX grains dispersed in the microstructure. Also, the PM alloy should be processed within the obtained optimized processing window with a large plastic degree (severe plastic deformation) of at least 70% to produce the desired power dissipation and microstructure. Unstable deformation occurs in the flow instability region (T < 1025 °C and $\dot{\varepsilon} > 1$ s^{-1}) and the hot working of PM Ti-5553 alloy should be avoided in this region.

4.6 Effect of processing parameters on microstructural evolution

The effect of deformation strain rate on the microstructure evolution characteristics has already discussed in Section 4.5.2 together with the DRX and DRV mechanism, so only the effects of deformation temperature (at the constant strain rate of 0.1 s^{-1}, deformation degree of 70%) and degree (at the constant strain rate of 0.1 s^{-1}, temperature of 900 °C, 1000 °C and 1050 °C) will be analysed and discussed in this section.

4.6.1 Effect of deformation temperature

Figure 4.26 shows the optical and SEM microstructures of the deformed PM Ti-5553 alloy subjected to various temperatures at the strain rate of 0.1 s^{-1} in (α+β) region (below 975 °C). It can be seen in the microstructures of the alloy deformed at 700 °C and 800 °C (Figure 4.26a-b), a large amount of α phase in the form of precipitation bands is distributed unevenly in the β matrix. Meanwhile, an apparent flow localization band can be clearly observed in the macrostructure of the 800 °C deformed specimen (Figure 4.26c). These characteristics reveal the dominated deformation mechanisms are flow localization and dynamic morphology change of the α precipitates at the temperature of 700 °C and 800 °C.

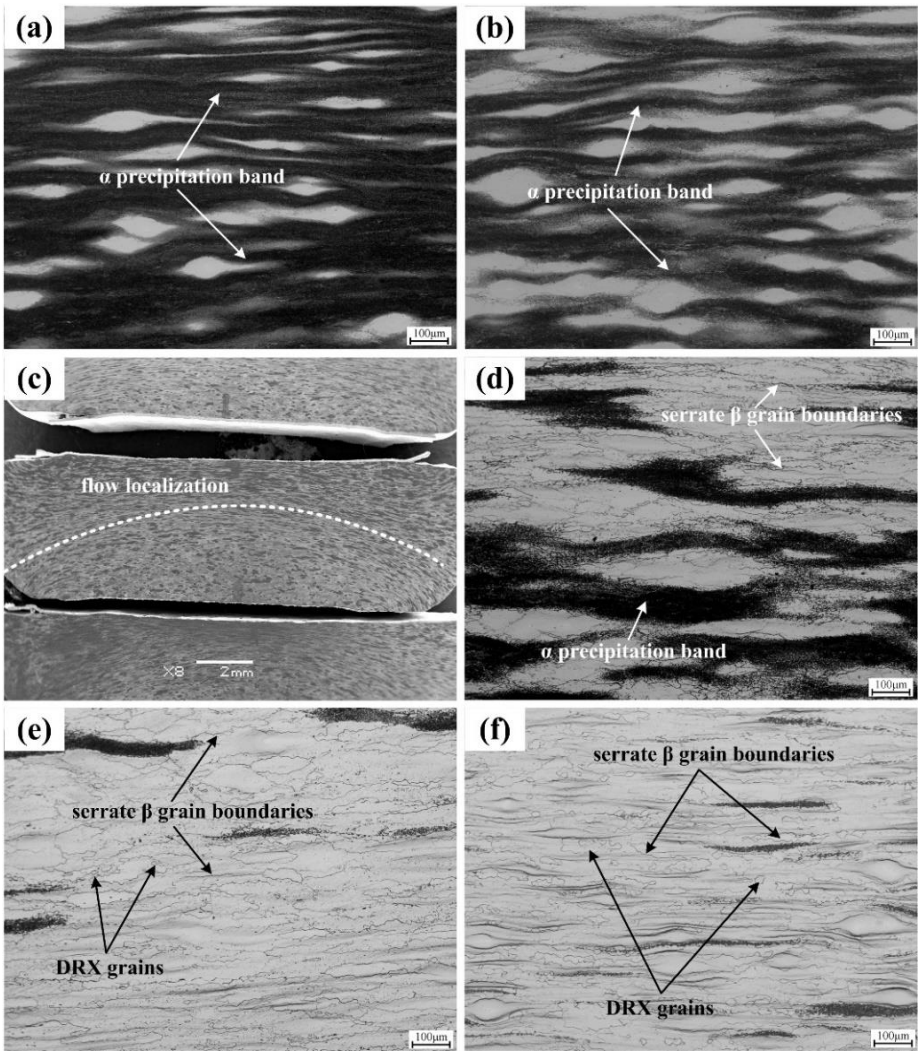

Figure 4.26 Optical and SEM images showing the microstructure of the deformed PM Ti-5553 alloy subjected to various temperatures at the strain rate of 0.1 s^{-1} in (α+β) region: (a) 700 °C; (b)-(c) 800 °C; (d) 850 °C; (e) 900 °C; (f) 950 °C. The deformation height reduction is 70%.

With increasing the deformation temperature to 850 °C (Figure 4.26d), elongated β grains with serrated grain boundaries and uneven α precipitation bands can be observed in the microstructure of the alloy, disclosing the dominated deformation mechanism is a combination of DRV and dynamic α morphology change under these conditions. Further increasing the deformation temperature to 900 °C and 950 °C (Figure 4.26e-f), some small equiaxed grains are visible at the serrated grain boundaries in the microstructures, indicating the occurrence of both DRV and DRX at these two conditions. Moreover, the size and proportion of the recrystallized grains increase and the amount of α precipitates decreases with increasing the deformation temperature.

Figure 4.27 shows the optical microstructures of the deformed PM Ti-5553 alloy subjected to various temperatures at the strain rate of 0.1 s^{-1} in β region (above 975 °C). In Figure 4.27a, a large number of equiaxed grains accompanied by some serrated grain boundaries can be clearly observed in the microstructure of the alloy deformed at 1000 °C. These features disclose that DRX and partial DRV become the dominated deformation mechanisms at this temperature. However, the DRX grains disappear from the alloy suddenly when the deformation temperature goes up to 1050 ℃-1150 °C (Figure 4.27b-d), while the microstructures are covered by coarsened grains with serrated and irregular grain boundaries at these conditions.

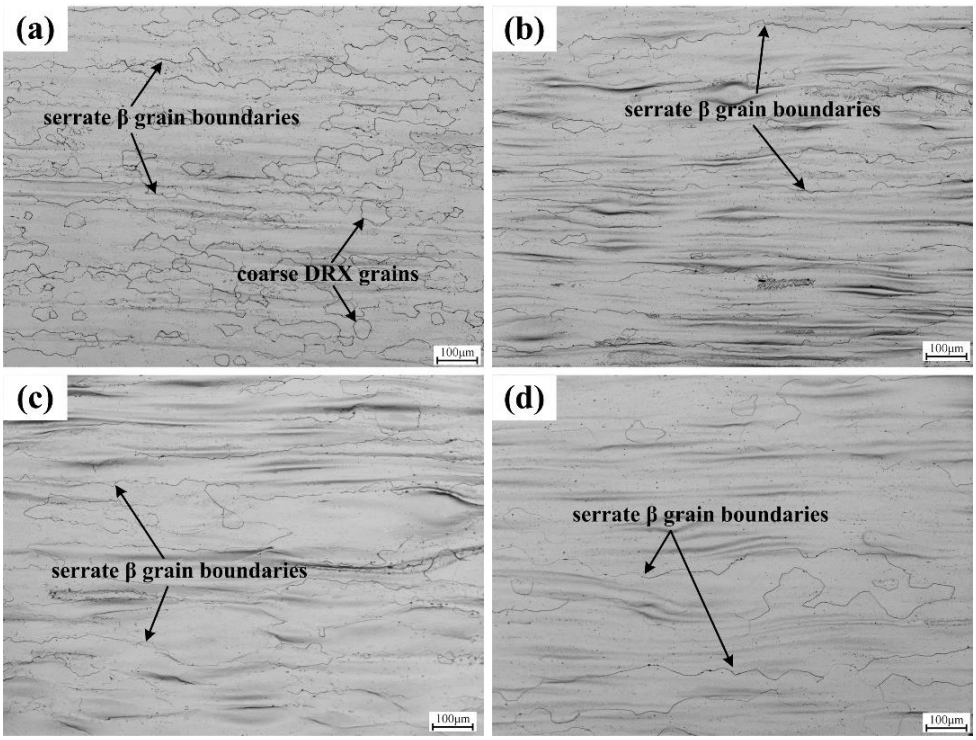

Figure 4.27 Optical images showing the microstructure of the deformed PM Ti-5553 alloy subjected to various temperatures at the strain rate of 0.1 s^{-1} in β region: (a) 1000 °C; (b) 1050 °C; (c) 1100°C; (d) 1150 °C. The deformation height reduction is 70%.

Similar to the result in Section 4.5, these results demonstrate that the process of DRX of the alloy is impeded at relatively high temperatures, and DRV becomes the only dominated deformation mechanism at 1050 °C-1150 ℃. The elimination of DRX phenomena at the high temperatures can be attributed to the relatively high stacking fault energy (SFE) of titanium alloys, as discussed in Section 4.5.3.

4.6.2 Effect of deformation degree and dynamic phase transformation

Figure 4.28 shows the optical microstructures of the deformed PM Ti-5553 alloy subjected to various temperatures and deformation degrees at the strain rate of 0.1 s^{-1} to reveal the effect of the deformation degree on the microstructure evolution features of the alloy.

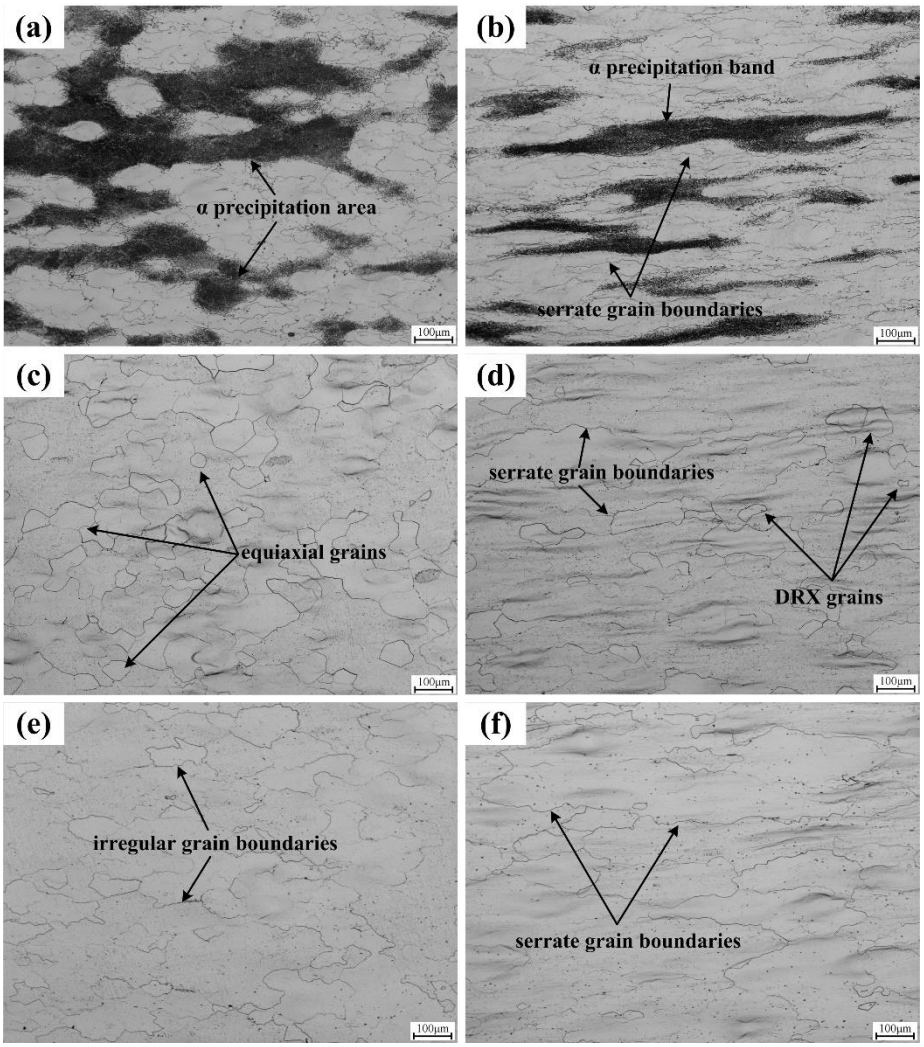

Figure 4.28 Optical images showing the microstructure of the deformed PM Ti-5553 alloy subjected to various temperatures and deformation degrees at the strain rate of 0.1 s^{-1}: (a) 900 °C/30%; (b) 900 °C/50%; (c) 1000 °C/30%; (d) 1000 °C/50%; (e) 1100 °C/30%; (f) 1100 °C/50%.

In Figure 4.28a, the majority of the β grains have retained the initial equiaxed shape and a large proportion of α precipitates can be found in the microstructure of the alloy deformed at 900 °C and the deformation degree of 30%. With increasing the deformation degree to 50% (Figure 4.28b) and 70% (Figure 4.26e), the grain boundaries become more and more serrated, while the proportion of α phase become less and less at 900 °C. As for the deformation at 1000 °C, the β grains are

only slightly compressed in the 30% deformed specimen (Figure 4.28c), and no DRV/DRX characteristics can be found in the microstructure. Whereas, small newly-formed equiaxed DRX grains can be clearly observed near grain boundaries at the 50% (Figure 4.28d) and 70% (Figure 4.27a) deformed specimens at 1000 °C, with the combinations of DRV features (serrated grain boundaries). Particularly, the size and the amount of the DRX grains are much bigger and larger in the 70% deformed specimen than those in the 50% deformed specimen at 1000 °C. In terms of the effect of the deformation degree at high temperature of 1100 °C, the β grains and their boundaries become more and more elongated and serrated when the deformation degree increases from 30% (Figure 4.28e) to 50% (Figure 4.28f) and 70% (Figure 4.27c), indicating the process of DRV can be enhanced with increasing deformation degree.

These observation results indicate that the DRV and DRX mechanisms are more promoted and encouraged at higher deformation degrees, and these two deformation mechanisms are difficult activate at the low deformation degree of 30%. Furthermore, the reduced proportion of α precipitates with the growing deformation degree of the alloy compressed at 900 °C and the continuously decreasing proportion of α precipitates in the materials with the increasing deformation temperature also illustrate the presence of the dynamic α→β phase transformation during the hot deformation of the alloy in (α+β) region. The higher deformation degree of the materials can provide higher external distortion energy and then promote the thermal diffusion process. Hereinafter, the dynamic α→β phase transformation is enabled at the temperatures below the measured β transformation temperature (975 °C).

4.7 Discussion

In the previous sections in this chapter, varying deformation mechanisms are characterized and disclosed at different conditions including DRV, DRX, dynamic phase globularization and flow localization, among which DRV and DRX are the most important and common softening mechanisms during the stable-state processing of the materials. Thus, in this discussion section, the detailed and specific DRX and DRV mechanisms are further characterized and analysed in depth.

4.7.1 Dynamic recrystallization mechanism and detailed process

DRX occurs in metallic materials during hot processing when the critical conditions (temperature, time, deformation degree) are met. During this process, the dislocation and distortion energy are significantly consumed, which cannot be addressed by DRV. There are mainly three common DRX mechanisms found in metallic materials according to previous researchers: discontinuous dynamic recrystallization (DDRX), continuous dynamic recrystallization (CDRX) and geometric dynamic recrystallization (GDRX) [48]. The specific DRX mechanism of the deforming materials is determined by the situation of the dislocation movement which can be related to the chemical composition, stacking fault energy, processing condition and starting microstructure of the material [49]. As the deformation and the DRX processes can be proceeded concurrently, the newly-formed DRX grains can also be further deformed and experience a second-round DRX when the critical conditions are met again.

In order to determine the DRX mechanism of β phase during hot deformation, EBSD analysis is carried out to collect the grain boundary information for the PM Ti-5553 alloy deformed at 950 °C and different strain rates, and the detailed results are shown in Figure 4.29. The high angle grain boundaries (HAGBs, $\theta > 15°$) and low angle grain boundaries (LAGBs, $\theta < 15°$) are highlighted using the solid black and green coloured lines, respectively. Moreover, the grain boundary misorientation angle charts at the corresponding conditions are exhibited in Figure 4.30 to demonstrate the detailed value and distribution of the grain boundary misorientation angle.

It can be seen in Figure 4.29a that the HAGBs of newly formed DRX grains are initiated at the prior serrated β grain boundaries for the alloy deformed at 1 s^{-1}, and the prior β grains are consisted of abundant LAGBs. With decreasing strain rate to 0.1 s^{-1}, the equiaxed DRX grains with HAGBs are more visible, and the amount of prior LAGBs is decreased correspondingly (Figure 4.29b). The DRX grains grow coarse when the alloy is deformed at 0.01 s^{-1}, and its grain boundaries are almost completely consisted of HAGBs, as shown in Figure 4.29c. With further decreasing the strain rate to 0.001 s^{-1} (Figure 4.29d), the DRX grains with HAGBs are significantly coarsened comparing to the PM Ti-5553 alloy deformed at other

conditions, even some of the DRX grains become irregularly shaped and new serrated grains with LAGBs form inside the coarse DRX grains.

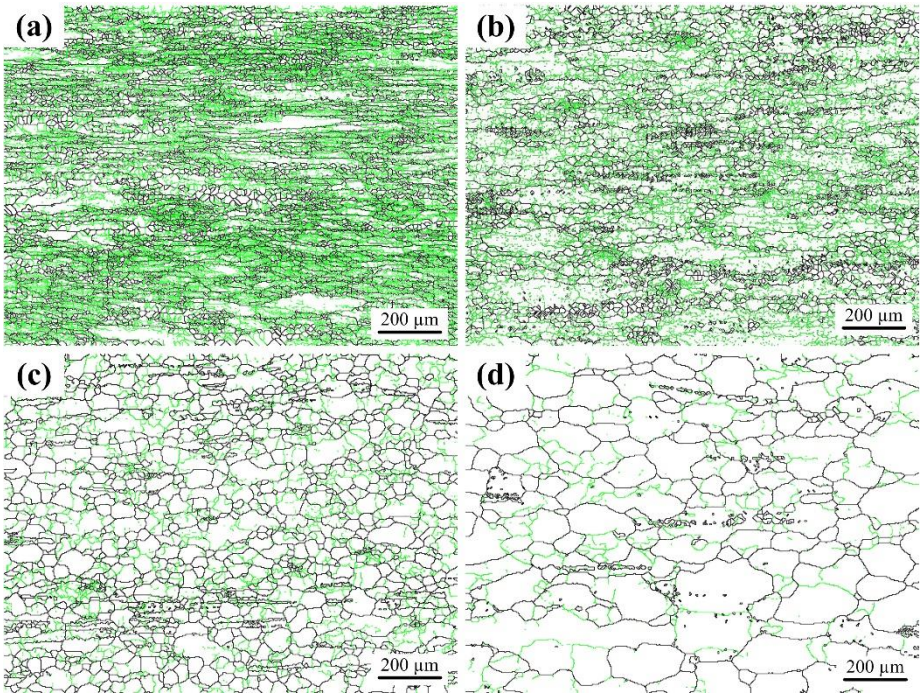

Figure 4.29 EBSD grain boundary maps of PM Ti-5553 alloy deformed at 950 °C: (a) 1 s^{-1}; (b) 0.1 s^{-1}; (c) 0.01 s^{-1}; (d) 0.001 s^{-1}.

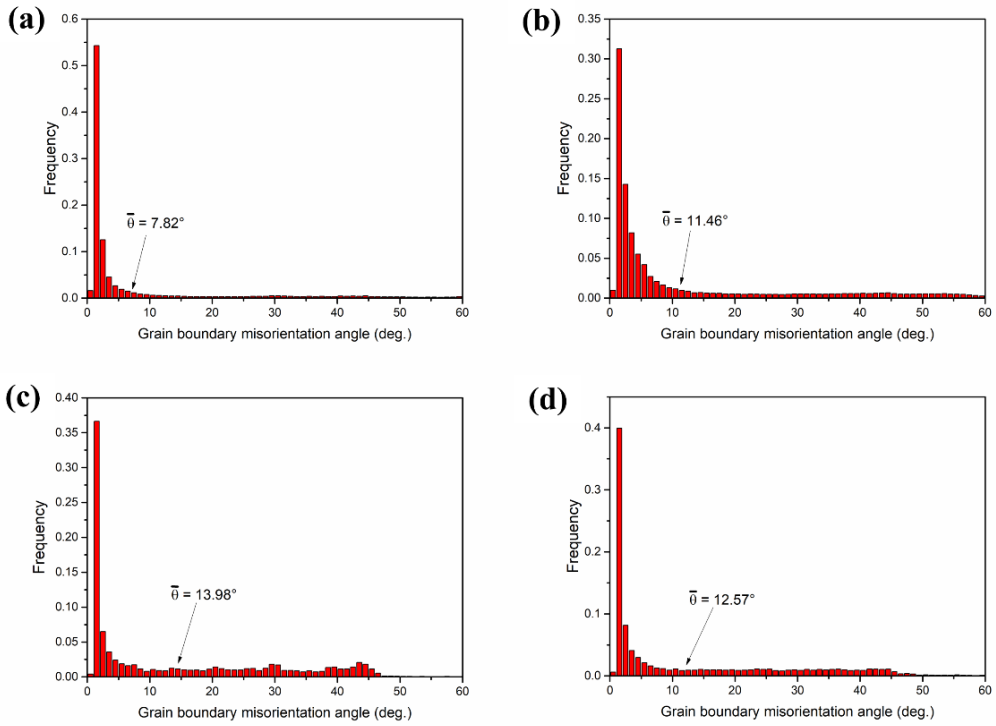

Figure 4.30 EBSD grain boundary misorientation angle distribution chart of PM Ti-5553 alloy deformed at 950 °C: (a) 1 s^{-1}; (b) 0.1 s^{-1}; (c) 0.01 s^{-1}; (d) 0.001 s^{-1}.

Meanwhile, the grain boundary misorientation angle charts suggest good correspondence with the maps. As shown in Figure 4.30, the proportion of the

LAGBs increases from the deformation at 1 s^{-1}, 0.1 s^{-1} and 0.01 s^{-1} with the average grain boundary misorientation angle of 7.82°, 11.46° and 13.98°. However, at the deformation of 0.001 s^{-1}, the average grain boundary misorientation angle begins to reduce with the value of 12.57°. These statistics results confirm the observation in the grain boundary map that the degree of DRX increases from 1 s^{-1} to 0.01 s^{-1}, and the well-developed DRX grains are further deformed at 0.001 s^{-1}.

In addition, representative TEM microstructures of the PM Ti-5553 alloy deformed at 950 °C and different strain rates are shown in Figure 4.31. The DRX nucleus appears at the triple-junction grain boundary and has low dislocation density for the alloy deformed at 1 s^{-1}, and the dislocation pile-up and dislocation wall surround the DRX nucleus (Figure 4.31a). This reveals that the lattice distortion is consumed and the dislocation density is reduced by the DRX nucleation process. An obvious DRX grain is formed at the initial β grain boundary, as shown in Figure 4.31b (0.01 s^{-1}), no obvious dislocation can be seen inside the DRX grain or the surrounding β grains. It can see in Figure 4.31c that both sub-grains and DRX grain with relatively high dislocation density are obvious for the alloy deformed at 0.001 s^{-1}. This confirms that the DRX grains grow with decreasing the strain rate and the DRX grains also experience post-deformation and subsequent DRV.

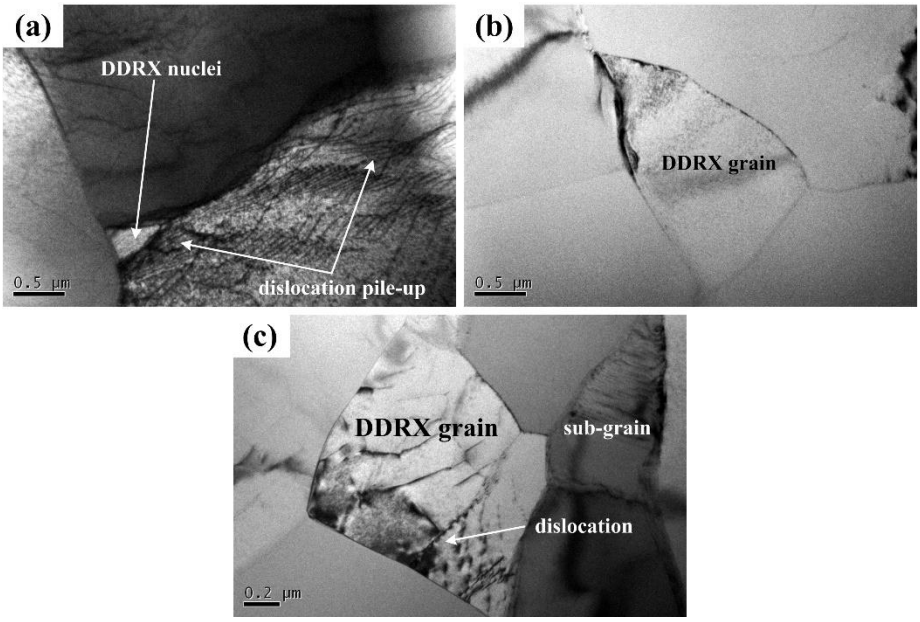

Figure 4.31 TEM microstructures of PM Ti-5553 alloy deformed at 950 °C: (a) 1 s^{-1}; (b) 0.01 s^{-1}; (c) 0.001 s^{-1}.

The discontinuous dynamic recrystallization (DDRX) grains always initiate at the prior grain boundaries due to the higher strain gradients, and their HAGBs always expand and migrate along the dislocation density gradient by absorbing the surrounding sub-structures and dislocations [50-52]. Thus, according to the above EBSD analysis and TEM microstructure observation, we can speculate that the DRX process for the PM Ti-5553 alloy processed at the medium temperature is controlled by DDRX mechanism.

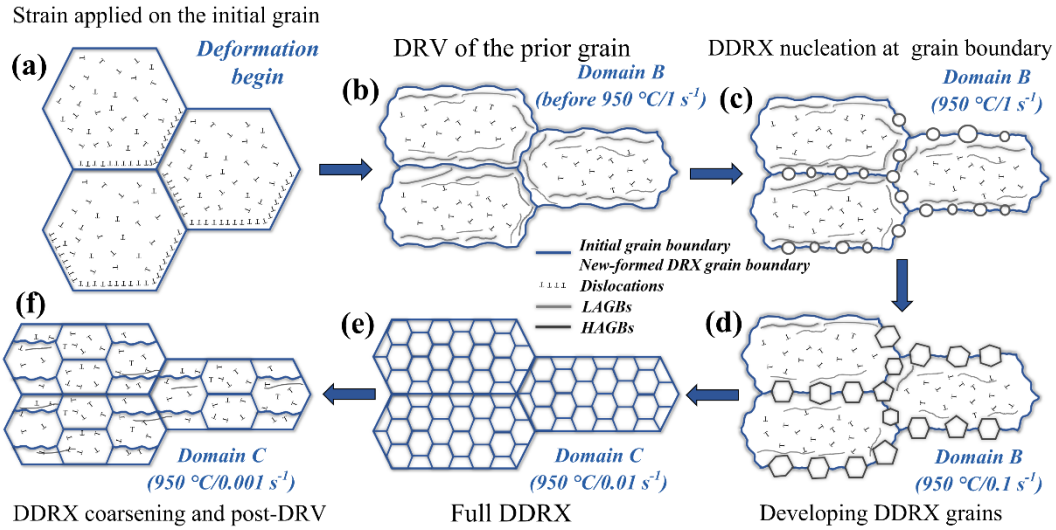

Figure 4.32 Schematic diagram illustrating the DDRX mechanism of PM Ti-5553 alloy during hot processing at 950 °C.

The schematic diagram, as shown in Figure 4.32, illustrates how the DDRX progresses for the hot processing of PM Ti-5553 in Domains B and C. The deformation initially happens in the prior grains as the hot processing begins, and strain concentrates at the grain boundaries (Figure 4.32a). Preliminary DRV of the prior grain occurs as the deformation is further progressed (Figure 4.32b), and this provides enough dislocation density, sub-structures (LAGBs) and distortion energy near the prior grain boundaries to promote the nucleation of the recrystallization grains (Figure 4.32c), which is confirmed by the TEM microstructure shown in Figure 4.31a. The HAGBs of DDRX nuclei start to migrate and extend, as illustrated in Figure 4.32d, because the surrounding dislocations and LAGBs are eliminated in the process of lower strain rate deformation (950 °C/0.1 s^{-1}), in which there is enough time for dislocations to be continuously consumed and/or generated [45, 53]. Subsequently, the microstructure is replaced by new and fine DDRX grains with expanded HAGBs due to consecutive growth of the DDRX nuclei (950 °C/0.01 s^{-1}, Figure 4.32e). Lastly, even the newly formed DDRX grains may

experience further deformation to form the elongated grains with serrated grain boundaries and LAGBs inside as the deformation strain rate is further reduced (950 °C/0.001 s^{-1}, Figure 4.32f).

4.7.2 Dynamic recovery mechanism and detailed process

As is discussed in the previous sections, DRV mechanisms are characterized and found in the deformed PM alloy at both low temperature (850 °C to 950 °C) and high temperature (1050 °C to 1150 °C). However, the specific DRV mechanism is highly dependent on the temperature, which can be different at the temperatures in (α+β) region, near the β transformation temperature (975 °C) and in β region. Figure 4.33 shows the optical DRV microstructures of the deformed PM Ti-5553 alloy at 850 °C/ 0.01 s^{-1}, 1000 °C/ 0.01 s^{-1} and 1100 °C/ 0.01 s^{-1}. Serrated grain boundaries can be observed in all microstructures, while the grains grow coarser with increasing temperature with widened grain boundaries. These results confirm that DRV happens at all of these conditions.

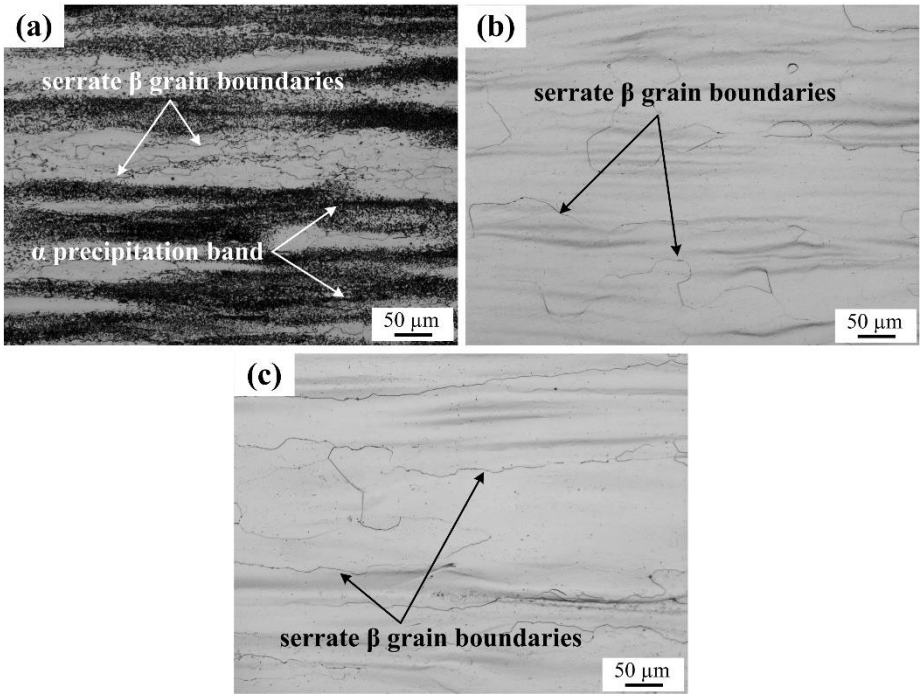

Figure 4.33 Optical images showing the DRV microstructures of the deformed PM Ti-5553 alloy subjected to various temperatures at the strain rate of 0.01 s^{-1}: (a) 850 °C; (b) 1000 °C; (c) 1100 °C.

In order to uncover the detailed and specific DRV mechanisms, TEM examinations were conducted at the above-mentioned conditions. As shown in Figure 4.34a-c, a large number of dense dislocations are seriously tangled against the grain

boundaries and some of them are assembled to form a new sub-grain boundary with a short length at the temperature of 850 °C. When the temperature comes to 1000 °C (Figure 4.34d-f), the dislocation density reduces obviously in the microstructure, many of the dislocations are assembled as sub-grain boundary and some dislocation tangles can also be observed as the predecessor of the sub-grain boundary. Further increasing the temperature to 1100 °C, as shown in Figure 4.34g-i, only a small amount of dislocations are observed and almost all the dislocations have been arranged as dislocation walls (polygonization structures) and clear sub-grain boundaries.

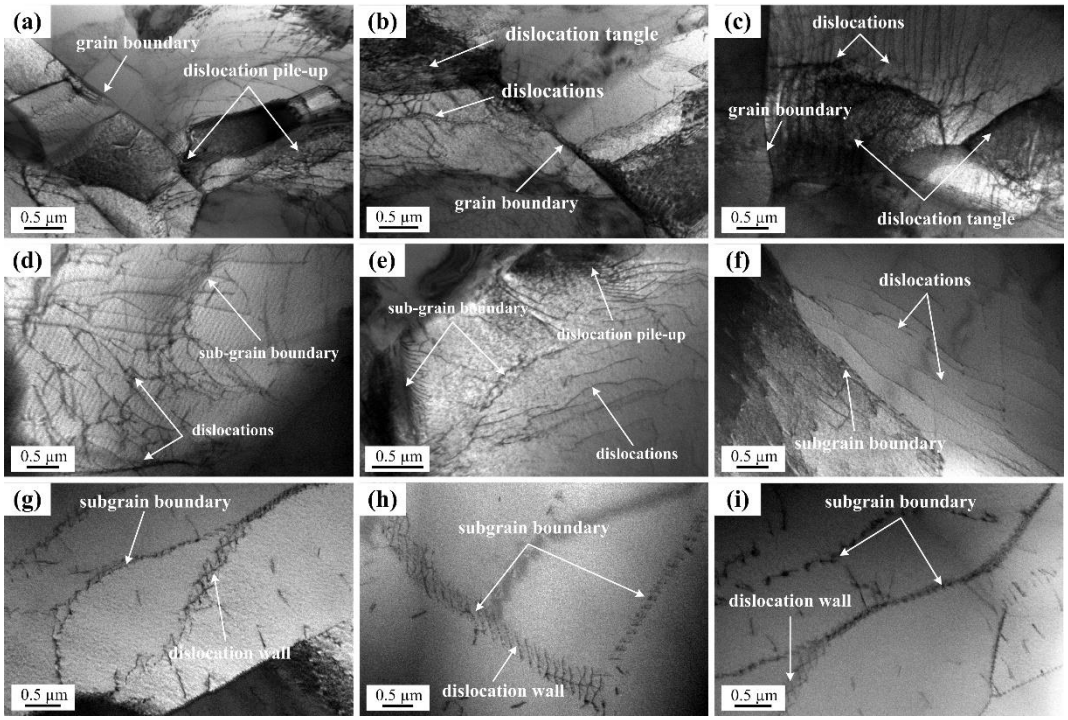

Figure 4.34 TEM microstructures of the deformed PM Ti-5553 alloy subjected to various temperatures at the strain rate of 0.01 s^{-1}: (a)-(c) 850 °C; (d)-(f) 1000 °C; (g)-(i) 1100 °C.

During the hot processing of the metallic materials at the specific conditions, when DRV occurs, dislocation multiplication and accumulation are promoted due to the deformation together with the rearrangement (gliding, climbing, reaction) of the dislocation enabled by thermal activation effect [54, 55]. The sub-grains (with LAGBs) are formed and extended inside the prior grain based on the dislocation structure. Meanwhile, the prior grains are obviously elongated and their boundaries become irregular and serrated due to the local migration in the microscopic-scale.

The different DRV mechanisms in the PM Ti-5553 alloy revealed in this section can be mainly attributed to the different rates of the dislocation movement and grain growth at various temperatures. Figure 4.35 shows the schematic diagram demonstrating three DRV processes at different conditions. When the deformation is performed at 850 °C/0.01 s^{-1} (Figure 4.35a), the dislocation density is high and the dislocation movement is slow, which leads to serious dislocation pile-up and small-size sub-grains with short LAGBs. Dislocation slip and climb are enhanced when temperature increases to 1000 °C (Figure 4.35b), resulting in the weakened dislocation accumulation and longer LAGBs. When the alloy is deformed at a high temperature of 1100 °C (Figure 4.35c), the dislocation movement and rearrangement are significantly thermally-accelerated, and the large-size sub-grains with long LAGBs are formed accordingly with the severely coarsened prior grains.

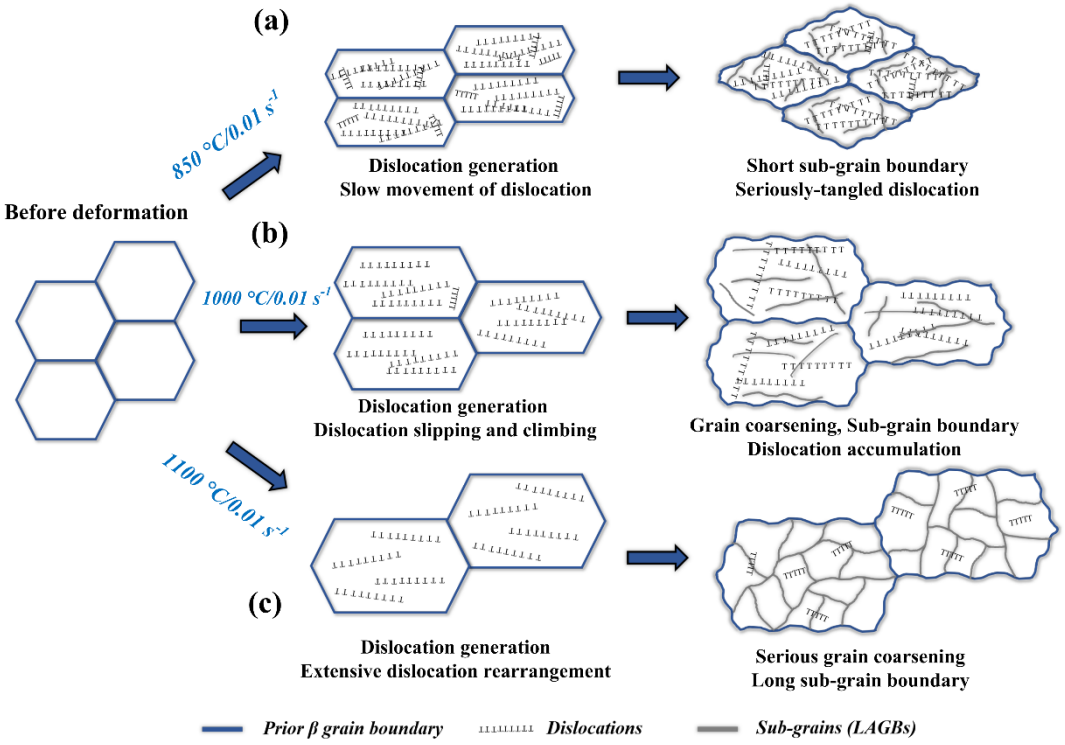

Figure 4.35 Schematic diagram illustrating the DRV mechanism of PM Ti-5553 alloy during hot processing at various temperatures: (a) 850 °C; (b) 1000 °C; (c) 1100 °C.

4.8 Summary

In this chapter, the hot deformation behaviour of as-consolidated PM Ti-5553 alloy was characterized and discussed comprehensively. The constitutive relationship and hot processing map were established successfully to evaluated the hot workability of the alloy. The underlying deformation mechanisms in each

processing region were analyzed and determined, especially the processes of dynamic recovery and dynamic recrystallization. Furthermore, the effects of processing parameters on the flow curves and microstructure were also investigated. Following bullet points can be summarized from the substantial results and intensive discussion:

(1) The flow stress of PM Ti-5553 alloy is primarily affected by the strain rate and deformation temperature, and it is increased with decreasing the deformation temperature and increasing the strain rate, and vice versa.
(2) The constitutive equations are established at the temperature of 700 °C to 1150 °C and the deformation activation energy is 371.65 kJ/mol in (α+β) region and 226.94 kJ/mol in β region, respectively.
(3) Four domains are identified in the hot processing map of PM Ti-5553 alloy, which are: the temperature between 800 °C and 900 °C and strain rate of 0.001 s^{-1} (Domain A); the temperature of about 950 °C and strain rate of 0.1 s^{-1} (Domain B); the temperature of about 950 °C and strain rate of 0.001 s^{-1} (Domain C); and the temperature above the β transformation temperature and strain rate of 0.01 s^{-1} (Domain D). The corresponding deformation mechanisms are dominated by α phase globularization and superplasticity (Domain A); a combination of DRV and DDRX nucleation (Domain B); complete DDRX and DDRX growth (Domain C); and DRV (Domain D).
(4) The optimal hot processing region is expanded and the process of DRV and DDRX is promoted with increasing the deformation degree. Unstable deformation happens when the deformation temperature is lower than 1025 °C and the strain rate is higher than 1 s^{-1}. Flow instability is attributed to flow localizations, and the flow instability becomes more serious as decreasing the deformation temperature and increasing the strain rate.
(5) The PM Ti-5553 alloy has a wider processing window and lower deformation resistance than those of the IM Ti-5553 alloys. The optimized hot processing window for the PM Ti-5553 alloy is at the medium deformation temperature (between 900 °C to 1050 °C) and moderate/moderate-low strain rates (less than 1 s^{-1}) with large plastic deformation degree (at least 70%). In addition, the processing condition of 950 °C/0.01 s^{-1} could be the potential "best" one, due to the occurrence of extensive DDRX to produce fine and homogeneous DRX grains dispersed in the microstructure.

(6) Dynamic α precipitation is prominent during the hot working of the PM Ti-5553 alloy processed in (α+β) region and the region near the β transformation temperature, which can also be enhanced by increasing the deformation degree.

Reference

[1] Y.C. Zhu, W.D. Zeng, J.L. Liu, Y.Q. Zhao, Y.G. Zhou, H.Q. Yu, Effect of processing parameters on the hot deformation behavior of as-cast TC21 titanium alloy, Mater. Des. 33 (2012) 264-272.

[2] T. Seshacharyulu, S.C. Medeiros, W.G. Frazier, Y.V.R.K. Prasad, Hot working of commercial Ti-6Al-4V with an equiaxed α-β microstructure: materials modeling considerations, Mater. Sci. Eng. A 284 (2000) 184-194.

[3] T. Seshacharyulu, S.C. Medeiros, W.G. Frazier, Y.V.R.K. Prasad, Unstable flow during supratransus working of Ti-6Al-4V, Mater. Lett. 47 (2001) 133-139.

[4] K.X. Wang, W.D. Zeng, Y.Q. Zhao, Y.J. Lai, Y.G. Zhou, Hot working of Ti-17 titanium alloy with lamellar starting structure using 3-D processing maps, J. Mater. Sci. 45 (2010) 5883-5891.

[5] J.K. Fan, H.C. Kou, M.J. Lai, B. Tang, H. Chang, J.S. Li, Characterization of hot deformation behavior of a new near beta titanium alloy: Ti-7333, Mater. Des. 49 (2013) 945-952.

[6] X.F. Bai, Y.Q. Zhao, W.D. Zeng, Z.Q. Jia, Y.S. Zhang, Characterization of hot deformation behavior of a biomedical titanium alloy TLM, Mater. Sci. Eng. A 598 (2014) 236-243.

[7] Y. Zhu, W. Zeng, F. Feng, Y. Sun, Y. Han, Y. Zhou, Characterization of hot deformation behavior of as-cast TC21 titanium alloy using processing map, Mater. Sci. Eng. A 528 (2011) 1757-1763.

[8] K. Hua, X.Y. Xue, H.C. Kou, J.K. Fan, B. Tang, J.S. Li, Characterization of hot deformation microstructure of a near beta titanium alloy Ti-5553, J. Alloys Compd. 615 (2014) 531-537.

[9] R.Q. Bao, X. Huang, C.X. Cao, Deformation behavior and mechanisms of Ti-1023 alloy, T. Nonferr. Metal. Soc. 16 (2006) 274-280.

[10] T.E. Mitchell, J.P. Hirth, A. Misra, Apparent activation energy and stress exponent in materials with a high Peierls stress, Acta Mater. 50 (2002) 1087-1093.

[11] Q.Y. Zhao, F. Yang, R. Torrens, L. Bolzoni, Evaluation of the hot workability and deformation mechanisms for a metastable beta titanium alloy prepared from powder, Mater. Charact. 149 (2019) 226-238.

[12] Y.C. Lin, Q.F. Li, Y.C. Xia, L.T. Li, A phenomenological constitutive model for high temperature flow stress prediction of Al-Cu-Mg alloy, Mater. Sci. Eng. A 534 (2012) 654-662.

[13] S. Waheed, Z.B. Zheng, D.S. Balint, F.P.E. Dunne, Microstructural effects on

strain rate and dwell sensitivity in dual-phase titanium alloys, Acta Mater. 162 (2019) 136-148.
[14] D. Banerjee, J.C. Williams, Perspectives on titanium science and technology, Acta Mater. 61 (2013) 844-879.
[15] H. Matsumoto, M. Kitamura, Y. Li, Y. Koizumi, A. Chiba, Hot forging characteristic of Ti-5Al-5V-5Mo-3Cr alloy with single metastable β microstructure, Mater. Sci. Eng. A 611 (2014) 337-344.
[16] K. Hua, X.Y. Xue, H.C. Kou, J.K. Fan, B. Tang, J.S. Li, High temperature deformation behaviour of Ti-5Al-5Mo-5V-3Cr during thermomechanical processing, Mater. Res. Innovations 18 (2014) S4-202-S204-206.
[17] S.L. Semiatin, T.R. Bieler, The effect of alpha platelet thickness on plastic flow during hot working of Ti-6Al-4V with a transformed microstructure, Acta Mater. 49 (2001) 3565-3573.
[18] S. Ankem, C.A. Greene, Recent developments in microstructure/property relationships of beta titanium alloys, Mater. Sci. Eng. A 263 (1999) 127-131.
[19] M.R. Barnett, A.G. Beer, D. Atwell, A. Oudin, Influence of grain size on hot working stresses and microstructures in Mg-3Al-1Zn, Scripta Mater. 51 (2004) 19-24.
[20] Y. Sun, Z.P. Wan, L.X. Hu, J.S. Ren, Characterization of hot processing parameters of powder metallurgy TiAl-based alloy based on the activation energy map and processing map, Mater. Des. 86 (2015) 922-932.
[21] M. Rezaee, A. Zarei, M. Ghambari, P. Dastranjy, E. Ghasemi, Flow characterization of a duplex near α Ti6242 alloy through interrelation of microstructural evolution, 3D activation energy map, and processing map, Adv. Eng. Mater. 18 (2016) 1075-1085.
[22] Z.J. Gronostajski, Development of constitutive equations of copper-silicon alloys, J. Mater. Process. Technol. 60 (1996) 621-627.
[23] M. Azarbarmas, M. Aghaie, J.M. Cabrera, J. Calvo, Microstructural evolution and constitutive equations of Inconel 718 alloy under quasi-static and quasi-dynamic conditions, Mater. Des. 94 (2016) 28-38.
[24] Y.Y. Dong, C.S. Zhang, G.Q. Zhao, Y.J. Guan, A.J. Gao, W.C. Sun, Constitutive equation and processing maps of an Al-Mg-Si aluminum alloy: Determination and application in simulating extrusion process of complex profiles, Mater. Des. 92 (2016) 983-997.
[25] F. Dyment, C.M. Libanati, Self-diffusion of Ti, Zr, and Hf in their hcp phases,

and diffusion of Nb95 in hcp Zr, J. Mater. Sci. 3 (1968) 349-359.
[26] J.F. Murdock, T.S. Lundy, E.E. Stansbury, Diffusion of Ti44 and V48 in titanium, Acta Metall. 12 (1964) 1033-1039.
[27] F. Warchomicka, C. Poletti, M. Stockinger, Study of the hot deformation behaviour in Ti-5Al-5Mo-5V-3Cr-1Zr, Mater. Sci. Eng. A 528 (2011) 8277-8285.
[28] H.Z. Zhao, L. Xiao, P. Ge, J. Sun, Z.P. Xi, Hot deformation behavior and processing maps of Ti-1300 alloy, Mater. Sci. Eng. A 604 (2014) 111-116.
[29] C.M. Sellars, W.J. McTegart, On the mechanism of hot deformation, Acta Metall. 14 (1966) 1136-1138.
[30] Y.V.R.K. Prasad, T. Seshacharyulu, Processing maps for hot working of titanium alloys, Mater. Sci. Eng. A 243 (1998) 82-88.
[31] Z. Wang, X.N. Wang, Z.S. Zhu, Characterization of high-temperature deformation behavior and processing map of TB17 titanium alloy, J. Alloys Compd. 692 (2017) 149-154.
[32] Y.F. Han, W.D. Zeng, Y.L. Qi, Y.Q. Zhao, Optimization of forging process parameters of Ti600 alloy by using processing map, Mater. Sci. Eng. A 529 (2011) 393-400.
[33] Y.V.R.K. Prasad, Processing maps: A status report, J. Mater. Eng. Perform. 12 (2003) 638-645.
[34] J.Q. Zhang, H.S. Di, H.T. Wang, K. Mao, T.J. Ma, Y. Cao, Hot deformation behavior of Ti-15-3 titanium alloy: a study using processing maps, activation energy map, and Zener-Hollomon parameter map, J. Mater. Sci. 47 (2012) 4000-4011.
[35] W.W. Peng, W.D. Zeng, Q.J. Wang, Q.Y. Zhao, H.G. Yu, Effect of processing parameters on hot deformation behavior and microstructural evolution during hot compression of as-cast Ti60 titanium alloy, Mater. Sci. Eng. A 593 (2014) 16-23.
[36] Y.V.R.K. Prasad, H.L. Gegel, S.M. Doraivelu, J.C. Malas, J.T. Morgan, K.A. Lark, D.R. Barker, Modeling of Dynamic Material Behavior in Hot Deformation - Forging of Ti-6242, Metall. Mater. Trans. A 15 (1984) 1883-1892.
[37] Y.V.R.K. Prasad, T. Seshacharyulu, Modelling of hot deformation for microstructural control, Int. Mater. Rev. 43 (1998) 243-258.
[38] S.V.S. Narayana Murty, B. Nageswara Rao, B.P. Kashyap, Instability criteria for hot deformation of materials, Int. Mater. Rev. 45 (2000) 15-26.
[39] S.F. Liu, M.Q. Li, J. Luo, Z. Yang, Deformation behavior in the isothermal compression of Ti-5Al-5Mo-5V-1Cr-1Fe alloy, Mater. Sci. Eng. A 589 (2014) 15-

22.
[40] M. Dikovits, C. Poletti, F. Warchomicka, Deformation mechanisms in the near-β titanium alloy Ti-55531, Metall. Mater. Trans. A 45 (2013) 1586-1596.
[41] H. Margolin, P. Cohen, Evolution of the equiaxed morphology of phases in Ti-6Al-4V, Titanium'80: Science and Technology 1 (1980) 1555-1561.
[42] I. Weiss, G.E. Welsch, F.H. Froes, D. Eylon, Mechanisms of microstructure refinement in Ti-6Al-4V alloy, Titanium Science and Technology 3 (1984) 1503-1510.
[43] L. Lapeire, J. Sidor, P. Verleysen, K. Verbeken, I. De Graeve, H. Terryn, L.A.I. Kestens, Texture comparison between room temperature rolled and cryogenically rolled pure copper, Acta Mater. 95 (2015) 224-235.
[44] A. Imandoust, C.D. Barrett, A.L. Oppedal, W.R. Whittington, Y. Paudel, H. El Kadiri, Nucleation and preferential growth mechanism of recrystallization texture in high purity binary magnesium-rare earth alloys, Acta Mater. 138 (2017) 27-41.
[45] W.W. Peng, W.D. Zeng, Q.J. Wang, H.G. Yu, Characterization of high-temperature deformation behavior of as-cast Ti60 titanium alloy using processing map, Mater. Sci. Eng. A 571 (2013) 116-122.
[46] Y.C. Lin, X.Y. Wu, X.M. Chen, J. Chen, D.X. Wen, J.L. Zhang, L.T. Li, EBSD study of a hot deformed nickel-based superalloy, J. Alloys Compd. 640 (2015) 101-113.
[47] P. Poelt, C. Sommitsch, S. Mitsche, M. Walter, Dynamic recrystallization of Ni-base alloys - Experimental results and comparisons with simulations, Mater. Sci. Eng. A 420 (2006) 306-314.
[48] K. Huang, R.E. Loge, A review of dynamic recrystallization phenomena in metallic materials, Mater. Des. 111 (2016) 548-574.
[49] Q. Zhao, F. Yang, R. Torrens, L. Bolzoni, Comparison of hot deformation behaviour and microstructural evolution for Ti-5Al-5V-5Mo-3Cr alloys prepared by powder metallurgy and ingot metallurgy approaches, Mater. Des. 169 (2019) 107682.
[50] H.T. Zhou, F.T. Kong, K. Wu, X.P. Wang, Y.Y. Chen, Hot pack rolling nearly lamellar Ti-44Al-8Nb-(W, B, Y) alloy with different rolling reductions: Lamellar colonies evolution and tensile properties, Mater. Des. 121 (2017) 202-212.
[51] C.K. Yan, A.H. Feng, S.J. Qu, G.J. Cao, J.L. Sun, J. Shen, D.L. Chen, Dynamic recrystallization of titanium: Effect of pre-activated twinning at cryogenic temperature, Acta Mater. 154 (2018) 311-324.

[52] X. Wang, L. Wang, L.S. Luo, X.D. Liu, Y.C. Tang, X.Z. Li, R.R. Chen, Y.Q. Su, J.J. Guo, H.Z. Fu, Hot deformation behavior and dynamic recrystallization of melt hydrogenated Ti-6Al-4V alloy, J. Alloys Compd. 728 (2017) 709-718.
[53] T. Sakai, A. Belyakov, R. Kaibyshev, H. Miura, J.J. Jonas, Dynamic and post-dynamic recrystallization under hot, cold and severe plastic deformation conditions, Prog. Mater. Sci. 60 (2014) 130-207.
[54] I. Weiss, S.L. Semiatin, Thermomechanical processing of beta titanium alloys - an overview, Mater. Sci. Eng. A 243 (1998) 46-65.
[55] Y.Q. Ning, X. Luo, H.Q. Liang, H.Z. Guo, J.L. Zhang, K. Tan, Competition between dynamic recovery and recrystallization during hot deformation for TC18 titanium alloy, Mater. Sci. Eng. A 635 (2015) 77-85.

5 Comparison of the hot deformation behaviour and mechanism of PM and IM Ti-5553 alloys

5.1 Introduction

*Partial contents (text and figures) in this chapter have been published in refereed journals:

1. **Qinyang Zhao**, Fei Yang, Rob Torrens, Leandro Bolzoni, Comparison of hot deformation behaviour and microstructural evolution for Ti-5Al-5V-5Mo-3Cr alloys prepared by powder metallurgy and ingot metallurgy approaches, ***Materials & Design***, 169 (2019) 107682.
2. **Qinyang Zhao**, Fei Yang, Rob Torrens, Leandro Bolzoni, Comparison of the cracking behavior of powder metallurgy and ingot metallurgy Ti-5Al-5Mo-5V-3Cr alloys during hot deformation, ***Materials***, 12 (2019) 457.

The hot working responses and underlying deformation mechanisms of metallic materials are highly dependent on the material manufacturing history, chemical composition and starting microstructure. However, there are seldom researches to contrast hot deformation behaviour and mechanisms between PM metallic materials and their IM counterparts, and no reports are available for PM and IM metastable beta titanium alloys in this regard.

To systematically compare the hot workability of PM and IM Ti-5553 alloy and identify their different response to hot working, the hot deformation behaviour and microstructural evolution of those two alloys were investigated, in this chapter, at a wide temperature range of 700 °C-1100 °C and strain rate of 0.001 s^{-1}-10 s^{-1}. The major differences in hot deformation behaviour and mechanisms for the two alloys were determined. The research undertaken in this chapter characterizes the hot deformation behaviour, provides informative instructions for hot processing of PM and IM Ti-5553 alloys and other metastable beta titanium alloys, and also reveals the discrepancies between PM and IM metallic alloys in hot working response and related underlying mechanisms.

5.2 Flow behaviour

5.2.1 True stress-true strain curves

The flow curves of PM and IM alloys compressed at 900 °C, 1000 °C and 1100 °C and various strain rates from 0.001 s^{-1} to 10 s^{-1} are shown in Figure 5.1. In general, the flow stress is first promptly increased to peak stress at the beginning of compression, and then drop to a certain value and remain at that value (referred to as steady-state) or the flow stress keeps continuing to decrease until the compression finished. The steady stages indicate that a balance between work hardening and dynamic softening (such as DRV, DRX, DαG) is achieved during the deformation at the corresponding conditions [1].

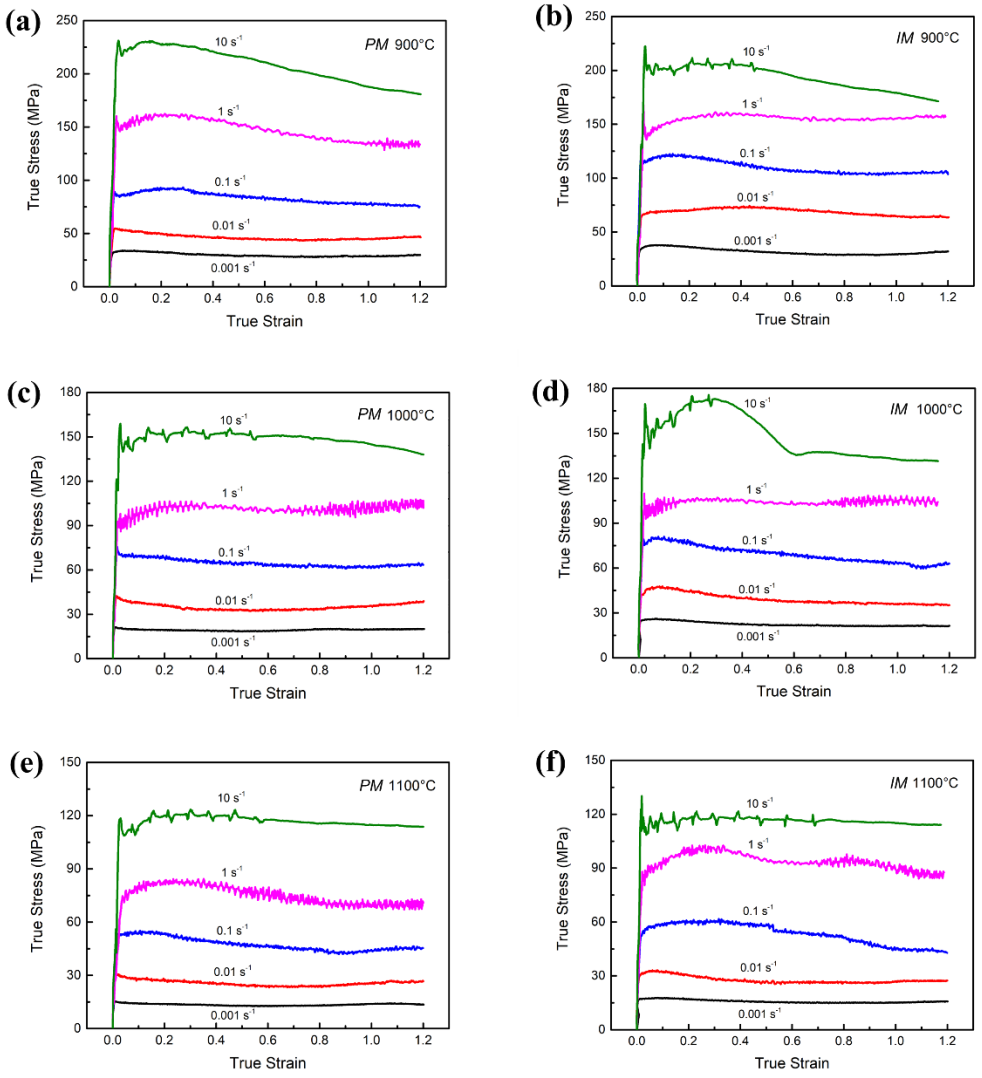

Figure 5.1 Typical true stress-true strain curves of Ti-5553 alloys at various temperatures and strain rates: (a) PM alloy, 900 °C; (b) IM alloy, 900 °C; (c) PM alloy, 1000 °C; (d) IM alloy, 1000 °C; (e) PM alloy, 1100 °C; (f) IM alloy, 1100 °C.

On the contrary, the continuously decreasing flow stress after yielding suggests that the adiabatic temperature rising (ATR) and/or flow instability are very significant when the alloy deforms at low temperatures (900 °C and 1000 °C) and high strain rates (1 s^{-1} and 10 s^{-1}). Both of the alloys show this continuously decreasing flow stress at the conditions of 900 °C/10 s^{-1}, but this tendency disappears when the PM alloy is deformed at the higher temperature of 1000 °C/10 s^{-1}. However, there is a significant flow stress-drop between the strain of 0.3 to 0.6 when the IM alloy is deformed at 1000 °C/10 s^{-1}, which suggests that the material is in a situation of severely unstable plastic flow (local material kinking, external cracking).

Typical DRX-type flow curves are observed in Figure 5.1a for PM alloy deformed at 900 °C/0.01 s^{-1}-1 s^{-1} and in Figure 5.1f for IM alloy deformed at 1100 °C/0.01 s^{-1}-1 s^{-1}. After the peak stress point, the stress keeps a gradually increasing trend for a while and then continuously dropped to the steady-state value. While, other curves almost display nearly the constant values immediately after the peak stress points, indicating that the dominated deformation mechanism at these conditions could be DRV or precipitation morphology change at these conditions [2].

Furthermore, similar to the PM alloy, the flow stress of IM alloy is also decreased with increasing the deformation temperature and decreasing the strain rate, which can be explained by the thermal kinetic energy of atoms and dislocation multiplication. From the above results, it can be deduced that the flow softening mode and the deformation mechanism of the two alloys deformed at varying conditions can be varied as well, which needs to be further confirmed by kinetic analysis and microstructural characterizations.

5.2.2 Flow stress values

Besides the differences in terms of the shape and flow softening mode of the flow curves of the two alloys, the gaps between the peak flow stress and steady-state stress of the two alloys at various conditions is also considerable. Figure 5.2 shows the variations of peak flow stress and steady-state stress (the flow stress at the true strain of 1.0) for PM and IM alloys deformed at 900 °C, 1000 °C and 1100 °C under different strain rates.

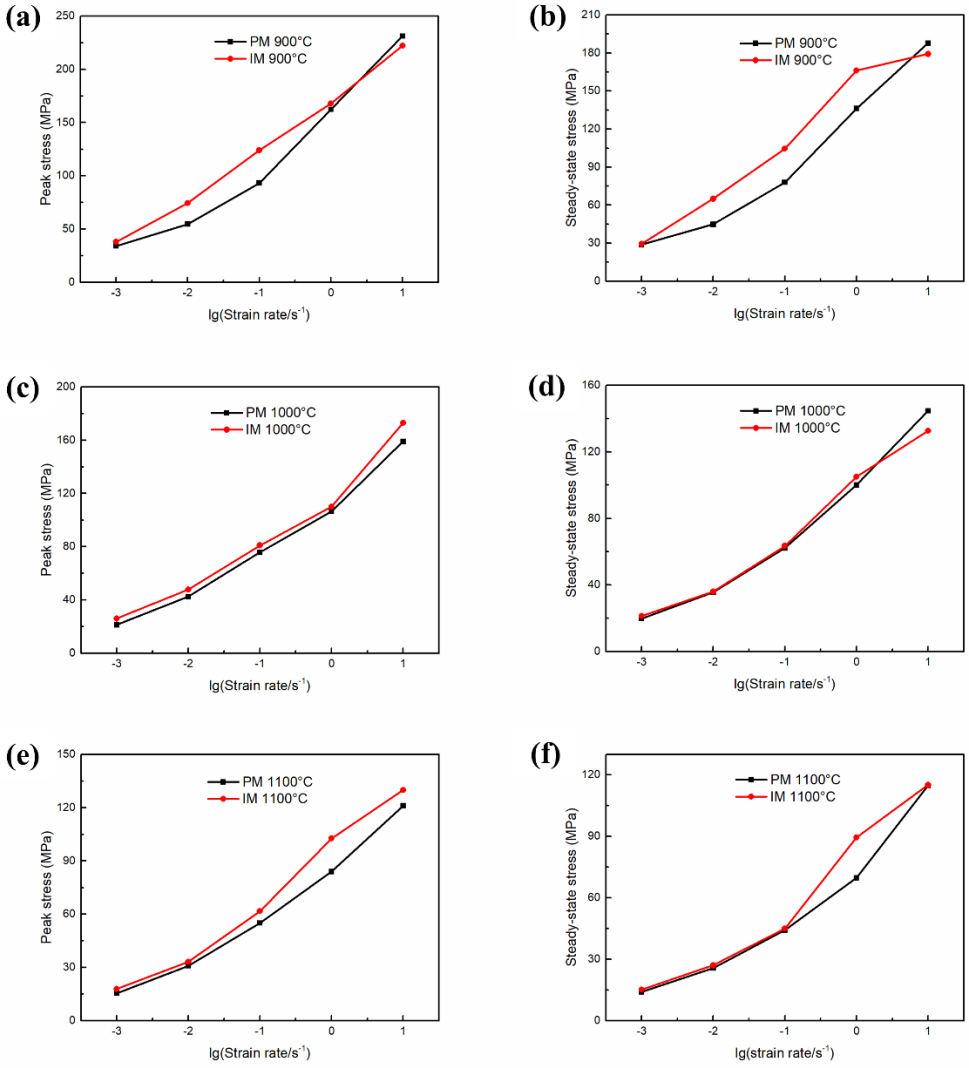

Figure 5.2 Comparisons of peak flow stress and steady-state stress (ε = 1.0) for PM and IM alloys deformed at various strain rates (0.001 s^{-1}-10 s^{-1}) under different temperatures: (a) peak flow stress at 900 °C; (b) steady-state stress at 900 °C; (c) peak flow stress at 1000 °C; (d) steady-state stress at 1000 °C; (e) peak flow stress at 1100 °C; (f) steady-state stress at 1100 °C.

First of all, it is clear that PM alloy has lower peak flow stresses and steady-state stresses than those of IM alloy under most of the conditions. Moreover, the gaps are larger when the alloys are deformed at 900 °C than 1000 °C and 1100 °C. However, these lower peak flow stress and steady-state stress of PM alloy disappear when the two alloys are deformed at the highest (10 s^{-1}) and lowest strain rates (0.001 s^{-1}).

The lower flow stress of PM alloy can be explained by its much finer initial grains and fewer precipitates in the starting materials that those of IM alloy. As is presented in Section 3.2, the IM alloy has coarse microstructure with the average grain size of 1000 μm, which is 10 times that of PM alloy with the average grain

size of 100 μm. The grains are able to glide along the grain boundaries during the hot deformation as a result of the viscous flow of grain boundaries [3-5], therefore, finer grain sizes result in a lower flow stress for PM alloy comparing to that of the IM alloy. Furthermore, the crystalline structure of β phase is body-centred cubic (BCC), in which deformation occurs more easily due there being more active slip systems than the α phase with close-packed hexagonal cubic structure (HCP), meaning the dislocations can glide and climb more easily in the PM Ti-5553 alloy rather than the IM Ti-5553 alloy [6, 7] (IM alloy has more α phase in the initial microstructure than PM alloy, as discussed in Section 3.2.2 and Section 3.3.3). The lower peak flow stress and steady-state stress of PM alloy demonstrate its lower hot-deformation resistance and better hot-workability than IM alloy at the corresponding conditions.

Table 5.1 Deformation time and total processing time of alloy specimens deformed at different strain rates (to the height reduction of 70%).

Strain rate (s^{-1})	Heating time (mins)	Deformation time (s)	Total time (s)
10	4	0.07	240.07
1	4	0.7	240.7
0.1	4	7	247
0.01	4	70	310
0.001	4	700	940

When the specimens are deformed at high deformation strain rate of 10 s^{-1}, the peak flow stress and steady-state stress gaps between the IM and PM alloys are eliminated because the dislocation movement and viscous flow of grain boundaries do not play dominated roles in such very short deformation time (the 10 s^{-1} deformation finished in only 0.1 seconds, as shown in Table 5.1), instead, the chemical composition of the alloys becomes the dominant factor affecting the flow stress due to the alloying strengthening effect. As is exhibited in Section 2.2.1, the actual measured composition of actual IM Ti-5553 alloy has higher alloying content than the PM Ti-5553 alloy, but the PM alloy has 0.28 wt.% more oxygen than the IM alloy. The better alloying strengthening effect of IM alloy than the PM alloy is counteracted some extent by the oxygen strengthening in the PM alloy, thus it leads to similar peak flow stress achieved for those two alloys at the deformation strain rate of 10 s^{-1}. However, the effects of the dislocation movement and grain size

become more and more significant with decreasing the strain rate, this is reflected by the enlarged gaps between the peak flow stress and steady-state stress of the PM and IM alloys.

For the deformation processed at the strain rate of 0.001 s^{-1}, the eliminations of peak flow stress and steady-state stress gaps between the IM and PM alloys can be mainly attributed to the long deformation time and the heating-induced grain coarsening of the two alloys. As shown in Table 5.1, the total heating and deformation times of the specimens deformed at the strain rates of 0.01 s^{-1}-10 s^{-1} are in the range of 240.07 s to 247 s. Nevertheless, the deformation at the strain rate of 0.001 s^{-1} has lasted for 940 s, which is much more than the 0.01 s^{-1}-10 s^{-1} specimens. The obvious longer deformation time can lead to the significant grain coarsening of the two alloys, especially at higher temperatures. The significant heating-induced grain coarsening at 0.001 s^{-1} will reduce the grain-size discrepancy of the two alloys and then undermine their flow stress gaps.

5.2.3 Discontinuous yielding phenomenon

As discussed in Section 4.2.1, discontinuous yielding phenomenon (DYP, characterized by the considerable yield drop after the peak stress point) is observed in PM alloy and is common in metastable beta titanium alloys. DYP always appears at the end of the initial work hardening stage, which is interesting and important for the hot deformation behaviour and processing of titanium alloys. This section will focus on the effect of deformation parameters and the comparison of DYP for PM and IM Ti-5553 alloys with underlying mechanisms.

Figure 5.3 shows the yield drop values after the peak stress of the PM and IM alloy deformed at the typical temperatures of 900 °C, 1000 °C and 1100 °C (no DYP observed at the temperature of 700 °C-850 °C), corresponding to Figure 5.1. The detailed stress drop values at each condition are indicated beside the curves. Moreover, the stress drop values at varying conditions are also exhibited in Table 5.2 to show the variation tendency of DYP more clearly.

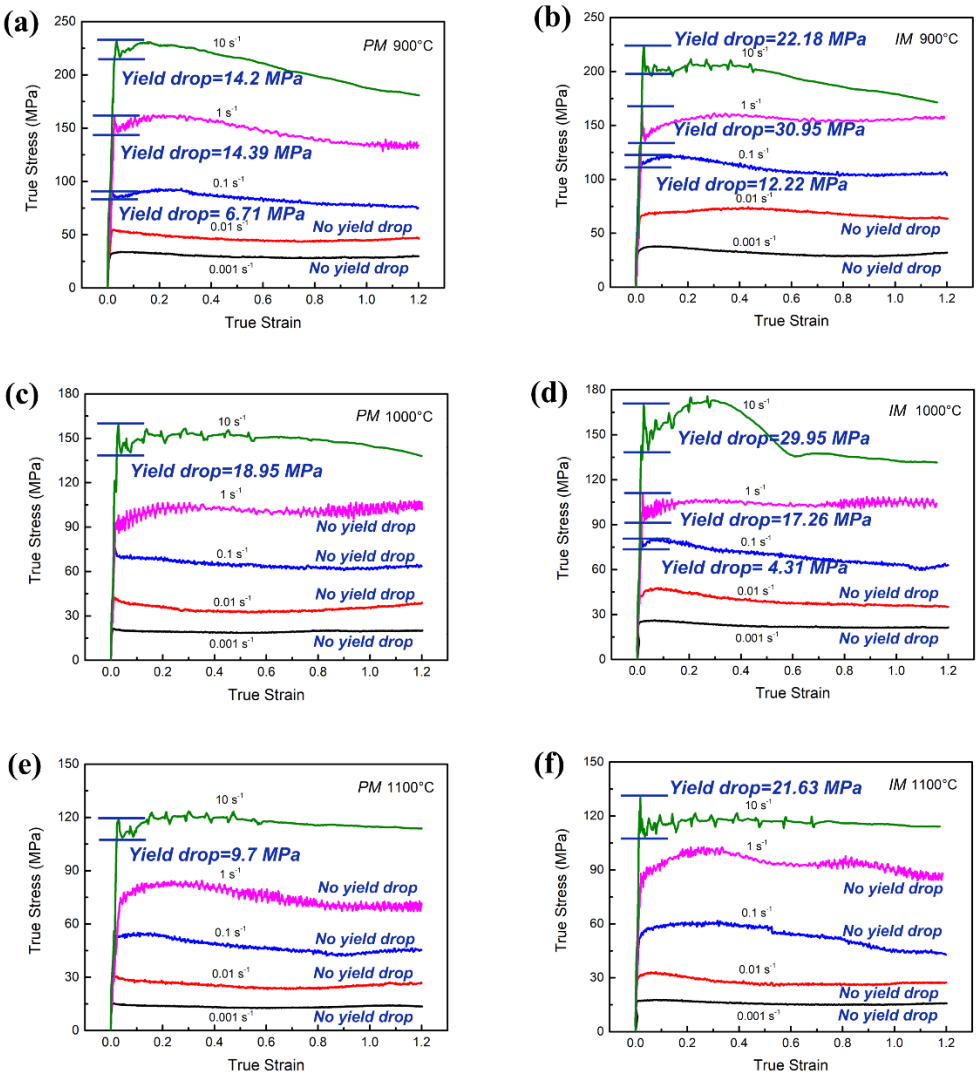

Figure 5.3 Typical true stress-true strain curves of Ti-5553 alloys at various temperatures and strain rates showing yield drop values after the peak stress: (a) PM alloy, 900 °C; (b) IM alloy, 900 °C; (c) PM alloy, 1000 °C; (d) IM alloy, 1000 °C; (e) PM alloy, 1100 °C; (f) IM alloy, 1100 °C.

Table 5.2 Detailed yield drop values of PM and IM alloys deformed at various conditions.

	900 °C		1000 °C		1100 °C	
	PM	IM	PM	IM	PM	IM
10 s^{-1}	14.20 MPa	22.18 MPa	18.95 MPa	29.95 MPa	9.7 MPa	21.63 MPa
1 s^{-1}	14.39 MPa	30.95 MPa	/	17.26 MPa	/	/
0.1 s^{-1}	6.71 MPa	12.22 MPa	/	4.31 MPa	/	/

* / indicates there is no DYP (0 MPa) at the specific condition. No DYP under any conditions was observed at 0.01 s^{-1} and 0.001 s^{-1} deformation.

From the curves and the table, it is clear that the magnitude of DYP varies with the deformation parameter and the discrepancy between PM and IM alloys is

considerable. Typically, in most of the relevant literature about titanium alloys, the DYP has a positive temperature and strain rate sensitivity of metallic materials [8-10]. That is to say, the DYP will be more obvious at elevated deformation temperature and strain rate. However, this tendency is not completely observed in the PM and IM alloy of this work. For the effect of strain rate, it is clear that the DYP is generally more obvious at high-strain-rate deformations rather than low-strain-rate deformations for both the two alloys at different temperatures. However, in terms of temperature, the two alloys show nearly negative temperature sensitivity. Obvious DYP can be observed at 0.1 s^{-1}-10 s^{-1} deformations when the temperature is 900 °C, while DYP is found only at 10 s^{-1} for the deformation at 1000 °C and 1100 °C, accompanied by diminished yield drop value as well.

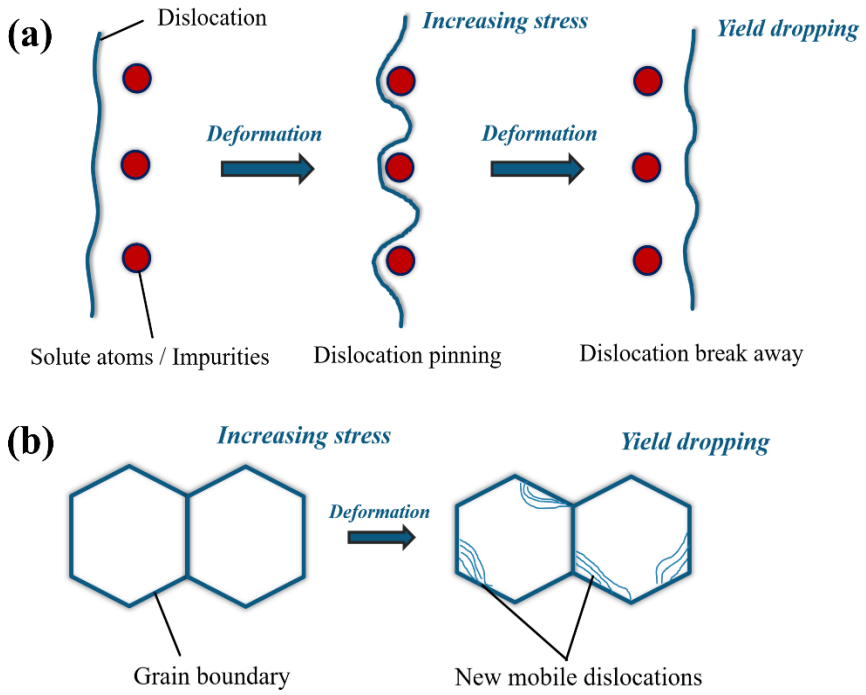

Figure 5.4 Schematic drawing of the developed discontinuous yielding phenomenon mechanisms of metallic materials during hot deformation: (a) static theory and (b) dynamic theory.

The occurrence of DYP can be mainly explained by two theories: (1) static theory (see Figure 5.4a), which associated with dislocation pinning and rebooting [10, 11]. In this theory, the dislocation movement is considered to be pinned by the solution atoms and/or impurities during hot deformation, and then loosen and rebooting of the dislocation from their pinning points are achieved when the external force reaches a certain critical value, which is reflected as the emergent yield drop in the flow curves. (2) dynamic theory (see Figure 5.4b), which associated with the sudden

generation of mobile dislocations from the grain boundary [2, 12]. In this theory, the dislocation density is suddenly increased when the hot deformation is processed to a critical degree, followed by the dislocations spreading to the grain interior with increasing of strain. Although the static theory has been used to explain DYP in some titanium alloys [10], however, it is hard to interpret the effect of deformation temperature and strain rate on DYP properly for the two alloys using this theory. Moreover, it can be difficult to pin the dislocation at high-temperature deformation by solution atoms and/or impurities, which was also proved by Ankem et al. [13] and Weiss et al [14]. Therefore, the DYP of the two studied alloys can be ascribed to the dynamic theory.

According to the dynamic theory, the prerequisite for DYP is that there is a high enough dislocation density at the grain boundary which is achieved by high strain rate and high deformation strain. As a result, the increasing strain rate can obviously enhance the DYP of the two alloys by faster dislocation accumulation and generation, and explain why there is no DYP at 0.01 s^{-1} and 0.001 s^{-1} deformation for all temperatures. When the deformation temperature is increased from 900 °C to 1000 °C and 1100 °C, the DYP is gradually weakened primarily due to the grain boundary characteristics changing and dislocation movement, which are more promoted at higher temperatures than at lower temperatures. This negative temperature sensitivity at high-temperature deformations has also been reported in beta titanium alloys by Li et al. [15] in Ti-3Al-5V-5Mo alloy and Vijayshankar et al. [16] in Ti-Mn alloys.

The grains will suffer from significant grain coarsening, and this will lead to a marked reduction in grain boundary density. In the dynamic theory, the grain boundary is acting as the source for new mobile dislocations, so reducing grain boundary density can cut the dislocation source for DYP, resulting in the reduction of yield drop value. Furthermore, when the deformation is processed at higher temperatures the subsequently higher driving force can promote dislocation movement and intensify dynamic softening (by DRV and DRX, discussed later in this chapter) which consumes the dislocations notably, and can then lead to weakening of DYP.

Most importantly, it can be obviously observed from Figure 5.3 and Table 5.2, IM alloy shows a higher degree of DYP than PM alloy at the same conditions, indicating that PM alloy has higher flow stability than IM alloy during high-strain-rate deformation. The less significant DYP of PM alloy can be ascribed to its higher initial dislocation density caused by the hot-pressing and subsequent fast cooling. The relative higher dislocation density in the microstructure can hinder the sudden generation of new mobile dislocation for DYP, and lower the magnitude of the discontinuous yield drop.

5.2.4 Adiabatic temperature rising

Adiabatic temperature rising (ATR) is a common phenomenon during hot processing (forging, extrusion, rolling and etc.) of metallic materials due to the external stress and work especially for titanium alloys at high-strain-rate deformation due to their low thermal conductivity. ATR can be advantageous to hot processing of the working pieces, in some situations, for retaining the desired processing temperature for a longer time. However, serious ATR will lead to adverse impacts on hot processing of the parts with reduction of the materials' hot workability, including the formation of adiabatic shear banding (ASB) [17, 18], thermal cracking and unexpected microstructure variation. Meanwhile, ATR can be associated with the kinetic analysis and influence the mechanical behaviour of the working pieces.

Table 5.3 Maximum temperature rising value of PM Ti-5553 alloy during thermal physical simulation at various conditions.

Temperature rising (°C)	700 °C	800 °C	900 °C	1000 °C	1100 °C
10 s^{-1}	68.4	46.0	33.2	18.5	6.6
1 s^{-1}	26.2	20.1	10.9	5.5	2.4
0.1 s^{-1}	9.2	6.4	4.6	/	/
0.01 s^{-1}	/	/	/	/	/
0.001 s^{-1}	/	/	/	/	/

* / indicates there is no ATR(0 °C) at the specific condition.

Therefore, it becomes meaningful for the industry to investigate ATR phenomenon of the materials at different conditions and bridge it with the materials' hot workability in actual materials processing. In this section, the effect of deformation

parameters on ATR phenomenon and the comparison of ATR for PM and IM Ti-5553 alloys is investigated using the temperature rising data recorded by the Gleeble® simulator during thermal physical simulation.

Table 5.3 and 5.4 show the maximum temperature rising value of PM and IM alloy during thermal physical simulation at different temperatures (700 °C-1100 °C, 100 °C interval) and strain rates (0.001 s^{-1}-10 s^{-1}), respectively. It is obvious that deformation variables have a significant effect on ATR for both PM and IM alloys, and the ATR discrepancy between the two alloys is also considerable.

Table 5.4 Maximum temperature rising value of IM Ti-5553 alloy during thermal physical simulation at various conditions.

Temperature rising (°C)	700 °C	800 °C	900 °C	1000 °C	1100 °C
10 s^{-1}	79.2	56.5	37.6	24.3	10.0
1 s^{-1}	47.8	28.4	11.3	6.8	3.6
0.1 s^{-1}	13.0	9.5	6.8	2.8	/
0.01 s^{-1}	2.5	/	/	/	/
0.001 s^{-1}	/	/	/	/	/

* / indicates there is no ATR(0 °C) at the specific condition.

There is a strong positive correlation between ATR value and strain rate but an equally strong negative correlation with deformation temperature for both the two alloys. Almost no ATR is observed when the deformation strain rate is lower than 1 s^{-1} and the temperature higher than 900 °C. The higher strain rate can provide more external energy and complete the deformation process in a shorter time, which leads to a higher degree of ATR. As for the effect of temperature, the material has lower deformation resistance and more active softening mechanisms at relatively higher temperatures, leading to the reduction of ATR. Additionally, PM alloy shows a lower degree of ATR at the same deformation condition comparing to IM alloy due to its better hot-deformation compatibility from the fine grain and lower flow stress. Meanwhile, the different deformation mechanisms at varying conditions of the two alloy also contribute to their different ATR, which will be discussed later in the microstructural evolution sections.

5.3 Deformation activation energy

As is demonstrated in the previous chapter, the deformation activation energy (Q) is very important for the characterization of hot deformation behaviour and the evaluation of hot workability of metallic materials. The lower Q the material suggests, the easier the material can be processed at the specific condition. The comparison of Q for PM and IM alloy is focused in this section using the developed activation energy map. Differently from the adoption of the mean value for the calculation of Q in (α+β) and β regions used in the previous chapter, a series of Q at varying conditions were calculated using the data (peak flow stress) from thermal physical simulation to obtain the distribution of Q with the changing the deformation parameters (temperature and strain rate). The detailed formulas for the calculation are listed and defined here (the derivation and calculation processes are in shown in Section 4.3):

$$Q = \mathrm{R}\left\{\frac{\partial \ln \dot{\varepsilon}}{\partial \ln[\sinh(\alpha\sigma)]}\right\}_T \cdot \left\{\frac{\partial \ln[\sinh(\alpha\sigma)]}{\partial (1/T)}\right\}_{\dot{\varepsilon}} \qquad (5.1)$$

It is defined in this equation: $n = \left(\frac{\partial \ln \dot{\varepsilon}}{\partial \ln[\sinh(\alpha\sigma)]}\right)_T$ and $N = \left\{\frac{\partial \ln[\sinh(\alpha\sigma)]}{\partial (1/T)}\right\}_{\dot{\varepsilon}}$

Then, Equation 5.1 can be transferred to :

$$Q = \mathrm{R} \cdot n \cdot N \qquad (5.2)$$

In this equation, n (unitless) is obtained at different temperatures, N (K) is obtained at different strain rates and R (molar gas constant) is 8.314 $\mathrm{J \cdot mol^{-1} \cdot K^{-1}}$. After that, the results of Q at each condition (700 °C-1100 °C, 0.001 $\mathrm{s^{-1}}$-10 $\mathrm{s^{-1}}$) can be obtained with the multiplication calculation of R, n and N. Equal interval interpolation (using Matlab® software) is utilized for the finer data gap of deformation temperature and strain rate. Meanwhile, cubic spline interpolation (introduced in Section 4.5.2, using Matlab® software) is employed on Q values for smoothing the data fluctuation. Finally, the raw data is transferred to Origin® software for plotting of the activation energy maps. Figure 5.5 shows the 3-Dimensional Q distribution map of PM and IM alloy with the changing temperature and strain rate, and the corresponding 2-Dimensional maps are displayed in Figure 5.6.

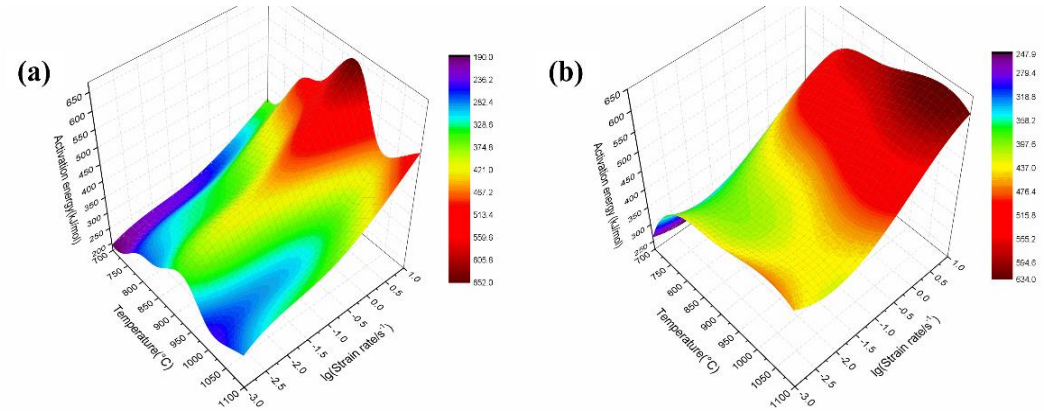

Figure 5.5 Three-dimensional deformation activation energy (at peak flow stress) distribution map of Ti-5553 alloys with the changing temperature and strain rate: (a) PM alloy and (b) IM alloy.

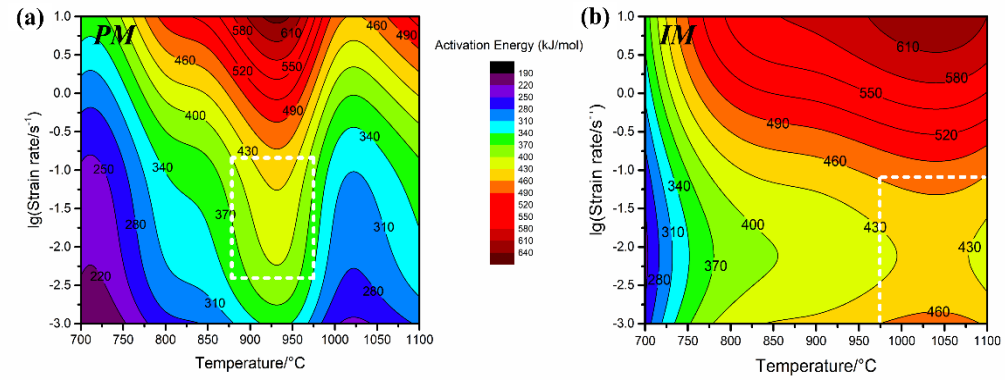

Figure 5.6 Two-dimensional deformation activation energy (at peak flow stress) distribution map of Ti-5553 alloys with the changing temperature and strain rate: (a) PM alloy and (b) IM alloy. The contour numbers represent the value of *Q*.

Firstly, it can be found that deformation parameters have a significant effect on *Q* for both PM and IM alloys, and discrepancy of *Q* between the two alloys is also considerable. It can be seen from the maps that the *Q* values are increased from 193.75 kJ·mol^{-1} to 633.80 kJ·mol^{-1} for PM alloy (average value = 368.17 kJ·mol^{-1}) and 242.32 kJ·mol^{-1} to 625.20 kJ·mol^{-1} for IM alloy (average value = 447.16 kJ·mol^{-1}), when deformation temperature increases from 700 °C to 1100 °C at the strain rate range of 0.001 s^{-1}-10 s^{-1}. Overall, PM alloy has lower *Q* values than that of IM alloy, this phenomenon becomes more obvious when the deformation strain rate is relatively low ($\dot{\varepsilon}$ < 1 s^{-1}), meaning that PM alloy is much easier to be processed at low-strain-rate compared to IM alloy. Additionally, the different distribution of *Q* value in the maps indicates that the active deformation mechanisms are varied for the two alloys at the same processing region. As for the influence of deformation temperature on the distribution of *Q*, PM alloy shows the peak at medium temperatures and PM alloy shows its maximum *Q* at high

temperatures. For strain rate, there are strong positive correlations between *Q* value and strain rate for both of the two alloys.

It has been reported that the domains with nearly constant and relatively high *Q* value in the activation energy map can be considered as a potential optimal processing windows [19, 20], so that the possible processing windows are 875 °C-975 °C/0.01 s^{-1}-0.1 s^{-1} for PM alloy and 975 °C-1100 °C/0.001 s^{-1}-0.1 s^{-1} for IM alloy (indicated as the white-dash squares in Figure 5.6). The alloy microstructure may be changed significantly in those processing regions, which will be further confirmed in later sections. On the contrary, both of PM and IM alloys are not safe to be processed in the domains consisting of low temperature (700 °C-850 °C) and high strain rate (1 s^{-1}-10 s^{-1}), and these domains have relatively small *Q* values with obvious fluctuation, indicating the presence of flow instability.

5.4 Hot processing map

In Section 4.5.2, the physical foundation of the dynamic material model (DMM) for metallic materials has been introduced and the detailed procedures for the construction of the maps have been provided as well. In this section, the hot processing maps of both PM and IM alloy were constructed at the same temperature (700 °C-1100 °C) and strain rate (0.001 s^{-1}-10 s^{-1}) ranges with varying deformation strain (0.6, 0.8 and 1.0) to investigate the differences of the power dissipation efficiency (η) and instability criterion (ξ) for the two alloys. Thereinafter, the comparison of the hot processing for the two alloys can be very helpful to disclose the deformation mechanism differences and to contrast the hot workability for the Ti-5553 alloy prepared by two metallurgy approaches from the perspective of kinetics and thermodynamic analyse.

Figure 5.7 shows the 3-Dimensional power dissipation maps of PM and IM Ti-5553 alloy constructed at three different true strains (deformation degree). Figure 5.8 shows the 2-Dimensional corresponding flow instability maps. Superimposing the two kinds of maps, the complete 2-Dimensional hot processing maps for the two alloys are shown in Figure 5.9.

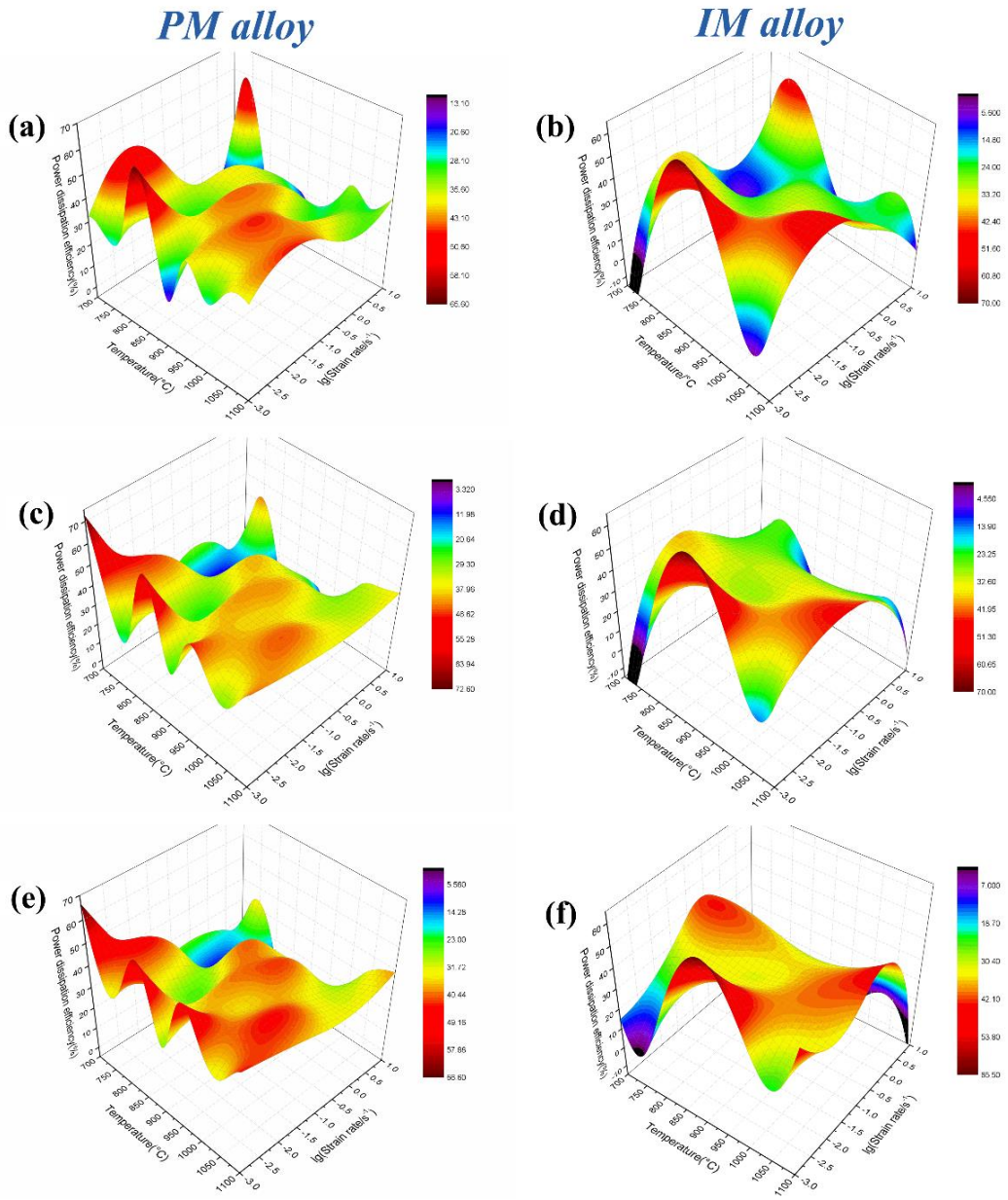

Figure 5.7 Three-dimensional power dissipation efficiency maps of PM and IM Ti-5553 alloy constructed in the temperature range of 700 °C-1100 °C and strain rate range of 0.001 s^{-1}-10 s^{-1} for various true strain: (a) PM alloy, 0.6; (b) IM alloy, 0.6; (c) PM alloy, 0.8; (d) IM alloy, 0.8; (e) PM alloy, 1.0; (f) IM alloy, 1.0.

As shown in Figure 5.7, PM and IM alloys have obvious differences in the distribution of the power dissipation efficiency (η) with the changing deformation temperatures and strain rate at the same deformation strain. The two alloys show their peak efficiency domains at different processing windows. Meanwhile, it cannot be ignored that the deformation degree has a significant effect on the η for both the two alloys. In Figure 5.7a, c and e, the values of η at the peak efficiency domains are increased with growing deformation degree. In Figure 5.7b, d and f, with increasing the deformation degree, not only is there improvement of the η values at the peak efficiency, there is also clear extension of the domains.

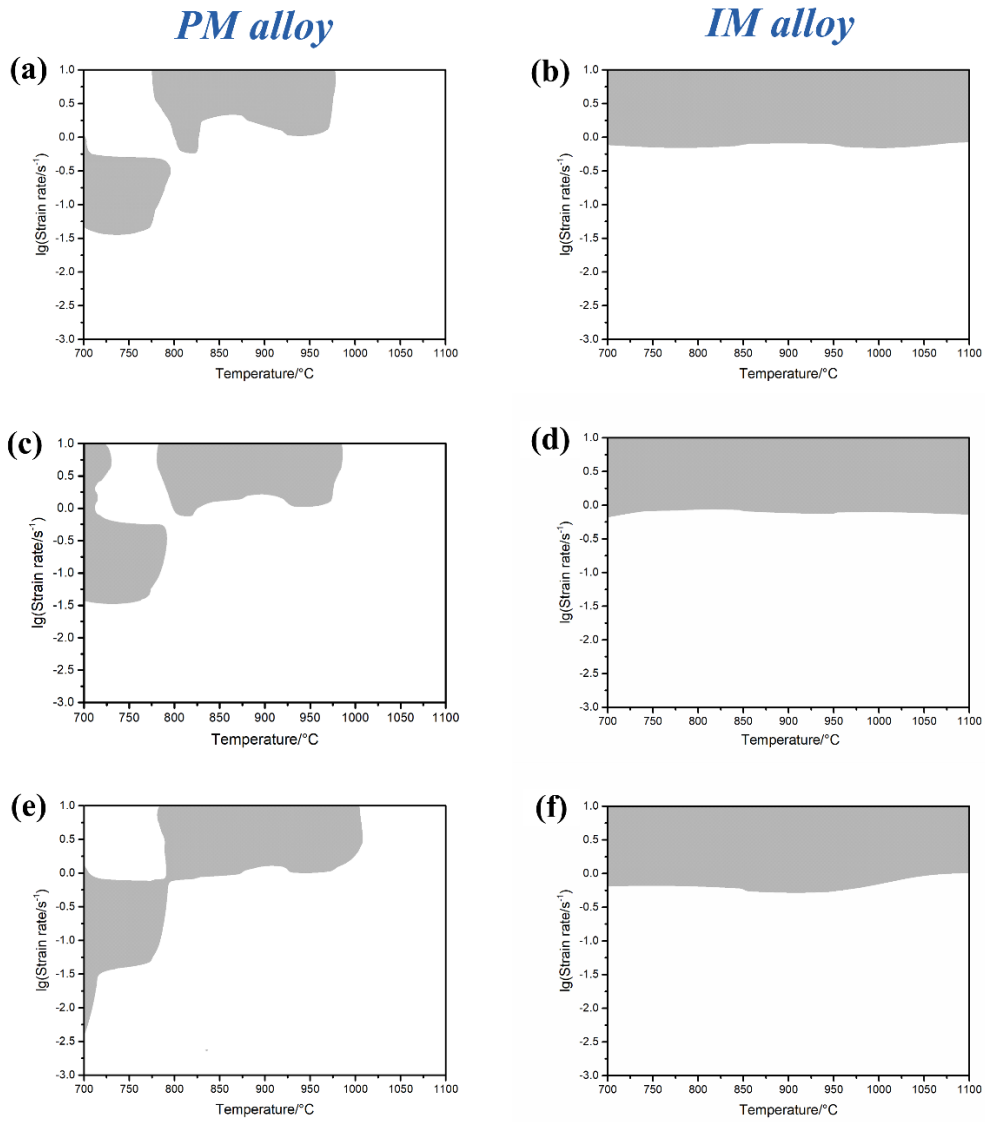

Figure 5.8 Two-dimensional flow instability maps of PM and IM Ti-5553 alloy constructed in the temperature range of 700 °C-1100 °C and strain rate range of 0.001 s^{-1}-10 s^{-1} for various true strain: (a) PM alloy, 0.6; (b) IM alloy, 0.6; (c) PM alloy, 0.8; (d) IM alloy, 0.8; (e) PM alloy, 1.0; (f) IM alloy, 1.0.

As shown in Figure 5.8, PM and IM alloys have obvious differences in the distribution of the flow instability criterion (ξ) with the varying deformation temperatures and strain rate at the same deformation strain. The unstable flow regions locate at low-temperature (700 °C-800 °C)/medium-strain-rate (0.1 s^{-1}-1 s^{-1}) and medium-temperature (800 °C-1000 °C)/high-strain-rate ($\dot{\varepsilon} > 1$ s^{-1}) areas for PM alloy, while IM alloy exhibits the constant unstable flow regions at all-temperature/high-strain-rate ($\dot{\varepsilon} > 1$ s^{-1}) areas. Moreover, as is demonstrated in Section 4.5.3, the flow instability region expanded at higher deformation degree. Whereas, the deformation degree has less impact on the flow instability domain of IM alloy, which almost remains the same situation with varying deformation strain.

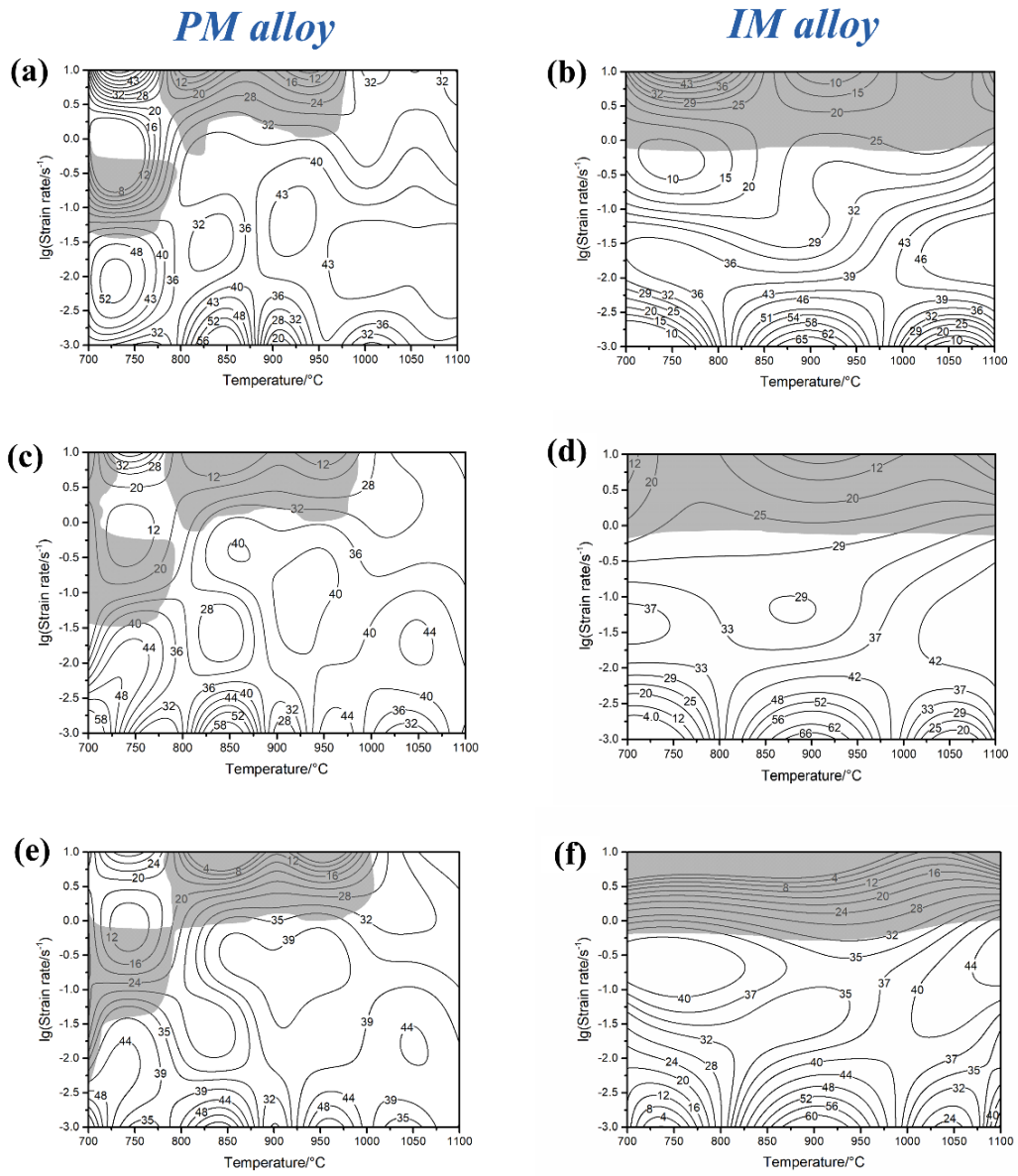

Figure 5.9 Two-dimensional complete hot processing maps of PM and IM Ti-5553 alloy constructed in the temperature range of 700 °C-1100 °C and strain rate range of 0.001 s^{-1}-10 s^{-1} for various true strain: (a) PM alloy, 0.6; (b) IM alloy, 0.6; (c) PM alloy, 0.8; (d) IM alloy, 0.8; (e) PM alloy, 1.0; (f) IM alloy, 1.0. The contour numbers represent the power dissipation efficiency η, and the grey-shaded regions represent the instability domains.

As shown in the complete hot processing maps (Figure 5.9), it can be clearly found that the optimal processing windows with favourable hot workability of the two alloys are quite disparate. Firstly, PM alloy shows a larger "safe" processing window with smaller flow instability domain than that of IM alloy. In addition, it can also be seen that the η value at the flow instability domains for both the two alloys is relatively low, illustrating the minor microstructural variation at these conditions, which confirms that these "unsafe" domains should be avoided during actual hot processing of the materials.

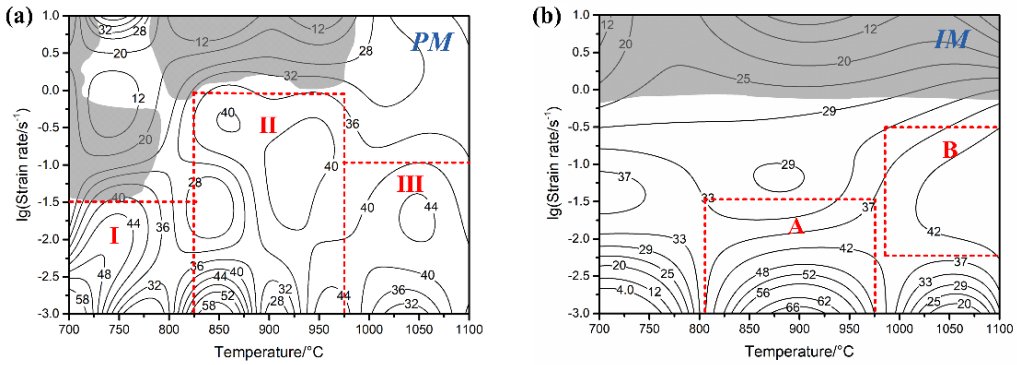

Figure 5.10 Typical hot processing maps of (a) PM and (b) IM alloys at the strain of 0.8. The contour numbers represent the power dissipation efficiency η, and the grey-shaded regions represent the instability domains.

Meanwhile, PM alloy also suggests the larger potential optimized processing windows than IM alloy with the η value higher than 35%. The processing maps at the true strain of 0.8 are further selected to compare their optimized processing windows regionally and in detail. There are roughly three domains having the optimal η ($\geq$ 35%) in Figure 5.10a of PM alloy, which are: 700 °C-825 °C/0.001 s^{-1}-0.01 s^{-1} (Domain I); 825 °C-975 °C/0.001 s^{-1}-1 s^{-1} (Domain II); and 975 °C-1100 °C/0.001 s^{-1}-0.1 s^{-1} (Domain III). Whereas, IM alloy only has mainly two domains with the optimal η value and both of these are located at medium and high-temperature regions (Figure 5.10b): 800 °C-975 °C/0.001 s^{-1}-0.01 s^{-1} (Domain A) and 975 °C-1100 °C/0.01 s^{-1}-0.1 s^{-1} (Domain B).

As is presented in the principle of DMM in Section 4.4.1, the optimal processing windows of the metallic materials is related to the significant microstructural change (DRV, DRX, super-plasticity and ect.), which consumes considerable input energy (power). The other destination of the power is thermal (heat) energy. Thus, the larger potential optimized processing window of PM alloy can also be associated with the ATR. As analysed in Section 5.2.4, PM alloy has a lower degree of ATR at the same deformation condition compared to IM alloy. That means more external power is transferred to for the evolution of microstructure rather than the heat generation in PM alloy when the two alloys are processed at the same condition. Therefore, the results of ATR further confirm the better hot workability and larger potential optimized processing window of PM alloy.

Although comparisons of flow behaviour and hot workability for the two alloys have already been made by thermodynamic and kinetic analysis, to further compare the deformation mechanisms directly for the two alloys deformed at the same condition and to confirm their potential optimal processing window, the microstructural evolution characteristics of PM and IM alloys deformed (70% height reduction) in related regions must be further characterized and analysed, as presented in the later sections.

5.5 Cracking behaviour

As is demonstrated in the principle of flow instability criterion in DMM, the unstable deformation of metallic materials in "unsafe" regions may be related to the occurrence of localized deformation, shear banding and external cracking, among which external cracking can be the most detrimental phenomenon during hot processing, always leading to the irreversible failure of the metallic working pieces. As a result, the occurrence of cracking will reduce the products' production rate and limit the thermomechanical processing of metallic materials within a certain degree [21, 22]. That is to say, the quality of hot-processed pieces is highly dependent on the forming process of metallic materials for achieving the desired shapes without the occurance of fracturing and cracking [23]. Thus, the cracking behaviour and mechanisms of the two alloys during hot processing are investigated and understood in this section to limit and reduce cracking phenomenon in the further hot processing and fabricate their forming products with satisfying shape and properties.

5.5.1 Cracking behaviour of PM alloy

The macroscopic views of PM alloy specimens deformed at different hot compression conditions (600 °C-850 °C, 0.1 s^{-1}-10 s^{-1}) are shown in Figure 5.11. It is obvious that the cracking behaviour just occurs for the specimens compressed at 600 °C/10 s^{-1}, with 45° shear fracture (Figure 5.11b), and at 700 °C/10 s^{-1}, with edge cracking accompanied by the 45° shear fracture tendency (Figure 5.11d). The specimens compressed at other conditions are free of external cracking. However, for the specimens compressed at the strain rate of 1 s^{-1} at 600 °C and 700 °C, obvious flow instability features can be seen. These suggest that the degree of cracking is sensitive to both deformation strain rate and temperature, the lower the

deformation temperature and higher the deformation rate, the higher possibility for cracking of the compressed specimens.

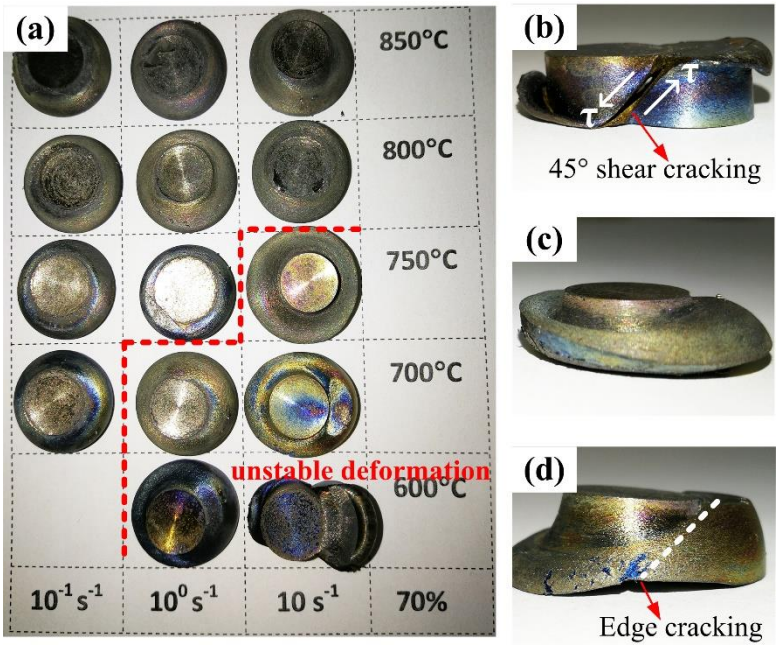

Figure 5.11 Macroscopic images of the hot-compressed PM Ti-5553 specimens under various conditions at: (a) 600 °C-800 °C/0.1 s^{-1}-10 s^{-1}; (b) 600 °C/10 s^{-1}; (c) 600 °C/1 s^{-1}; and (d) 700 °C/10 s^{-1}.

Shear fracture of the materials at 45° is formed on the basis of 45° shear bands, which initiates at the centre of the specimen and propagates along the maximum shear stress direction. The crack's expansion velocity is increased with increasing the strain rate, this explains why the cracking mode is transformed, for the compressed specimens at 600 °C, from edge cracking (1 s^{-1}, Figure 5.11c) to 45° shear fracture (10 s^{-1}, Figure 5.11b).

Although no cracks are found at other conditions, evident unstable and inhomogeneous deformation features can be observed in the specimens compressed at 600 °C/1 s^{-1}, 700 °C/1 s^{-1} and 750 °C/10 s^{-1} (Figure 5.11a, on the right side of the red dashed line). Furthermore, cracks are absent and the specimen deformation tends to become more and more homogenous and stable with increasing plasticity and hot workability due to increasing of the compression temperature and decreasing the deformation strain rate. Homogenous and stable deformation could be seen for the specimens compressed at the strain rate of 0.1 s^{-1} at 800 °C and 850 °C.

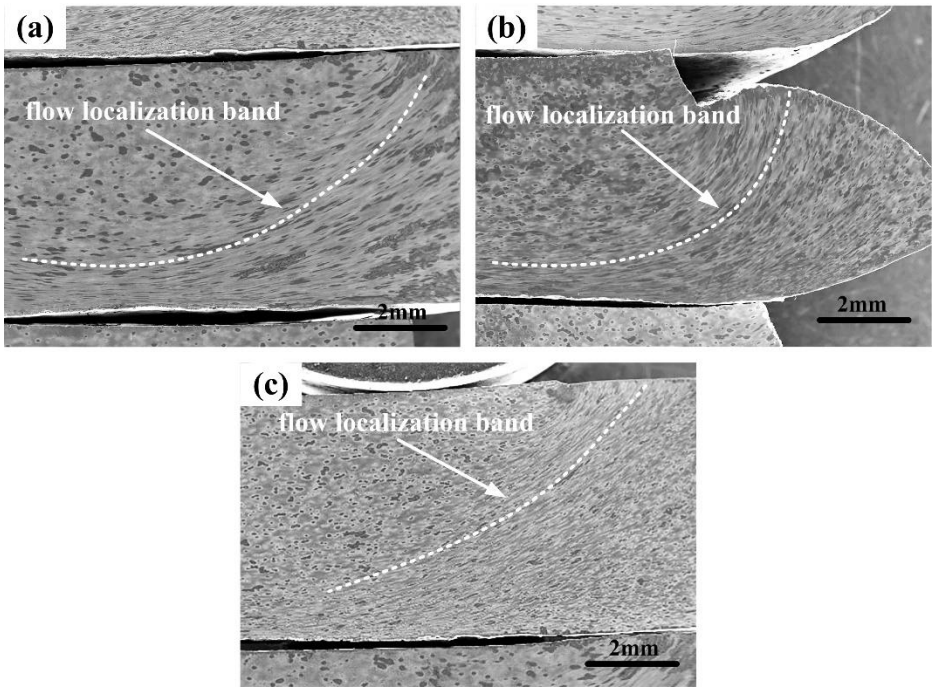

Figure 5.12 SEM images showing the flow localization situations of unstable deformed PM Ti-5553 alloy specimens: (a) 700 °C/10 s^{-1}; (b) 600 °C/1 s^{-1}; and (c) 700 °C/1 s^{-1}.

As shown in Figure 5.12, the plastic flow localization bands, with typical unstable and inhomogeneous deformation, are seen in the specimens compressed at 700 °C /10 s^{-1}, 600 °C /1 s^{-1}, and 700 °C/1 s^{-1}, respectively. The effect of deformation parameters on the degree of flow localization is significant, the most serious localized plastic flow can be found in the specimen compressed at 700 °C/10 s^{-1} (Figure 5.12a), and the localized plastic flow is getting weak when the specimen is compressed at 600 °C/1 s^{-1} (Figure 5.12b) and even weaker when compressed at 700 °C/1 s^{-1} (Figure 5.12c). This phenomenon can be attributed to the larger heat generation and the greater temperature rising when the specimens are compressed at high strain rate and low temperature than that at low strain rate and high temperature [24].

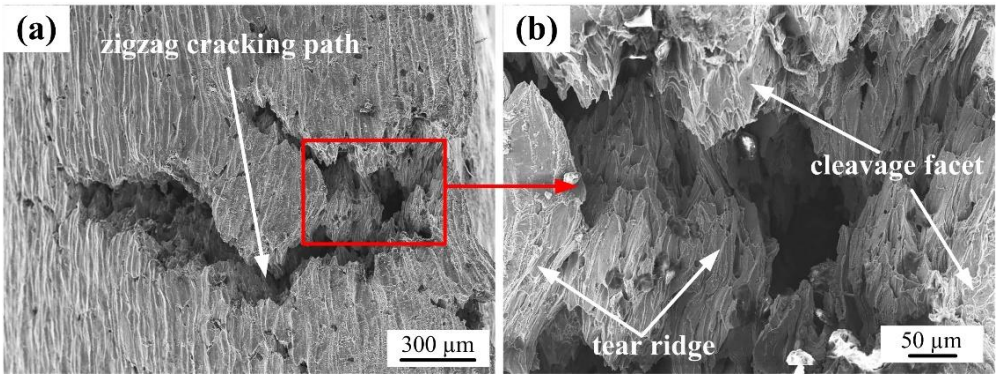

Figure 5.13 SEM images showing cracking morphology on the compressed PM Ti-5553 alloy specimen at 700 °C/10 s^{-1}.

The cracking mechanism of PM alloy can be revealed by investigating the detailed morphology of the cracked area of specimen compressed at 700 °C/10 s^{-1}. As shown in Figure 5.13a, deep cracks with zigzag cracking paths can be seen. At more magnified cracking area observation, as shown in Figure 5.13b, the appearance of cleavage facets, tear ridges and river-like patterns are obvious. These suggest that a brittle cleavage trans-granular cracking mechanism is dominant and the PM Ti-5553 alloy has little plastic deformation at the compression condition of 700 °C/10 s^{-1}.

5.5.2 Cracking behaviour of IM alloy

The fracture and cracking situations of IM Ti-5553 alloy specimens, hot compressed at 700 °C and various strain rate of 10 s^{-1}, 1 s^{-1} and 0.01 s^{-1}, are shown in Figure 5.14. It is clear that cracking occurs in all compressed specimens, and the degree of fracturing and cracking of IM alloy specimens is decreased with decreasing the strain rate. 45° shear fracture can be seen in the specimen compressed at 10 s^{-1} specimen (Figure 5.14a), and the specimens exhibit free-surface longitudinal cracking when it is compressed at strain rates of 1 s^{-1} (Figure 5.14b) and 0.01 s^{-1} (Figure 5.14c). These results demonstrate that the macroscopic fracturing and cracking mechanism of IM alloy are highly dependent on the strain rate. Unlike 45° shear fracture, the free-surface longitudinal cracking is mainly caused by the secondary tensile stresses. These stresses mainly come from the upsetting of the specimen during the uniaxial hot compression, and they are applied perpendicular to the compression direction [25].

Figure 5.14 Fracture and cracking modes of compressed IM Ti-5553 alloy specimens at various conditions: (a) 700 °C/10 s^{-1}; (b) 700 °C/1 s^{-1}; and (c) 700 °C/0.01 s^{-1}.

The detailed morphologies of cracked areas for IM alloy specimens compressed at 700 °C/1 s^{-1} and 700 °C/0.01 s^{-1} are shown in Figure 5.15. The serrated trans-granular cracking path can be easily seen for the specimen compressed at 700 °C/1 s^{-1} (Figure 5.15a), but the cracking surface is very smooth and has small and shallow

dimples (Figure 5.15b). For the specimen compressed at 700 °C/0.1 s^{-1}, the cracking path is straight, however, the cracking surface is rough and spreads with large and deep dimples. This indicates that IM alloy has a ductile cracking characteristic. Moreover, it can be noticed that the cracking ductility of IM alloy at 700 °C is more prominent when the deformation strain rate is low (Figure 5.15c and d). This is mainly attributed to the crack expansion velocity which is slow when the deformation strain rate is low, leading to only slight free-surface longitudinal cracking observed for the specimen compressed at 700 °C/0.1 s^{-1}.

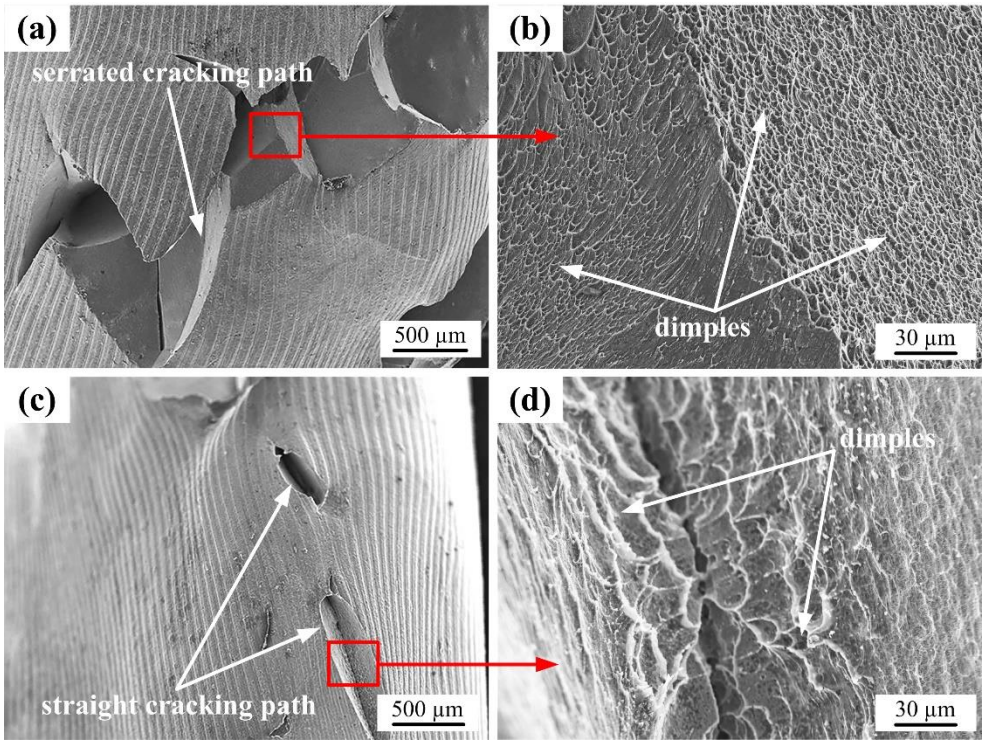

Figure 5.15 SEM images showing the cracking morphologies of compressed IM Ti-5553 alloy specimens: (a) and (b) 700 °C/1 s^{-1}; (c) and (d) 700 °C/0.01 s^{-1}.

5.5.3 Flow curves and microstructure characteristics associated with cracking behaviour

The true stress-strain curves of PM alloy, compressed at 600 °C and 700 °C and various strain rates of 0.01 s^{-1}-10 s^{-1}, and IM alloy, compressed at 700 °C and strain rates of 0.01 s^{-1}-10 s^{-1}, are exhibited in Figure 5.16. As the curves suggest, the flow stress at most compression conditions increase rapidly at the beginning of deformation to the peak stress and then decrease gradually to the steady states with increasing the deformation strain. Particularly, for the PM alloy specimens compressed at 600 °C/10 s^{-1} (Figure 5.16a) and the IM alloy specimen compressed

at 700 °C/10 s^{-1} (Figure 5.16b), the flow stress, after reaching the peak stress, drops rapidly to a minimum level and then gradually increases and become stable with further increasing the deformation strain.

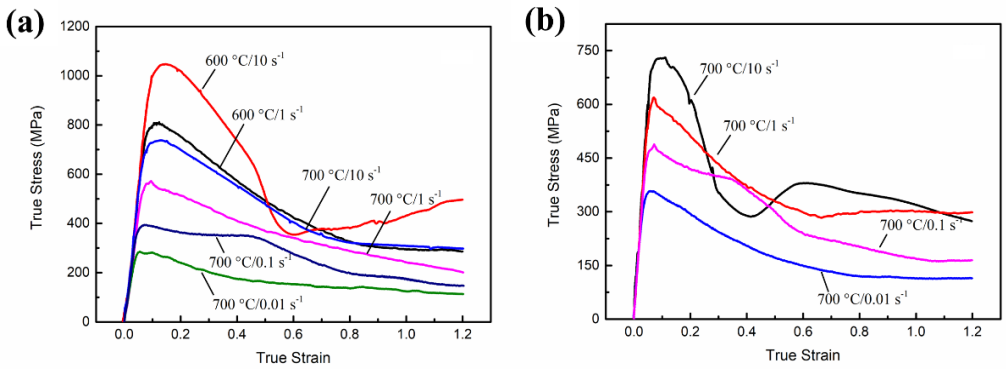

Figure 5.16 Flow curves of PM and IM Ti-5553 alloy at various conditions: (a) PM alloy at 600 °C and 700 °C; (b) IM alloy at 700 °C.

At the initial stage of deformation, the dislocation density is increased rapidly so that the work hardening is more significant than dynamic softening, this results in the corresponding true stress-strain curves are sharply increased to the peak stress. After that, the role of dynamic softening becomes more and more important with increasing the deformation strain, untill at some extent, the balance between work hardening and dynamic softening is achieved, then the curves go into the steady stage [2, 26]. Severe 45° shear fracture (as illustrated in the Figure 5.10b and Figure 5.13a) can cause obvious flow instability and subsequent dramatic softening, this is accounted for by the rapid drops of the flow stress at the conditions of 600 °C/10 s^{-1} and 700 °C/10 s^{-1}. Moreover, cracking along 45° and longitudinal directions of the specimens, as shown in Figure 5.10 and 5.13, are the reasons for flow softening under other deformation conditions, in particular at low temperature and high strain rate deformation.

5.5.4 Differences of cracking behaviour between PM and IM alloys

As shown in Figure 5.11 and Figure 5.14, 45° shear cracking occurs in the PM alloy specimen at 600 °C/10 s^{-1}, while edge cracks can be found in the specimen deformed at 700 °C/10 s^{-1}. Moreover, the likelihood of cracking and unstable deformation of the PM alloy specimens is getting less and less with increasing the deformation temperature and decreasing deformation strain rate. When the strain rate is lower than 10 s^{-1} or the deformation temperature is higher than 700 °C, crack-free specimens can be produced under any researched conditions. However,

cracking still occurs when the IM alloy specimens compressed at 700 °C, with 45° shear fracture at 10 s^{-1} and longitudinal cracks at 1 s^{-1} and 0.01 s^{-1}. The sketch in Figure 5.17 illustrates the cracking modes of PM and IM Ti-5553 alloys at the conditions discussed above.

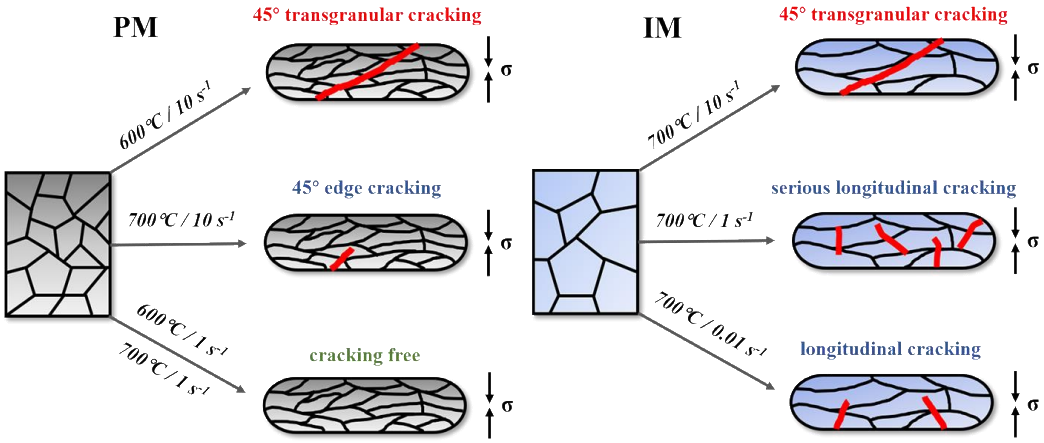

Figure 5.17 Schematic illustrating the cracking modes of PM and IM Ti-5553 alloys.

Moreover, as discussed in Section 5.2.2, PM alloy exhibits obvious lower flow stresses than IM alloy under moderate and low strain rate (0.001 s^{-1} to 1 s^{-1}) compression conditions. These results indicate that PM alloy has better hot-compression workability and higher cracking resistance than IM alloy. Also, PM alloy can be hot compressed to 70% height reduction without cracking at a lower temperature (100 °C lower) and higher strain rate (up to 1 s^{-1}) than IM alloy.

PM alloy exhibits a better thermal-mechanical workability and higher crack resistance than IM alloy, but it shows a lower ductility in the cracking areas. These differences between PM and IM alloys can be ascribed to the following reasons:

(1) The microstructure of PM alloy is composed of primary β phase and very few α precipitates, which provide better hot deformation ability and higher cracking resistance due to the BCC crystalline structure (β phase) and absence of the strengthening effect of the dispersed α precipitates. Meanwhile, the ductility and strength of the alloy are low because of the nearly single equiaxed β phase without α precipitate strengthening.

(2) PM alloy presents more grain boundaries than IM alloy, which offers an easy path for grain gliding during hot deformation, leading to higher cracking resistance for PM alloy than IM alloy.

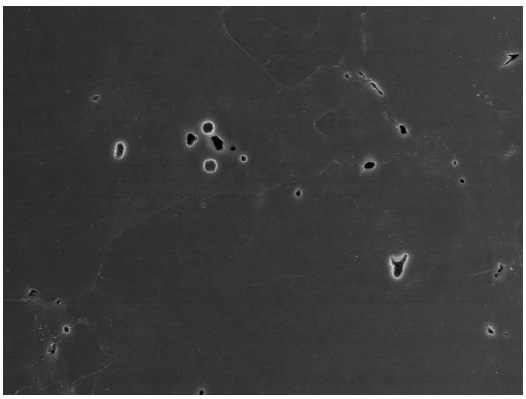

Figure 5.18 SEM images showing the residual micropores in the microstructure of PM Ti-5553 alloy.

(3) There are still some visible residual micropores, with a size of about 2 μm, in the partial microstructure of PM alloy (as shown in Figure 5.18). These micropores can be eliminated and reduced during hot compression, which improves the cracking resistance and hot workability for PM alloy as they absorb extra energy.

5.6 Microstructural evolution characteristics

The comparisons of the microstructural evolution characteristics for the two alloys deformed at various temperatures and strain rates are conducted in detailed in this section to disclose the deformation mechanisms and confirm the potential processing windows predicted by the thermodynamics and kinetics analysis.

5.6.1 Low-temperature region

Figure 5.19 shows the macrostructures and microstructures of PM and IM alloys deformed at 700 °C under different strain rates (1 s^{-1} and 0.01 s^{-1}). The samples deformed at 700 °C /1 s^{-1} show an obvious flow localization (FL) band containing non-uniformly deformed α precipitation band for PM alloy (Figure 5.19a and b), and severe longitudinal free-surface cracking and a distinct adiabatic shear band (ASB) microstructure (Figure 5.18e and f) for IM alloy. With decreasing the strain rate to 0.01 s^{-1} at 700 °C, PM alloy exhibits a homogeneous deformed microstructure (Figure 5.19c) and uniform α precipitation band (Figure 5.19d), indicating that PM alloy can be safely processed at this condition. However, free-surface cracking (Figure 5.19g) and weakened adiabatic shearing band (Figure 5.19h) are observed for IM alloy.

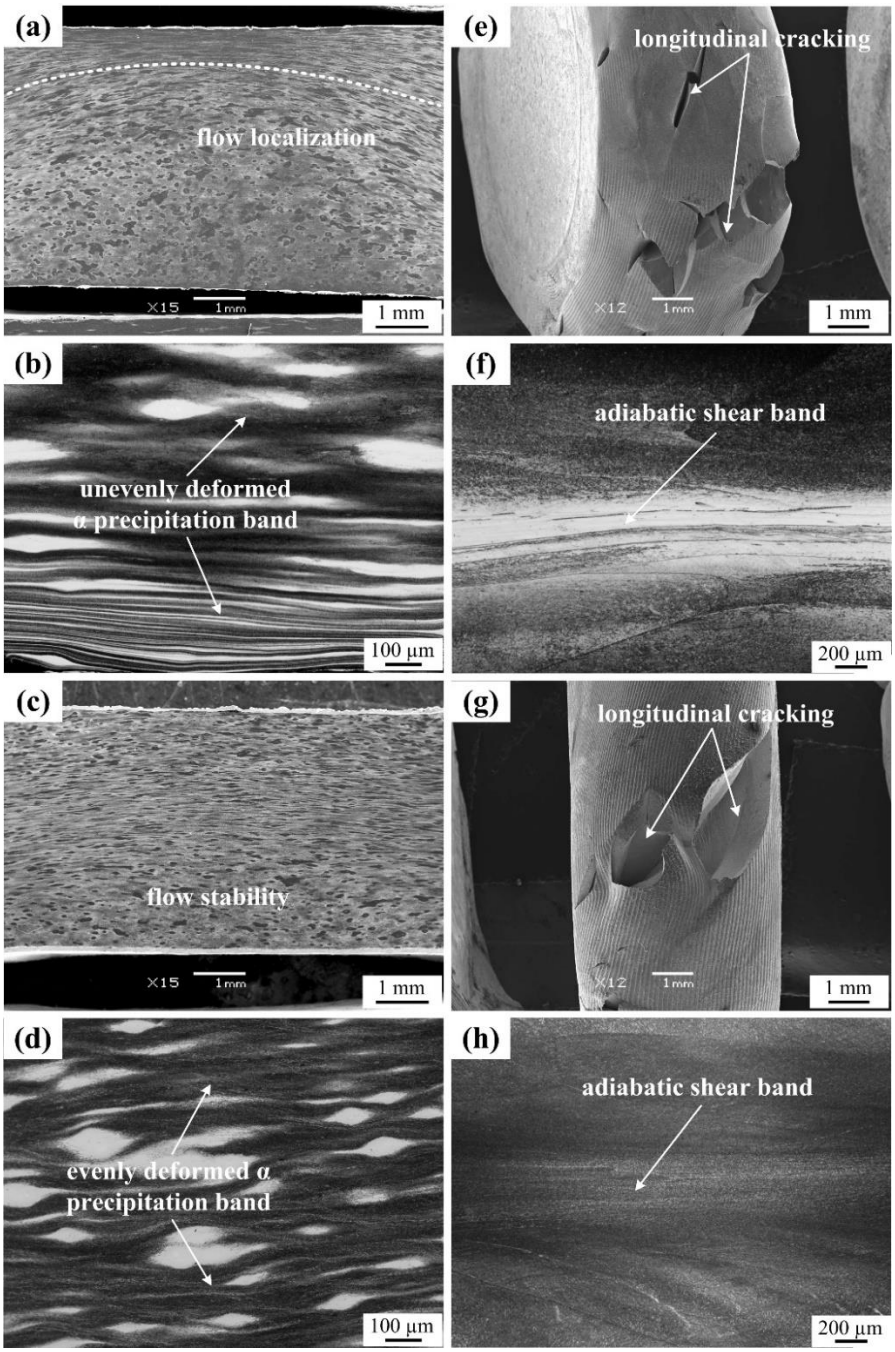

Figure 5.19 Macrostructures and microstructures of the two alloys deformed at 700 °C. PM alloy: (a)-(b) 1 s^{-1} and (c)-(d) 0.01 s^{-1}; IM alloy: (e)-(f) 1 s^{-1} and (g)-(h) 0.01 s^{-1}.

Figure 5.20 shows the macrostructures and microstructures of PM and IM alloys deformed at 800 °C under different strain rates (1 s^{-1} and 0.01 s^{-1}). A mild FL band composed of elongated α precipitation bands are observed for PM alloy deformed at 800 °C/1 s^{-1} (Figure 5.20a and b), however, a serious FL band is found in the microstructure of IM alloy deformed at the same condition (Figure 5.20e), and the FL band contains non-uniformly deformed grains with straight boundaries (Figure 5.20f).

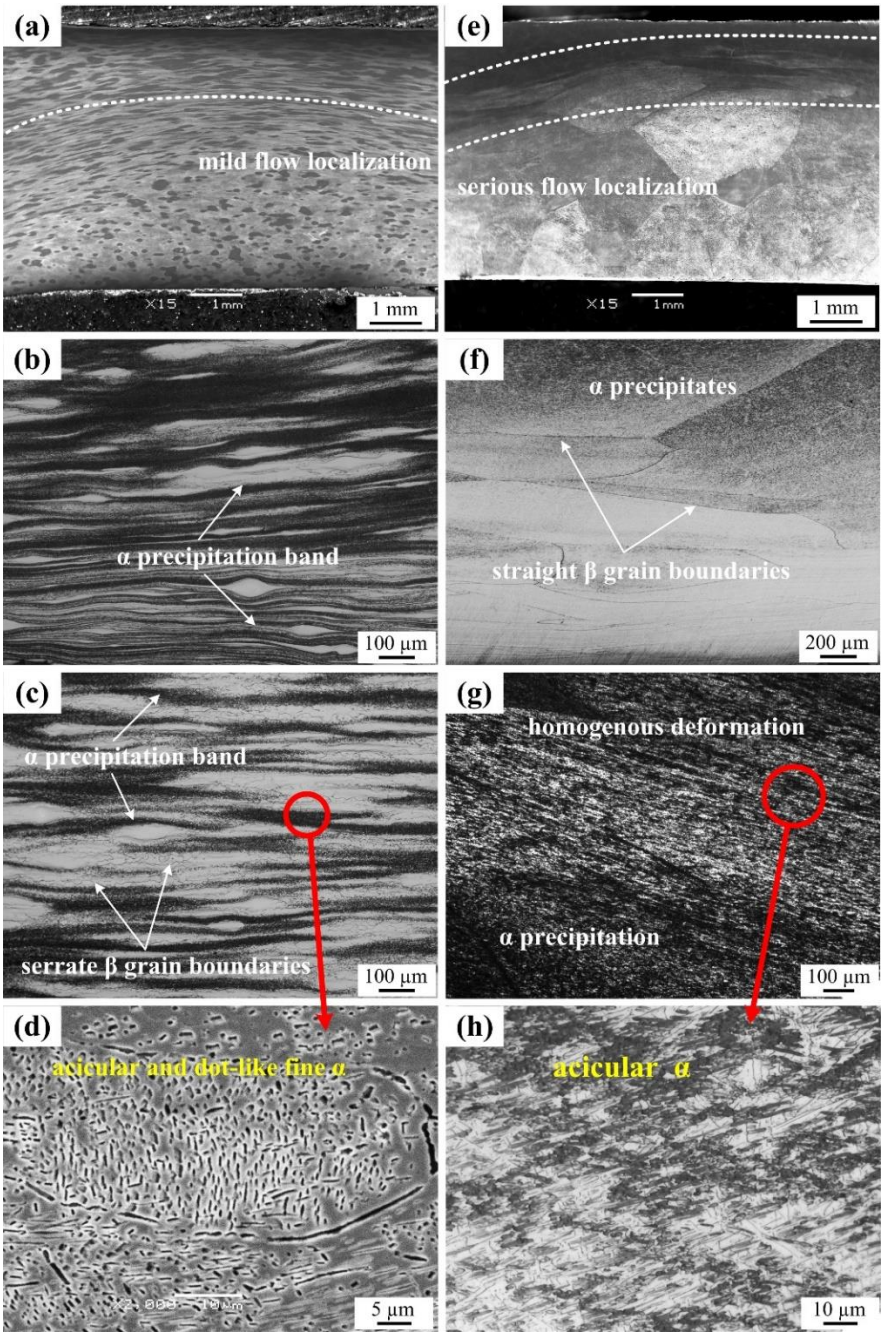

Figure 5.20 Macrostructures and microstructures of the two alloys deformed at 800 °C. PM alloy: (a)-(b) 1 s^{-1} and (c)-(d) 0.01 s^{-1}; IM alloy: (e)-(f) 1 s^{-1} and (g)-(h) 0.01 s^{-1}.

Figure 5.21 presents the EBSD examination results of PM and IM alloys deformed at 800 °C/0.1 s^{-1}. In the grain boundary maps, the grain boundaries with a misorientation angle (θ) higher than 15° are recognized as high angle grain boundaries (HAGBs), while those grain boundaries have the θ lower than 15° are defined as low angle grain boundaries (LAGBs). The elongated grains with serrated boundaries with a high LAGB density inside (Figure 5.21a and b) and the homogeneously distributed precipitation bands primarily composed of fine α grains (Figure 5.21c) can be observed in the deformed microstructure of PM alloy. These

features demonstrate that the active deformation mechanism is DαG and the initiation of DRV without flow instability. For IM alloy, as shown in Figure 5.21d and e, it is clear that some elongated grains, having substantial LAGBs, contain obvious sub-structures with different orientations, while other grains are almost free of sub-structures. The dispersed α grains are distributed heterogeneously (Figure 5.21f), and the fraction of α grains is much less than those of PM alloy deformed at the same condition, suggesting that the globularization process is promoted in PM alloy more than in IM alloy. All these EBSD examination results further confirm that localized deformation and dynamic α precipitation happens in IM alloy at 800 °C/0.1 s^{-1}.

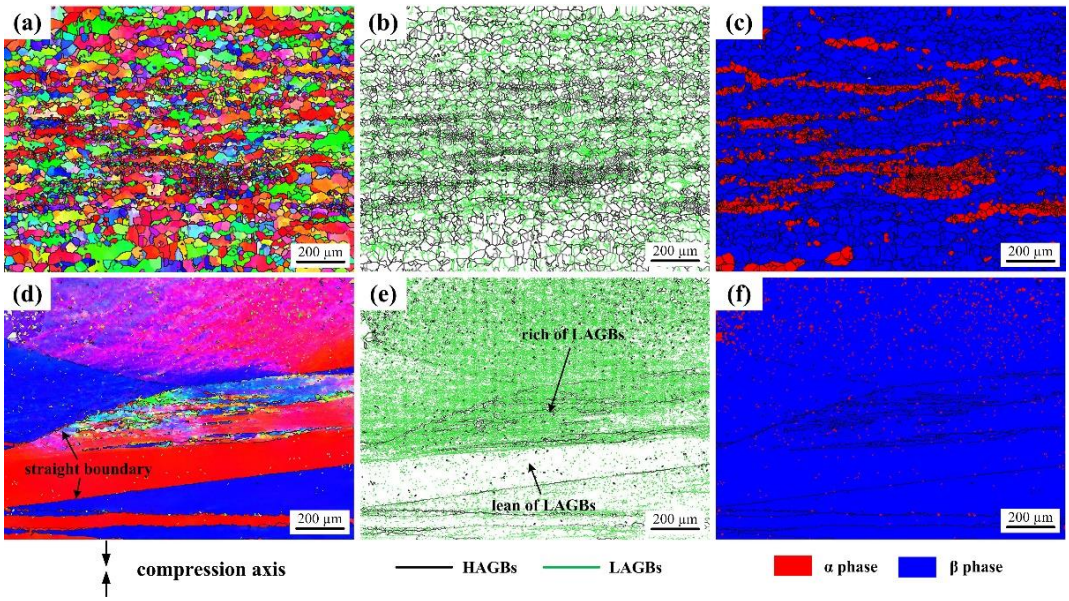

Figure 5.21 EBSD analysis results of the two alloys deformed at 800 °C/0.1 s^{-1}. PM alloy: (a) IPF map; (b) grain boundary map; (c) phase distribution map and IM alloy: (d) IPF map; (e) grain boundary map; (f) phase distribution map.

Decreasing the strain rate to 0.01 s^{-1} at 800 °C, the microstructure of PM alloy is composed of elongated grains with serrated grain boundaries and α precipitation bands (Figure 5.20c), and the α precipitation bands are consisted of fine acicular and dot-like structures (Figure 5.20d), which suggests the dominant deformation mechanisms is the combination of intense DαG and DRV. However, the microstructure of IM alloy deformed at 800 °C/0.01 s^{-1} contains only lath α phase with different sizes and without clear grain boundaries (Figure 5.20g and h), implying that the most likely dominated deformation mechanism is only dynamic α precipitation in the form of phase shearing without obvious globularization.

5.6.2 Medium-temperature region

The EBSD analysis results of PM and IM alloys deformed at 900 °C/0.1 s^{-1} are exhibited in Figure 5.22. The β matrix with serrated grain boundaries is obviously elongated along the direction perpendicular to the compression axis for PM alloy, and some necklace shaped grains are located at the matrix grain boundaries, as shown in Figure 5.22a. The elongated grains contain a large number of LAGBs and small necklace-shaped grains that are mainly surrounded by HAGBs (Figure 5.22b). The activation of deformation mechanisms during hot processing is always associated with the dislocation density variation. The Kernel average misorientation (KAM) maps are applied to analyse the dislocation density in the microstructures. The areas with a low KAM value (blue fields) have low dislocation density, while the red region in the KAM maps possesses the highest dislocation density.

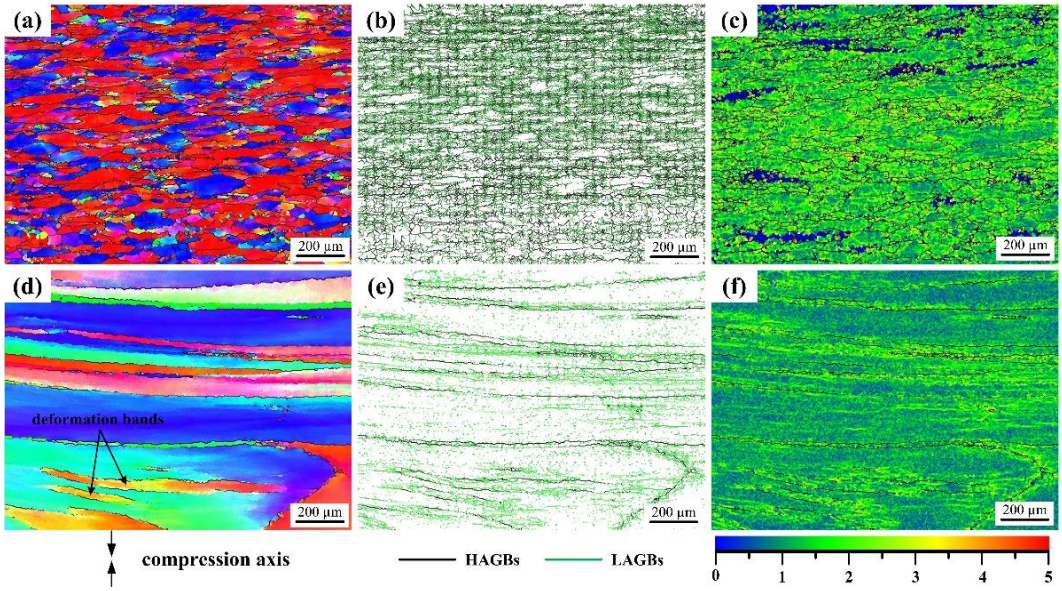

Figure 5.22 EBSD analysis results of the two alloys deformed at 900 °C/0.1 s^{-1}. PM alloy: (a) IPF map; (b) grain boundary map; (c) KAM map and IM alloy: (d) IPF map; (e) grain boundary map; (f) KAM map.

The dislocation density at the region near the HAGBs/LAGBs is relatively high and inside of the necklace-shaped grains is low, as shown in Figure 5.22c, and this indicates that the dominated deformation mechanism for PM alloy is a combination of DRV and DRX. As the strain rate decreases to 0.01 s^{-1}, it can be seen in Figure 5.23a that the microstructure contains a large number of equiaxed grains, which are much finer than the initial microstructure of PM alloy, and several coarsened β matrix grains, suggesting that extensive DRX happens at 900 °C/0.01s^{-1} for PM alloy. Further decreasing the strain rate to 0.001 s^{-1}, the grains are obviously

coarsened but some of them still have DRX features (Figure 5.23b), showing obvious DRX growth and post-DRV characteristics.

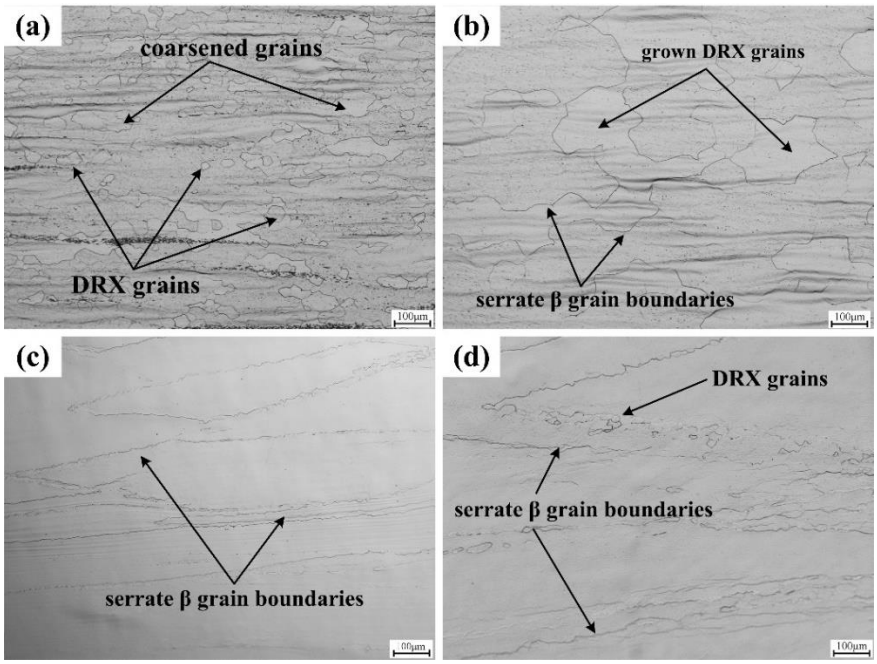

Figure 5.23 Optical microstructures of the two alloys deformed at 900 °C. PM alloy: (a) 0.01 s^{-1}; (b) 0.001 s^{-1} and IM alloy: (c) 0.01 s^{-1}; (d) 0.001 s^{-1}.

IM alloy deformed at 900 °C/0.1 s^{-1} has quite different microstructures compared to PM alloy, as shown in Figure 5.22d. Only the elongated coarse β grains are observed and no DRX grains are visible. The elongated β grains have massive LAGBs appearing inside. HAGBs are also visible for the coarse grains (Figure 5.22e), and they are parallel to the grain boundaries and separate the coarse prior β grains apart, illustrating that deformation bands (DB) are formed at this condition due to the localized deformation. Furthermore, a higher dislocation density can be clearly observed at the areas near the LAGBs and HAGBs in the KAM map (Figure 5.22f), and this indicates that the dislocations are significantly blocked and tangled at the boundaries to form the substructures and strong DRV occurs.

Representative TEM microstructures (Figure 5.24a and b) clearly present flat/zigzag sub-grain boundaries and dislocation nets that are derived from dislocation pile-up and accumulation, confirming that strong DRV happens for IM alloy during the deformation at 900 °C/0.1 s^{-1}. The distortion energy is consumed by DRV and this leads to that the sub-grain structure having a steady polygonization characteristic and low correlated misorientation angle. DB is prone to occur in metallic materials with coarse grains, which can impede the DRX process, and DB

is usually associated with the activation of the preferred slip system with the lowest deformation energy consumption [8, 27]. The strips of parallel dislocations are visible inside the grains and across the grain boundaries, as shown in Figure 5.24c and d, and this further confirms that the particular slip system is selected during the deformation and DBs are formed.

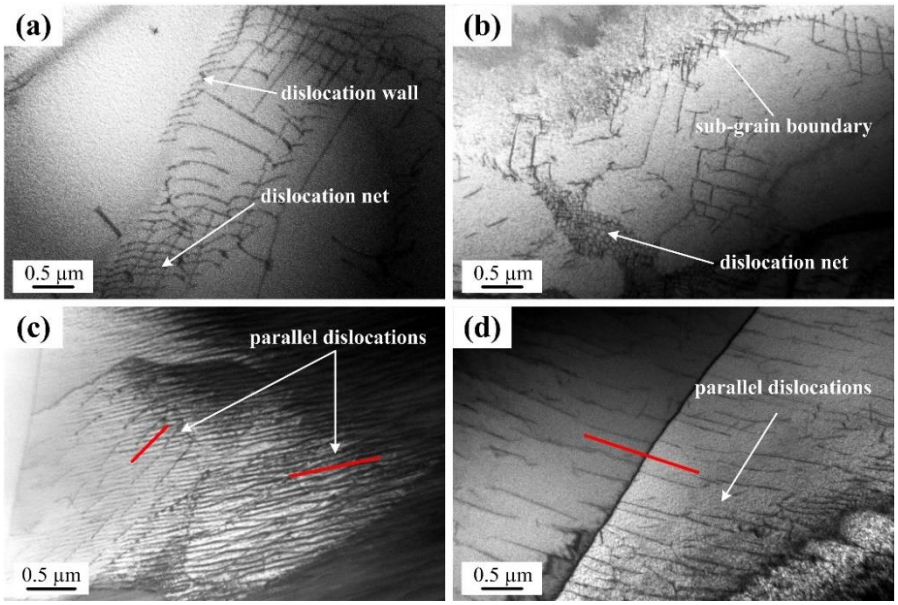

Figure 5.24 TEM microstructures of IM alloys deformed at 900 °C/ 0.1 s^{-1}: (a) and (b) sub-grain morphologies; (c) and (d) parallel dislocation configurations.

Decreasing the strain rate to 0.01 s^{-1} at 900 °C, it can see in Figure 5.23c that the microstructure of IM alloy is similar to that of the IM alloy deformed at 0.1 s^{-1}, having elongated and serrated grain boundaries and no DRX grains. However, when the strain rate is further decreased to 0.001 s^{-1}, a small amount of DRX grains are observed (Figure 5.23d) beside DRV features, indicating that the dominated deformation mechanisms are DRV accompanied by the inclination tendency of DRX.

5.6.3 High-temperature region

Figure 5.25 presents the microstructures of PM and IM alloys deformed at 1000 °C under various strain rates (0.1 s^{-1} and 0.01 s^{-1}). Coarse β grains with serrated boundaries and a small amount of fine equiaxed grains can be clearly seen in the microstructure of PM alloy deformed at 1000 °C/0.1 s^{-1} (Figure 5.25a), showing the characteristics of DRX and DRV. With decreasing the strain rate to 0.01 s^{-1} at 1000 °C, the equiaxed grains are much coarser in Figure 5.25b than that in Figure

5.25a, and as well as β grains with serrated boundaries are visible. These suggest that the dominated deformation mechanisms are DRV and DRX grain growth. For IM alloy, when the strain rate is 0.1 s^{-1}, besides small ribbon-shaped new DRX grains are visible alongside, obvious DRV features, such as β grains with irregular and serrated boundaries, are seen in Figure 5.25c. While, the DRX grains become coarser and the amount of DRX grains are less when decreasing the strain rate from 0.1 s^{-1} to 0.01 s^{-1}, as shown in Figure 5.25.

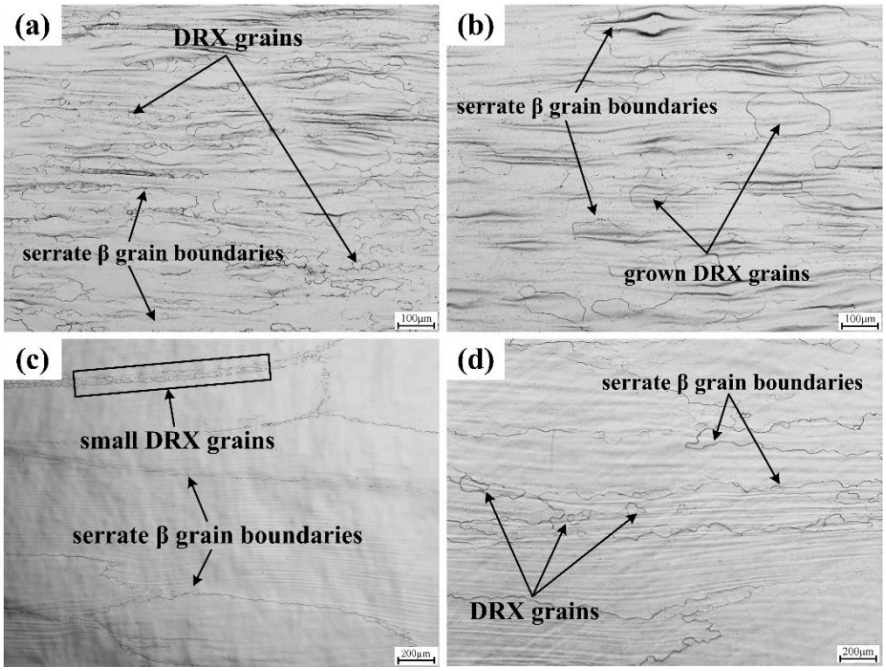

Figure 5.25 Optical microstructures of the two alloys deformed at 1000 °C. PM alloy: (a) 0.1 s^{-1}; (b) 0.01 s^{-1} and IM alloy: (c) 0.1 s^{-1}; (d) 0.01 s^{-1}.

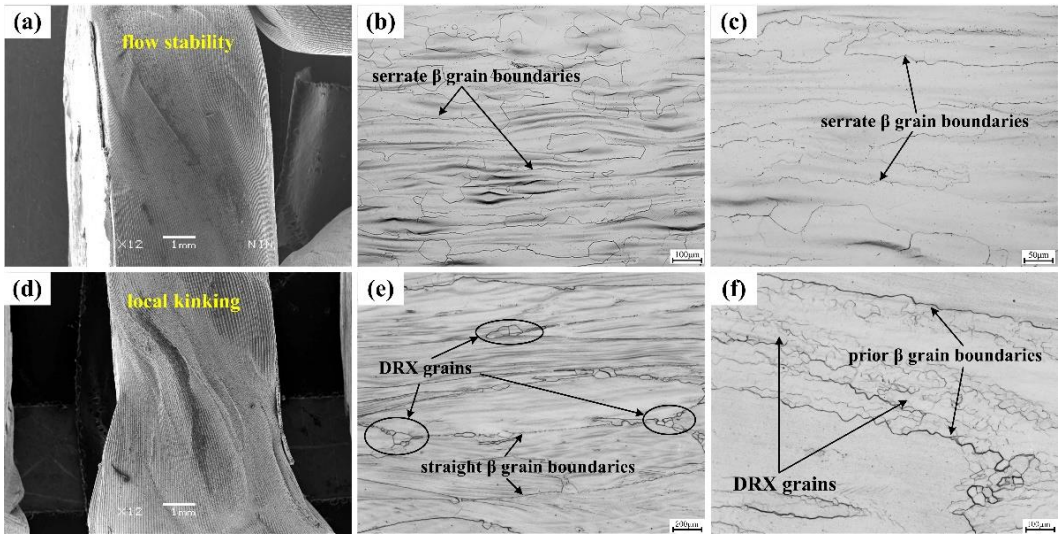

Figure 5.26 Macrostructures and microstructures of the two alloys deformed at 1100 °C. PM alloy: (a)-(b) 10 s^{-1}; (c) 0.01 s^{-1} and IM alloy: (d)-(e) 10 s^{-1}; (f) 0.01 s^{-1}.

PM alloy deformed at 1100 °C/10 s^{-1} displays a homogeneous microstructure and no obvious localized deformation characteristics can be observed in Figure 5.26a, and more detailed microstructure observation in Figure 5.26b suggests that the grains have serrated boundaries and no DRX grains are visible. This indicates that the dominant deformation mechanism is DRV. IM alloy deformed at the same condition shows obvious inhomogeneous deformation with local kinking (as shown in Figure 5.26d), however, Figure 5.26e shows that the equiaxed grains are found at the triple-junction of the grain boundaries. Thus, these features suggest that a combination of FL and DRX as the dominant deformation mechanism.

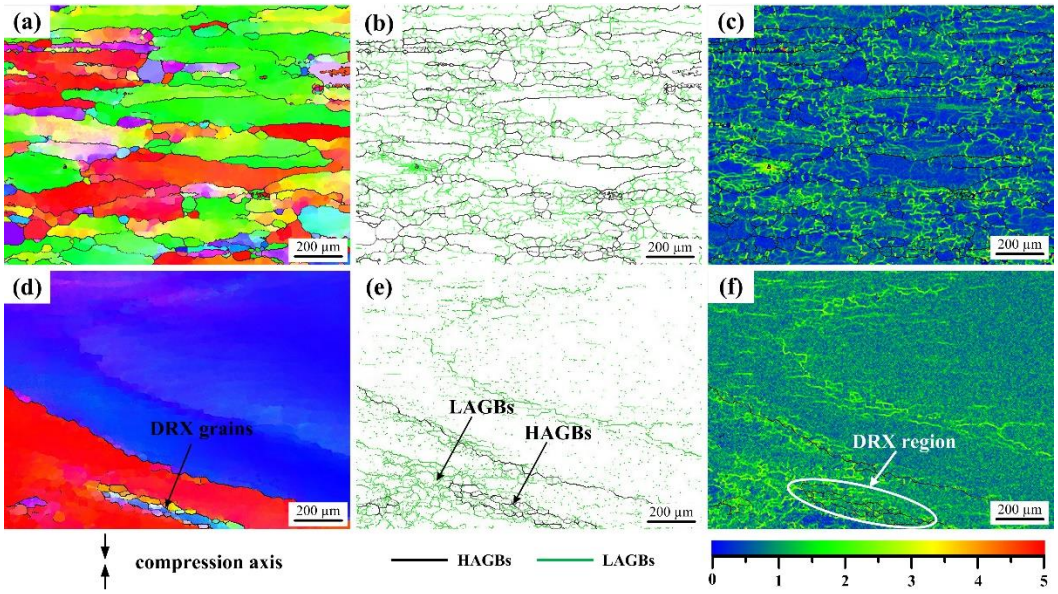

Figure 5.27 EBSD analysis results of the two alloys deformed at 1100 °C/0.1 s^{-1}. PM alloy: (a) IPF map; (b) grain boundary map; (c) KAM map and IM alloy: (d) IPF map; (e) grain boundary map; (f) KAM map.

Figure 5.27 shows the EBSD analysis results of PM and IM alloys deformed at 1100 °C/0.1 s^{-1}. It can see from Figure 5.27a and b that PM alloy has wide and serrated HAGBs that contain a large number of coarse sub-grains with different orientations. The dislocations distribute inhomogeneously in the microstructure and assemble at the LAGBs (Figure 5.27c). These above results reveal that the deformation is dominated by strong DRV at this condition. The observation from Figure 5.27d and e also suggest that the elongated grains with serrated boundaries and large amount LAGBs are formed for IM alloy, however, a small number of equiaxed grains with HAGBs are found in the elongated grains. This confirms that the primary deformation mechanism is DRV, but DRX happens as well. It is also obvious that the recrystallized grains with HAGBs are accumulated inside of the

grains with LAGBs (see Figure 5.27d), which means that the newly formed HAGBs are transformed gradually and consecutively from the preceding LAGBs. Particularly, Figure 5.27f also demonstrates that there is no obvious dislocation-lean structure in the DRX region of IM alloy, comparing to PM alloy in Figure 5.22c.

When the strain rate decreases to 0.01 s^{-1} (Figure 5.26c), PM alloy presents the microstructure features similar to that of the alloy deformed at 0.1 s^{-1}, having coarser grains with serrated boundaries and almost no DRX grains are observed. Whereas, small DRX grains can be observed in the microstructure of the IM alloy deformed at 1100 °C/0.01 s^{-1} (Figure 5.26f), which indicates the microstructure has been fully recrystallized and DRX is prone to occur in IM alloy as the strain rate decreases.

5.7 Discussion

Through the above analyse, it can be confirmed that all the potential hot processing regions suggested by activation energy maps (Figure 5.6) and hot processing maps (Figure 5.9) are highly consistent for both of PM and IM alloys. The dominant deformation mechanisms for those two alloys under respective processing conditions match well with the understanding obtained from the variation trends of flow curves and kinetic calculations. However, the dynamic α precipitation and DRX mechanisms that occur in PM and IM alloys are different, and this will be further discussed in this section. After summarizing the thermodynamics calculation and microstructure evolution characterization results in this chapter, the precise deformation mechanism maps of the two alloys are eventually developed for the comprehensive comparisons of their active deformation mechanism in varying processing windows. Lastly, the underlying principles for the deformation mechanism and hot workability differences of the two alloys are revealed profoundly.

5.7.1 Comparison of dynamic α precipitation mechanism

As is mentioned in Section 4.5.1, the dynamic α globularization phenomenon of PM Ti-5553 alloy has been observed. In this section, more detailed results and the

comparison of dynamic α precipitation mechanisms between PM and IM alloy will be provided and discussed.

Figure 5.28 shows the TEM microstructures of PM and IM alloys deformed at 800 °C. Both lath-shaped and globular α precipitates (confirmed by the SAED pattern in the inset) are observed in Figure 5.28a and dislocations are visible around the α precipitates. It can been clearly seen that the large α plate is sheared into two short α laths at the same level in Figure 5.28b. Meanwhile, the short α laths can also be formed through grain boundary separation and the wedging of β phase (Figure 5.28c), the similar processes were also observed by Fan et. al [2] in their metastable beta Ti-7773 alloy. Additionally, the size of α precipitates is observed as 200 nm-500 nm, and it can be speculated that the growth speed of the precipitates is very fast during the hot deformation (the growth process of α precipitates is observed and indicated in the images).

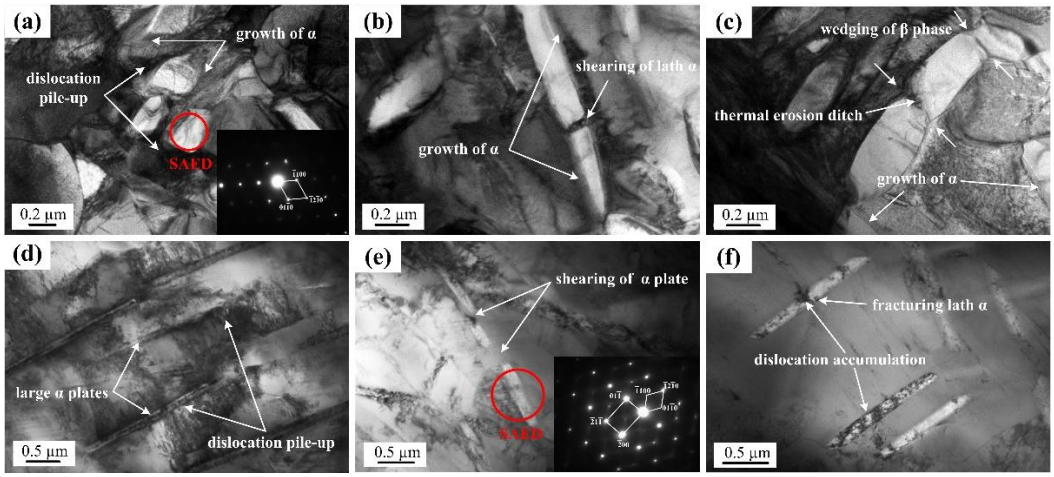

Figure 5.28 TEM microstructures and SAED patterns showing the dynamic α precipitation mechanisms of Ti-5553 alloys. PM alloy at: (a) and (b) 800 °C/0.1 s^{-1}; (c) 800 °C/0.01 s^{-1} and IM alloy at: (d)-(f) 800 °C/0.1 s^{-1}.

For IM alloy, only lath α (confirmed by the SAED patterns in the inset of Figure 5.28e) is formed by shearing and fracturing of the large α plate (similar processes were also observed by Jones et. al [28] in their heat-treated Ti-5553 alloy), as shown in Figure 5.28d-f. The size of the α plates is obviously larger than that of PM alloy, with a length of 500 nm-2.5 μm. In Figure 5.28d and e, the remarkable dislocation tangles can be clearly seen against the α plates, indicating the deformation is concentrated at these areas. It can also be seen in Figure 5.28f that the dislocation density is very high near the fracture point inside the lath α plate. Based on these

observations, it can be declared that the shearing and fracturing of dynamic α precipitation are achieved by the local stress concentration.

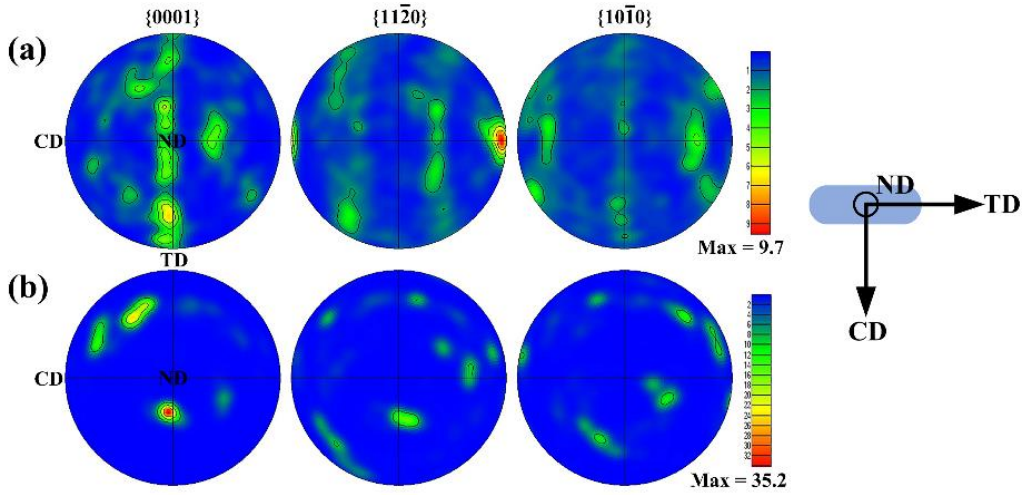

Figure 5.29 EBSD α phase pole figures of Ti-5553 alloys deformed at 800 °C/0.1 s^{-1}: (a) PM alloy and (b) IM alloy.

Figure 5.29 shows the α phase pole figures of PM and IM alloys deformed at 800 °C/0.1 s^{-1}. A weak <11-20>//CD fibre texture (maximum intensity is 9.7 times the random texture) is identified in PM alloy (Figure 5.29a). Nevertheless, a very strong nearly <0001>//ND (30° incline to TD) fibre texture (maximum intensity is 35.2 times of the random texture) can be observed in Figure 5.29b, for IM alloy. Therefore, it can be deduced that the dynamic α precipitation in IM alloy has a strongly preferred crystalline orientation and this texture is not affected by mechanical shearing. On the contrary, the weak texture for the α precipitates in PM alloy indicates that the crystalline orientation of α precipitates may be varied during the process of dynamic globularization and coarsening.

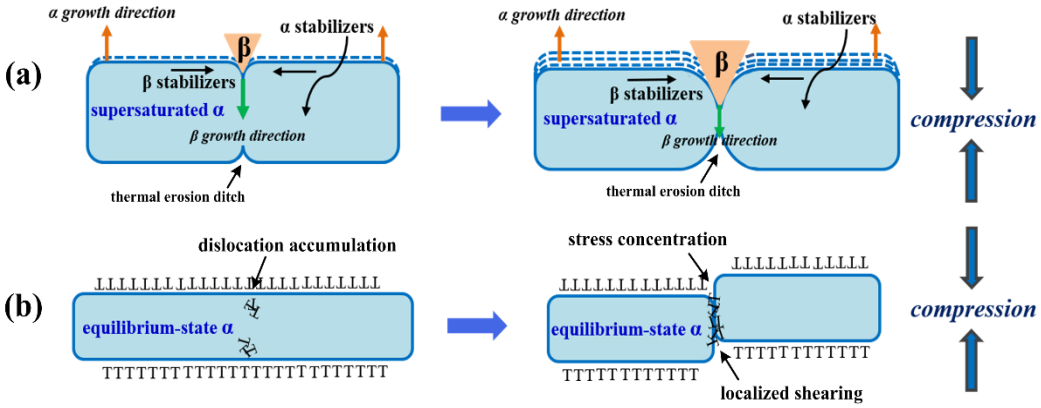

Figure 5.30 Schematic diagram showing the dynamic α precipitation mechanisms for: (a) β phase wedging and α phase coarsening in PM alloy; (b) mechanical α phase shearing in IM alloy.

The PM alloy is supersaturated after the hot pressing and fast cooling to room temperature, and it has far fewer α precipitates than that of the IM alloy (initial microstructure). When heating and compressing the PM samples, the original α precipitates will grow large and coarse (to become the large-size lath α phase in Figure 5.28b-c), and some new globular α precipitates are also formed. The α precipitates in PM alloy have a higher content of β stabilizers (V, Mo and Cr) and the β matrix has a higher content α stabilizers (Al, O) than those of IM alloy [29-32] due to the much higher cooling rate after consolidation. During the hot compression, the saturated V, Mo and Cr will diffuse from α through the thermal erosion ditch to the adjacent β phase, leading to a β phase wedging into α and separating the α precipitates into two parts. Meanwhile, Al and O at the non-equilibrium β matrix will migrate towards the α precipitates, resulting in the dynamic α phase coarsening accompanied by the grain orientation variation. These two processes are enabled and promoted by both the elements concentration gradient and the external driving force introduced by hot deformation. However, for IM alloy, the dynamic mechanical shearing and fracturing of the equilibrium-state large α precipitates (developed from the primary α phases) are realized by the intense local stress concentration without the redistribution of alloying elements. The sketch illustration showing these processes for PM and IM alloy are displayed in Figure 5.30a and b, respectively.

Furthermore, the different aspect ratios of α precipitates leads to the competition of the two DαG modes in PM alloy. The grown original α precipitates in PM alloy have a high aspect ratio and are fractured following the same mechanism as that happened in IM alloy. However, most of the newly formed α precipitates in PM alloy are prone to be separated by β phase wedging, because the local stress concentration is restrained around the newly formed α precipitates that have a low aspect ratio and elemental diffusion would play a more important role in the process of DαG. The sketch illustration showing the whole dynamic α precipitation mechanism of the two alloys are shown in Figure 5.31.

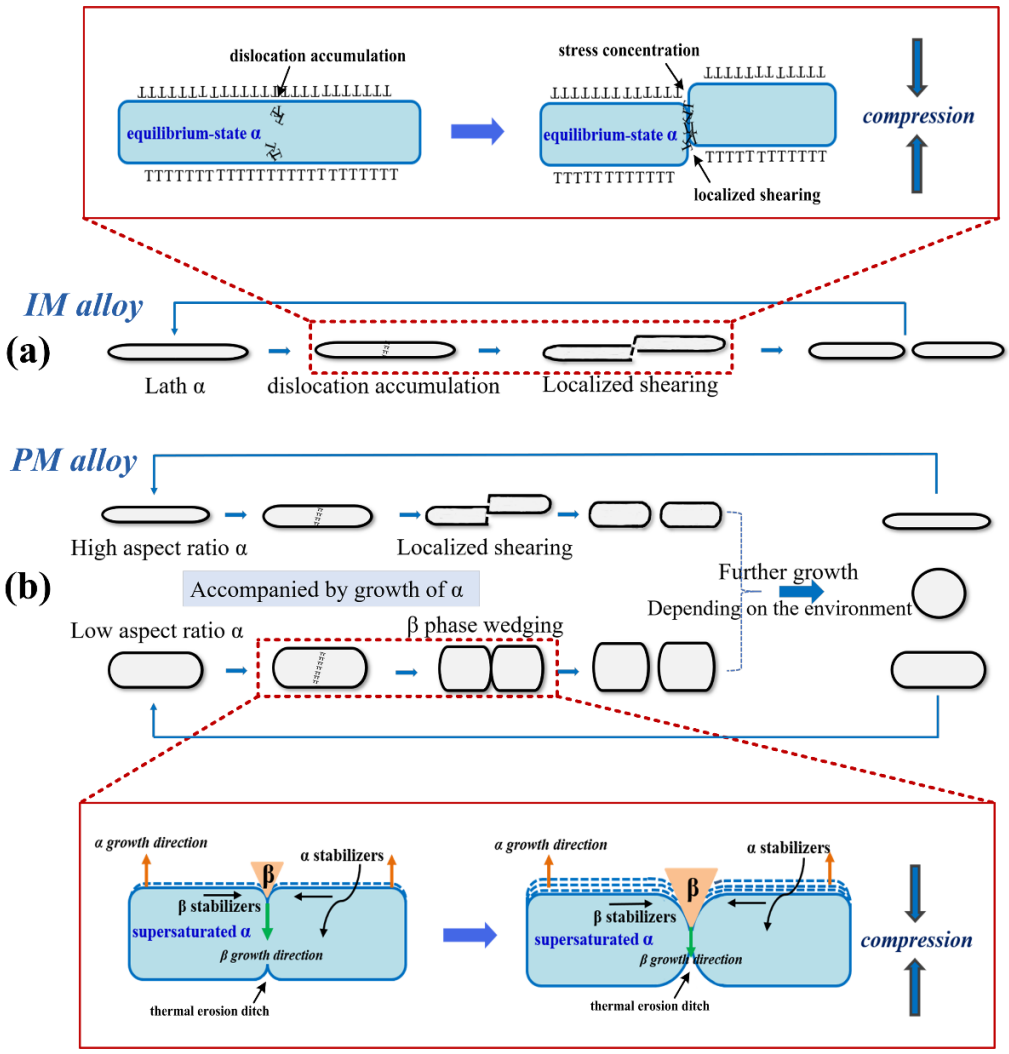

Figure 5.31 Schematic diagram showing the whole dynamic α precipitation mechanisms of the two alloys during their hot deformation at 800 °C: (a) PM alloy; (b) IM alloy.

5.7.2 Comparison of dynamic recrystallization mechanism

As is discussed in Section 4.7.1, the mechanism of dynamic recrystallization phenomenon in PM alloy has been determined as discontinuous mechanism DDRX. In this section, more detailed results and the comparison of DRX mechanism between PM and IM alloy will be provided and conducted.

The DRX grains and their HAGBs in PM alloy are primarily formed at the original grain boundaries with necklace-shaped structures (Figure 5.22a-b). Whereas, for IM alloy, the HAGBs are transformed gradually and consecutively from LAGBs, and the DRX grains are mainly nucleated on the inside of prior grains (Figure 5.27d-e). In addition, the dislocation density of the DRX grain inside is higher in IM alloy than in PM alloy (Figure 5.22c and Figure 5.27f). These suggest that the DRX

mechanisms are different for the two alloys. The cumulative misorientation (point to origin) and local misorientation (point to point) along the vectors, labelled at the segment enlarged images of EBSD IPF maps in Figure 5.22a and Figure 5.27d, are calculated to further investigate the DRX mechanisms of the alloys, and the results are shown in Figure 5.32. It can be seen that both of the angles of cumulative and local misorientation alongside the DRX nuclei vectors (A1 and A2), for PM alloy, are less than 3.5° for A1 and 1.6° for A2. Whereas, for IM alloy, the misorientation variations are distinctly large at the DRX grains interior, where HAGBs are not fully formed yet (vector B1 and B2), and the cumulative and local misorientation angles are higher than 15° for B1 and 13° for B2. These results indicate that the rotation of sub-grain takes a significant role in the formation of DRX grains for IM alloy compared to PM alloy.

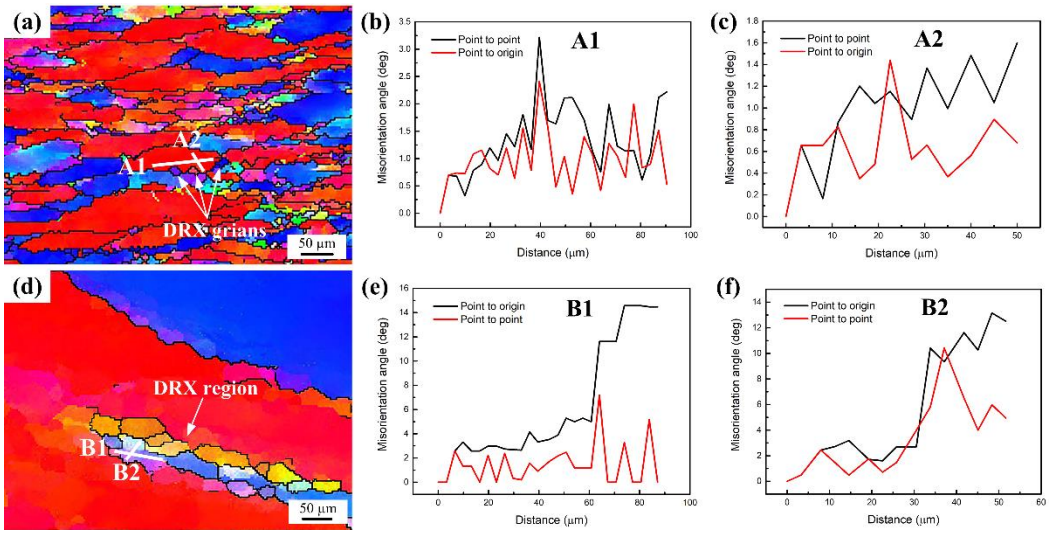

Figure 5.32 Segment enlarged EBSD IPF maps: (a) PM alloy deformed at 900 °C/0.1 s^{-1}; (d) IM alloy deformed at 1100 °C/0.1 s^{-1} and variations of misorientation angles along the labelled vector of (b) A1; (c) A2; (e) B1; (f) B2.

The high magnification TEM microstructures showing the different DRX mechanisms at the temperature of 900 °C for PM alloy and 1100 °C for IM alloy (the temperatures that DRX processes extensively occur in the two alloys) are presented in Figure 5.33. As shown in Figure 5.33a-d, a DRX nucleus appears at the triple-junction of (Figure 5.33a-b) or next to (Figure 5.32c-d) the prior β grain boundaries. Afterwards, the growth of the DRX nucleus is caused by the migration and extension of prominent HAGBs towards the prior β matrix (Figure 5.33e). Moreover, it is clearly found that, the dislocation density is low inside the DRX grains but much higher in the β matrix close to the HAGBs of the DRX nucleus

(Figure 5.33b-e). Figure 5.33f shows the morphology of a well-grown DRX grain, the grain size is much larger than the DRX grains at initiation and growing stages, and it is free of internal dislocation.

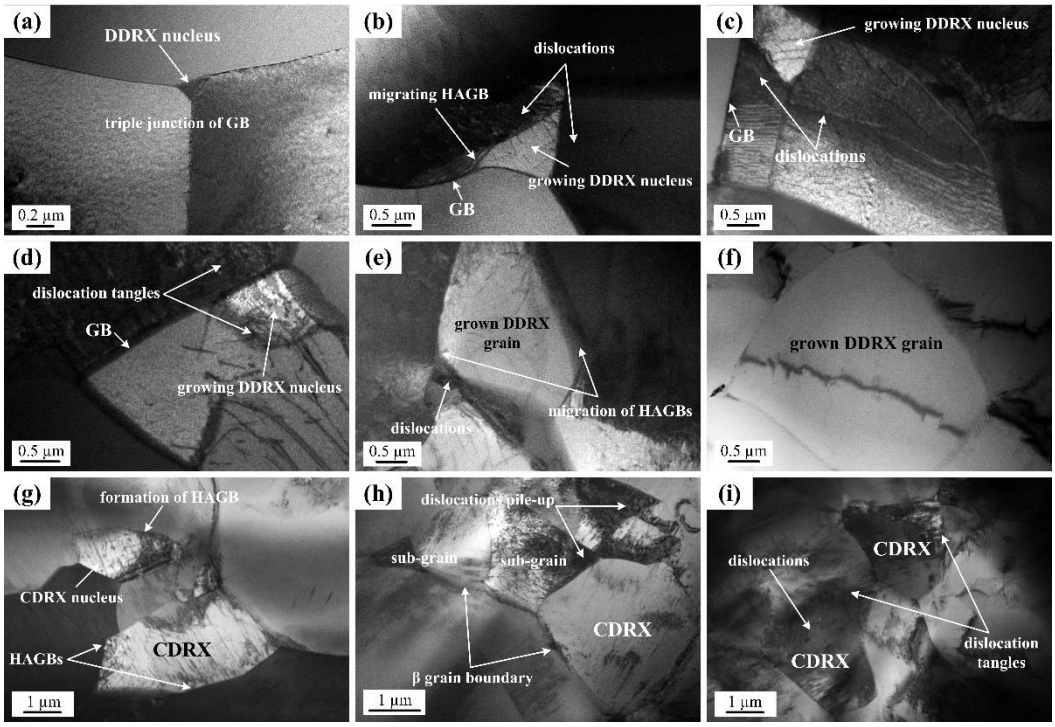

Figure 5.33 TEM microstructures showing the DRX mechanisms of Ti-5553 alloys: PM alloy at: (a)-(d) 900 °C/0.1 s^{-1}; (e)-(f) 900 °C/0.01 s^{-1}. IM alloy at: (g) 1100 °C/0.1 s^{-1}; (h)-(i) 1100 °C/0.01 s^{-1}. GB refers to grain boundary.

As for IM alloy, the DRX nucleus is formed internally in the preceding β grain and their boundary is transformed from vague LAGBs into HAGBs, while the grown DRX grain is already surrounded by distinct HAGBs (as shown in Figure 5.33g). In Figure 5.33h, the growing DRX grain is observed against the prior β grain boundary and it is surrounded by abundant dislocations and sub-grains. Meanwhile, the TEM image in Figure 5.33i also shows that the grown DRX grains are located in the β matrix and the dislocations are still visible in the DRX grain, but the dislocation density is obviously lower than that in β matrix. These suggest that the DRX grains in IM alloy are formed by merging previous sub-grains and their HAGBs are growing by aggregating the adjacent LAGBs.

From the above analysis, we can speculate that the DRX mechanism in PM alloy is discontinuous dynamic recrystallization (DDRX), which is predominately controlled by the nucleation of the new grains at the original grain boundaries and the subsequent migration of their HAGBs induced by the distortion strain energy.

This mechanism is often found in metallic materials with low stacking fault energy (SFE) [33]. The growth of DDRX grains is promoted by the dislocation gradient that is perpendicular to the HAGBs where the deformation concentrates on. During the migration of the HAGBs of DDRX grains, the near-by dislocations are constantly absorbed and sub-grains are not obviously rotated [34]. For IM alloy, the DRX mechanism is dominated by continuous dynamic recrystallization (CDRX), which is the main mechanism for the metallic materials with high SFE and processed at elevated temperatures [35]. The formation of new grains is governed by the progressive rotation of adjacent sub-grains, and the transformation of LAGBs into new HAGBs is implemented by a homogeneous increase of misorientation (HIM) with dislocation slip and climb along the LAGBs. This leads to the variation of dislocation density smaller inside and outside of the CDRX grains than DDRX grains. The schematics in Figure 5.34 illustrate the different DRX nucleation mechanisms for PM and IM alloys.

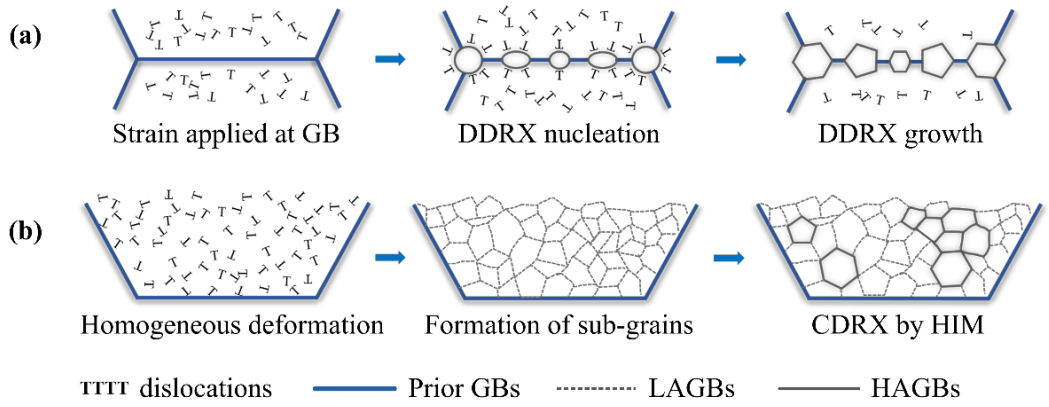

Figure 5.34 Schematic diagram showing the DRX nucleation mechanisms for (a) PM alloy and (b) IM alloy. GB refers to the grain boundary.

5.7.3 Construction and analysis of deformation mechanism maps

After the detailed characterization and analysis of the deformation mechanism of the two alloys processed in all the different conditions, with the combination of the activation energy and processing maps, the precise deformation mechanism maps during their hot processing can finally be established. The schematic maps illustrating the dominated deformation mechanisms of PM and IM alloy processed at the temperature ranging from 700 °C to 1100 °C and the strain rate between 0.001 s^{-1} and 10 s^{-1} are exhibited in Figure 5.35 and 5.36, respectively. The dominated active deformation mechanism of the alloy (large plastic deformation, 70% height

reduction) during its hot processing can be read directly and accurately from the map when the deformation parameters (temperature and strain rate) are determined.

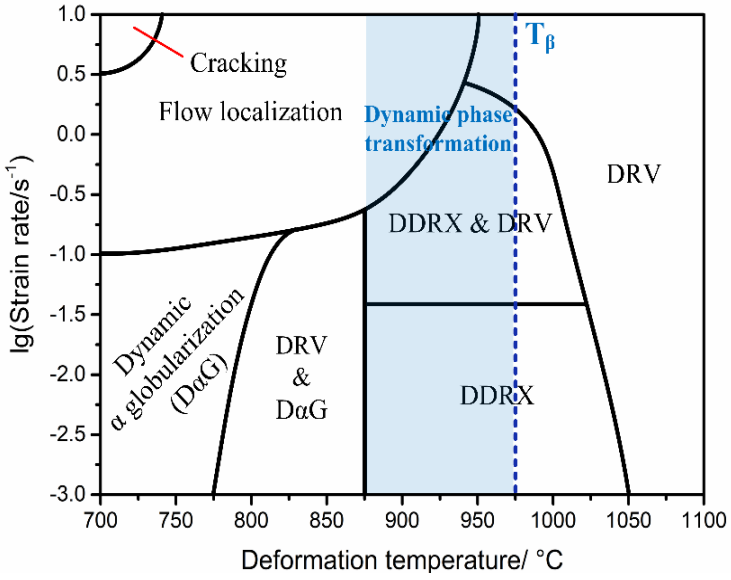

Figure 5.35 Schematic mapping of the dominated deformation mechanism of PM Ti-5553 alloy with varying deformation temperature and strain rate.

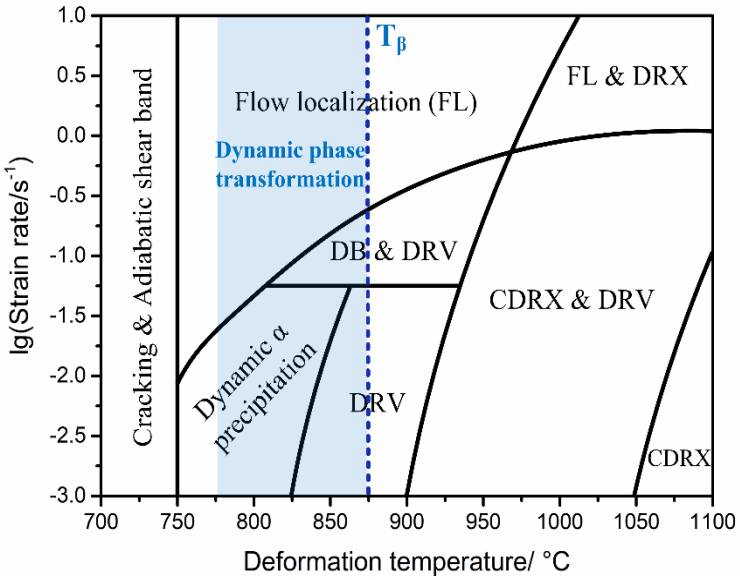

Figure 5.36 Schematic mapping of the dominated deformation mechanism of IM Ti-5553 alloy with varying deformation temperature and strain rate.

Overall, both the PM and IM alloys suggest various deformation mechanisms with changing the deformation parameters, and they display distinct contrasting mechanisms at the same domain. IM alloy has a large flow instability domain which is located in the wide regions of both $T < 750$ °C and $\dot{\varepsilon} > 1$ s^{-1} domains, with dominant mechanisms of external cracking, ASB and FL (Figure 5.36). While the unsafe domain of PM alloy is relatively narrow and only located at the left top area of the map with the deformation mechanism of cracking and FL (Figure 5.35). In

the low temperature /low strain rate region ($T < 950$ °C/$\dot{\varepsilon} > 0.1$ s^{-1}), PM alloy shows significant microstructural change by DαG and α phase coarsening rather than simple shearing of dynamic α precipitation happening in IM alloy, as discussed in the previous sections. Most importantly, PM alloy shows a full DRX region that is located at the moderate temperature /low strain rate region, and this is larger than that of IM alloy, which only appears at the right bottom corner at the high-temperature region. Moreover, the recrystallization process of PM alloy is controlled by DDRX, but CDRX is the primary recrystallization mechanism for IM alloy. Additionally, PM alloy exhibits the dynamic phase transformation region at a higher temperature (about 875 °C-975 °C) than that of IM alloy (about 775 °C-875 °C), attributed to its higher beta transus temperature.

The larger safe-processing window, lower complete DRX temperature and different DRX mechanism of PM alloy can be primarily attributed to the different initial microstructure characteristics and higher oxygen content compared to IM alloy. Similar to the influence of the grain size on the flow stress of PM and IM alloys, the grain refinement of PM alloy can offer easier glide path along the boundaries for grains that have the viscous flow effect, resulting in the reduction of deformation resistance and the shrinkage of the instability domain. However, the coarse-grain IM alloy is more likely to induce inhomogeneous and localized deformation, resulting in further ASB, FL, DB and cracking. Furthermore, the finer grain size and the resultant higher grain boundary density also promote the DRX process of PM alloy, especially for DDRX that is developed from the nuclei situated at the grain boundaries by providing more nucleation sites. It is also well accepted that the DRX process is controlled by thermal diffusion of the elements. The existence of high grain boundary density in PM alloy can act as a channel for fast diffusion [36, 37], contributing to the progress of DRX at a much less extreme condition.

The high oxygen level of PM alloy also plays a positive role in promoting DRX to occur at the lower temperature region. Oxygen is a solid solution element in titanium alloys in the form of interstitial atoms [38]. It can form pairs with vacancies and stabilize a higher vacancy concentration, and thus increase the element thermal diffusion rate in the alloy [39, 40]. Concurrently, the dislocation movement can be pinned due to the asymmetric distortions in the lattice caused by the presence of oxygen interstitials. Thus, higher oxygen content can also accelerate dislocation

generation and then make it easier for DRX nucleation. Moreover, the extra solution effect caused by oxygen leads to the reduction of SFE of PM alloy [41, 42], which promotes the occurrence of DDRX at a relatively low temperature. In addition, the low SFE will lead to generating wider stacking faults, and this will make it difficult for dislocations to slip and climb. As a result, the dislocation tangling will be serious in PM alloy, and then the local dislocation density gradient will become high enough to initiate the formation of new DDRX grains. On the contrary, in IM alloy, the dislocation movement is flexible because of the high SFE, so that dislocation accumulation and sub-structure rotation are suppressed. Thus, the coarse grains and high SFE of IM alloy promote the progress of CRDX but impede DDRX.

5.8 Summary

In this chapter, a comprehensive comparative investigation of hot deformation behaviour and softening mechanisms for the as-consolidated PM and as-cast IM Ti-5553 alloys was performed. The flow behaviour, discontinuous yielding phenomenon and the adiabatic temperature rising were investigated and compared with the flow curves of the two alloys. Furthermore, the deformation activation energy maps and hot processing maps were established successfully to contrast the hot workability of the two alloys. Microstructural evolution characteristics of the two alloys were studied and analyzed to disclose their detailed deformation mechanisms at different processing conditions, and then the precise deformation mechanism maps of the two alloys were constructed for comparing their deformation mechanisms at varied processing conditions. The primary conclusions are summarized as below:

(1) PM alloy exhibits lower flow stress, slighter discontinuous yielding phenomenon and less adiabatic temperature rising than IM alloy during hot deformation.
(2) PM alloy has lower average activation energy, larger optimal processing windows and smaller flow instability regions than IM alloy.
(3) PM alloy has better hot workability and higher cracking resistance than the IM alloy during hot compression: 45° shear cracking occurs in IM alloy specimens when the deformation condition is at 700 °C/10 s^{-1}, however, only edge cracking appears in PM alloy at the same condition.

(4) Adiabatic shear banding, external cracking and flow localization are the dominant deformation mechanisms in the wide instability domain of IM alloy, while the unstable processing region of PM alloy is obviously shirked and the deformation mechanism is primarily dominated by flow localization.

(5) Dynamic α globularization and coarsening are the dominated mechanisms for PM alloy deformed at low temperature (700 °C to 800 °C) and low strain rate ($\dot{\varepsilon} \leq 0.1\ s^{-1}$), while IM alloy is governed by dynamic α precipitation and its fracturing with strong texture when deformed at the same condition.

(6) The dynamic recrystallization temperature of PM alloy is lower than that of IM alloy, and the full DRX region is at 900 °C-1050 °C/0.001 s^{-1}-0.1 s^{-1} for PM alloy and 1050 °C-1100 °C/0.001 s^{-1}-0.1 s^{-1} for IM alloy. The DRX mechanism is controlled by DDRX for PM alloy and CDRX for IM alloy.

Reference

[1] Y. Zhu, W. Zeng, F. Feng, Y. Sun, Y. Han, Y. Zhou, Characterization of hot deformation behavior of as-cast TC21 titanium alloy using processing map, Mater. Sci. Eng. A 528 (2011) 1757-1763.

[2] J.K. Fan, H.C. Kou, M.J. Lai, B. Tang, H. Chang, J.S. Li, Characterization of hot deformation behavior of a new near beta titanium alloy: Ti-7333, Mater. Des. 49 (2013) 945-952.

[3] R.A. Masumura, P.M. Hazzledine, C.S. Pande, Yield stress of fine grained materials, Acta Mater. 46 (1998) 4527-4534.

[4] A. Bussiba, A. Ben Artzy, A. Shtechman, S. Ifergan, M. Kupiec, Grain refinement of AZ31 and ZK60 Mg alloys-towards superplasticity studies, Mater. Sci. Eng. A 302 (2001) 56-62.

[5] M.R. Barnett, A.G. Beer, D. Atwell, A. Oudin, Influence of grain size on hot working stresses and microstructures in Mg-3Al-1Zn, Scripta Mater. 51 (2004) 19-24.

[6] S. Nemat-Nasser, W.G. Guo, J.Y. Cheng, Mechanical properties and deformation mechanisms of a commercially pure titanium, Acta Mater. 47 (1999) 3705-3720.

[7] D.R. Chichili, K.T. Ramesh, K.J. Hemker, The high-strain-rate response of alpha-titanium: experiments, deformation mechanisms and modeling, Acta Mater. 46 (1998) 1025-1043.

[8] X.G. Fan, Y. Zhang, P.F. Gao, Z.N. Lei, M. Zhan, Deformation behavior and microstructure evolution during hot working of a coarse-grained Ti-5Al-5Mo-5V-3Cr-1Zr titanium alloy in beta phase field, Mater. Sci. Eng. A 694 (2017) 24-32.

[9] I. Philippart, H.J. Rack, High temperature dynamic yielding in metastable Ti-6.8Mo-4.5Fe-1.5Al, Mater. Sci. Eng. A 243 (1998) 196-200.

[10] J. Fan, H. Kou, M. Lai, B. Tang, H. Chang, J. Li, High temperature discontinuous yielding in a new near β titanium alloy Ti-7333, Rare Metal Met. Eng. 43 (2014) 808-812.

[11] P. Wanjara, M. Jahazi, H. Monajati, S. Yue, J.P. Immarigeon, Hot working behavior of near-α alloy IMI834, Mater. Sci. Eng. A 396 (2005) 50-60.

[12] Z.L. Zhao, H. Li, M.W. Fu, H.Z. Guo, Z.K. Yao, Effect of the initial microstructure on the deformation behavior of Ti60 titanium alloy at high temperature processing, J. Alloys Compd. 617 (2014) 525-533.

[13] S. Ankem, J.G. Shyue, M.N. Vijayshankar, R.J. Arsenault, The effect of

volume per cent of phase on the high temperature tensile deformation of two-phase Ti-Mn alloys, Mater. Sci. Eng. A 111 (1989) 51-61.
[14] I. Weiss, S.L. Semiatin, Thermomechanical processing of beta titanium alloys - an overview, Mater. Sci. Eng. A 243 (1998) 46-65.
[15] L.X. Li, Y. Lou, L.B. Yang, D.S. Peng, K.P. Rao, Flow stress behavior and deformation characteristics of Ti-3Al-5V-5Mo compressed at elevated temperatures, Mater. Des. 23 (2002) 451-457.
[16] M.N. Vijayshankar, S. Ankem, High temperature tensile deformation behavior of β-Ti alloys, Mater. Sci. Eng. A 129 (1990) 229-237.
[17] Y.H. Jiang, Z.Y. Chen, C.K. Zhan, T. Chen, R.K. Wang, C.M. Liu, Adiabatic shear localization in pure titanium deformed by dynamic loading: Microstructure and microtexture characteristic, Mater. Sci. Eng. A 640 (2015) 436-442.
[18] B. Huang, X. Miao, X. Luo, Y. Yang, Y. Zhang, Microstructure and texture evolution near the adiabatic shear band (ASB) in TC17 Titanium alloy with starting equiaxed microstructure studied by EBSD, Mater. Charact. 151 (2019) 151-165.
[19] J.Q. Zhang, H.S. Di, H.T. Wang, K. Mao, T.J. Ma, Y. Cao, Hot deformation behavior of Ti-15-3 titanium alloy: a study using processing maps, activation energy map, and Zener-Hollomon parameter map, J. Mater. Sci. 47 (2012) 4000-4011.
[20] Y. Sun, Z.P. Wan, L.X. Hu, J.S. Ren, Characterization of hot processing parameters of powder metallurgy TiAl-based alloy based on the activation energy map and processing map, Mater. Des. 86 (2015) 922-932.
[21] Y. Zhu, W. Zeng, F. Zhang, Y. Zhao, X. Zhang, K. Wang, A new methodology for prediction of fracture initiation in hot compression of Ti40 titanium alloy, Mater. Sci. Eng. A 553 (2012) 112-118.
[22] Z.H. Cao, Y. Sun, Z.P. Wan, L.X. Hu, Investigation on cracking behavior and development of a fracture model of Ti-47Al-2Nb-2Cr alloy during hot deformation, J. Mater. Eng. Perform. 27 (2018) 5360-5369.
[23] Z. Yancun, Z. Weidong, Z. Yongqing, Influence of deformation parameters on fracture mechanism of Ti40 titanium alloy, Rare Metal Met. Eng. 46 (2017) 1207-1213.
[24] C. Zheng, F. Wang, X. Cheng, J. Liu, T. Liu, Z. Zhu, K. Yang, M. Peng, D. Jin, Capturing of the propagating processes of adiabatic shear band in Ti–6Al–4V alloys under dynamic compression, Mater. Sci. Eng. A 658 (2016) 60-67.
[25] W. Chen, Y. Yamamoto, W.H. Peter, Investigation of pressing and sintering

processes of CP-Ti powder made by armstrong process, Key Eng. Mater. 436 (2010) 123-130.
[26] Y.C. Zhu, W.D. Zeng, J.L. Liu, Y.Q. Zhao, Y.G. Zhou, H.Q. Yu, Effect of processing parameters on the hot deformation behavior of as-cast TC21 titanium alloy, Mater. Des. 33 (2012) 264-272.
[27] M.R. Jandaghi, H. Pouraliakbar, Study on the effect of post-annealing on the microstructural evolutions and mechanical properties of rolled CGPed Aluminum-Manganese-Silicon alloy, Mater. Sci. Eng. A 679 (2017) 493-503.
[28] N.G. Jones, M. Jackson, On mechanism of flow softening in Ti–5Al–5Mo–5V–3Cr, Mater. Sci. Technol. 27 (2013) 1025-1032.
[29] X.X. Gao, W.D. Zeng, S.F. Zhang, Q.J. Wang, A study of epitaxial growth behaviors of equiaxed alpha phase at different cooling rates in near alpha titanium alloy, Acta Mater. 122 (2017) 298-309.
[30] Y.Q. Chen, E. Francis, J. Robson, M. Preuss, S.J. Haigh, Compositional variations for small-scale gamma prime precipitates formed at different cooling rates in an advanced Ni-based superalloy, Acta Mater. 85 (2015) 199-206.
[31] F.M. Qiang, H.C. Kou, B. Tang, L. Song, J.S. Li, Effect of cooling rate on microstructure evolution of Ti-45Al-8.5Nb-0.2W-0.2B-0.02Y alloy during multi-step heat treatment, Mater. Charact. 145 (2018) 210-217.
[32] M. Meng, X.G. Fan, H. Yang, L.G. Guo, M. Zhan, P.F. Gao, Precipitation of secondary alpha in competition with epitaxial growth of primary alpha in two-phase titanium alloys, J. Alloys Compd. 714 (2017) 294-302.
[33] S. Wang, J.R. Luo, L.G. Hou, J.S. Zhang, L.Z. Zhuang, Physically based constitutive analysis and microstructural evolution of AA7050 aluminum alloy during hot compression, Mater. Des. 107 (2016) 277-289.
[34] X. Wang, L. Wang, L.S. Luo, H. Yan, X.Z. Li, R.R. Chen, Y.Q. Su, J.J. Guo, H.Z. Fu, High temperature deformation behavior of melt hydrogenated (TiB + TiC)/Ti-6Al-4V composites, Mater. Des. 121 (2017) 335-344.
[35] S. Emami, T. Saeid, R.A. Khosroshahi, Microstructural evolution of friction stir welded SAF 2205 duplex stainless steel, J. Alloys Compd. 739 (2018) 678-689.
[36] H. Iwaoka, M. Arita, Z. Horita, Hydrogen diffusion in ultrafine-grained palladium: Roles of dislocations and grain boundaries, Acta Mater. 107 (2016) 168-177.
[37] M.S. Hooshmand, C. Niu, D.R. Trinkle, M. Ghazisaeidi, First-principles prediction of oxygen diffusivity near the (10-12) twin boundary in titanium, Acta

Mater. 156 (2018) 11-19.
[38] Q. Yu, L. Qi, T. Tsuru, R. Traylor, D. Rugg, J.W. Morris, Jr., M. Asta, D.C. Chrzan, A.M. Minor, Metallurgy. Origin of dramatic oxygen solute strengthening effect in titanium, Science 347 (2015) 635-639.
[39] Y.V.R.K. Prasad, T. Seshacharyulu, S.C. Medeiros, W.G. Frazier, Influence of oxygen content on the forging response of equiaxed (α+β) preform of Ti–6Al–4V: commercial vs. ELI grade, J. Mater. Process. Technol. 108 (2001) 320-327.
[40] A.D. LeClaire, Diffusion in body-centered cubic metals, ASM, Metals Park, Ohio 3 (1965).
[41] P. Kwasniak, M. Muzyk, H. Garbacz, K.J. Kurzydlowski, Influence of C, H, N, and O interstitial atoms on deformation mechanism in titanium-First principles calculations of generalized stacking fault energy, Mater. Lett. 94 (2013) 92-94.
[42] R. Salloom, R. Banerjee, S.G. Srinivasan, Effect of β-stabilizer elements on stacking faults energies and ductility of α-titanium using first-principles calculations, J. Appl. Phys. 120 (2016) 175105.

6 Thermomechanical processing and heat treatment of PM Ti-5553 alloy

6.1 Introduction

Based on the understanding of hot deformation behaviour, processing maps and microstructural evolution characteristics obtained from the thermal physical simulation (in Chapters 4 and 5), the thermomechanical processing conditions were determined for the as-consolidated PM Ti-5553 alloy billets, then the designed one-step open-die forging was performed at different conditions (temperatures, strain rates and cooling modes) to produce large-size forged alloy pancake with low cost. The as-forged PM alloy's microstructure, mechanical properties as well as the microstructural evolution mechanisms were examined and revealed. Furthermore, the post-heat treatments were carried out to tailor the as-forged PM alloy's microstructure and mechanical properties. Finally, the processing-microstructure-mechanical property relationship was established for the PM Ti-5553 alloy.

6.2 Determination of varying hot forging processes

According to the hot processing map and microstructural evolution characteristics of PM Ti-5553 alloy during thermal physical simulation (as discussed in Chapters 4 and 5), the optimal processing window is suggested as: the deformation temperature is between 900 °C-1050 °C, the strain rate is below 1 s^{-1}, and the deformation degree is higher than 70% of height reduction. The PM Ti-5553 alloy exhibits excellent hot workability with stable flow and satisfied microstructure control within this processing window. Furthermore, the condition of 950 °C/0.01 s^{-1} could be the potential "best" processing region, as the occurrence of extensive DRX with significant grain refinement. Further considering the processing cost, one-step thermomechanical processing (TMP) process is preferred than multi-pass TMP processes. Therefore, four simple one-step TMP routes are finally selected for processing the as-consolidated PM Ti-5553 alloy billet, as shown in Figure 6.1.

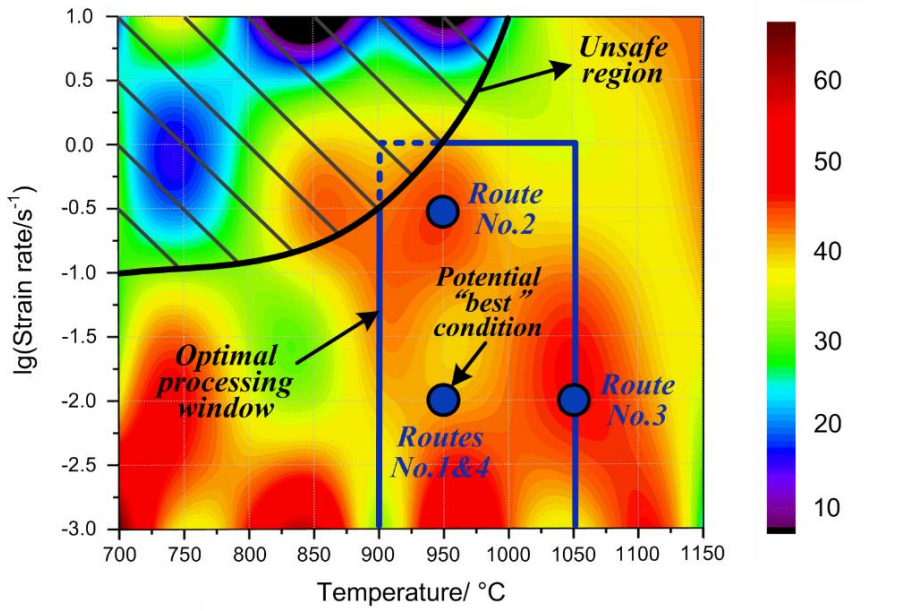

Figure 6.1 The indications of applied TMP conditions on the power dissipation map ($\dot{\varepsilon}$=1.0) of PM Ti-5553 alloy with the indications of unsafe, optimal, and "best" windows/conditions.

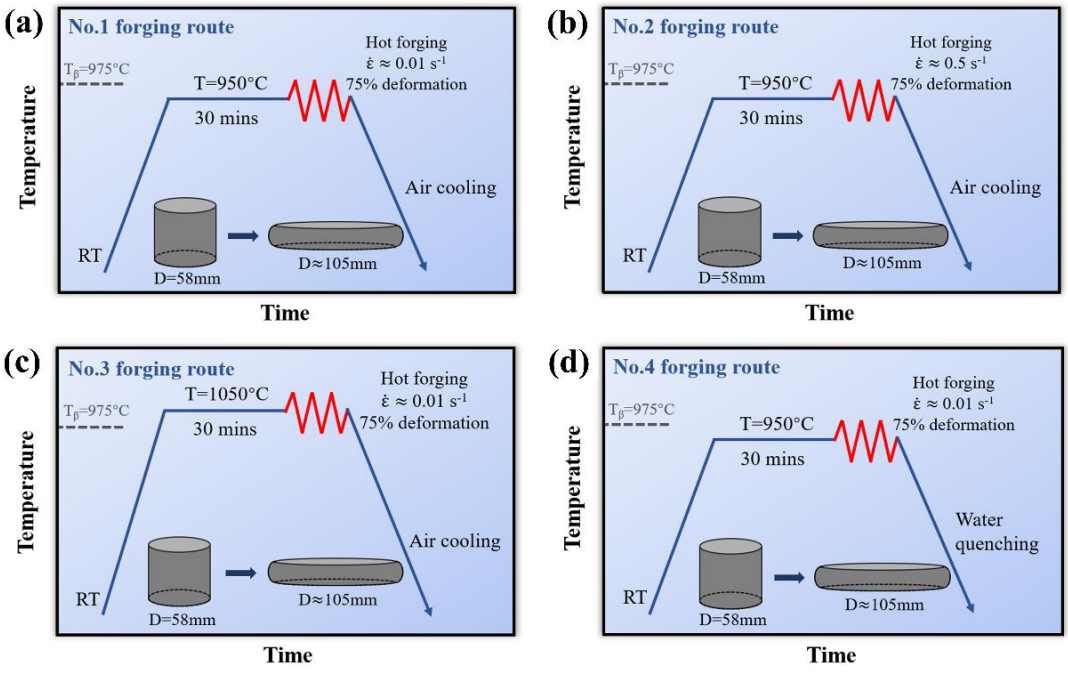

Figure 6.2 Schematic diagrams showing various thermomechanical processing routes for the as-consolidated PM Ti-5553 alloy billets: (a) Route No.1, single uniaxial forging at 950 ℃ and strain rate about 0.01 s^{-1} followed by air cooling; (b) Route No.2, single uniaxial forging at 950 ℃ and strain rate about 0.5 s^{-1} followed by air cooling; (c) Route No.3, single uniaxial forging at 1050 ℃ and strain rate about 0.01 s^{-1} followed by air cooling; (d) Route No.4, single uniaxial forging at 950 ℃ and strain rate about 0.01 s^{-1} followed by water quenching.

The detailed processing procedures for the various TMP routes of PM Ti-5553 alloy are summarized as below, and the related sketches are shown in Figure 6.2.

1. Route No.1, near-β forging: The alloy billet was heated up to 950 °C and held the temperature for 30 minutes, subsequently forged into pancake at the strain rate of about 0.01 s^{-1} and with a large deformation degree of 75% height reduction, and then air-cooled (AC) to room temperature. The alloy produced following this route is referred as to FR-1.

2. Route No.2, near-β forging: The alloy billet was heated up to 950 °C and held the temperature for 30 minutes, subsequently forged into pancake at the strain rate of about 0.5 s^{-1} and with a large deformation degree of 75% height reduction, and then air-cooled to room temperature. The alloy produced following this route is referred as to FR-2.

3. Route No.3, β forging: The alloy billet was heated up to 1050 °C and held the temperature for 30 minutes, subsequently forged into pancake at the strain rate of about 0.01 s^{-1} and with a large deformation degree of 75% height reduction, and then air-cooled to room temperature. The alloy produced following this route is referred as to FR-3.

4. Route No.4, Near-β forging: The alloy billet was heated up to 950 °C and held the temperature for 30 minutes, subsequently forged into pancake at the strain rate of about 0.01 s^{-1} and with a large deformation degree of 75% height reduction, and then water-quenched (WQ). The alloy produced following this route is referred as to FR-4.

6.3 Appearance and basic characteristics of the as-forged PM Ti-5553 alloy pancakes

6.3.1 Appearance of the pancakes

Figure 6.3 shows the overall appearance of the PM Ti-5553 alloy pancake processed following Route No.1. It is clear that the pancake has a regular/uniform shape, good surface quality without obvious external cracks, indicating that the PM Ti-5553 alloy is processed safely without seriously unstable deformation.

Figure 6.3 Appearance of the as-forged PM Ti-5553 alloy pancake (following Route No.1).

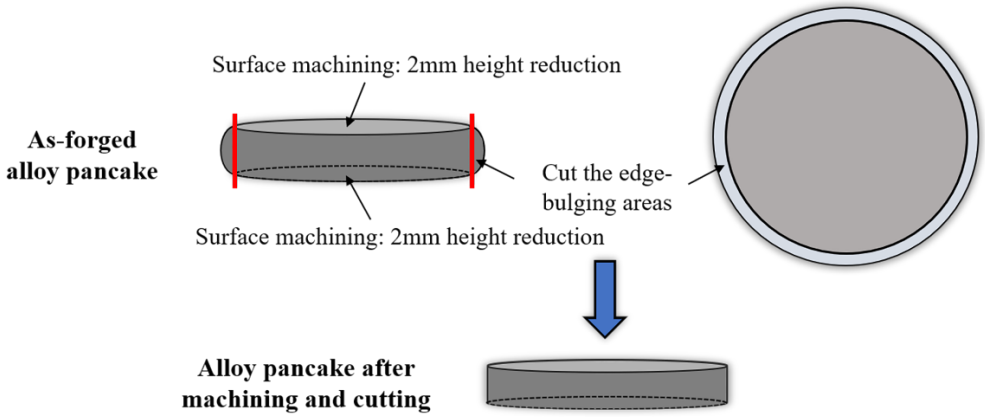

Figure 6.4 Schematic diagram showing the surface machining and edge-bulging-area cutting details of the as-forged alloy pancakes.

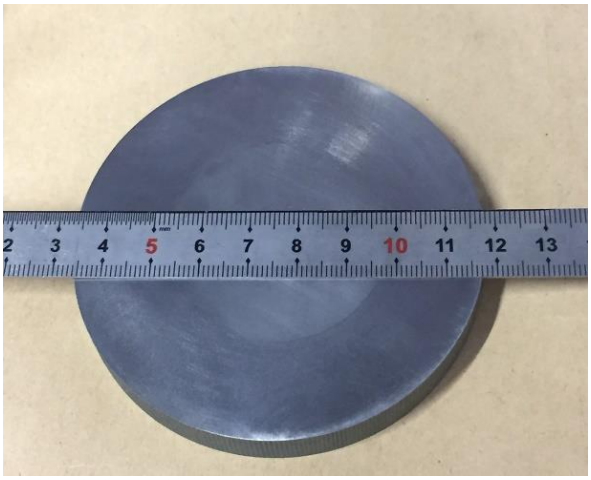

Figure 6.5 Appearance of as-forged PM Ti-5553 alloy pancake (processed following Route No.1) after edge-bulging-area cutting and surface machining.

During the uniaxial forging, a thin layer near the top and bottom surfaces of the forged pancakes experienced a relatively small degree of deformation and become

so-called “dead zone” due to the die friction and chilling effects [1, 2], and the deformation at the edge bulging areas is neglected as well [3, 4]. Therefore, these less-deformed areas on the as-forged alloy pancakes are machined-off or cut-off (see the sketch in Figure 6.4), and only the large deformed areas of the pancake are kept for further investigation. Figure 6.5 shows the overall appearance of the as-forged PM Ti-5553 alloy pancake (processed following Route No.1) after cutting the edge-bulging-area and machining the top and bottom surfaces.

6.3.2 Chemical composition and density of the as-forged alloy pancakes

Chemical composition analysis and density measurement are conducted for all the as-forged PM Ti-5553 alloys (the sampling position is indicated in Figure 6.6), and the results are listed in Table 6.1 and Table 6.2, respectively.

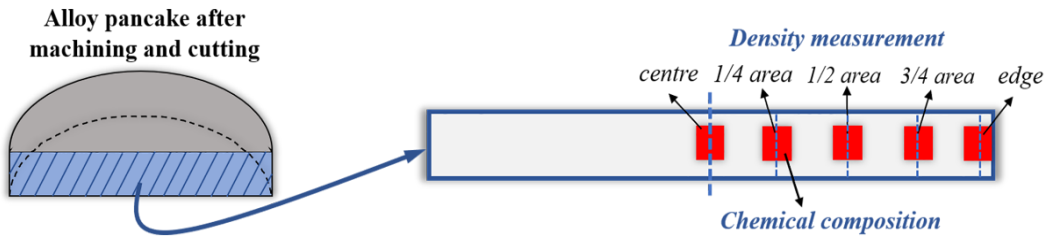

Figure 6.6 Schematic diagram showing the sampling positions on the as-forged PM Ti-5553 alloy pancakes for density and chemical composition measurements.

Table 6.1 Chemical compositions of the as-consolidated and as-forged PM Ti-5553 alloys (wt.%).

Composition (wt. %)	Ti	Al	V	Mo	Cr	O	N
As-consolidated	Bal.	4.99	4.93	4.94	2.90	0.36	0.021
FR-1 alloy	Bal.	5.01	4.96	4.95	2.93	0.35	0.023
FR-2 alloy	Bal.	4.97	5.01	4.94	2.85	0.36	0.020
FR-3 alloy	Bal.	5.03	4.92	5.03	2.96	0.34	0.024
FR-4 alloy	Bal.	4.96	4.98	4.90	3.04	0.37	0.021

Note: FR-i (i=1, 2, 3, and 4) alloy represent the PM Ti-5553 alloy forged following route i (i=1, 2, 3, and 4).

As shown in Table 6.1, chemical composition for the primary alloying elements of all as-forged PM Ti-5553 alloys is very similar to those of the as-consolidated alloy, which is also close to the nominal alloy composition of Ti-5Al-5Mo-5V-3Cr, and

the oxygen and nitrogen contents are kept almost unchanged before and after TMP. These results suggest that the chemical composition is stable and there is no internal oxidation/nitrogenation during hot processing.

Table 6.2 Relative density of the as-forged PM Ti-5553 alloy pancakes (wt.%) at different sampling positions (see Figure 6.6).

Relative density (%)	Centre	1/4 area	1/2 area	3/4 area	Edge
FR-1 alloy	99.9	99.7	99.8	99.6	99.2
FR-2 alloy	99.8	99.6	99.7	99.7	98.9
FR-3 alloy	99.6	99.5	99.5	99.6	99.2
FR-4 alloy	99.5	99.4	99.6	99.5	99.0

Note: FR-i (i=1, 2, 3, and 4) alloy represent the PM Ti-5553 alloy forged following route i (i=1, 2, 3, and 4).

Table 6.2 exhibits the calculated relative density of the as-forged PM Ti-5553 alloy pancakes, and it is apparent that all the as-forged alloy pancakes have very high relative density (RD) along the radius direction, with a value of > 99.5% (full dense), except the edge areas with RD of about 99.0% (almost-full dense).

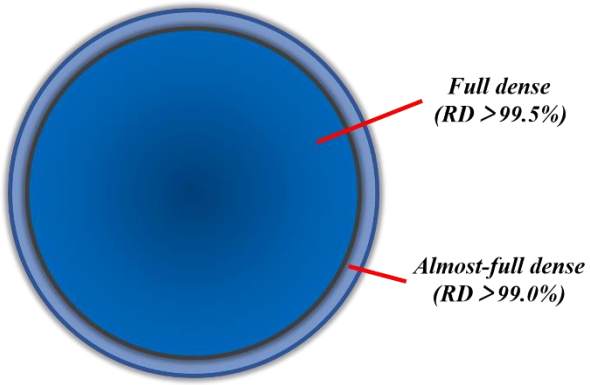

Figure 6.7 Schematic diagram showing the relative density distribution of as-forged PM Ti-5553 alloy pancakes processed via various routes.

The schematic diagram exhibited in Figure 6.7, shows the RD distribution of as-forged PM Ti-5553 alloy pancakes processed via various routes. These results confirm that the processed alloy pancakes have the homogenous density distribution with RD of > 99.5% .

6.4 Microstructure and mechanical properties of the as-forged PM Ti-5553 alloy

As the microstructures of as-forged PM Ti-5553 alloy in the longitudinal-section well represent the features of processed alloy comparing to those in the cross-section, therefore, microstructure observation in this chapter was performed on the samples obtained along the longitudinal direction of as-forged and heat-treated PM Ti-5553 alloys. Meanwhile, the microstructures of as-forged alloy are expected to be varied along the radius direction due to non-uniform deformation. Therefore, microstructure observation should be carried out at different positions along the radius direction. Figure 6.8 shows the optical microstructures of FR-2 alloy at different sampling positions along the radius direction. Microstructures at 3/4 radius, 1/2 radius, 1/4 radius and centre position are similar, showing the well-deformed characteristics, however, the microstructure at the edge area of the pancake is distinct with that at other selected positions, having obvious less-deformed features.

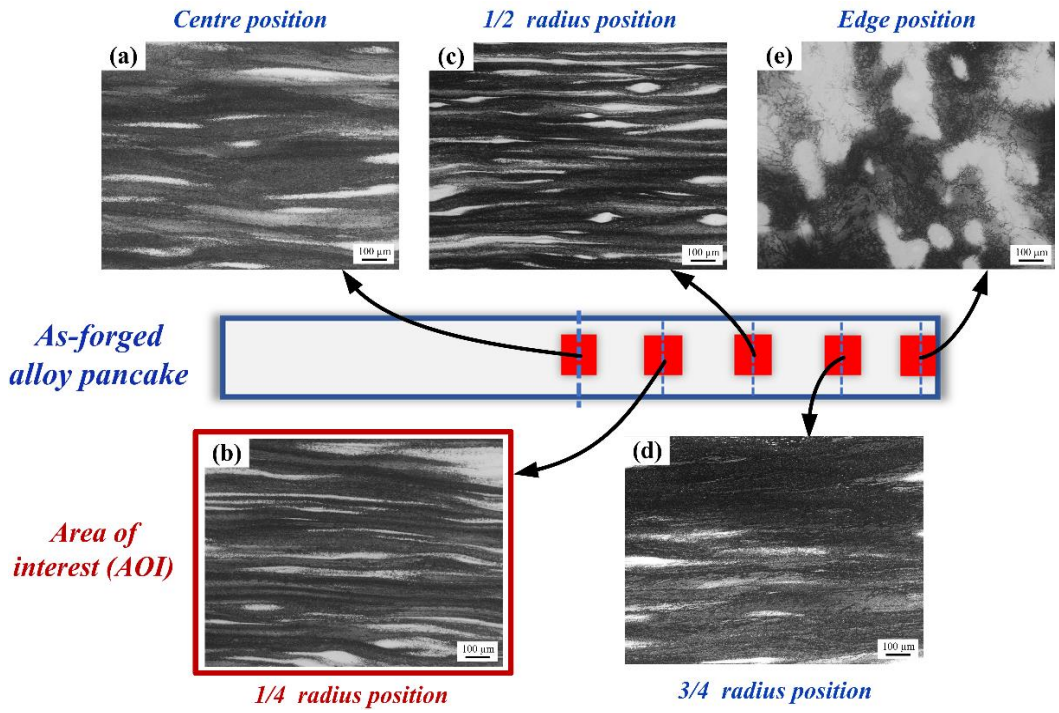

Figure 6.8 Optical images of FR-2 alloy at different sampling positions.

Hence, the microstructure at 1/4 radius position is selected to represent as-forged alloy's microstructure in this chapter, and edge area is excluded from later testing. Samples will be cut from the area showing in Figure 6.9 for further mechanical testing and heat treatment investigation.

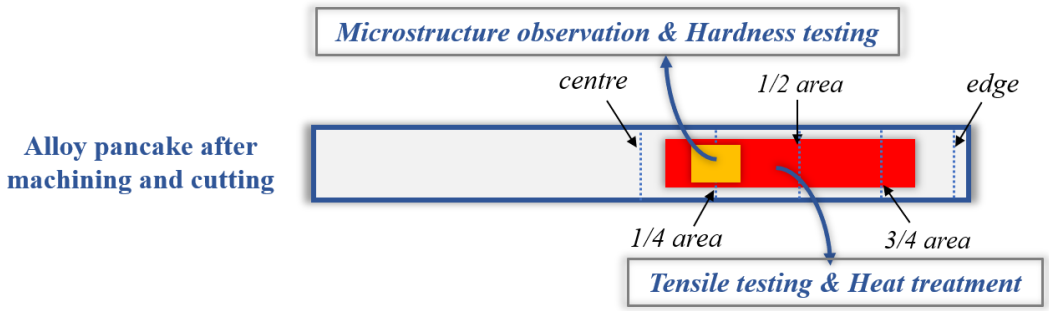

Figure 6.9 Schematic illustrations of the sampling positions at the as-forged alloy pancakes for microstructure observation, mechanical testing and heat treatment.

6.4.1 Microstructure of the processed alloy

Figures 6.10 and 6.11 show the OM and SEM microstructures of the as-forged PM Ti-5553 alloy processed following various routes, respectively. Overall, the microstructure characteristics, including grain size/structure, precipitation proportion/distribution and phase morphology, are highly depended on the processing conditions.

As shown in Figure 6.10a-c, FR-1 alloy possesses a heterogeneous grain structure that is composed of slightly elongated coarse grains (CG) and near-equiaxed ultra-fine grains (UFG). The CG has an average grain size of 100-250 μm, while the average grain size for UFG is only about 10-20 μm. Furthermore, two types of α phases are observed, including primary α phase (α_p) colony and very fine α phase in transformed β (β_{TF}) structure. Additionally, there is also a large proportion of β grains in the microstructure without α phase. SEM observation (Figure 6.11a-c) also suggests that the UFG primarily contains β_{TF} structure and surrounded by continuous grain boundary α phase (GB-α), while the CG is precipitation-free β phase (matrix). The α_p colonies are located near grain boundaries (Figure 6.10b and 6.11b), especially near the UFG boundaries. β_{TF} structure can also be found between the lath α_p phases (Figure 6.11c), showing a lot of fine α precipitates on the original β phase.

This kind of heterogeneous grain structure showed in F-R1 alloy has been introduced in many advanced metallic materials [5-11] including metastable β titanium alloy [12] and β titanium alloy [13] to achieve the ultra-high strength without a significant trade-off in ductility [14-17]. The UFG can significantly increase the alloy's strength, while the CG can act as a dislocation sink and absorb

higher energy during deformation for achieving good ductility [15, 18, 19]. As for the α phase hierarchy in the metastable β titanium alloys, the coarse α_p can accommodate deformation strain, while very fine α and GB-α phases contribute to high strength [20-23]. Therefore, the FR-1 alloy that contains a harmonious combination of hierarchical microstructure features and heterogeneous grain structure has a great potential capacity to achieve high strength and ductility [24]. The detailed microstructural variation mechanisms for this harmonious combination microstructure will be discussed together with other forging conditions later.

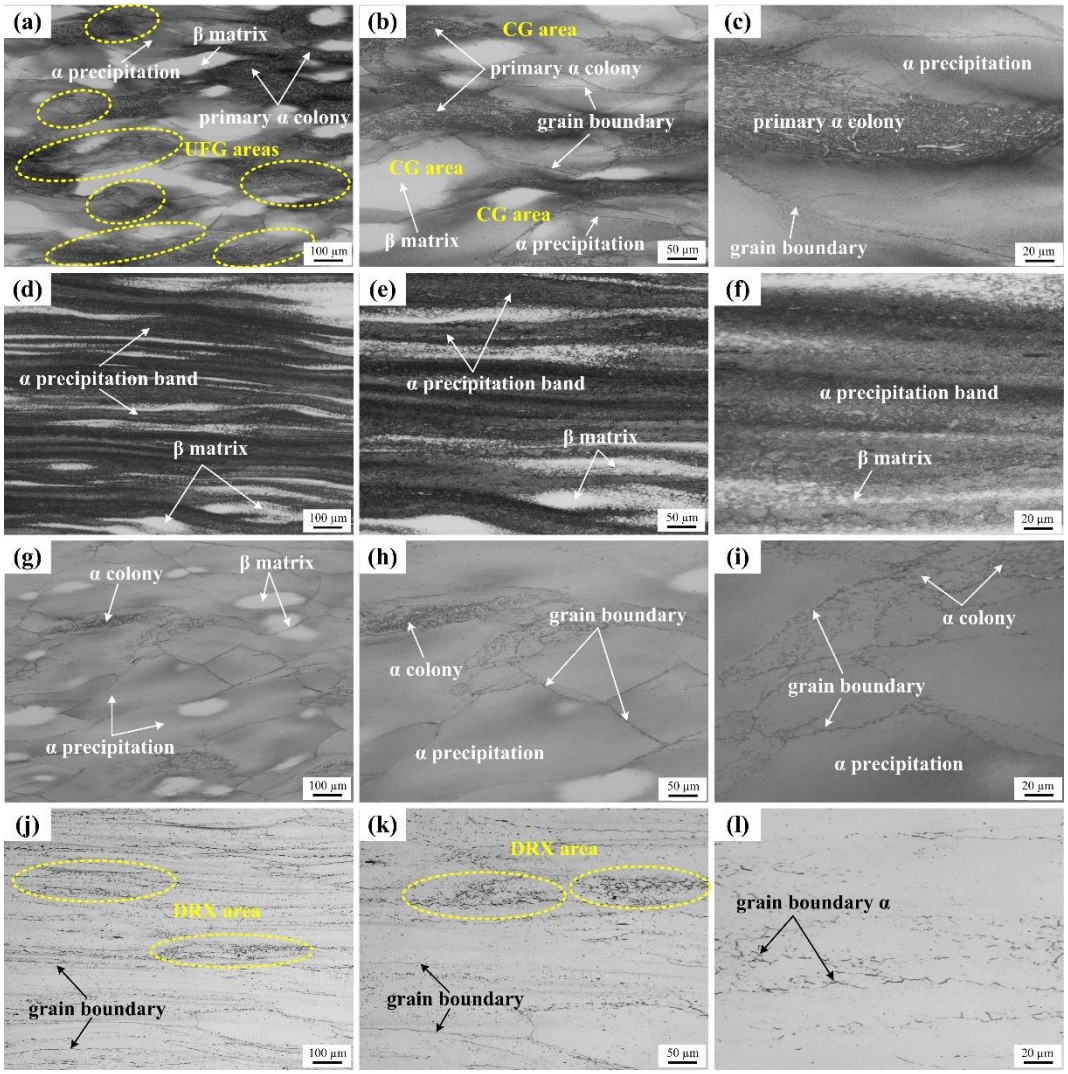

Figure 6.10 Optical microstructures of as-forged PM Ti-5553 alloy pancakes processed via various routes: (a)-(c) FR-1 alloy; (d)-(f) FR-2 alloy; (g)-(i) FR-3 alloy; (j)-(l) FR-4 alloy. Forging was performed along the vertical direction.

For FR-2 alloy, as shown in Figure 6.10d-f, the microstructure is composed of α precipitation bands and β phase matrix. The α precipitation band and β phase matrix are alternately distributed, with the dominance of precipitation band. Moreover,

there is no large-sized α_p and grain boundary (GB) is invisible in the microstructure. In the corresponding SEM images (Figure 6.11d-f), large prior β grains are still at the severely-elongated stage with serrated GBs. The α precipitation bands are made up of widespread β_{TF} structures that have small-sized acicular α and residual β phases. The small-sized α phase in β_{TF} structure of FR-2 alloy is much coarser than those in FR-1 alloy but its size distribution is homogeneous.

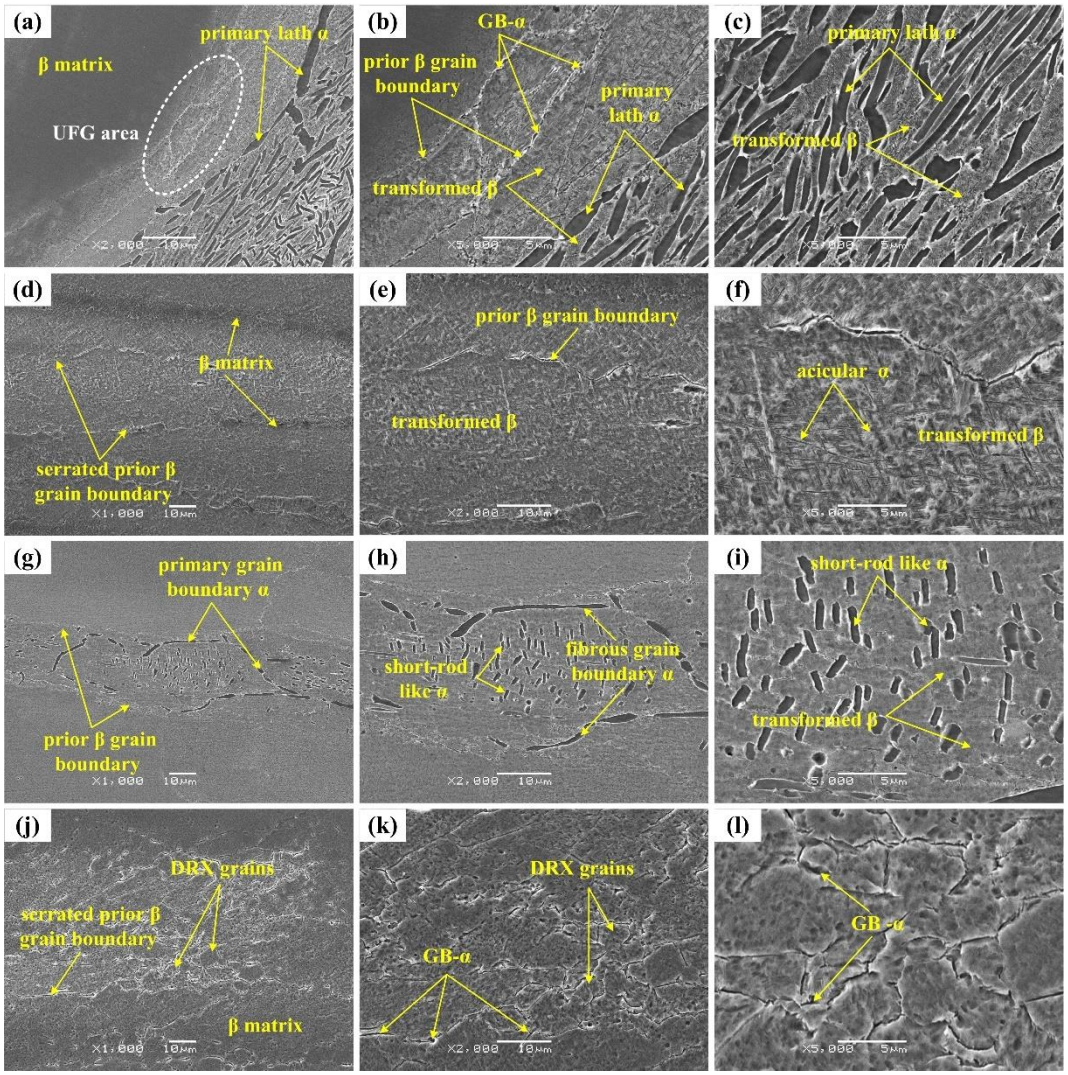

Figure 6.11 SEM microstructures of as-forged PM Ti-5553 alloy pancakes processed via various routes: (a)-(c) FR-1 alloy; (d)-(f) FR-2 alloy; (g)-(i) FR-3 alloy; (j)-(l) FR-4 alloy. Forging was performed along the vertical direction.

The microstructure of FR-3 alloy shows distinct features comparing to FR-1 and FR-2 alloys. As shown in Figure 6.10g-i, the microstructure of FR-3 alloy has near-equiaxed shape (Figure 6.10g) and its grain size is obviously coarser than that of FR-1 alloy, with an average grain size of > 300 μm. Dispersive α precipitates are observed besides several isolated precipitate-free β phase, and some α_p phase is appeared at the β-GB and in inside of the prior β grain. Figure 6.11g-i show that

lath and fibrous-shaped α_p is distributed along the prior β-GB, forming long GB-α phases, while the α_p phases located in the inside of prior β grain present in short rod-like shape. It is uncovered that the widespread precipitation area in FR-3 alloy (Figure 6.11i) is also primarily composed of β_{TF}, which is very similar to the β_{TF} structure showed in the FR-1 alloy (Figure 6.11c).

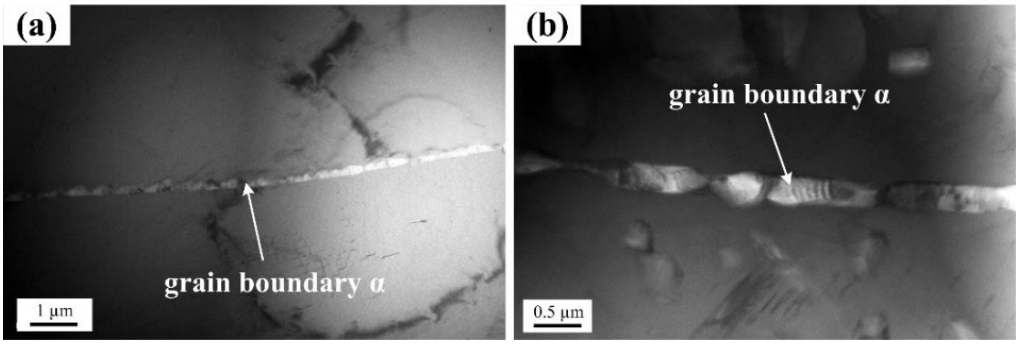

Figure 6.12 TEM images showing the morphology of grain boundary α phases in FR-4 alloy.

Figure 6.10j-l shows the microstructure of FR-4 alloy, and obvious rapid-cooling features are observed. The β grains are elongated along the horizontal direction with serrated GB, and some small equiaxed grains are distributed along and/or near the prior β-GB with more prominent boundaries (Figure 6.10l). These observation results indicate that both DRV and partial DDRX take effect during forging the alloy following Routes No.1 and No.4 (at the potential "best" TMP condition shown in Figure 6.1). SEM images (Figure 6.11j-l) reveal that the newly-formed DDRX grains with a size of 5-10 μm are dressed by fine α precipitates at their boundaries. Furthermore, some fine α precipitates are also observed at the serrated β-GB. The existence of continuously long GB-α phase in FR-4 alloy is confirmed by TEM observation (see Figure 6.12). These observation results suggest that the fine α precipitations at the DDRX and prior β grain boundaries are separated from the β matrix dynamically during the forging process. Furthermore, there is no β_{TF} structure appeared in the water-quenched FR-4 alloy, which further demonstrates that the β_{TF} structure in FR-1, FR-2 and FR-3 alloys are formed during air cooling (much slower cooling rate comparing to rapid water-quenching).

At last, there are no obvious and visible residual pores observed in the microstructure of all the alloys processed following various TMP routes. These results prove that the 2% residual pores in the alloy at as-consolidated stage have

been completely eliminated after TMP, which further verified the aforementioned (Section 6.3.2) very-high RD of the as-forged alloy pancakes.

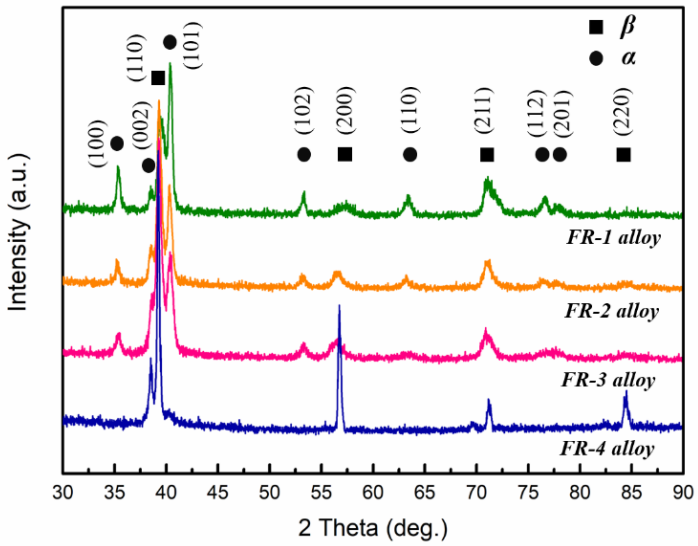

Figure 6.13 XRD patterns of as-forged PM Ti-5553 alloys processed following different routes.

XRD patterns of the as-forged PM Ti-5553 alloys at different conditions are presented in Figure 6.13. It suggests that the peaks of α and β are indexed in all forged alloys (FR-1, FR-2, FR-3 and FR-4). Moreover, FR-1 alloy has the highest α peak intensity, while the number of α peaks and their intensity becomes significantly less and lower, but β peaks are stronger in FR-4 alloy comparing to other alloys. FR-1, FR-2 and FR-3 alloys have extensive α_p and/or fine α precipitation in β_{TF} structures, leading to the strong indexed α peaks in the XRD patterns. On the contrary, only limited proportion of fine α precipitation located along GBs in FR-4 alloy is the main reason to cause weak α peaks that observed in its XRD pattern.

6.4.2 Microstructural evolution mechanism during forging

Based on the above microstructure observation results of the as-forged alloy pancakes processed following different TMP routes, the detailed microstructure variation mechanisms of PM Ti-5553 alloy under each specific TMP route can be revealed and deduced.

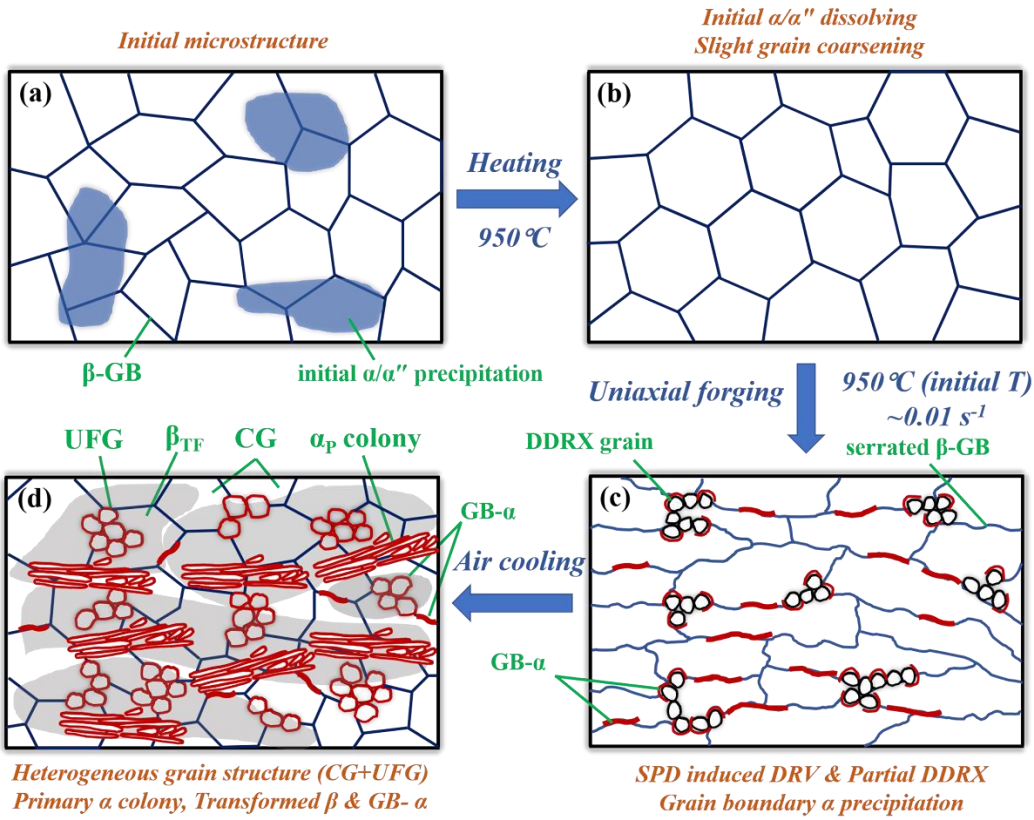

Figure 6.14 Schematic illustration of the microstructural evolution mechanism for FR-4 and FR-1 alloys during TMP: (a) initial microstructure; (b) microstructure after heating; (c) microstructure evolution during forging for FR-4 alloy (after WQ); (d) final microstructure after AC for FR-1 alloy.

The microstructural evolution processes of the PM Ti-5553 alloy forged at the potential "best" processing condition (Figure 6.1, 950 °C/~0.01 s^{-1}) can be clarified by the combined microstructure analysis of FR-1 and FR-4 alloys. A schematic diagram is presented in Figure 6.14 to demonstrate the detailed microstructure variation process at this condition. As discussed in Chapter 3, the original microstructure of as-consolidated PM Ti-5553 alloy is composed of beta phase matrix and a small amount of α/α″ precipitates which are agglomerated, as shown in Figures 3.2a and 3.10 (in Chapter 3), which are represented in the sketch of Figure 6.14a. While heating the as-consolidated PM T-5553 alloy up to 950 °C and held the temperature for 30 mins before forging, the initial α/α″ precipitates would be completely dissolved in the β matrix and the β matrix is also coarsening slightly due to the temperature is close to the measured beta phase transform temperature of 975 °C (as represented in Figure 6.14b). Afterwards, during the hot forging deformation, the microstructure of the alloy is changed significantly to produce the mixed-grain structure consisted of elongated large grains and small equiaxial grains attributed to the concurrent softening mechanisms of localized/partial DDRX and

extensive DRV induced by severe plastic deformation (SPD). Furthermore, some α phases are generated dynamically along/near the serrated β grain and the new DDRX grain boundaries to form GB-α phase during forging. As is revealed in Chapters 5 (see Figures 5.34 and 5.35), dynamic α→β phase transformation occurs when the PM Ti-5553 alloy is deformed at 950 °C/0.01 s^{-1}, and the resultant deformed structure after thermal physical simulation is free of α phase. However, the practical forging is not performed/done under isothermal deformation condition as thermal physical simulation, die chilling effect would reduce the practical deformation temperature dynamically during forging, although the forging die is preheated up to 500 °C. Furthermore, there is almost no adiabatic temperature rising during hot forging the PM Ti-5553 alloy at 950 °C/0.01 s^{-1}, as discussed in the Section of 5.2.4 (in Chapter 5). Because of those two reasons, there is a possibility that a small amount of α phase are formed in the microstructure of FR-1 and FR-4 alloys during forging. In addition, the pre-existed GBs become the preferred nucleation sites for the newly-generated α phase attributed to the local lower nucleation energy and higher elemental diffusion rate. Hereinafter, upon the completion of the forging processes, the water quenching processes leads to that FR-4 alloy keep the current microstructure that composed of elongated β grains with some fine DDRX grains located at the grain boundary, as represented in Figure 6.14c.

During air cooling after hot forging at 950 °C/~0.01 s^{-1} (Figure 6.14d), the elongated β grains become wider and coarser with reduction of the grain aspect ratio, forming the microstructure of slightly-elongated CG in FR-1 alloy. The newly-formed fine DDRX grains also grow coarse with near-equiaxed shape, becoming the UFGs in the microstructure of FR-1 alloy. Meanwhile, large-sized α_p lath colonies are formed by coarsening the unevenly generated GB-α on the prior β-GB. Moreover, GB-α phase that is around the newly-formed DDRX grains is developed into the surrounding α phase of the UFG, while very fine α precipitation is also separated out at the same time in some β matrix areas in the form of β_{TF} structure.

For the FR-2 alloy (the corresponding schematic diagram is presented in Figure 6.15), the initial microstructure and microstructure changes are similar with that of FR-1 alloy before forging start, as shown in Figure 6.15a and b. The different

microstructural evolution characteristics occurs in the process of hot forging due to different deformation strain rates.

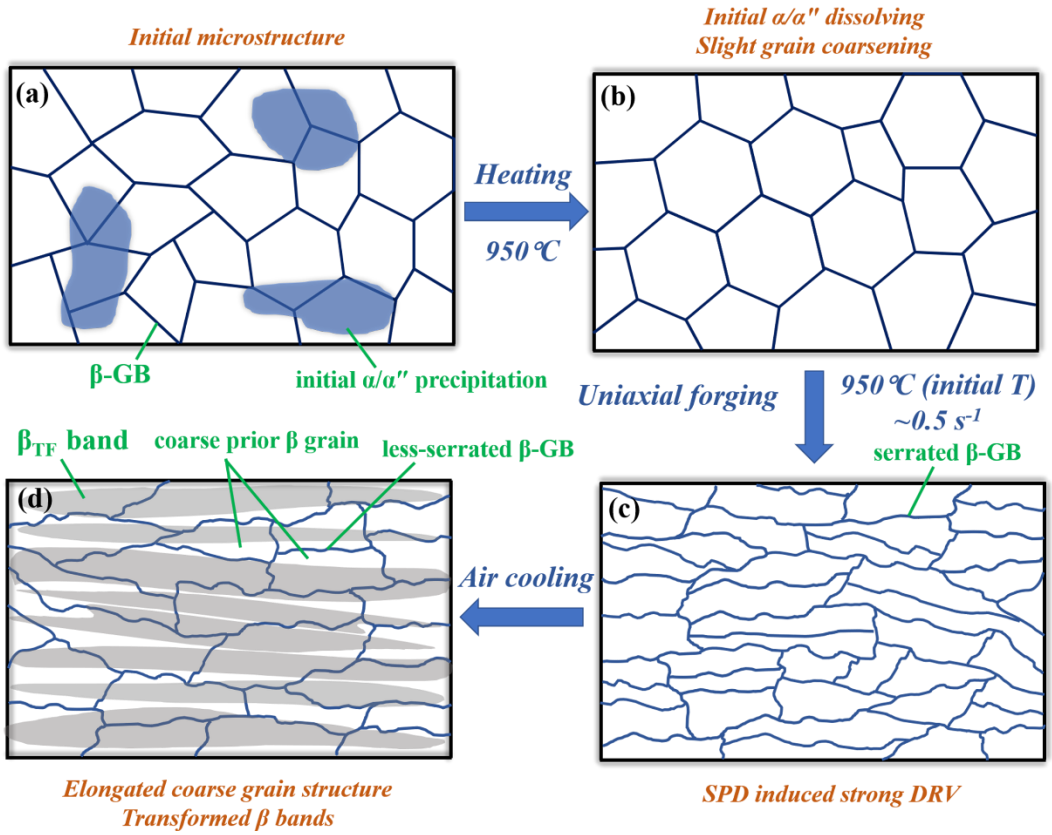

Figure 6.15 Schematic illustration of the microstructural evolution mechanism for FR-2 alloy during TMP: (a) initial microstructure; (b) microstructure after heating; (c) microstructure evolution during forging; (d) final microstructure after AC.

From the discussion in Chapters 4 and 5, it suggests that the high-strain-rate deformation impedes the occurrence of DDRX in PM alloy but triggers strong DRV comparing to low-strain-rate deformation at the temperature of 950 °C. Thus, the PM Ti-5553 alloy would show strong DRV characteristics in the hot forging at 950 °C/~0.5 s^{-1}, (Figure 6.15c). Moreover, there is no GB-α generated dynamically during forging at this condition because of α phase is difficult to nucleate with the lacking of effective thermal activation and elemental diffusion in relatively short forging time (only about 1/50 of the deformation time for FR-1/FR-4 alloy) [25, 26]. The high-strain-rate deformation and strong DRV also lead to formation of the narrow elongated-grain structure with serrated GB. These characteristics are considered to have decisive effects to form the final microstructure for FR-2 alloy after air cooling from the hot forging temperature, as indicated in Figure 6.15d. After the alloy air-cooling to room temperature, the coarse prior β grains still remain elongated shape with serrated GB due to the inadequate thermal diffusion. The fast forging also introduces higher storage energy and dislocation density in the alloy,

resulting in the precipitation of larger-sized acicular α in widespread β_{TF} bands after air cooling [27-29].

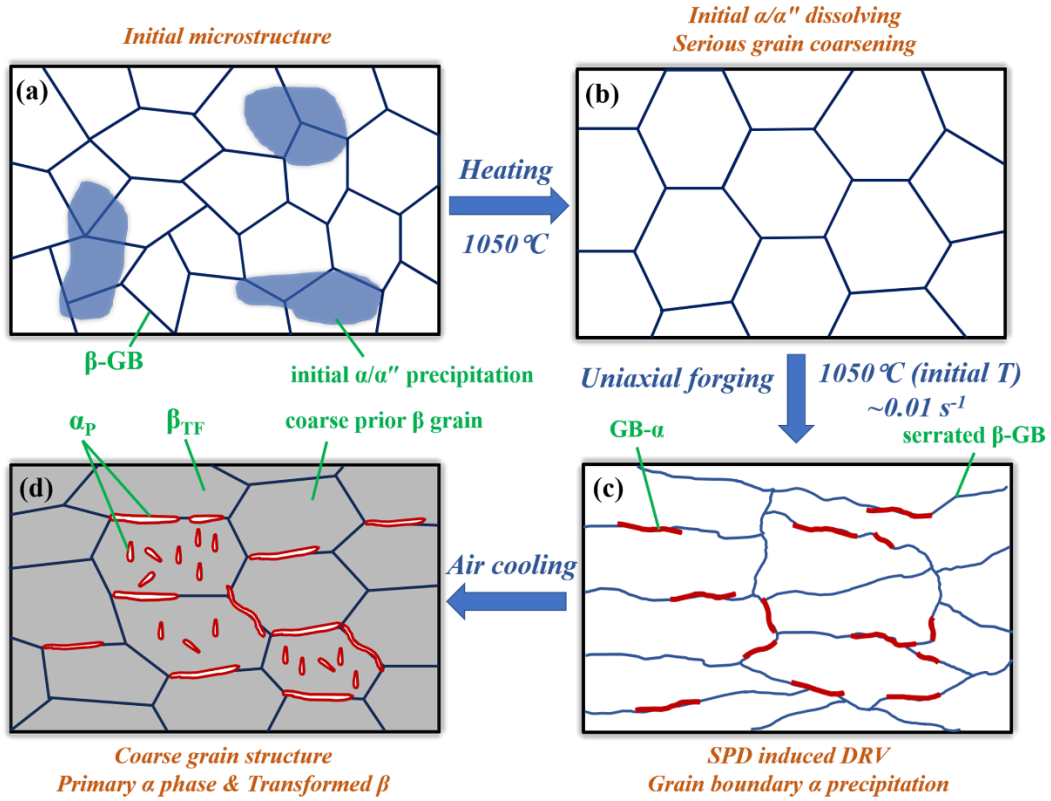

Figure 6.16 Schematic illustration of the microstructural evolution mechanism for FR-3 alloy during TMP: (a) initial microstructure; (b) microstructure after heating; (c) microstructure evolution during forging; (d) final microstructure after AC.

Schematic diagram in Figure 6.16 shows the microstructural evolution of FR-3 alloy during hot forging at 1050 °C/~0.01 s^{-1} and subsequent air-cooling process. Comparing to the alloys are processed in (α+β) region, the grain structure of FR-3 alloy is seriously coarsened while it is heated up to 1050 °C (75 °C above the β transformation temperature), as illustrated in Figure 6.16b [30-32]. Considering the microstructure features of FR-3 alloy and the results discussed in Chapters 4 and 5, it suggests that DRV is the predominated behaviour rather than DRX for the PM Ti-5553 alloy processed at this high temperature (1050 °C). Similar to FR-1 and FR-4 alloys, dynamic initiation of GB-α phase is induced by the low-strain-rate deformation and the dynamic reduction of the actual forging temperature (Figure 6.16c). Subsequently, the wide and elongated grains are evolved into coarse grains with near-equiaxed shape during the air cooling (Figure 6.16d). Meanwhile, the large α_p phases, which are along β-GB and in the inside of the coarse grain, are growing coarse. The proportion of α_p phase in FR-3 alloy is lower than that of FR-1 alloy, this is because the GB density is low and there are no DDRX grains in FR-

3 alloy. Additionally, very fine α precipitates are also formed in the β matrix (β_{TF} structure). The amount of β_{TF} structure in the FR-3 alloy is larger than that in FR-1 alloy, attributed to the high forging starting temperature and subsequent longer cooling time.

6.4.3 Mechanical properties of the processed alloys

The mechanical properties of as-forged PM Ti-5553 alloys following different TMP routes are listed in Table 6.3, together with the mechanical properties of the alloy at as-consolidated stage.

Table 6.3 Mechanical properties of PM Ti-5553 alloys at as-consolidated state and forged via various TMP routes.

Alloy condition	YS* (MPa)	UTS* (MPa)	Elongation* (%)	Hardness (HV)
As-consolidated	852.5	912.6	1.72	357.2
FR-1 alloy	1374.3	1450.9	3.23	492.4
FR-2 alloy	1333.8	1434.2	2.07	469.8
FR-3 alloy	1292.6	1316.5	1.54	421.7
FR-4 alloy	1152.3	1193.2	1.22	394.2

* Using the dog-bone-shaped cross-section specimens for the tensile tests here.

Overall, it is apparent that the mechanical properties of PM Ti-5553 alloy are increased significantly by TMP, with values of yield stress (YS) and ultimate tensile stress (UTS) increased from 852.5 MPa and 912.6 MPa (as-consolidated state) to 1152.3 MPa-1374.3 MPa and 1193.2 MPa-1450.9 MPa (as-forged state), and these increases are 35.2%-61.1% for YS and 30.7%-59.0% for UTS. The micro-harness improvement is calculated as 10.3%-37.8% from 357.2 HV (as-consolidate state) to 394.2 HV-492.4 HV (as-forged state). Moreover, forging also helps to improve the ductility for FR-1 and FR-2 alloys with the increased elongation (EL) from 1.72% (as-consolidated state) to 3.23% and 2.07%, but the ductility is decreased for the FR-3 and FR-4 alloys after forging. Several reasons are considered to cause these improvements for the PM Ti-5553 alloy after forging and summarised as below:

1. Grain structure evolution. The grain structure of the alloy is changed remarkably through TMP, and the grain morphology change can bring

significant enhancement of mechanical properties, such SPD-induced grain refinement (for grain size heterogeneity in FR-1 alloy).

2. Precipitation phase constitution variation. The α precipitations such as α_p colony and/or α phases in the inside of β_{TF} structure (except the water-quenched FR-4 alloy) could strengthen and toughen the alloy considerably.

3. Elimination of the brittle phase. Hard orthorhombic α″ phase and grain boundary α phase in the as-consolidated alloy are revealed to initiate serious dislocation accumulation and microcrack generation during room-temperature deformation, leading to early brittle fracture for the alloy. During the process of heating and soaking before forging, these unstable detrimental phases are dissolved completely in the β matrix, and thus the unexpected failure at the early stage of plastic deformation of the alloy is successfully avoided.

4. Elimination of residual porosity. The density of the alloy is increased from 98% to near-full density (> 99.5%) after TMP, and the residual pores are disappeared in the microstructure of as-forged alloys. The elimination of the residual porosity in the alloy will remove the defects and lower the risk of stress concentration during the early stage of the deformation and thus increase the strength, hardness and ductility of the alloy.

The mechanical properties of as-forged PM Ti-5553 alloys followed by various processing routes are distinct, this is mainly attributed to the difference in the resultant microstructures. FR-1 alloy exhibits the highest strength, hardness and ductility (UTS=1450.9 MPa, MH=492.4 HV and EL=3.23%) among the as-forged alloys, followed by FR-2 alloy (UTS=1434.2 MPa, MH=469.8 HV and EL=2.07%) and FR-3 alloy (UTS=1316.5 MPa, MH=421.7 HV and EL=1.54%), and then FR-4 alloy (UTS=1193.2 MPa, MH=394.2 HV and EL=1.22%).

The incorporation of positive grain structure heterogeneity and precipitation hierarchy is observed in FR-1 alloy, while the microstructure of FR-2 alloy is composed of elongated β grains and dispersed β_{TF} band. FR-3 alloy shows seriously coarsened β grains with widespread β_{TF} structure in its microstructure, while there are only β grains and very limited-amount GB-α in the water-quenched FR-4 alloy.

These results confirm that the grain structure and the precipitation distribution play important roles in the mechanical performance of PM Ti-5553 alloy. The presence of α_p and fine grains in the microstructure is beneficial to the outstanding mechanical properties. On the contrary, simple coarse grains and insufficient/single precipitation in the microstructure are verified against the improvement of mechanical performance of the alloy. Meanwhile, it is also revealed that the previously-predicated potential "best" TMP condition produces the alloy component with the highest mechanical properties at as-forged state. Conversely, TMP conducted in single β region and/or high strain rate has no effects on improving the mechanical properties of this studied PM alloy.

FR-1 and FR-2 alloys exhibit excellent room-temperature tensile strength and hardness, which are comparable and/or even better than those of other Ti-5553 alloys manufactured by conventional IM routes [33-43] and other expensive PM approaches such as HIP [44] and SLM [45]. The high strength and hardness of the as-forged alloys can be attributed to the PM Ti-5553 alloy containing high interstitial element (O and N) contents, which strengthen the α solid solution and β_{TF} structure significantly by occupying the octahedral interstice in the crystal lattice of Ti [46-49]. In addition, the dislocation movement in the O (N)-rich PM Ti-5553 alloy is pinned remarkably, leading to the further improvement of its strength and hardness [50, 51]. However, these can also become the possible reasons to limit the ductility increase for the as-forged alloys.

Figure 6.17 shows the typical tensile fracture surface morphology of the as-forged PM Ti-5553 alloys. Small cleavage facets having river-like patterns and tear ridges around are observed in FR-1 alloy (Figure 6.17a-b). Meanwhile, there is a large number of small dimples to distribute randomly on the fracture surface, meaning that the alloy is plastically deformed to some extent during the tensile test. These above observations indicate that the fracture of FR-1 alloy is dominated by the ductile-brittle mixed mechanism. It can be seen in Figure 6.17c-d that the fracture surface of FR-2 alloy has large cleavage facets featured by river-like patterns and tear ridges. Moreover, dimples and intergranular fracture characteristics are also observed, but the amount and size of the dimples are much less and smaller than those of FR-1 alloy. Thus, it can be inferred that the FR-2 alloy is fractured by

brittle cleavage mechanism with the combination of intergranular and transgranular features, and the plastic deformation degree is low during the tensile test.

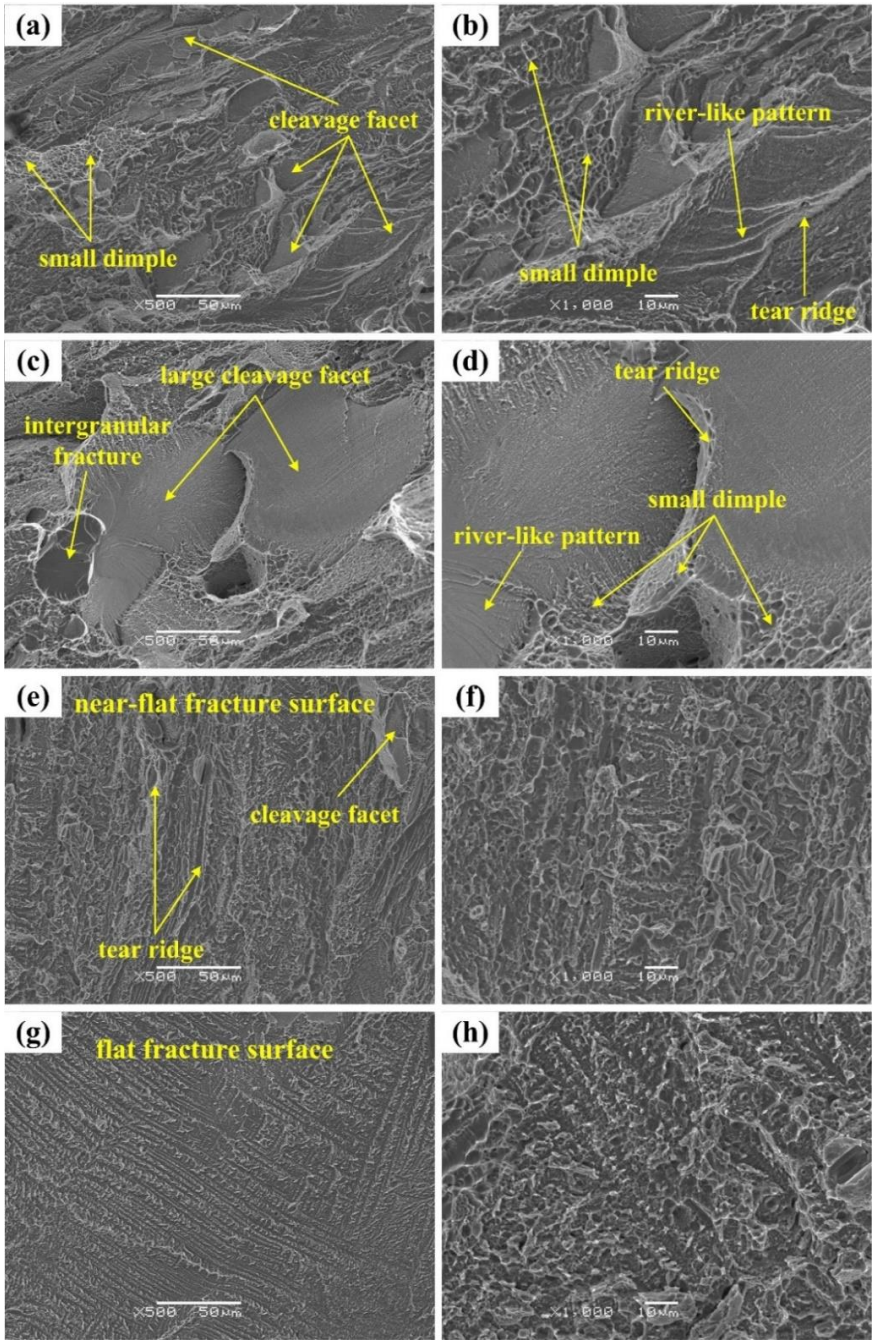

Figure 6.17 Representative SEM fracture surface of the as-forged PM Ti-5553 alloy pancakes after tensile testing: (a)-(b) FR-1 alloy; (c)-(d) FR-2 alloy; (e)-(f) FR-3 alloy; (g)-(h) FR-4 alloy.

As shown in Figure 6.17e-f, a near-flat fracture surface is observed for the FR-3 alloy specimen, with the appearance of cleavage facets and tear ridges. Besides, dimples are almost disappeared from the fracture surface, which illustrates that the brittle transgranular cleavage mechanism dominates the fracture of FR-3 alloy. Completely different failure characteristics are observed in the fracture surface of

FR-4 alloy (Figure 6.17g-h), including a very flat and smooth cleavage facture surface without other obvious features. These results mean that the fracture mechanism of FR-4 alloy is complete brittle cleavage with no plastic deformation.

The abovementioned fracture surface morphology and fracture mechanisms of the as-forged alloys comply well with the tensile ductility results for those related as-forged alloys. There is a continuous deterioration tendency of the ductility from FR-1 to FR-4 alloy (FR-1 alloy shows the highest ductility and FR-4 alloy has the lowest among the as-forged alloys), corresponding to the fracture mode varies from mixed ductile-brittle fracture to complete brittle fracture.

6.5 Determination of varying heat treatment processes

Although the PM Ti-5553 alloys processed following various forging routes show enhanced mechanical properties comparing to that of the as-consolidated alloy, its ductility, with a value of 1.22-3.23%, is still not acceptable for practical engineering applications. Post-heat treatments become a necessity to be performed on the as-forged alloys to reform their microstructure and improve the ductility, without significantly sacrifice in their strength. For the conventional IM metastable β titanium alloys, the most common heat treatment processes are the combination of solution treatment and subsequent aging (STA) [20, 23, 40, 52-54]. Solution treatment is usually performed above/near the β transformation temperature to allow alloying elements completely dissolve into the β matrix, and then uniformly distributed α phase can precipitate from the matrix during low-temperature aging. As mentioned in Chapter 3, the PM Ti-5553 alloy we fabricated via the developed TPC route shows a relatively high β transformation temperature of 975 °C than the IM Ti-5553 alloys (their β transformation temperatures are reported as 845 °C-870 °C) [40, 55-60], due to the high interstitial-element contents. Therefore, a similar solution treatment condition that performed on the conventional IM Ti-5553 alloy would not be appropriate for the forged PM-Ti-5553 alloys, because of the consideration of avoiding serious grain coarsening and retaining the high strength. Heat treatment conditions need to be optimised to achieve the following objectives: (1) Introduce enough α precipitations with various morphology and multiple hierarchies; (2) Avoid serious grain coarsening; (3) Relieve residual stress and increase the stability of as-forged alloys; (4) Retain heterogeneous grain structure

and α_p colony; (5) Simplify heat treatment process and shorten heat treatment time to minimize the manufacturing cost.

Thus, the designed heat treatment conditions are: heat treatment temperatures are at 600 °C-850 °C, the time for holding the temperature is 1 hour, and air cooling is selected to cool the treated alloys to room temperature. Only FR-1 (has the highest mechanical properties among the forged alloys) and FR-4 (microstructure can be significantly changed since the alloy is supersaturated after water quenching) alloys are selected for further investigating heat treatment effects on the alloys' microstructure and mechanical properties.

6.6 Effect of post-heat treatment on the processed alloy

6.6.1 Microstructure of the heat-treated alloy

Figure 6.18 shows the SEM microstructures of heat-treated FR-1 alloy. As shown in Figure 6.18a_1-b_5, FR-1 alloys heat-treated at 600 °C and 650 °C have microstructures containing heterogeneous grain and hierarchical (tri-model) phase structures. Both prior β-CG and β-UFG are observed in the microstructure. Meanwhile, it can be observed that the luxuriant α precipitation hierarchy of the alloy heat-treated at these conditions is composed of α_p colony, GB-α, acicular secondary α phase (α_s) and β_{TF} structure. Similar microstructures are obtained for the FR-1 alloy heat-treated at 700 °C and 750 °C with that of the alloy treated at 600 °C and 650 °C, as shown in Figure 6.18c_1-d_5, except that some α_s phases grows coarse and become thick acicular, rod-like and spherical shapes. Furthermore, with increasing the heat treatment temperature from 600 °C to 750 °C, more rod-like and spherical α_s phases are observed than the acicular α_s.

TEM images (see Figure 6.19) show the detailed microstructure of FR-1 alloy heat-treated at 700 °C. The α precipitations exhibit clear tri-hierarchical features composed of large-sized lath α_p (verified by the SAED pattern in Figure 6.19b), fine acicular/rod-like α_s and nanoscale needle-like tertiary α (α_t, located inside of β_{TF} structure). The co-existence of α_t and β phase in inside of the β_{TF} structure is further confirmed by the SAED patters in Figure 6.19c. Dispersed acicular/rod-like α_s phases are distributed randomly in the microstructure with various directions, and the β_{TF} structure is distributed between lath α_p and α_s phases. Meanwhile, the

dislocation density is very low in the microstructure, which means the residual stress of FR-1 alloy is almost eliminated by static recovery and the alloy's microstructure stability is significantly improved after heat treatment at 700 °C.

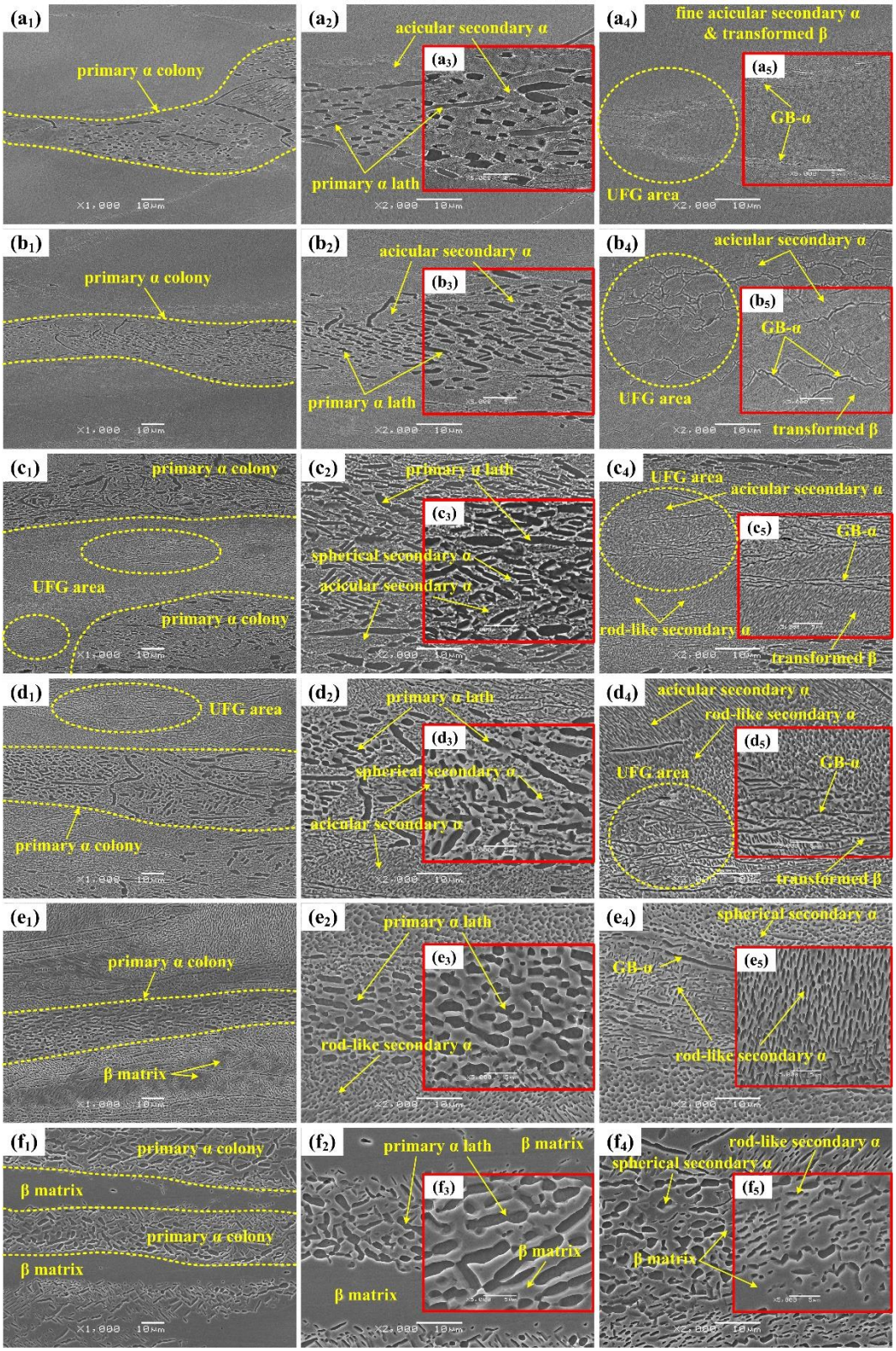

Figure 6.18 SEM microstructures of FR-1 alloy heat-treated at : (a_1)-(a_5) 600 °C; (b_1)-(b_5) 650 °C; (c_1)-(c_5) 700 °C; (d_1)-(d_5) 750 °C; (e_1)-(e_5) 800 °C; (f_1)-(f_5) 850 °C, for 1hour, followed by air cooling.

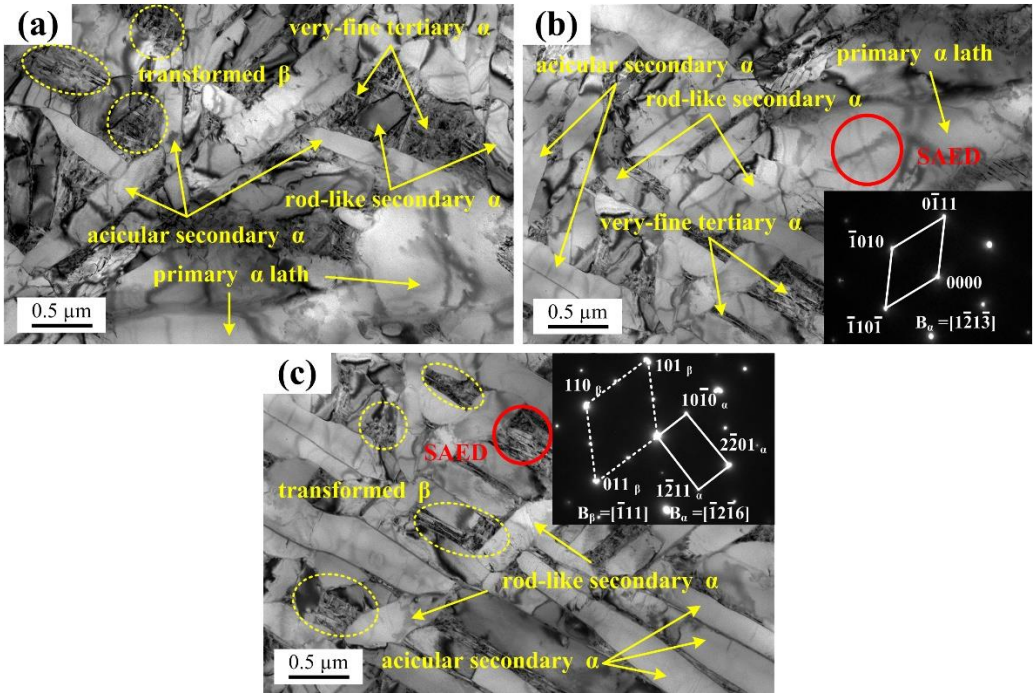

Figure 6.19 High magnification TEM images showing the detailed microstructures of FR-1 alloy heat treated at 700 °C/1h.

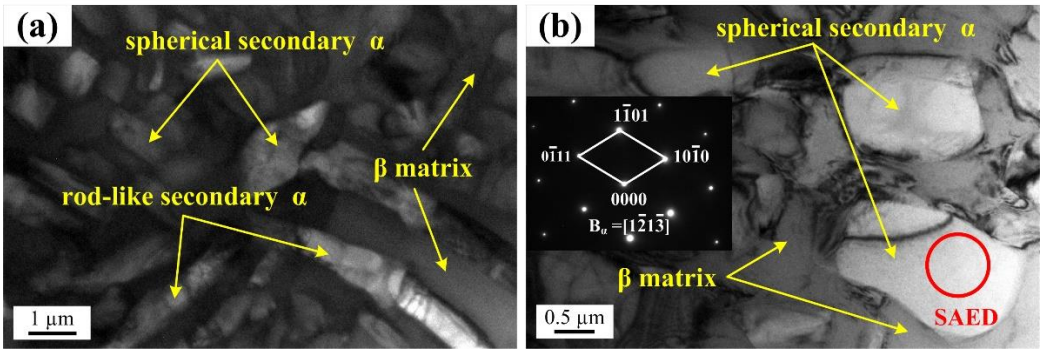

Figure 6.20 High magnification TEM images showing the detailed microstructures of FR-1 alloy heat-treated at 850 °C/1h.

When increasing the heat treatment temperature to relatively high temperatures of 800 °C and 850 °C, the microstructures of heat-treated FR-1 alloy become markedly different comparing to the alloy heat-treated at 600 °C-750 °C, as shown in Figure 6.18e_1-f_5. The prior β-UFG structure showed in the forged alloy is disappeared, coarse α_s phases with shapes of dot-like and spherical are visible, and the lath α_p phases show obvious coarsening and spheroidization tendency. Furthermore, there are some precipitation free areas composed of only β phase. Figure 6.20 shows the detailed TEM microstructure of FR-1 alloy heat-treated at 850 °C. It is apparent that only coarsened α_s phases (rod-like and spherical shape, the phase type is confirmed by the SAED patterns in Figure 6.20b) and β matrix are observed and no β_{TF} structures, α_t phases, dislocations are visible.

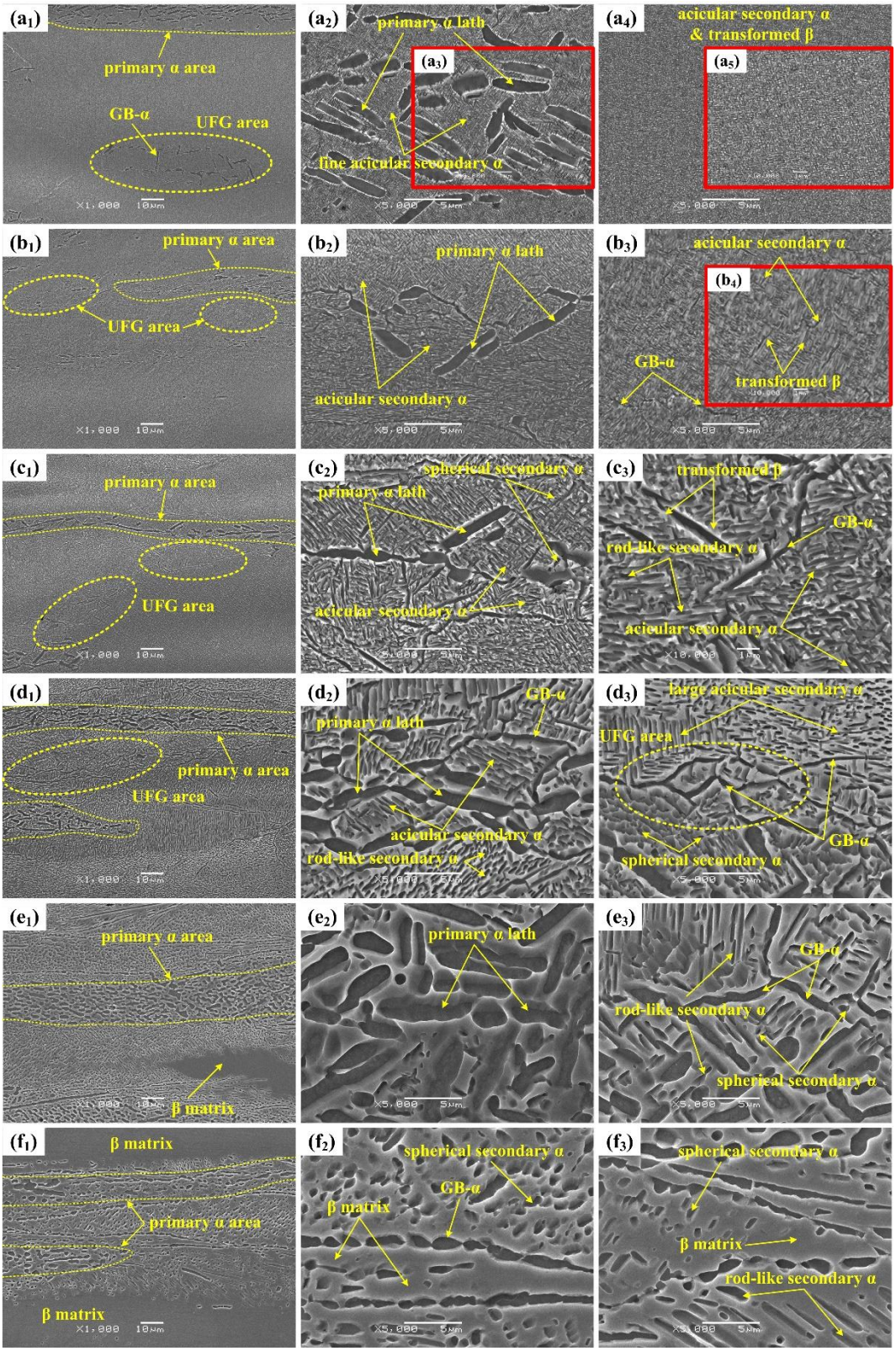

Figure 6.21 SEM microstructures of FR-4 alloy heat-treated at : (a_1)-(a_5) 600 °C; (b_1)-(b_4) 650 °C; (c_1)-(c_3) 700 °C; (d_1)-(d_3) 750 °C; (e_1)-(e_3) 800 °C; (f_1)-(f_3) 850 °C, for 1hour, followed by air cooling.

Figure 6.21 shows the SEM images of FR-4 alloy heat-treated at different temperatures. It can be observed that primary α_p colonies appear in the microstructures of all heat-treated FR-4 alloys. The width of α_p colonies (about 10

μm) is smaller in the heat-treated FR-4 alloy than in the heat-treated FR-1 alloy (larger than 30 μm), although the α_p lath has similar morphology. Similar to the FR-1 alloy, FR-4 alloy also possesses a heterogeneous grain structure (CG and UFG) with tri-hierarchical α precipitation (lath α_p, acicular/rod-like/spherical α_s and nanoscale needle-like α_t within β_{TF} structure) features when the heat treatment is conducted at the temperatures between 600 °C and 750 °C (see Figure 6.21a_1-d_3).

With increasing the heat treatment temperature to 800 °C and 850 °C (see Figure 6.21e_1-f_3), FR-4 alloy has a microstructure showing dot-like/spherical α_s precipitation and spheroidizing lath α_p phases on the β matrix. It is noticed that the size of α_s phases and spheroidization/growth tendency of α_s and α_p are larger and more serious in FR-4 alloy than in FR-1 alloy when the alloys are heat-treated at identical temperature.

6.6.2 Microstructural evolution mechanism of the alloy during heat treatment

From above microstructure observation results of the heat-treated alloys, it suggests that the processed PM Ti-5553 alloys have serious microstructure heredity (from the microstructure of the TMPed alloys) and high microstructural sensitivity to the variable (heat treatment temperature) during post-HT. In this section, the specific and detailed microstructural evolution mechanisms of the as-forged alloys (FR-1 and FR-4), during post-HT, are discussed.

Figure 6.22 shows the schematic diagram illustrating the microstructure evolution mechanisms of FR-1 alloy during heat treatment. When the alloy is treated at the temperatures of 600 °C to 750 °C (see Figure 6.22a and b), dispersed acicular α_s phases (some rod-like and spherical α_s phases are also visible in the 700 °C and 750 °C heat-treated samples) are able to be generated in the β matrix and previous β_{TF} structure due to the thermal activation and elemental diffusion effects. Meanwhile, the previous β_{TF} structure is inclined to expand and form a certain amount of nano-sized α_t precipitates internally at these heat-treated temperatures, and then become the new β_{TF} structure that dominates the FR-1 alloy (the previous precipitation-free regions are eliminated). The CG/UFG grain mixture and lath α_p colonies appeared in the heat-treated FR-1 alloy are integrally inherited from the

original as-forged microstructure. Hence, the heat-treated FR-1 alloy exhibits a heterogeneous grain microstructure that includes tri-hierarchical α precipitations.

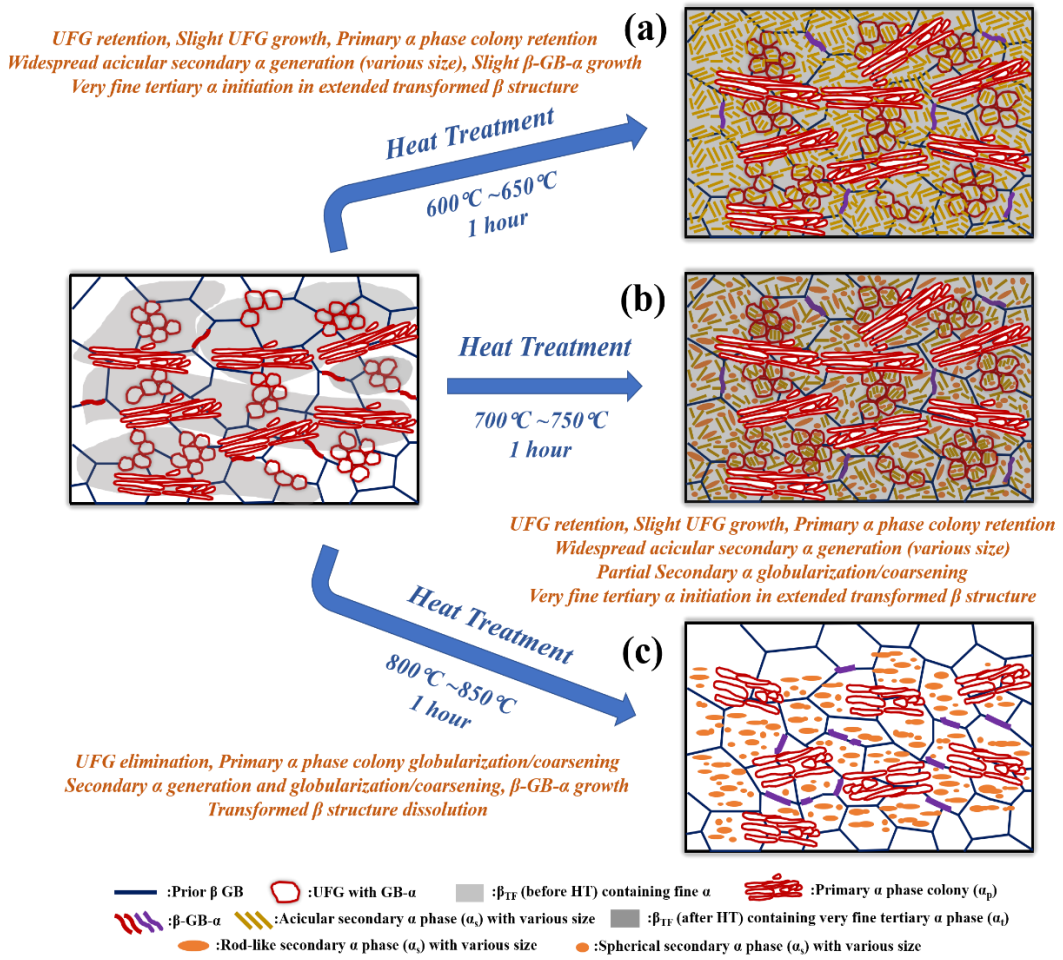

Figure 6.22 Schematic illustration and description of the microstructure evolution mechanism for FR-1 alloy during heat treatment at various temperatures: (a) 600 °C-650 °C; (b) 700 °C-750 °C; (c) 800 °C-850 °C.

The tri-modal precipitation structure has also been obtained in some other IM titanium alloys such as TA-15 (near-α type, Ti-6Al-2Zr-1Mo-1V) [61-65], TC-11 (α+β type, Ti-6.5Al-3.5Mo-1.5Zr-0.3Si) [66] and modified Ti-6Al-4V [67] alloys, which has been verified to have a great contribution to their excellent mechanical properties. However, the tri-modal structures in those IM alloys are introduced through the combination of multiple-step TMP and complicated post-HT processes. The formation of tri-modal α precipitation structure in the studied PM Ti-5553 alloy (via one-step forging plus simple post-heat treatment) is attributed to the PM alloy we produced has fine-grain structure and high oxygen content. Furthermore, the morphology of α_p phase is different between the studied PM and other IM Ti-5553 alloys. The α_p phase in the IM titanium alloys with tri/bi-modal α precipitation structure usually has equiaxed shape and is distributed uniformly in the

microstructure, while the α_p phase in the PM Ti-5553 alloy possesses a lathed shape and the α_p laths are gathered to form α_p colonies. These are related to the single uniaxial open-die forging process.

The α_s phase morphology is sensitive to the heat treatment temperature. The size of acicular α_s phase is getting larger as increasing the heat treatment temperature from 600 °C to 750 °C, leading to the formation of the rod-like and spherical α_s phases. Meanwhile, UFG in the microstructure also is coarsened after heat treatment, and its growth becomes more obvious at relatively high heat treatment temperature. However, α_p colonies and GB-α show have a relatively high thermal stability at the temperature range of 600 °C to 750 °C, and their structures are almost kept unchanged.

When the FR-1 alloy is heat-treated at the temperatures of 800 °C to 850 °C (see Figure 6.22c), the alloy's microstructure is significantly changed comparing to the alloy treated at lower temperatures. The tri-modal α precipitation structure and grain gradient are disappeared as the dissolution of β_{TF} structure and UFG growth happen at the temperature higher than 800 °C. These results indicate that the critical heat treatment temperature for FR-1 alloy to maintain the harmonious coexistence of grain heterogeneity and α precipitation hierarchy is 750 °C, and the coarsening and spheroidization processes of α_s phase, α_p colonies and GB-α phase also are accelerated with increasing the heat treatment temperature, to form the dot-like and spherical α_s phases with the remarkable reduction of their phase aspect ratio.

Actually, the coarsening and spheroidization phenomena of α_s phase, α_p colonies and GB-α phase are processed with the mechanism of static α phase globularization. Different from the dynamic α phase globularization mechanisms discussed in Chapters 4 and 5, the static globularization is only driven by thermal activation energy without external stress during post-HT. According to the series of researches carried out by Xu et al. [68-72] on TC-17 alloy (α+β type, Ti-5Al-2Sn-2Zr-4Mo-4Cr), the static α phase globularization processes during HT can be divided into two stages. The first stage is the generation of detached β phase due to release of distortion energy (after TMP) and thermal-induced elemental diffusion. Subsequently, the α stabilizers diffuse from the terminal position to the low-curvature position controlled by termination migration and Ostwald ripening

mechanisms (see the sketches in Figure 6.23 [68]), resulting in α phase's globularization and coarsening during post-HT. These explain why the larger globularization and coarsening degrees are observed for FR-1 alloy at the heat treatment temperature of > 800 °C (no phase globularization happens at 600 °C-650 °C, partial α_s phase globularization are observed at 700 °C-750 °C, while remarkable globularization/coarsening processes of α_s phase, α_p colonies and GB-α appear at 800 °C-850 °C). This is because higher thermal driving force is provided for elemental diffusion at higher temperature than at lower heat treatment temperature, thus promoting the α precipitation's static globularization and coarsening. Furthermore, α_s phases are observed to suffer a higher degree of globularization/coarsening than α_p and GB-α phases at the same heat treatment temperature, this is because α_s phase has smaller size and relatively less elemental stability, which help enhance the termination migration process and Ostwald ripening effects.

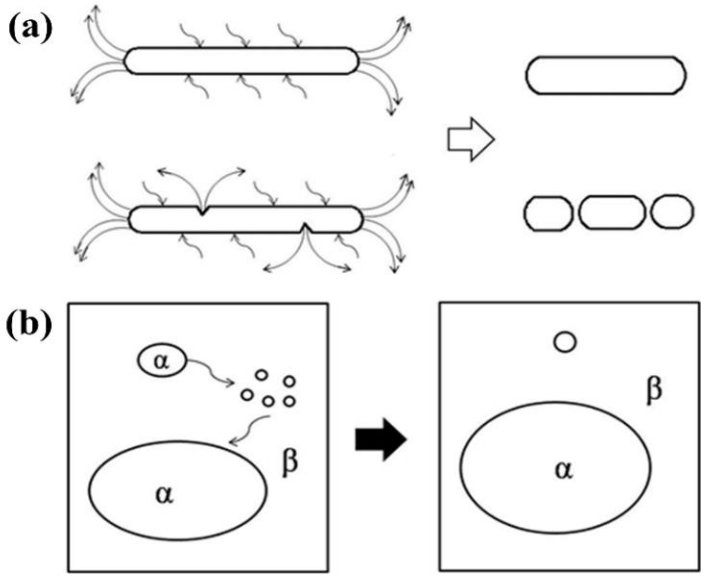

Figure 6.23 Schematic illustration of (a) termination migration mechanism and (b) Ostwald ripening mechanism for static α phase globularization during HT of titanium alloys [68].

Figure 6.24 exhibits the schematic diagram demonstrating the microstructure evolution mechanisms for FR-4 alloy during heat treatments. Similar to the FR-1 alloy, the FR-4 alloy also possesses the heterogeneous grain structure with tri-hierarchical α precipitations after heat-treated at 600 °C-750 °C (Figure 6.24 a and b). However, the width and amount of α_p colony are narrower and smaller in treated FR-4 alloy than in the treated FR-1 alloy, because the α_p is newly formed from GB-α in FR-4 alloy but is inherited from the as-forged alloy in FR-1 alloy. Different

from the air-cooled FR-1 alloy after TMP, the deformation energy induced by significant plastic deformation during TMP is remained in the water-quenched FR-4 alloy. Therefore, post-HT becomes the great chance for the plentiful deformation storage energy in FR-4 alloy to be released intensively, which lead to the belated formation of large-scale lath α_p colony. The higher amount of released storage energy of FR-4 alloy during post-HT also make it understandable that why the size and static globularization tendency of α_s phases are bigger and stronger for FR-4 alloy than those for FR-1 alloy at the same post-HT temperature between 600 °C-750 °C.

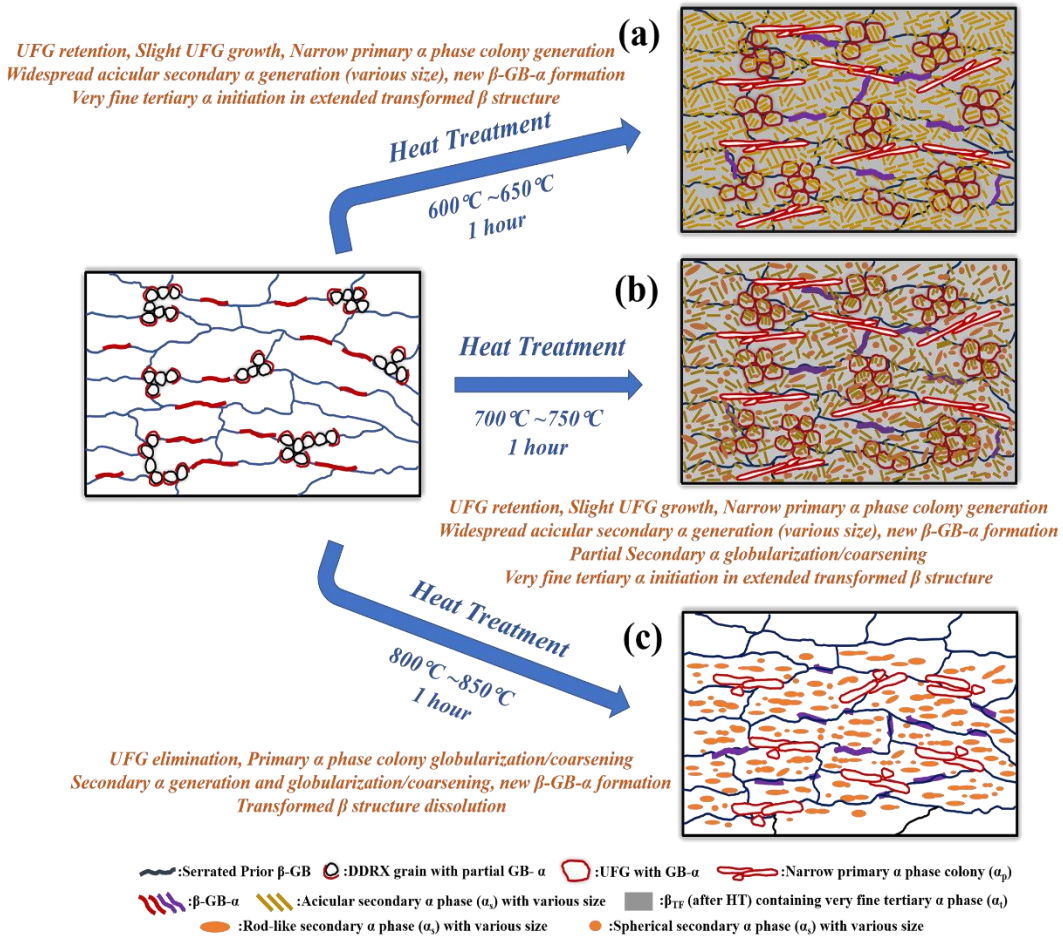

Figure 6.24 Schematic illustration and description of the microstructure evolution mechanism for FR-4 alloy during heat treatment at various temperatures: (a) 600 °C-650 °C; (b) 700 °C-750 °C; (c) 800 °C-850 °C.

After heat-treating at relatively high temperatures of 800 °C and 850 °C, similar microstructures are observed for FR-1 and FR-4 alloys (see Figure 6.18e_1-f_5 and Figure 6.21e_1-f_3), suggest that the primary microstructures of FR-4 and FR-1 are evolved in a similar way during the post-HT at these conditions (as illustrated in

Figure 6.24c), except globularized α_p colony size is smaller and narrower in FR-4 alloy than in FR-1 alloy.

6.6.3 Mechanical properties of the heat-treated alloy

The mechanical properties (room-temperature tensile testing) of FR-1 alloy heat-treated at different temperatures are listed in Table 6.4. It is clear that the properties of as-forged alloy have been improved and/or adjusted remarkably after heat treatment. When the alloy heat-treated at the temperatures between 600 °C and 750 °C, the as-heat-treated alloy's ductility is significantly improved comparing to the as-forged FR-1 alloy. Also, the ductility is continually improving with the increase of heat treatment temperature, showing a value of 3.82% for the 600 °C-treated FR-1 alloy and 8.64% for the 750 °C-treated FR-1 alloy. The corresponding strength is slightly reduced compared to the as-forged FR-1 alloy, having a UTS of 1420.2 MPa and hardness of 488.6HV for the 600 °C-treated alloy, and UTS of 1252.3 MPa and hardness of 410.2HV for the 750 °C-treated FR-1 alloy. Particularly, two excellent strength-ductility combinations (UTS and elongation) are achieved for the FR-1 alloy heat-treated at 700 °C and 750 °C, with values of 1386.5 MPa/6.76% and 1252.3 MPa/8.64%, respectively. These two strength-ductility balances are not only acceptable for metastable β titanium alloys in engineering applications but also comparable to or even better than those of the same PM alloys manufactured by other methods [45, 73-75] and IM [40, 52, 76] counterparts. Both ductility and strength/hardness are lower for the 800 °C and 850 °C heat-treated FR-1 alloy than the as-forged FR-1 alloy, with a UTS lower than 1200 MPa, hardness lower than 400 HV, and elongation of lower than 3.6%.

Table 6.4 Tensile properties of FR-1 alloy after heat treatment at various temperatures.

NFA temperature	YS* (MPa)	UTS* (MPa)	Elongation* (%)	Hardness (HV)
600 °C	1335.5	1420.2	3.82	488.6
650 °C	1304.6	1392.8	5.13	461.2
700 °C	1295.3	1386.5	6.76	453.2
750 °C	1170.5	1252.3	8.64	410.2
800 °C	1075.9	1157.2	3.55	388.8
850 °C	988.5	1030.0	2.98	359.4

* Using the dog-bone-shaped cross-section specimens for the tensile tests here.

Combined with the microstructure observation results and the revealed microstructural evolution mechanisms of FR-1 alloy, it can be understood that the growth and partial globularization of α_s phases and residual stress relief are beneficial to enhance the ductility, but lead to a slight reduction of strength/hardness for the alloy heat-treated at 600 °C-750 °C.

The high strength of FR-1 alloy after heat treatment at 600 °C-750 °C is mainly attributed to the generation of high-density α_s and nanoscale-dispersed α_t phases. Firstly, the α_s and α_t phases initiated by diffusion-induced transformation can introduce severe lattice distortion in their structure, and this limits the mobility of the dislocations during tensile deformation by the highly-defected sub-structures. Secondly, the high-density distribution of α_s and α_t phases introduce a large amount of α/β interface in the alloy, causing significant interface strengthening effect. Thirdly, α_s and α_t phases in FR-1 alloy also have the configuration of multi-variant (dimension and direction) precipitation (see Figure 6.23), which further increase the strength by extra dislocation slip transfer resistance. At last, the prior UFG and their GB-α phase in the alloy also contribute to the strength enhancement of FR-1 alloy remarkably, just like the reinforcement in composite materials, which block the deformation (grain structure and dislocation) slip.

As for the improved ductility of FR-1 alloy, the widespread tri-hierarchical α structure is the most important factor to be considered. After heat treatment, the large-sized α_p phase is relatively soft in the microstructure of metastable β titanium alloys [20, 77], comparing to α_s and β_{TF} structure. During tensile deformation, large lath α_p colony in the alloy can accommodate dislocation movement, sustain the displacement, and absorb the external deformation energy, thus increasing the alloy's ductility [23, 78]. Furthermore, the dispersed α phases with multi-hierarchy in the microstructure can improve the stress/strain compatibility, homogenize the strain partitioning, and resist the cracking propagation during deformation [20], and thus help increase the ductility of FR-1 alloy as well.

The existence of fine and large number of α_s/α_t phases generates high α/β interface density and a large number of sub-structures, and these would cause a significant strengthening effect on the alloy. However, the over-strong strengthening effect also leads to the degradation of ductility (at 600 °C and 650 °C), according to the

widely-accepted metallic materials' strength-ductility trade-off [15, 24, 79]. That is why the ductility of heat-treated FR-1 alloy is increased dramatically with increasing the heat treatment temperature from 600 °C to 750 °C, and the superior strength-ductility balance is achieved for the 700 °C and 750 °C heat-treated FR-1 alloys which have balanced microstructures (see Figure 6.22b, CG+UFG grain mixture, widespread tri-modal precipitation, wide α_p colonies, partial α_s phase globularization) after post-HT.

When the α_p and α_s phases are completely globularized/coarsened for the alloy treated at 800 °C-850 °C, both strength and ductility are significantly decreased for the FR-1 alloy. Furthermore, significant reduction in the amount of α precipitation and subsequently reduced α/β interface, as well as the lack of UFG and tri-hierarchical α structure in the microstructure are other reasons to cause low strength and ductility for 800 °C and 850 °C heat-treated FR-1 alloy comparing to the lower temperature treated FR-1 alloy. Because of the completely globularized/coarsened α_p/α_s phases and the absence of α_t phase (β_{TF} structure) in the microstructure of FR-1 alloy after post-HT at 800 °C and 850 °C, both the α precipitation phase density and α/β interface density are reduced remarkably, which makes the alloy less strengthened. UFG no longer exists in the microstructure at these two conditions, and this makes the strength reduction situation more serious. Moreover, the loss of tri-hierarchical α structure and emergence of precipitation-free regions also make the alloy brittle. Additionally, relatively inhomogeneous precipitation distribution and single β matrix in the microstructure lead to degradation of stress/strain compatibility and easy propagation of cracking during tensile deformation. Therefore, FR-1 alloy has low strength and poor ductility at 800 °C, and it becomes even worse at 850 °C.

Figure 6.25 shows the typical SEM fracture surface morphology FR-1 alloys heat-treated at various temperatures. As shown in Figure 6.25a, cleavage facets, tear ridges and some small/shallow dimples are observed in the fracture surface of the alloy heat-treated at 600 °C, which indicates that alloy is fractured with the ductile-brittle mixed cleavage mechanism. Similar features are seen in the fracture surface of 650 °C-treated FR-1 alloy (see Figure 6.25b_1-b_2), showing larger amount and size of dimples than that of the alloy treated at 600 °C, and this implies that the tensile ductility is improved. A large amount of dispersed deep dimples are

appeared on the fracture surface of the FR-1 alloy heat-treated at 700 °C and 750 °C, as shown in Figure 6.25c_1-c_2 and Figure 6.25d_1-d_2, and no cleavage fracture characteristics visible. Furthermore, secondary cracks and deep ravines are also observed on the fracture surface of 750 °C heat-treated alloy, suggesting that very high tensile ductility is achieved. For the FR-1 alloy heat-treated at 800 °C and 850 °C (see Figure 6.25e-f), the failures of tensile specimens are dominated by complete brittle cleavage mechanism, and this is proved by the large-scale cleavage facets, features of river-like patterns without dispersive dimples on the fracture surface.

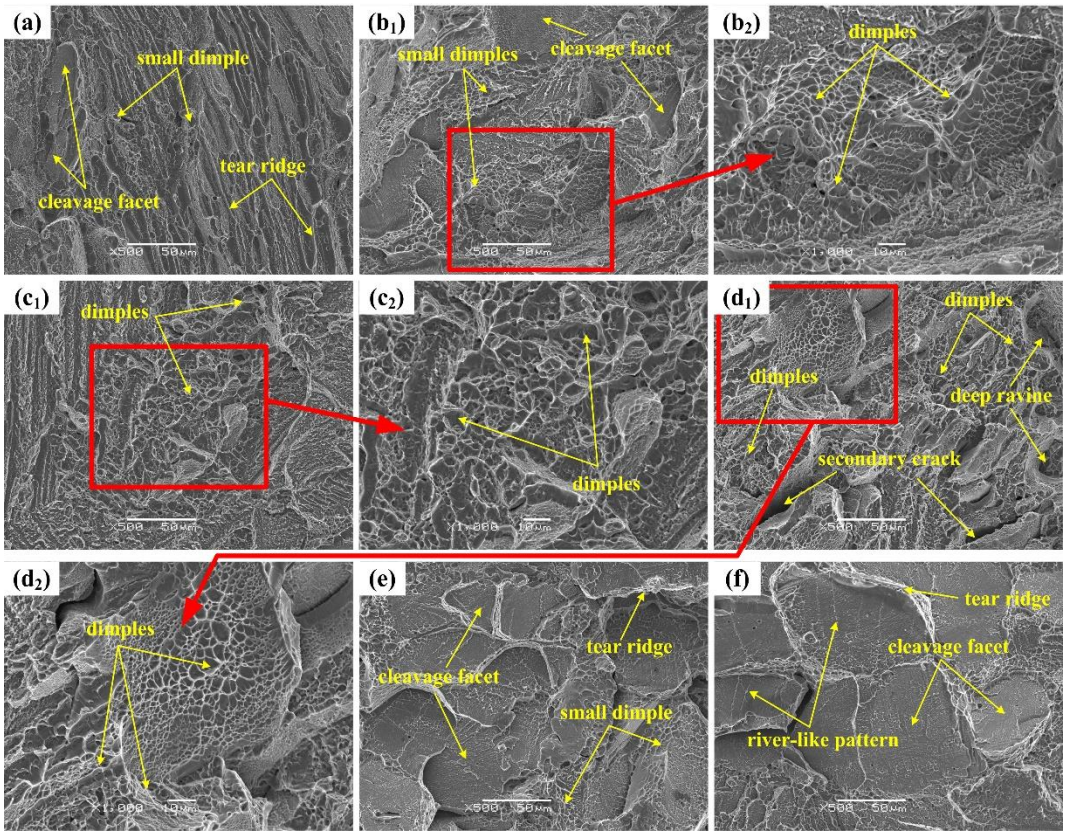

Figure 6.25 Representative SEM fracture surface of the heat-treated (various NFA temperatures) FR-1 alloy after tensile testing: (a) 600 °C; (b_1)-(b_2) 650 °C; (c_1)-(c_2) 700 °C; (d_1)-(d_2) 750 °C; (e) 800 °C; (f) 850 °C.

The mechanical properties of FR-4 alloy heat-treated at different temperatures are displayed in Table 6.5. It is apparent that the mechanical performance response of FR-4 alloy to heat treatment is similar to that of FR-1 alloy. Both of strength and hardness of the heat-treated alloy is decreased with increasing the heat treatment temperature from 600 °C to 850 °C, but the respective ductility of the heat-treated FR-4 alloy is firstly increased and then decreased. The highest ductility achieved for the FR-4 alloy is 5.63% when the alloy treated at 750 °C. Whereas, relatively

low ductility and strength/hardness are obtained for the FR-4 alloy heat-treated at 800 °C and 850 °C, with a UTS lower than 1030 MPa, hardness lower than 350 HV and elongation lower than 3.5%.

Table 6.5 Tensile properties of FR-4 alloy after heat treatment at various temperatures.

NFA temperature	YS* (MPa)	UTS* (MPa)	Elongation* (%)	Hardness (HV)
600 °C	1320.6	1405.5	3.68	468.9
650 °C	1299.5	1383.2	4.14	455.2
700 °C	1258.6	1357.5	4.78	428.8
750 °C	1158.5	1235.7	5.63	397.6
800 °C	965.5	1025.2	3.18	347.9
850 °C	957.9	1013.5	3.48	334.5

* Using the dog-bone-shaped cross-section specimens for the tensile tests here.

The primary microstructure discrepancy between the heat-treated FR-1 alloy and the heat-treated FR-4 alloy are that the width/proportion of α_p colony and static globularization tendency of α_s phases. The width/proportion of α_p colonies (about 10 μm) is smaller in the heat-treated FR-4 alloy than in the heat-treated FR-1 alloy (larger than 30 μm), and the static globularization tendency of α_s phases are significantly stronger for FR-4 alloy than those for FR-1 alloy at the same post-HT temperatures (see Figure 6.22 and Figure 6.24). Thus, it can be concluded that wide/massive α_p colony and appropriately-globularized α_s phase in the microstructure are beneficial to achieve the balanced mechanical properties for PM Ti-5553 alloy.

6.7 Summary

In this chapter, we investigate the effects of various TMP processes, which are selected based on the guidance of hot processing maps and deformation mechanism maps established in Chapters 4 and 5, and post-heat treatment on the microstructure and mechanical properties of the as-consolidated PM Ti-5553 alloy. Moreover, the underlying microstructural evolution mechanisms during the various processes of TMP and heat treatment are also revealed. The primary findings are summarised as below:

(1) The as-consolidated PM Ti-5553 alloy shows excellent hot workability and is safely thermomechanical-processed at the optimal processing conditions suggested by the hot processing maps and deformation mechanism maps (as discussed in Chapters 4 and 5).

(2) The as-forged PM Ti-5553 alloy processed at 950 °C/~0.01 s^{-1} (FR-1 alloy) shows the highest mechanical properties during room-temperature tensile testing (UTS=1450.9 MPa, elongation=3.23%), comparing to the alloy processed at other conditions, and this is attributed to the generated heterogeneous grain and hierarchical α precipitation structures.

(3) Superior strength-ductility combinations are achieved for FR-1 alloy after heat treatment at 700 °C and 750 °C, with tensile UTS of 1386.5 MPa and elongation of 6.76% for the 700 °C-treated alloy and UTS of 1252.3 MPa and elongation of 8.64% for the 750 °C-treated alloy. These excellent mechanical properties are comparable or even better than those of some IM-manufactured metastable β titanium alloys.

(4) The excellent strength-ductility synergy achieved for the heat-treated PM-Ti-5553 alloy is attributed to the alloy contains heterogeneous grain structure with tri-hierarchical α precipitation. Conversely, the absence of primary α phase and grain size heterogeneity in the alloy's microstructure leads to deterioration of the resultant strength and ductility.

Reference

[1] Z.X. Zhang, S.J. Qu, A.H. Feng, J. Shen, D.L. Chen, Hot deformation behavior of Ti-6Al-4V alloy: effect of initial microstructure, J. Alloys Compd. 718 (2017) 170-181.

[2] X.G. Fan, Y. Zhang, P.F. Gao, Z.N. Lei, M. Zhan, Deformation behavior and microstructure evolution during hot working of a coarse-grained Ti-5Al-5Mo-5V-3Cr-1Zr titanium alloy in beta phase field, Mater. Sci. Eng. A 694 (2017) 24-32.

[3] Z.X. Zhang, S.J. Qu, A.H. Feng, X. Hu, J. Shen, The low strain rate response of as-cast Ti-6Al-4V alloy with an initial coarse lamellar structure, Metals 8 (2018).

[4] X.G. Fan, H. Yang, P.F. Gao, R. Zuo, P.H. Lei, The role of dynamic and post dynamic recrystallization on microstructure refinement in primary working of a coarse grained two-phase titanium alloy, J. Mater. Process. Technol. 234 (2016) 290-299.

[5] X.L. Wu, Y.T. Zhu, Heterogeneous materials: a new class of materials with unprecedented mechanical properties, Mater. Res. Lett. 5 (2017) 527-532.

[6] W. Chrominski, M. Lewandowska, Precipitation phenomena in ultrafine grained Al-Mg-Si alloy with heterogeneous microstructure, Acta Mater. 103 (2016) 547-557.

[7] X. Wu, M. Yang, F. Yuan, G. Wu, Y. Wei, X. Huang, Y. Zhu, Heterogeneous lamella structure unites ultrafine-grain strength with coarse-grain ductility, Proc. Natl. Acad. Sci. 112 (2015) 14501-14505.

[8] X. Wu, P. Jiang, L. Chen, F. Yuan, Y.T. Zhu, Extraordinary strain hardening by gradient structure, Proc. Natl. Acad. Sci. 111 (2014) 7197-7201.

[9] Y. Ma, F.P. Yuan, M.X. Yang, P. Jiang, E. Ma, X.L. Wu, Dynamic shear deformation of a CrCoNi medium-entropy alloy with heterogeneous grain structures, Acta Mater. 148 (2018) 407-418.

[10] Y. Wang, M. Chen, F. Zhou, E. Ma, High tensile ductility in a nanostructured metal, Nature 419 (2002) 912-915.

[11] W. Guo, Z.R. Pei, X.H. Sang, J.D. Poplawsky, S. Bruschi, J. Qu, D. Raabe, H.B. Bei, Shape-preserving machining produces gradient nanolaminate medium entropy alloys with high strain hardening capability, Acta Mater. 170 (2019) 176-186.

[12] J. Gao, J. Nutter, X. Liu, D. Guan, Y. Huang, D. Dye, W.M. Rainforth, Segregation mediated heterogeneous structure in a metastable beta titanium alloy with a superior combination of strength and ductility, Sci. Rep. 8 (2018) 7512.

[13] S. Shin, C. Zhu, C. Zhang, K.S. Vecchio, Extraordinary strength-ductility synergy in a heterogeneous-structured β-Ti alloy through microstructural optimization, Mater. Res. Lett. 7 (2019) 467-473.
[14] R.X. Zheng, G.D. Li, Z. Zhang, Y.T. Zhang, S.Y. Yue, X. Chen, K. Ameyama, C.L. Ma, Manipulating the powder size to achieve enhanced strength and ductility in harmonic structured Al alloy, Mater. Res. Lett. 7 (2019) 217-224.
[15] S.W. Wu, G. Wang, Q. Wang, Y.D. Jia, J. Yi, Q.J. Zhai, J.B. Liu, B.A. Sun, H.J. Chu, J. Shen, P.K. Liaw, C.T. Liu, T.Y. Zhang, Enhancement of strength-ductility trade-off in a high-entropy alloy through a heterogeneous structure, Acta Mater. 165 (2019) 444-458.
[16] C.E. Slone, J. Miao, E.P. George, M.J. Mills, Achieving ultra-high strength and ductility in equiatomic CrCoNi with partially recrystallized microstructures, Acta Mater. 165 (2019) 496-507.
[17] G. Chen, J.W. Qiao, Z.M. Jiao, D. Zhao, T.W. Zhang, S.G. Ma, Z.H. Wang, Strength-ductility synergy of $Al_{0.1}$CoCrFeNi high-entropy alloys with gradient hierarchical structures, Scripta Mater. 167 (2019) 95-100.
[18] R.X. Zheng, M.W. Liu, Z. Zhang, K. Ameyama, C.L. Ma, Towards strength-ductility synergy through hierarchical microstructure design in an austenitic stainless steel, Scripta Mater. 169 (2019) 76-81.
[19] C. Zhang, C.Y. Zhu, K. Vecchio, Non-equiatomic FeNiCoAl-based high entropy alloys with multiscale heterogeneous lamella structure for strength and ductility, Mater. Sci. Eng. A 743 (2019) 361-371.
[20] W. Zhu, J. Lei, C. Tan, Q. Sun, W. Chen, L. Xiao, J. Sun, A novel high-strength β-Ti alloy with hierarchical distribution of α-phase: The superior combination of strength and ductility, Mater. Des. 168 (2019) 107640.
[21] S.A. Mantri, D. Choudhuri, T. Alam, G.B. Viswanathan, J.M. Sosa, H.L. Fraser, R. Banerjee, Tuning the scale of α precipitates in β-titanium alloys for achieving high strength, Scripta Mater. 154 (2018) 139-144.
[22] A. Devaraj, V.V. Joshi, A. Srivastava, S. Manandhar, V. Moxson, V.A. Duz, C. Lavender, A low-cost hierarchical nanostructured beta-titanium alloy with high strength, Nat. Commun. 7 (2016) 11176.
[23] W. Zhu, J. Lei, Z. Zhang, Q. Sun, W. Chen, L. Xiao, J. Sun, Microstructural dependence of strength and ductility in a novel high strength β titanium alloy with Bi-modal structure, Mater. Sci. Eng. A 762 (2019) 138086.
[24] S. Shukla, D. Choudhuri, T.H. Wang, K.M. Liu, R. Wheeler, S. Williams, B.

Gwalani, R.S. Mishra, Hierarchical features infused heterogeneous grain structure for extraordinary strength-ductility synergy, Mater. Res. Lett. 6 (2018) 676-682.
[25] J.K. Fan, H.C. Kou, M.J. Lai, B. Tang, H. Chang, J.S. Li, Characterization of hot deformation behavior of a new near beta titanium alloy: Ti-7333, Mater. Des. 49 (2013) 945-952.
[26] R. Dong, J. Li, J. Fan, H. Kou, B. Tang, Precipitation of α phase and its morphological evolution during continuous heating in a near β titanium alloy Ti-7333, Mater. Charact. 132 (2017) 199-204.
[27] G. Yang, H. Kou, J. Yang, J. Li, H. Fu, In-situ investigation on the β to α phase transformation in Ti-45Al-8.5Nb-(W,B,Y) alloy, J. Alloys Compd. 663 (2016) 594-600.
[28] N. Kherrouba, M. Bouabdallah, R. Badji, D. Carron, M. Amir, Beta to alpha transformation kinetics and microstructure of Ti-6Al-4V alloy during continuous cooling, Mater. Chem. Phys. 181 (2016) 462-469.
[29] X.X. Gao, W.D. Zeng, S.F. Zhang, Q.J. Wang, A study of epitaxial growth behaviors of equiaxed alpha phase at different cooling rates in near alpha titanium alloy, Acta Mater. 122 (2017) 298-309.
[30] J.W. Lu, Y.Q. Zhao, P. Ge, H.Z. Niu, Microstructure and beta grain growth behavior of Ti-Mo alloys solution treated, Mater. Charact. 84 (2013) 105-111.
[31] T. Wang, H.Z. Guo, L.J. Tan, Z.K. Yao, Y. Zhao, P.H. Liu, Beta grain growth behaviour of TG6 and Ti17 titanium alloys, Mater. Sci. Eng. A 528 (2011) 6375-6380.
[32] S.L. Semiatin, P.N. Fagin, M.G. Glavicic, I.M. Sukonnik, O.M. Ivasishin, Influence on texture on beta grain growth during continuous annealing of Ti-6Al-4V, Mater. Sci. Eng. A 299 (2001) 225-234.
[33] P. Manda, U. Chakkingal, A.K. Singh, Hardness characteristic and shear band formation in metastable β-titanium alloys, Mater. Charact. 96 (2014) 151-157.
[34] D.Y. Qin, Y.F. Lu, Q. Liu, L. Zhou, Effects of Si addition on mechanical properties of Ti-5Al-5V-5Mo-3Cr alloy, Mater. Sci. Eng. A 561 (2013) 460-467.
[35] V.C. Opini, C.A.F. Salvador, K.N. Campo, E.S.N. Lopes, R.R. Chaves, R. Caram, α phase precipitation and mechanical properties of Nb-modified Ti-5553 alloy, Mater. Sci. Eng. A 670 (2016) 112-121.
[36] D. Qin, Y. Lu, D. Guo, L. Zheng, Q. Liu, L. Zhou, Tensile deformation and fracture of Ti-5Al-5V-5Mo-3Cr-1.5Zr-0.5Fe alloy at room temperature, Mater. Sci. Eng. A 587 (2013) 100-109.

[37] B.Z. Jiang, S. Emura, K. Tsuchiya, Microstructural evolution and its effect on the mechanical behavior of Ti-5Al-5Mo-5V-3Cr alloy during aging, Mater. Sci. Eng. A 731 (2018) 239-248.
[38] B. Jiang, S. Emura, K. Tsuchiya, Improvement of ductility in Ti-5Al-5Mo-5V-3Cr alloy by network-like precipitation of blocky α phase, Mater. Sci. Eng. A 722 (2018) 129-135.
[39] S.K. Kar, S. Suman, S. Shivaprasad, A. Chaudhuri, A. Bhattacharjee, Processing-microstructure-yield strength correlation in a near β Ti alloy, Ti-5Al-5Mo-5V-3Cr, Mater. Sci. Eng. A 610 (2014) 171-180.
[40] S. Shekhar, R. Sarkar, S.K. Kar, A. Bhattacharjee, Effect of solution treatment and aging on microstructure and tensile properties of high strength β titanium alloy, Ti-5Al-5V-5Mo-3Cr, Mater. Des. 66 (2015) 596-610.
[41] D. Qin, Y. Lu, Q. Liu, L. Zheng, L. Zhou, Transgranular shearing introduced brittlement of Ti-5Al-5V-5Mo-3Cr alloy with full lamellar structure at room temperature, Mater. Sci. Eng. A 572 (2013) 19-24.
[42] D. Qin, Y. Lu, D. Guo, L. Zheng, Q. Liu, L. Zhou, On preparation of bimodal Ti-5Al-5V-5Mo-3Cr-0.4Si (Ti-5553s) alloy: α+β forging and heat treatment, Mater. Sci. Eng. A 609 (2014) 42-52.
[43] N. Wain, X.J. Hao, G.A. Ravi, X. Wu, The influence of carbon on precipitation of α in Ti-5Al-5Mo-5V-3Cr, Mater. Sci. Eng. A 527 (2010) 7673-7683.
[44] N. Perevoshchikova, C.R. Hutchinson, X. Wu, The design of hot-isostatic pressing schemes for Ti-5Al-5Mo-5V-3Cr (Ti-5553), Mater. Sci. Eng. A 657 (2016) 371-382.
[45] H. Schwab, F. Palm, U. Kuhn, J. Eckert, Microstructure and mechanical properties of the near-beta titanium alloy Ti-5553 processed by selective laser melting, Mater. Des. 105 (2016) 75-80.
[46] F. Geng, M. Niinomi, M. Nakai, Observation of yielding and strain hardening in a titanium alloy having high oxygen content, Mater. Sci. Eng. A 528 (2011) 5435-5445.
[47] D. Banerjee, J.C. Williams, Perspectives on titanium science and technology, Acta Mater. 61 (2013) 844-879.
[48] P. Kwasniak, M. Muzyk, H. Garbacz, K.J. Kurzydlowski, Influence of C, H, N, and O interstitial atoms on deformation mechanism in titanium-first principles calculations of generalized stacking fault energy, Mater. Lett. 94 (2013) 92-94.
[49] M. Yan, W. Xu, M.S. Dargusch, H.P. Tang, M. Brandt, M. Qian, Review of

effect of oxygen on room temperature ductility of titanium and titanium alloys, Powder Metall. 57 (2014) 251-257.
[50] Q. Yu, L. Qi, T. Tsuru, R. Traylor, D. Rugg, J.W. Morris, Jr., M. Asta, D.C. Chrzan, A.M. Minor, Metallurgy. Origin of dramatic oxygen solute strengthening effect in titanium, Science 347 (2015) 635-639.
[51] C. Kale, P. Garg, B.G. Bazehhour, S. Srinivasan, M.A. Bhatia, P. Peralta, K.N. Solanki, Oxygen effects on crystal plasticity of titanium: a multiscale calibration and validation framework, Acta Mater. 176 (2019) 19-32.
[52] J. Fan, J. Li, H. Kou, K. Hua, B. Tang, Y. Zhang, Influence of solution treatment on microstructure and mechanical properties of a near β titanium alloy Ti-7333, Mater. Des. 83 (2015) 499-507.
[53] P. Manda, R.M. Samudrala, M.K. Mohan, A.K. Singh, Microstructure, texture, and mechanical properties of β solution-treated and aged metastable β titanium alloy, Ti-5Al-5Mo-5V-3Cr, Metall. Mater. Trans. A 48 (2017) 4539-4552.
[54] L. Ren, W. Xiao, H. Chang, Y. Zhao, C. Ma, L. Zhou, Microstructural tailoring and mechanical properties of a multi-alloyed near β titanium alloy Ti-5321 with various heat treatment, Mater. Sci. Eng. A 711 (2018) 553-561.
[55] S.K. Kar, A. Ghosh, N. Fulzele, A. Bhattacharjee, Quantitative microstructural characterization of a near beta Ti alloy, Ti-5553 under different processing conditions, Mater. Charact. 81 (2013) 37-48.
[56] S. Nag, R. Banerjee, R. Srinivasan, J.Y. Hwang, M. Harper, H.L. Fraser, ω-Assisted nucleation and growth of α precipitates in the Ti-5Al-5Mo-5V-3Cr-0.5Fe β titanium alloy, Acta Mater. 57 (2009) 2136-2147.
[57] A. Ghosh, S. Sivaprasad, A. Bhattacharjee, S.K. Kar, Microstructure-fracture toughness correlation in an aircraft structural component alloy Ti-5Al-5V-5Mo-3Cr, Mater. Sci. Eng. A 568 (2013) 61-67.
[58] S. Mandal, B.T. Gockel, S. Balachandran, D. Banerjee, A.D. Rollett, Simulation of plastic deformation in Ti-5553 alloy using a self-consistent viscoplastic model, Int. J, Plasticity 94 (2017) 57-73.
[59] J.C. Fanning, Properties of TIMETAL 555 (Ti-5Al-5Mo-5V-3Cr-0.6Fe), J. Mater. Eng. Perform. 14 (2005) 788-791.
[60] K. Hua, X.Y. Xue, H.C. Kou, J.K. Fan, B. Tang, J.S. Li, Characterization of hot deformation microstructure of a near beta titanium alloy Ti-5553, J. Alloys Compd. 615 (2014) 531-537.
[61] H.L. Wu, Z.C. Sun, J. Cao, Z.K. Yin, Formation and evolution of tri-modal

microstructure during dual heat treatment for TA15 Ti-alloy, J. Alloys Compd. 786 (2019) 894-905.
[62] Z.N. Lei, P.F. Gao, H.W. Li, Y. Cai, Y.X. Li, M. Zhan, Comparative analyses of the tensile and damage tolerance properties of tri-modal microstructure to widmanstatten and bimodal microstructures of TA15 titanium alloy, J. Alloys Compd. 788 (2019) 831-841.
[63] Z.N. Lei, P.F. Gao, H.W. Li, Y. Cai, M. Zhan, On the fracture behavior and toughness of TA15 titanium alloy with tri-modal microstructure, Mater. Sci. Eng. A 753 (2019) 238-246.
[64] P.F. Gao, G. Qin, X.X. Wang, Y.X. Li, M. Zhan, G.J. Li, J.S. Li, Dependence of mechanical properties on the microstructural parameters of TA15 titanium alloy with tri-modal microstructure, Mater. Sci. Eng. A 739 (2019) 203-213.
[65] P.F. Gao, Y. Cai, M. Zhan, X.G. Fan, Z.N. Lei, Crystallographic orientation evolution during the development of tri-modal microstructure in the hot working of TA15 titanium alloy, J. Alloys Compd. 741 (2018) 734-745.
[66] Y.G. Zhou, W.D. Zeng, H.Q. Yu, An investigation of a new near-beta forging process for titanium alloys and its application in aviation components, Mater. Sci. Eng. A 393 (2005) 204-212.
[67] G.H. Zhang, H.B. Dong, S.L. Zhu, C. Liu, X.P. Yu, Tri-modal structure of TC4-DT alloy through triple heat treatment, Rare Metal Mat. Eng. 45 (2016) 2454-2457.
[68] J.W. Xu, W.D. Zeng, H.Y. Ma, D.D. Zhou, Static globularization mechanism of Ti-17 alloy during heat treatment, J. Alloys Compd. 736 (2018) 99-107.
[69] J.W. Xu, W.D. Zeng, X.Y. Zhang, D.D. Zhou, Analysis of globularization modeling and mechanisms of alpha/beta titanium alloy, J. Alloys Compd. 788 (2019) 110-117.
[70] J.W. Xu, W.D. Zeng, Z.Q. Jia, X. Sun, J.H. Zhou, Static globularization kinetics for Ti-17 alloy with initial lamellar microstructure, J. Alloys Compd. 603 (2014) 239-247.
[71] J.W. Xu, W.D. Zeng, Z.Q. Jia, X. Sun, J.H. Zhou, Prediction of static globularization of Ti-17 alloy with starting lamellar microstructure during heat treatment, Comp. Mater. Sci. 92 (2014) 224-230.
[72] J.W. Xu, W.D. Zeng, X. Sun, Z.Q. Jia, J.H. Zhou, Static coarsening behavior of the lamellar alpha in Ti-17 alloy, J. Alloys Compd. 631 (2015) 248-254.
[73] H.D. Carlton, K.D. Klein, J.W. Elmer, Evolution of Microstructure and mechanical properties of selective laser melted Ti-5Al-5V-5Mo-3Cr after heat

treatments, Sci. Technol. Weld. Joi. 24 (2019) 465-473.
[74] W. Chen, C. Chen, X. Zi, X. Cheng, X. Zhang, Y.C. Lin, K. Zhou, Controlling the microstructure and mechanical properties of a metastable β titanium alloy by selective laser melting, Mater. Sci. Eng. A 726 (2018) 240-250.
[75] M. Ahmed, T. Li, G. Casillas, J.M. Cairney, D. Wexler, E.V. Pereloma, The evolution of microstructure and mechanical properties of Ti-5Al-5Mo-5V-2Cr-1Fe during ageing, J. Alloys Compd. 629 (2015) 260-273.
[76] J. Fan, J. Li, H. Kou, K. Hua, B. Tang, Y. Zhang, Microstructure and mechanical property correlation and property optimization of a near β titanium alloy Ti-7333, J. Alloys Compd. 682 (2016) 517-524.
[77] C. Tan, Q. Sun, L. Xiao, Y. Zhao, J. Sun, Characterization of deformation in primary α phase and crack initiation and propagation of TC21 alloy using in-situ SEM experiments, Mater. Sci. Eng. A 725 (2018) 33-42.
[78] Z. Sun, X. Mao, H. Wu, H. Yang, J. Li, Tri-modal microstructure and performance of TA15 Ti-alloy under near-β forging and given subsequent solution and aging treatment, Mater. Sci. Eng. A 654 (2016) 113-123.
[79] Y.J. Wei, Y.Q. Li, L.C. Zhu, Y. Liu, X.Q. Lei, G. Wang, Y.X. Wu, Z.L. Mi, J.B. Liu, H.T. Wang, H.J. Gao, Evading the strength-ductility trade-off dilemma in steel through gradient hierarchical nanotwins, Nat. Commun. 5 (2014) 3580.

7 Conclusions and perspectives

7.1 Conclusions

In the present PhD work, the PM Ti-5553 metastable β titanium alloy was fabricated via the low-cost TPC routes from blended elemental powder mixture, the detailed investigation on the alloy's deformation behaviour (at both room and high temperature) and microstructural evolution during hot processing was carried out, and the hot processing map and deformation mechanisms were established and determined. For comparison, similar research has been undertaken for the IM counterpart Ti-5553 alloy which was prepared by vacuum-arc melting. Optimized forging parameters were identified for the PM Ti-5553 alloy based on the understanding of the hot deformation behaviour and the established hot processing map, then sound PM Ti-5553 alloy pancakes were successfully produced, and subsequent heat treatment effects on the forged alloy were investigated. From abovementioned research, primary conclusions can be drawn:

(1) PM Ti-5553 alloy has been cost-effectively consolidated from blended elemental powder mixture via TPC process, which can reduce 30%-40% and 40%-50% manufacturing cost than conventional IM and PA-PM routes, respectively. The as-consolidated PM alloy has much finer grain size, higher β phase transformation temperature and higher interstitial element (oxygen and nitrogen) content than those of the IM counterpart.

(2) The PM alloy exhibits lower load-bearing capacity and tensile ductility than those of IM alloy during the in-situ tensile test, and the coalesced GB-α and widened α″/β microcracks contribute to its early brittle failure. The IM alloy has better compatible-slip-deformation capability than PM alloy, and the serious cracking at the V-shape notch and the microcracks near α/β interfaces together lead to gradual fracture of the IM alloy specimen. The residual pores and microvoids existed in PM alloy have little effects on the alloy's slip deformation and fracture behaviour.

(3) The hot deformation parameters significantly affect the PM alloy's flow stress, activation energy and softening mechanism. The flow stress is increased with decreasing the deformation temperature and increasing the strain rate, and vice

versa. The deformation activation energy of PM alloy is 371.65 kJ/mol in the (α+β) region and 226.94 kJ/mol in the β region, respectively.

(4) Hot processing maps and specific deformation mechanisms in different processing region are established and determined for the PM Ti-5553 alloy. The optimal processing window for PM Ti-5553 alloy is determined: processing temperatures of 900 °C-1050 °C, combined with deformation strain rates below 1 s^{-1} with the high deformation degree to at least 70% of height reduction. The potential "best" processing condition is recommended as the medium deformation temperature (about 950 °C) and the moderate-low strain rate (about 0.01 s^{-1}). Furthermore, because of flow localization and external cracking, unstable deformation happens when the deformation temperature is lower than 1025 °C and the strain rate is higher than 1 s^{-1}, and this region should be avoided for processing PM Ti-5553 alloy.

(5) The PM Ti-5553 alloy exhibits lower flow stress, slighter discontinuous yielding phenomenon and less adiabatic temperature rising than its IM counterpart at the identical processing conditions. Comparing to IM Ti-5553 alloy, the PM Ti-5553 alloy has lower average activation energy, larger optimal processing windows, smaller flow instability region and higher cracking resistance.

(6) Dynamic α globularization and coarsening are the dominated mechanisms for PM Ti-5553 alloy deformed at low temperature (700 °C to 800 °C) and low strain rate ($\dot{\varepsilon} \leq 0.1$ s^{-1}), while IM Ti-5553 alloy is governed by dynamic α precipitation and its fracturing with strong preferred crystal orientation. The complete dynamic recrystallization temperature for PM alloy is about 100 °C lower than that of the IM counterpart, and DRX mechanism is controlled by DDRX for the PM alloy but CDRX for the IM counterpart.

(7) Based on the guidance of the hot processing map, the as-consolidated PM Ti-5553 alloy is safely forged at the optimal processing window (temperature between 900 °C-1050 °C, strain rate less than 1 s^{-1} and 75% of height reduction). The alloy forged at 950 °C/~0.01 s^{-1} (FR-1 alloy) shows the highest mechanical properties (UTS: 1450.9 MPa, elongation: 3.23% and MH: 492.4 HV), comparing to those processed at either higher temperature or higher strain rate.

(8) Various heat treatments have been carried out for the forged PM Ti-5553 alloy to tailor the alloy's microstructure for achieving strength-ductility balance. Attributed to the harmonious concurrence of hierarchical α precipitation and

heterogeneous grain structure, superior strength-ductility combinations are eventually achieved for the FR-1 alloy after the fast heat treatment at 700 °C and 750 °C, with the UTS and elongation values of 1386.5 MPa/6.76% and 1252.3 MPa/8.64%, respectively. These strength-ductility matchings are comparable and/or even better than other IM metastable β titanium alloys.

7.2 Perspectives

Based on the primary findings of the current research, further investigations are suggested below:

(1) For the hot deformation behaviour of PM and IM Ti-5553 alloys, the present work is mainly focused on microstructural evolution and related softening mechanisms. However, the pre-existing and newly-formed textures may have a significant influence on the materials' deformation behaviour. Therefore, it is meaningful to investigate the PM and IM Ti-5553 alloys' crystallographic orientation variation during hot deformation, and identify how those variations affect the different softening mechanisms.

(2) It is well known that twinning induced plasticity (TWIP effect) and phase transformation induced plasticity (TRIP effect) phenomena may occur in the metastable β titanium alloys with unstable microstructure. Although these effects have not been observed during in-situ tensile tests of the as-consolidated PM alloy, they may occur under compressive load. Thus, the compression tests at room temperature can be considered for the PM alloy to investigate the TWIP and TRIP effects at different strain rates and deformation degrees.

(3) Simple forging and heat treatments were designed in the current work to minimize the cost of processing high-quality PM Ti-5553 alloy component. It is valuable to design more complicated TMP and post-HT processes for the PM Ti-5553 alloy to achieve even higher mechanical properties. To be specific, multiple cogging/upsetting forging routes can be applied for the PM Ti-5553 alloy, and multiple-step annealing/aging can be designed and utilised for tailoring the processed Ti-5553 alloy's microstructure and the resultant mechanical properties.

(4) As both hot deformation behaviour and HT response were involved in the current research for PM alloy, there is an opportunity to make comparisons

between dynamic microstructure evolution mechanisms and static microstructure evolution mechanisms of the alloy. For example, dynamic α phase globularization/coarsening was observed during hot deformation (Chapter 4) and static α phase globularization/coarsening was found during post-HT (Chapter 6) of PM alloy. In a similar way, static recovery and recrystallization mechanisms can also be investigated during post-HT at varying conditions, and then contrast them to the dynamic ones.

(5) Considering practical engineering applications, fracture toughness and fatigue resistance are expected to be further examined for the PM Ti-5553 alloy to provide systematic mechanical performance evaluation.